
Tunable Antennas for Handsets Supporting MIMO

June 2016

Group 951/1051

Master Thesis

Title:

Tunable Antennas for Handsets Supporting MIMO

Theme:

Master Thesis

Project Period:

September 2015–June 2016

Project Group:

951/1051

Authors:

Lasse Thomsen

Henrik Aarup Vesterager

Søren Bøgeskov Nørgaard

Supervisors:

Samantha Caporal del Barrio
Shuai Zhang

Number of Prints:

3

Number of Pages:

167

Date for Submission:

June 1, 2016

Abstract:

The internal antennas of today's smartphones are often placed along the edge of the phone due to limited space and strict size requirements. As a result, the antennas are in very close proximity to the user. This results in detuning of the antenna and power absorption by the user. As the demand for higher data rates and bandwidth keeps increasing, it is desirable to counteract the detuning [1].

This project will investigate the development of digitally tunable LTE antennas, with minimized ground clearance, supporting MIMO. The solution proposes the use of a digitally controllable MEMS tuner in the matching network.

To investigate the tunable performance and the user effect interaction, three prototype designs have been simulated and measured. Three user effect cases have been simulated for each prototype and generally, the antennas show detuning as an effect of the user interaction. The prototype results have been compared and the best performing antenna design has been moved to and measured on a PCB with a WiSpry WS1040 digital tuner for each antenna.

A ground clearance investigation has been carried out and it was found, that a decent bandwidth can be obtained with only 5 mm of ground clearance. This lead to a new antenna design with 5 mm ground clearance, which has been measured on the tuner PCB.

Moving the two antenna designs from the prototype PCB to the tuner PCB introduces some high band coverage problems. The antenna and the transmission line have been modified to counteract these problems.

A MIMO tunable antenna solution has been presented with a minimized ground clearance of 5 mm. The results show promising and comparable performance with state-of-the-art antenna designs with much higher ground clearance.

Contents

I Analysis	3
1 Problem Analysis	4
1.1 LTE	4
1.2 Basic Antenna Parameters	7
1.3 Matching Circuits and Tuners	14
1.4 Basic Propagation Models	22
1.5 User Effects	24
1.6 MIMO in Handsets	27
1.7 Example LTE Link Budget	34
1.8 Finite Difference Time Domain	35
1.9 Vector Network Analyzer	40
1.10 Satimo StarLab Anechoic Chamber	41
1.11 Problem Statement	42
2 Requirements Specification	43
2.1 Functional Requirements	43
2.2 Specific Requirements	43
3 Test Specification	44
II Technical Solution	45
4 Preliminary Design and Simulation	46
4.1 Monopole Antenna	46
4.2 Triangle-Feed Antenna	51
4.3 Dual-Feed Antenna	55
4.4 Conclusion	59
5 User Effect Simulations	60
5.1 Monopole Antenna	61
5.2 Triangle-Feed Antenna	71
5.3 Dual-Feed Antenna	81
5.4 Conclusion	91
6 Prototypes	92
6.1 Monopole Antenna	92
6.2 Triangle-Feed Antenna	97
6.3 Dual-Feed Antenna	102
6.4 Conclusion	105
7 Minimized Antenna	106
7.1 Ground Clearance Simulation	106
7.2 Simulation	107
7.3 Measurements	110

7.4 Conclusion	113
8 Printed Circuit Board	114
8.1 Triangle-Feed Antenna	114
8.2 Modified Minimized Antenna	118
9 Conclusion	135
III Appendix	137
A Automatic Testing	138
A.1 Optical RFFE Communication	138
A.2 VNA Automatic Test	142
A.3 Satimo Automatic Test	144
B Post Processing	146
B.1 Installation	146
B.2 Data Format	146
B.3 Satimo Library	147
B.4 CST Library	149
B.5 3D Library	149
B.6 Plotting Library: aauplot	150
B.7 Examples	151
C CST Macros	159
C.1 Sweep Total Efficiency	159
Bibliography	163

Introduction

The mobile phone era began to take its modern form in the eighties when the development of analog cell-based mobile phone systems began. The AMPS systems, developed by Bell Labs and installed in the United States in 1982, being the most successful of the first generation mobile phone systems, proved that mobile personal telephony was here to stay [2]. In the second generation, speech was transmitted in digital form instead of analog. The GSM system from Europe became the de-facto world wide standard for 2G, while still only being aimed at voice communication [2]. Towards the third generation, and with the transition towards smartphones, mobile phones were no longer only a means of communicating voice and short messages, but also a means of accessing the Internet and exchanging data. The increase in music and video services online made the demand for higher data rates larger and larger while the number of users increased as well.

The technology for the fourth generation is the Long Term Evolution (LTE). The fourth generation of mobile phone systems aimed to increase the data rates as well as getting a more seamless interaction with wired and wireless IP networks [2]. A way of getting there is the use of MIMO, i.e. having multiple antennas in the mobile phones, making it possible to either communicate data in parallel, increasing the data rate, or to increase the signal strength using diversity techniques. For this reason, the LTE specification supports multiple antennas to be integrated for LTE MIMO and diversity use [3].

In order to achieve good MIMO and diversity performance, the correlation between the radiation patterns of the LTE antennas should be low, i.e. the signals received by the two should be as different as possible in order to gain the most [4]. Patterns can be decorrelated by spacing the antennas far apart compared to the wavelength. However, this is not practical in a mobile phone at the low band frequencies as the free-space wavelength at 700 MHz is 429 mm. The correlation can be improved by having the antennas polarized differently but this is no easy task.

The demand for bandwidth increases as more and more users desire a greater throughput, new bands are being licensed. Part of the spectrum around 600 MHz, previously used for television broadcasting, is being considered for extending the LTE bands [5]. While the lower frequencies provide great penetration for long-range communication, the wavelength, and hence the antennas, tend to either increase in size or decrease the efficiency or bandwidth [1].

In modern mobile phones, the screen is the dominant user interface, taking up almost all of the front-side of the phone. This means that only little space, along the edge of the phone, is available for antennas. As described in [1], the smaller available area means that either the efficiency or the bandwidth must decrease.

As the antennas are placed close to the edge of the phone, they are in very close proximity to the user. This has the effect of absorbing part of the power and also detuning the antenna [6]. The antennas can be designed to have resonances which are determined by a matching circuit placed immediately before the antenna but as the antenna changes its resonance based on whether or not a user is present, the matching circuitry would need to be variable to account for different use cases.

The solution to the low available bandwidth and the detuning caused by the user, is to use a digitally controllable tuner in the matching network. This makes it possible to have a lower bandwidth, covering a minimum of only the largest LTE band – not all at the same time – and then re-tune the resonance to the desired band. This way, all bands could be covered at a decent efficiency and the loading caused by the user could be minimized by counter-tuning the antenna based on the user's behavior.

Several solutions exist for digitally tunable capacitors. Varactor diodes can be used as tunable capacitors by altering the bias voltage while CMOS tunable capacitors consist of banks of capacitors which are switched in and out of circuit using CMOS technology. MEMS tunable capacitors come in two variants where one uses MEMS switches to switch capacitors like the CMOS tuners. The other variant alters the proximity of two parallel plates, thereby changing the capacity [7].

Previous antenna designers have dealt with developing tunable antennas for the LTE bands supporting MIMO. Using MEMS tunable capacitors, [8] managed to design a quite efficient design with two antennas. The ground clearance for this design is 15 mm and may be closing in on the size constraints for practical implementation in a phone. In [9], a single antenna was designed using a MEMS tuner. While being small and rather efficient, this design only consisted of a single antenna and does, for this reason, not support MIMO for LTE. In [10], a CMOS tuner was used and a very compact and efficient design has been developed while still only for a single antenna. A MEMS tuner was used for tuning the side antenna in [11] while the top antenna was fixed and showed good results. This design, however, did only cover the low bands below 960 MHz. Finally, in [12], a design for reaching towards

5G was designed. Showing very good results, the design only consisted of a single antenna.

In this project, a dual resonance antenna design for LTE supporting MIMO will be designed. The goal is to minimize the ground clearance so the antenna would be attractive in a practical design. The aim is to investigate how ground clearance affects the bandwidth and design a MIMO antennas system using the smallest practical clearance, covering all LTE bands from 700 MHz to 960 MHz and from 1710 MHz to 2650 MHz.

The first part of the report – Chapter 1 – contains a problem analysis. The goal of this chapter is to cover all the theory and background knowledge needed in order to successfully set up requirements and design the final product. Everything from basic antenna parameters to the background of LTE and measurement techniques will be described in this chapter. In Chapter 2, all functional and specific requirements for the antenna design will be summarized in the requirement specification. The requirements define the frequency bands of interest as well as measures of bandwidth, etc. Chapter 3 – the test specification – describes how the specific requirements from the requirement specification will be tested. After the requirements and test procedures have been defined, the product development will begin from Chapter 4. Here, three preliminary antenna designs will be developed and simulated in free-space. In Chapter 5, the preliminary designs will be simulated in three different use cases: Data mode, play mode, and talk mode, to observe the effect of a user holding the phone. Here, the Specific Absorption Rate (SAR) will also be simulated in order to ensure compliance with the requirements for this. The preliminary designs will be prototyped and measured in Chapter 6 with discrete components for the matching network and tuner. The most promising of these designs will later be used on a PCB with two MEMS tuners. A smaller design, more suited for practical implementation in a phone, will be developed in Chapter 7. The antenna will be simulated and measured. In Chapter 8, the most promising design from Chapter 6 as well as a modified version of the design from Chapter 7 will be moved to a PCB with a MEMS tuner for each antenna. The designs will be modified to fit the new board and a sweep measurement of the S-parameters and the total efficiency will be carried out for each design. Finally, in Chapter 9, a conclusion will be summing up the results from the report.

In Appendix A, automatic testing software developed during the project will be described. Software is developed for automatically sweeping a Vector Network Analyzer (VNA) and the measurements in an anechoic chamber. A circuit for fiber optic communication in the anechoic chamber is developed to automate adjusting of the tuner from outside the chamber. Appendix B describes the Python libraries developed for post processing data from the VNA, the anechoic chamber, and from CST Microwave Studio. The library for plotting the graphs, used in this report, is also documented here. Lastly, Appendix C shows a CST script for automatically sweeping and exporting the total efficiency from CST Microwave Studio.

Reading Guidelines

Throughout the report, a lot of sweep plots will be presented with many plots per figure. The color order presented in Figure 1 is used for all sweeps so the first plot is always blue, the next is green, and so forth.



Figure 1: Color order for sweep plots in the report.

When two-port S -parameter measurements are mentioned in the report, port 1 is always the top antenna and port 2 is the side antenna unless otherwise noted.

The design files for the circuits, as well as source code and Python libraries, developed in the appendices of the report can be downloaded at <http://github.com/16gr1051>.

Part I

Analysis

Chapter 1

Problem Analysis

This chapter covers all the theory and background knowledge needed in order to begin development, simulations, and measurements of a technical solution. This includes the basic antenna parameters, the background of LTE, and the measurement techniques used throughout the report.

1.1 LTE

In this part, an overview of the allocated LTE frequency bands will be provided together with a general description of the LTE spectrum. In addition to the allocated LTE bands a more detailed description on the bands covered in this project will be provided.

1.1.1 The History of the Mobile Telephone System

In this section, a brief overview of the development leading up to 4G and LTE will be given to clarify the need for LTE.

1G

The first generation of mobile phone systems were solely used for speech. In Europe, many different systems were developed and deployed [13] making it impossible to use the same mobile phones for all of Europe. In USA, the government was in charge of the deployment. For this reason, the AMPS (Advanced Mobile Phone System) was deployed all over the country. The same system was used in England under the name TACS and in Japan under the name MCS-L1 [2]. Because of the US governments interaction, the AMPS system became the most deployed of the first generation system.

AMPS, like the other first generation systems, divided geographical areas into cells, each containing a base station, to which the users transmit, and a Mobile Switching Center which connects the base stations and handles the connections to the phone network. Each cell uses a different set of frequencies than its neighbors, to not avoid interfering with each other. The set of frequencies – the “channels” – are split into different categories: Control channels for managing of the system, paging channels for alerting the users of incoming calls, access channels for setup and channel assignment, and finally data channels for carrying voice [2]. The data channels are analog voice channels while all other channels are digital (FSK) channels with error-correcting code [2].

The disadvantages of the first generation of mobile systems included the fact that no world-wide standard existed so mobile phones could only be used in the area for which they were designed. Another disadvantage was that the channels were analog and thus unencrypted. This made eavesdropping possible. The second generation tried to address these problems.

2G

In Europe, a lesson had been learned from the first generation system. A single European 2G standard was developed by a telecommunication group – Groupe Specialé Mobile (GSM). In USA, the task of deploying a second generation mobile system was moved from the government to the marketplace. This resulted in several standards being developed. A digital version of AMPS – D-AMPS – was developed. It was designed to coexist with AMPS [2]. A second system, developed by Qualcomm, was described in International Standard IS-95 but was not a dominant 2G system. It did, however, make use of CDMA – Code Division Multiple Access – which later became the basis for the third generation of mobile systems. Later on, GSM got deployed in the US as well and has now become the de facto world standard for 2G [13].

The major difference from the first to the second generation was the change from analog speech to digitally coded speech. This made it possible to encrypt the speech, addressing the eavesdropping issue of the first generation [2]. Apart from this, the mobile phone and the subscription itself was split into two separate parts. The user would now buy a SIM (Subscriber Identity Module) card which can be used in whatever mobile phone the user desired.

GSM uses frequency bands at around 900 MHz, 1800 MHz, and 1900 MHz. Each band is split into smaller bands (channels), each split into eight time-divided slots so that eight separate connections can be active at the same time [2]. The channels are of two

groups – one for uplink and one for downlink. The channels are illustrated in Figure 1.1.

Using compression, it is possible for GSM to achieve the equivalent of a 64 kbps PCM voice signal with little loss in quality [2]. While this may be fine for speech, a higher data rate would be needed to carry data as well. This led to the development of the third generation.

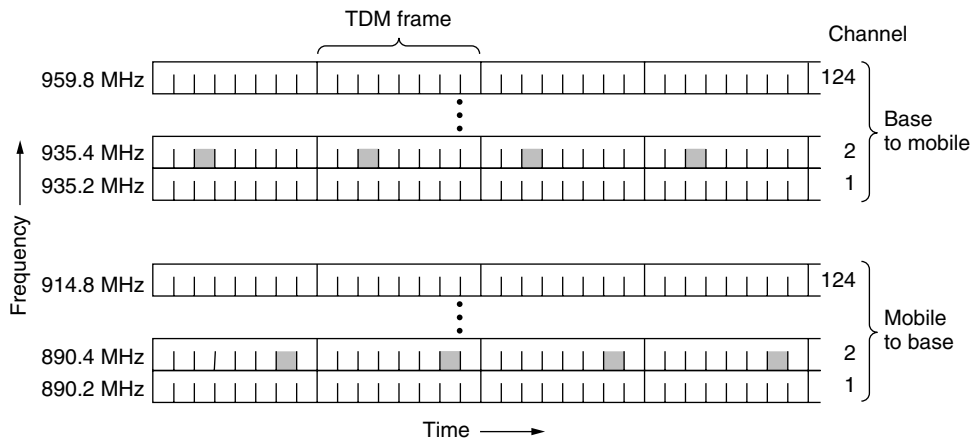


Figure 1.1: Illustration of GSM channels [2].

3G

The third generation was designed for carrying digital data and speech at higher data rates than previously. Two similar systems were developed in Europe and in USA: UMTS (Universal Mobile Telecommunications System) and CDMA2000, respectively. Europe wanted coexistence with GSM and USA wanted coexistence with IS-95.

The third generation used CDMA as multiple-access scheme. In CDMA, all users communicate the same time, jumping between frequency and time slots in a pre-defined code. The code is shared between transmitter and receiver. Ideally, the codes would be orthogonal so that only one user would communicate on one frequency in one time slot. While this type of synchronization is easily performed in the downlink, it is very difficult in the uplink as the mobile units do not connect directly. Instead, pseudo-random sequences, which can be generated locally, are used as codes. These codes have a low cross-correlation and auto-correlation so that the interference between users is averaged out along the code word [2].

The transmitted power from the mobile phone in a CDMA system is controlled in a fast loop so that the transmitted power is the inverse of the power received from the base station [2]. This makes the received power from each user equal at the base station, so the interference between users is lowered.

The CDMA variants used in the third generation of mobile networks makes it possible to assign different data rates to different users. At the same time, these systems can take advantage of periods where a user is not speaking, etc. This will not be described further, but is described in [2].

The third generation made it possible to obtain a data rate between 144 kbps (mobile users) and 2 Mbps (indoor users) [2]. HSPA and HSPA+ are evolutions of the UMTS network, enabling higher data rates – up to 14 Mbps and 42 Mbps, respectively, pushing the limits of the deployed Wideband CDMA [3]. Some of the goals for fourth generation are higher bandwidths and more seamless integration with wired and wireless IP networks [2]. The peak data rate evolution, presented by 3GPP, is illustrated in Figure 1.2.

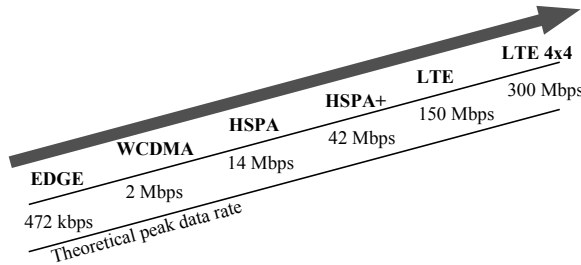


Figure 1.2: Peak data rate evolution of 3GPP technologies [3].

4G

LTE (Long Term Evolution) is an evolution of the UMTS, HSPA (High Speed Packet Access), and HSPA+ (Evolved High Speed Packet Access) 3G communication standards. HSPA and HSPA+ are upgrades to UMTS with the primary goal to improve the data rates on the 3G communication network. The LTE standard is marketed as a 4G network, even though the LTE standard does not meet the requirements set by the 4G standard [14].

The LTE provides much higher data rates than the 3G HSPA+ standard, using Orthogonal Frequency Division Multiplex (OFDM) in downlink and Single Carrier-Frequency Division Multiple Access (SC-FDMA) in uplink. These access scheme technologies do also enable the LTE network to use MIMO technologies, which has resulted in MIMO being an integral part of LTE [14].

MIMO technologies improves the throughput even further by having the option to add up multipath signals. A further description of MIMO is given in Section 1.6. A comparison of the UMTS, HSPA, and LTE speeds can be seen in Figure 1.2.

1.1.2 LTE Frequency Band Allocation

As seen in Table 1.1, the available LTE bands for uplink and downlink are allocated in the frequencies from 452.5 MHz to 3600 MHz. The whole spectrum between 452.5 MHz to 3600 MHz is not occupied by the mobile communication systems, as other network systems, such as WiFi, GPS, TV, etc., also have the rights (licenses) to some of the frequency bands within this spectrum.

However, the transition from analog to digital broadcast television signals has freed some frequency bands for mobile communication. In USA in 2009, the 700 MHz band covering 698 MHz to 806 MHz [15] was auctioned and latest the spectrum around 600 MHz has also been freed and was put on auction in 2015 [5]. Furthermore, in 2013 the 800 MHz band, which was also freed due to the digital TV transition, and the 2600 MHz band were auctioned off by Ofcom [16].

As the mobile communication is evolving, the need for higher data rates also increases, leading to the need for more bandwidth. The freed bands increase the mobile communication spectrum both in the low and high frequencies, which can be used for different environments.

High and Low Frequency Bands

The high and low frequency bands both have advantages and disadvantages. As seen in Table 1.1, the bandwidth varies form 5 MHz to 90 MHz; the high frequencies providing high bandwidth and the low frequencies low bandwidth. This means that the high band frequencies provide greater capacity. One of the primary advantages of low band frequencies is the large wavelength. The large wavelength makes the waves able to travel long distances and is suitable for rural areas [17]. The greater capacity at the high band frequencies makes these bands ideal for communication in urban areas as cities or other dense areas.

Multiband LTE

Most countries use several frequency bands across the LTE spectrum, which implies that a multi-band phone/antenna is needed. Until now, it has not been possible to agree on the same LTE band allocations across the world because of the different regulatory positions in different countries. Also, in some cases across the different countries, the LTE bands are overlapping as a consequence of different frequency availability around the world, thus limiting the accessibility of all users to use the same frequencies [14].

In this section, an overview of the history of LTE was given. A brief overview of the techniques used in LTE was also given along with a table of the LTE bands currently in use. This gives an overview of what frequency bands the antennas designed in this project needs to cover.

In this project, the frequencies of interest are 700 MHz to 960 MHz, 1710 MHz to 2170 MHz, 2300 MHz to 2400 MHz, and 2550 MHz to 2650 MHz. These frequencies cover most of the LTE bands as seen in Table 1.1. The bandwidth within this frequency range reaches from 10 MHz to 80 MHz. The main goal of this project is for the MIMO antennas to be frequency reconfigurable within the above mentioned frequency range. The MIMO antenna design will consist of two resonances: One covering the low frequencies from 700 MHz to 960 MHz and one covering the high frequencies from 1710 MHz to 2650 MHz. The antennas should be able to cover the highest bandwidth within these frequency spectra, which includes the downlink and uplink bandwidth and the band gap. When the bands are located far apart, several resonances may be exploited to cover both uplink and downlink at the same time [14].

The next Section will give a short introduction to the basic antenna parameters used in the design, simulations, and measurements of antennas.

LTE band number	Uplink (MHz)	Downlink (MHz)	Bandwidth (MHz)	Duplex spacing (MHz)	Band Gap (MHz)	Total Span (MHz)
1	1920–1980	2110–2170	60	190	130	250
2	1850–1910	1930–1990	60	80	20	140
3	1710–1785	1805–1880	75	95	20	170
4	1710–1755	2110–2155	45	400	355	445
5	824–849	869–894	25	45	20	70
6	830–840	875–885	10	35	25	55
7	2500–2570	2620–2690	70	120	50	190
8	880–915	925–960	35	45	10	80
9	1749.9–1784.9	1844.9–1879.9	35	95	60	130
10	1710–1770	2110–2170	60	400	340	460
11	1427.9–1452.9	1475.9–1500.9	20	48	28	73
12	698–716	728–746	18	30	12	48
13	777–787	746–756	10	−31	41	41
14	788–798	758–768	10	−30	40	40
15	1900–1920	2600–2620	20	700	680	720
16	2010–2025	2585–2600	15	575	560	590
17	704–716	734–746	12	30	18	42
18	815–830	860–875	15	45	30	60
19	830–845	875–890	15	45	30	60
20	832–862	791–821	30	−41	71	71
21	1447.9–1462.9	1495.5–1510.9	15	48	33	63
22	3410–3500	3510–3600	90	100	10	190
23	2000–2020	2180–2200	20	180	160	200
24	1625.5–1660.5	1525–1559	34	−101.5	13	135.5
25	1850–1915	1930–1995	65	80	15	145
26	814–849	859–894	30/40		10	80
27	807–824	852–869	17	45	28	62
28	703–748	758–803	45	55	10	100
29	N/A	717–728	11			11
30	2305–2315	2350–2360	10	45	35	55
31	452.5–457.5	462.5–467	5	10	5	14.5

Table 1.1: LTE frequency band allocation (only frequency division duplex) [14]. Note that negative duplex spacing means that the uplink band is higher in frequency than the downlink.

1.2 Basic Antenna Parameters

This section will give a summary of the fundamental theories and parameters that are used to describe antennas. This should give a basic understanding of antennas. The parameters described in this section are used throughout the report.

1.2.1 Antenna Definition

The IEEE defines an antenna as “a means for radiating or receiving radio waves”. In other words, the purpose of an antenna is to make the transition from a signal in a transmission line to electromagnetic fields in the air. An antenna will radiate an electric field (E-field) in a given direction, which then induces a magnetic field (H-field) orthogonal to the E-field. This relation is described by Maxwell’s Equations which is covered in Section 1.8 [18].

1.2.2 Isotropic Radiator

An isotropic antenna, can be represented as a point source. The isotropic antenna radiates its power uniformly in a sphere. The power density, S_{iso} , can be expressed as the source power P_s over the surface area of a sphere which is given by $4\pi r^2$ [18]:

$$S_{\text{iso}} = \frac{P_s}{4\pi r^2} \quad (1.1)$$

Clearly, it is not possible to construct such an antenna. However, this is used as a reference for quantifying other properties of an antenna. These properties could be the gain or directivity (see Section 1.2.5), and the unit would then be in dBi rather than dB.

1.2.3 Radiation Pattern

The radiation pattern describes how the antenna emits or receives radiated power. This is commonly visualized by a 3D plot or 2D cuts of the 3D plot in specific coordinates. The unit of power used is often gain or directivity (see Section 1.2.5) and this is often compared to the isotropic antenna [18].

1.2.4 Field Regions

The waves transmitted from the antenna are usually grouped into three regions of radiation, based on how the waves propagate and the field structure [18]. Obviously, there is no abrupt change, but rather a continuous change.

- The Reactive near-field.
- The Radiating near-field (Fresnel).
- The Farfield.

The reactive near-field is defined as the portion of the near-field region immediately surrounding the antenna wherein the reactive field predominates [18]. The outer boundary for this region is given by [18]

$$R < 0.62\sqrt{D^3/\lambda} \quad (1.2)$$

where D is the largest dimension of the antenna. To be valid, D must also be large compared to the wavelength.

The radiating near-field is defined as the region between the reactive near-field and the far-field. This field may not exist in the case that the overall antenna dimension is very small compared to the wavelength. The outer boundary for this is defined as [18]

$$R \leq 2D^2/\lambda \quad (1.3)$$

The far-field region is defined as the region of the field where the angular field distribution is independent of the distance, that is the radiation pattern does not change shape with distance. The far-field is also dominated by fields where the E- and H-fields are orthogonal and propagates as plane waves. The inner boundary is given as [18]

$$R > 2D^2/\lambda \quad (1.4)$$

The three different regions are illustrated on Figure 1.3.

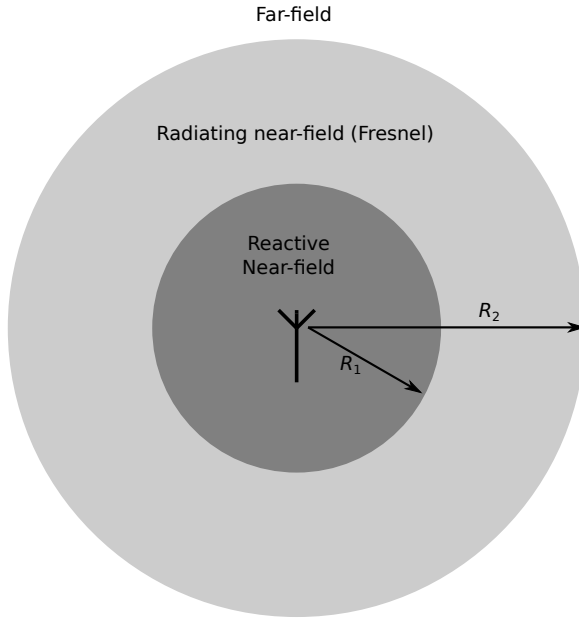


Figure 1.3: Visualization of different fields [18].

1.2.5 Directivity and Gain

Directivity is defined as the ratio of the power radiated at a point with a certain angle and distance from the antenna compared to what would be radiated from a reference isotropic antenna. Mathematically, it can be written as [18]

$$D = \frac{U}{U_0} = \frac{4\pi U}{P_{rad}} \quad (1.5)$$

where

D = Directivity.

U = Radiation intensity.

U_0 = Radiation intensity of an isotropic source.

P_{rad} = Total radiated power.

It should be noted, that for this equation to be valid, the waves must propagate as plane waves, thus being in the farfield region.

Gain is a measure closely related to directivity. It takes the efficiency of the antenna into account as well as the direction. The gain is defined as the ratio of the intensity in a given direction to the radiant intensity that would be obtained if it was radiated isotropically. In mathematical form, it can be expressed as [18]:

$$G = 4\pi \frac{\text{radiation intensity}}{\text{total accepted input power}} = 4\pi \frac{U(\theta, \phi)}{P_{in}} \quad (1.6)$$

In many cases, the relative gain is used, which is defined as the ratio of the power gain in a given direction to the power gain of a reference antenna in its referenced direction. The reference antenna could be a dipole, horn, etc.

The gain can also be calculated using the directivity, since they are only related by the efficiency. This is given as [18]

$$G(\theta, \phi) = \eta_{cd} D(\theta, \phi) \quad (1.7)$$

1.2.6 Impedance, Return Loss, and VSWR

The impedance and matching is an important part of the antenna design to ensure maximum power transfer. The input impedance of an antenna is defined as Z_{in} . From the classical circuit theory it is known that the maximum power transfer occurs when the in- and output impedance is matched (see Section 1.3). If there is a mismatch, some of the power will be reflected back into the source, and thus not transmitted from the antenna. The reflection coefficient Γ is defined as [17]

$$\Gamma = \frac{Z_{in} - Z_0}{Z_{in} + Z_0} \quad (1.8)$$

where

Z_0 = The characteristic impedance, which is typically 50Ω .

The reflection coefficient is often expressed in dB.

Another closely related figure is the Voltage Standing Wave Ratio (VSWR), and is defined as [17]

$$\text{VSWR} = \frac{1 + |\Gamma|}{1 - |\Gamma|} \quad (1.9)$$

1.2.7 Bandwidth

The bandwidth of an antenna defines the usable spectrum of the antenna. The required bandwidth is dependent on the modulation schemes used, which makes the bandwidth an important part of the antenna design. The bandwidth is typically defined with respect to a given reflection coefficient or VSWR, e.g. at a reflection coefficient of 0.25 (or -6 dB).

1.2.8 Polarization

The polarization in a certain direction is simply defined as the polarization of the transmitted wave by the antenna. It describes the time-varying direction at a relative magnitude of the E-field vector analogously to the polarization of light. Polarization can be classified into groups such as linear, circular, or elliptical polarization. If a transmit antenna and a receive antenna are of different polarization, this will introduce a polarization mismatch loss to the system [18].

1.2.9 Antenna Efficiency

There are a lot of different measures for antenna efficiency depending on which losses that are taken into account. The total efficiency takes the losses from the input terminal and within the antenna structure into account [18]. This can in general be expressed as [18]

$$\eta_0 = \eta_r \eta_c \eta_d \quad (1.10)$$

where

η_0 = Total efficiency.

η_r = Mismatch loss.

η_c = Conduction efficiency.

η_d = Dielectric loss.

The conduction and dielectric losses are hard to compute, and by measurements they cannot be separated [18].

Radiation Efficiency

The radiation efficiency is defined as the conduction-dielectric efficiency $\eta_r = \eta_{cd}$ which is defined as the ratio of the power delivered to the radiation resistance, R_r , to the power delivered to R_r and R_L (loss) in total [18]. This can be written as [18]

$$\eta_r = \frac{P_{\text{radiated}}}{P_{\text{input}}} = \frac{R_r}{R_L + R_r} \quad (1.11)$$

1.2.10 Antenna Q-Factor

As it will be described in Section 1.2.13, the size of an antenna sets the lowest achievable Quality Factor (or *Q*-factor) of an antenna. In this section, the relation between *Q*-factor and antenna bandwidth will be described as well as the impact of having multiple antennas on the *Q*-factor.

The *Q*-factor is a measure of loss in a resonant circuit [17]. A higher *Q* means lower loss. In an antenna, it is desired to have loss due to radiation while mismatch loss, conductive loss, and dielectric loss is undesirable. The *Q* due to radiation should therefore be low to get a high degree of radiation.



Figure 1.4: Series and parallel resonant circuit equivalent of a single-resonance antenna.

For a single-resonance antenna, a resonant circuit can often be used as an equivalent for the antenna. A series and a parallel equivalent circuit is shown in Figure 1.4. A circuit is at resonance when the reactive part, $X_0 = 0$. For an antenna, it is desired to have a resonance where R_0 is equal to the characteristic impedance of the system (e.g. 50Ω). For a multi-resonance antenna, a resonant circuit equivalent can be used for each resonance, given that the bandwidth of observation is chosen narrow enough (by altering the β -parameter below) [19].

An investigation of the relation between impedance, bandwidth, and *Q* of antennas by Yaghjian and Best [19]. They developed the following exact expression for the *Q*-factor:

$$Q(\omega_0) = \left| \frac{\omega_0}{2R_0(\omega_0)} X'_0(\omega_0) - \frac{2\omega_0}{|I_0|^2 R_0(\omega_0)} [W_L(\omega_0) + W_R(\omega_0)] \right| \quad (1.12)$$

where

ω_0 = Radian frequency at which the antenna is tuned.

$R_0(\omega_0)$ = Input resistance at resonance.

$X'_0(\omega_0)$ = Derivative of the input reactance with respect to ω , evaluated at ω_0 .

I_0 = Current fed to the antenna.

W_L = Energy associated with power loss in the antenna, computed from the electric and magnetic fields.

W_R = Energy associated with the power radiated by the antenna, computed from the farfield.

In the same paper, an approximate expression is developed for the Q -factor based on the input impedance at resonance. Furthermore, an approximation is developed based on the fractional bandwidth, FBW_V :

$$Q(\omega_0) \approx \frac{\omega_0}{2R_0(\omega_0)} |Z'_0(\omega_0)| \quad (1.13)$$

$$\approx \frac{2\sqrt{\beta}}{\text{FBW}_V(\omega_0)}, \quad \sqrt{\beta} = \frac{s-1}{2\sqrt{s}} \leq 1 \quad (1.14)$$

where s is the requirement VSWR at which the bandwidth is determined. The approximation is based on the assumption that W_L and W_R are ohmic losses in the resonance equivalent circuits [19]. Furthermore, the derivatives, $R'_0(\omega)$ and $X'_0(\omega)$ must not change greatly over the bandwidth of the antenna – which holds by choosing the bandwidth narrow enough [19]. Finally, it is assumed that the antenna is linear (i.e. there is a linear relationship from the \mathbf{B} and \mathbf{D} fields to the \mathbf{H} and \mathbf{E} fields), passive (non-gain media), and tuned by only passive circuitry [19].

The approximation in Equation 1.13 can be used to compute the Q of an antenna by knowing its input impedance. This relation explains how the Q may be affected by having multiple antennas by taking into account the mutual impedance between the antennas [18].

The approximation in Equation 1.14 is useful for approximating the bandwidth of an antenna based on a Q -factor. This Q could, for example, be computed using the Chu limit (see Section 1.2.13) and thus, the highest possible bandwidth of an antenna of a given size could be computed. Alternatively, the formula could be used to approximate the Q of an antenna with a given resonance by rearranging the equation.

1.2.11 Mobile Antenna Limitations

As the requirements for mobile antennas get more and more strict, some trade off's need to be considered when designing an antenna. The design constrains when designing antennas is a trade off between size, bandwidth, and efficiency, as illustrated in Figure 1.5. The trade off relationship can be expressed as [1]

$$\frac{\Delta f}{f} \propto \frac{(a/\lambda)^3}{\eta} \quad (1.15)$$

where

λ = Wavelength.

η = Efficiency.

$\Delta f/f$ = Bandwidth.

a^3 = Antenna volume.

This relationship describes that it is hard to design a small antenna with excellent efficiency performance and a high bandwidth. Therefore, when designing mobile antennas that requires high bandwidth and small antenna structures, a trade-off is needed to ensure that the antenna performs as required [1].

In the case of this project, the antenna is required to have a bandwidth from 700 MHz to 960 MHz in the low band and from 1710 MHz to 2650 MHz in the high band. Furthermore, it needs to be very small with a maximum ground clearance of 10 mm and an efficiency above 50 % in the entire bandwidth. Due to the constraints on the antenna size when designed for mobile phones, the bandwidth and efficiency will be limited. This leads to design challenges in exploiting the available and limited volume within a sphere [18]. As it is hard to get both high efficiency and high bandwidth with a small fixed-tuned antenna, a frequency reconfigurable antenna system could be one way of covering a high bandwidth with a small antenna [1].

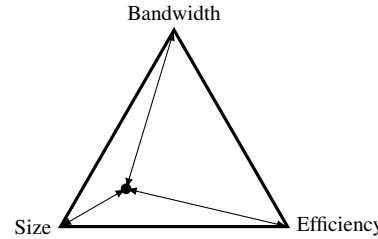


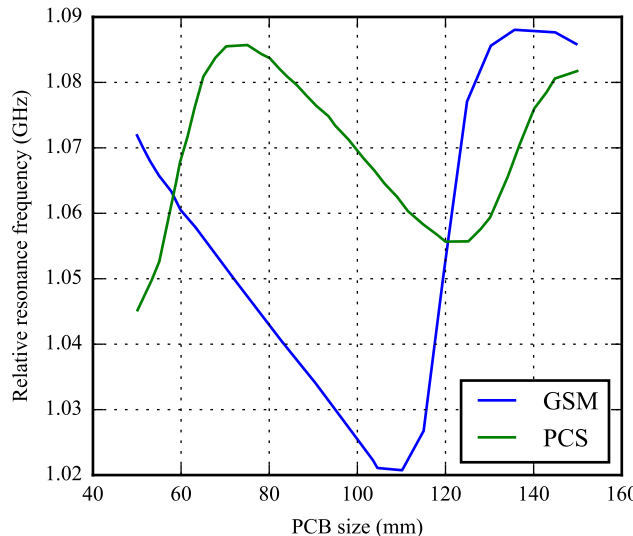
Figure 1.5: Antenna design trade-off's.

1.2.12 Internal Antennas

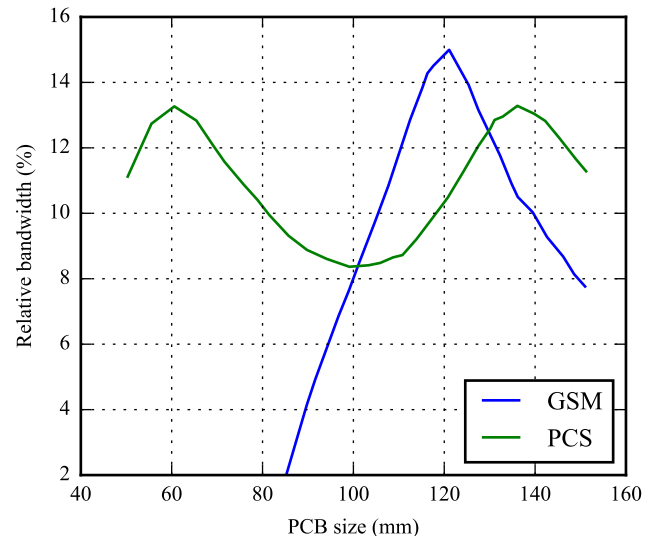
As described in the antenna limitation section, Section 1.2.11, the size restriction of mobile phone antennas limits the bandwidth and efficiency. These are only a few of the affected parameters considered when dealing with internal antennas. Going from external to internal antenna designs influences the radiation pattern, matching, and impedance bandwidth. The losses and detuning caused by the user can also have a higher influence, as the hand of the user generally moves closer to the antenna structure compared to the external antenna case [20].

The internal antenna design is also deeper affected by the chassis and PCB size [21]. An example of the influence of the PCB size on the resonant frequency and the bandwidth can be seen in Figure 1.6. The example is done with a $40\text{ mm} \times 1\text{ mm}$ dual-band patch antenna over a metallic ground plane for the frequencies 900 MHz in the GSM band and 1975 MHz in the DCS band. The exact frequencies used in the simulation is the center frequency of each band.

As seen in the Figure 1.6, both the resonant frequency and the bandwidth is greatly affected by the size of the ground plane – especially the GSM band at 900 MHz. When the ground plane and the antenna both are in resonance state, the maximum bandwidth is achieved. In the case of MIMO antenna designs with two antennas, one on the bottom and one of the side of the PCB, the maximum bandwidth is hard to achieve with two identical antenna designs [21].



(a) Ground plane size effect on the resonance frequency.



(b) Ground plane size effect on the bandwidth at -6 dB.

Figure 1.6: Ground plane size effect on the resonance frequency and the bandwidth [21].

For internal antennas, the small size, high efficiency, and high bandwidth are only a few of the design requirements. The design requirements also include [20]:

- Light weight.
- Compactness.
- Low profile.
- Robustness.
- Flexibility.

- Integration with nearby materials.

Most of these requirements and factors needs to be considered in the design and choosing of the antenna type. Robustness comes with the fact that it is an internal antenna and therefore is protected by the phone case. Some of the most used antenna types for mobile antennas are the PIFA and the folded monopole antennas. Both designs are suitable for mobile phones, as the antenna size is a $1/4\lambda$ [20].

As mentioned, the PCB has a big influence on the antenna, but the antenna performance is also degraded by other components such as the display, camera, flex-films, speaker, microphone, etc. When activated, these digital components work at high speed and will degrade the receiving sensitivity and cause problems to the receiving bands, as the components emits RF noise. When the components are deactivated, the components will work as passive lossy loading elements. Close to the antenna, the passive components will cause reduction to the effective antenna volume, detuning, and ohmic losses [20].

Because of the large battery size in today's smartphones, the battery can have a significant impact on the antenna performance. If placed closely to the antenna, the battery can introduce an induced current on the antenna and affect the performance. To have as little impact as possible from the battery it should be placed at a distance of 4 mm to 6 mm or more from the antenna [20].

The display is parallel to the PCB ground plane and is made of lossy dielectric material, which can change the EM near field of the antenna. In most phones, the display is large and can have a big influence on the antenna performance, as the display introduces some induced currents on the antenna [20].

1.2.13 Electrically Small Antennas

The concept and definition of electrically small antennas was introduced by Wheeler in 1947 [22], and is given by

$$ka \ll 1 \quad (1.16)$$

where

$k = 2\pi/\lambda$ is the wave number.

a = The radius of a sphere enclosing the maximum dimension of the antenna.

The parameter a is illustrated in Figure 1.7. Inserting the definition of k yields that

$$\frac{2\pi a}{\lambda} \ll 1 \quad (1.17)$$

in order for an antenna to be defined as electrically small. It should also be noted that if the antenna is used with a small ground plane, which often is the case, then the ground plane itself becomes a dominant part of the antenna structure. In this case, the entire ground plane must be included in the sphere and thus in the definition of a .

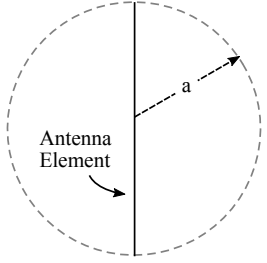


Figure 1.7: Illustration of ESA definition.

Fundamental Limits of Q

L. J. Chu quantified the relationship between the minimum Q of an electrically small antenna and the physical size relative to the wavelength [23]. This relationship was later corrected by McLean [24] to be

$$Q_L = \frac{1}{k^3 a^3} + \frac{1}{ka} \quad (1.18)$$

for a linear antenna in free space.

1.2.14 Friis Transmission Equation

The Friis transmission equation relates the power received with the power transmitted. In the most simple form, the Friis transmission equation is based on the free-space path loss (FSPL), the gains of the antennas, and the transmit power. The free-space path loss (or “path gain” as this notation is a decaying with distance) is defined as [18]

$$\text{FSPL} = \left(\frac{\lambda}{4\pi d} \right)^2 \quad (1.19)$$

where

λ = Wavelength.

d = Distance from the transmitter to the receiver.

This assumes that the energy spreads out in a sphere and that the only loss is from the distance. It is seen that the power decreases with the square of the range, which is plotted in Figure 1.8 for a 2.6 GHz link.

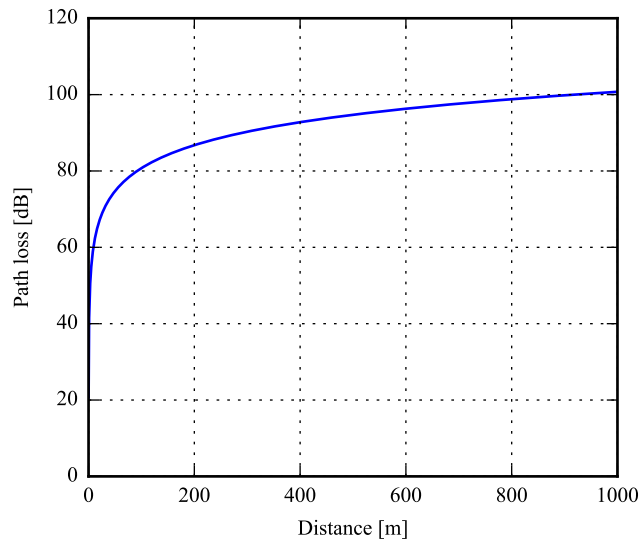


Figure 1.8: free-space path loss in dB for a 2.6 GHz link.

The Friis Transmission equation in its most basic form can be written as [18]

$$\frac{P_r}{P_t} = \left(\frac{\lambda}{4\pi d} \right)^2 G_t G_r \quad (1.20)$$

where

P_r = Power received.

P_t = Power transmitted.

G = Transmitter and receiver gains.

In this case, it is assumed that there is no impedance or polarization mismatch. It is also assumed that the two antennas are aligned perfectly. Finally, it is assumed that the path loss is described by FSPL, which in reality is a very rare case. The next section will describe a few more realistic propagation models.

Throughout this section the basic antenna parameters have been described. In the next section, the effect of matching circuitry and tuners will be described.

1.3 Matching Circuits and Tuners

In this section, the effect of adding a matching circuit to the feed line of an antenna will be described. Different types of digital tuners will also be described as well as equivalent circuit models for a tuner, based on S -parameter measurements.

From transmission line theory, it is known that the voltage and current waves present on a transmission line is composed of an incident and a reflected wave. The voltage and current at any distance, z , from the load are [17]

$$V(z) = V^+ e^{-j\beta z} + V^- e^{j\beta z} \quad (1.21)$$

$$I(z) = \frac{V^+}{Z_0} e^{-j\beta z} - \frac{V^-}{Z_0} e^{j\beta z} \quad (1.22)$$

where

$V(z)$ = Voltage at distance z [V].

$I(z)$ = Current at distance z [A].

V^+ = Amplitude of the incident wave [V].

V^- = Amplitude of the reflected wave [V].

Z_0 = Characteristic impedance of the transmission line [Ω].

z = Distance from load to the considered point [m].

β = The wave number = $2\pi/\lambda$ [rad/m].

The load impedance is the voltage-to-current ratio where $z = 0$,

$$Z_L = \frac{V(0)}{I(0)} = \frac{V^+ + V^-}{V^+ - V^-} Z_0 \quad (1.23)$$

Solving this for V^- yields

$$V^- = \frac{Z_L - Z_0}{Z_L + Z_0} V^+ \quad (1.24)$$

The ratio between the reflected and incident wave is known as the *reflection coefficient*, denoted Γ ,

$$\Gamma = \frac{V^-}{V^+} = \frac{Z_L - Z_0}{Z_L + Z_0} \quad (1.25)$$

Generally, the reflection coefficient along a transmission line can be written as [25]

$$\Gamma(z) = \Gamma e^{j2\beta z} \quad (1.26)$$

Note that Γ without parameters indicates $\Gamma(0)$.

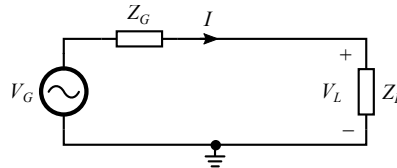


Figure 1.9: Equivalent circuit of a generator with given output impedance, Z_G , delivering power to a load of a given impedance, Z_L .

To maximize the power transferred from a generator to a load, it is desired to have a reflection coefficient that is zero so that only forward waves are present on the transmission line. Figure 1.9 shows an equivalent circuit for this situation. The average power delivered to the load is found as [17]

$$P = \frac{1}{2} \operatorname{Re} \{ V_L I^* \} = \frac{1}{2} \operatorname{Re} \left\{ \frac{|V_L|^2}{Z_L} \right\} = \frac{1}{2} |V_L|^2 \operatorname{Re} \left\{ \frac{1}{Z_L} \right\} \quad (1.27)$$

where

P = Average power delivered to the load.

V_L = Voltage drop across the load.

$Z_L = R_L + jX_L$ is the load impedance.

I = Current through the load.

Using basic circuit theory, Equation 1.27 can be expressed in terms of V_G and Z_G , making it possible to derive the optimal $Z_G = R_G + jX_G$ for a fixed, complex load. Continuing from Equation 1.27,

$$\begin{aligned} P &= \frac{1}{2} \left| V_G \frac{Z_L}{Z_L + Z_G} \right|^2 \operatorname{Re} \left\{ \frac{1}{Z_L} \right\} \\ &= \frac{1}{2} |V_G|^2 \frac{|Z_L|^2}{|Z_L + Z_G|^2} \operatorname{Re} \left\{ \frac{1}{Z_L} \right\} \\ &= \frac{|V_G|^2}{2} \frac{R_L^2 + X_L^2}{(R_L + R_G)^2 + (X_L + X_G)^2} \frac{R_L}{R_L^2 + X_L^2} \\ &= \frac{|V_G|^2}{2} \frac{R_L}{(R_L + R_G)^2 + (X_L + X_G)^2} \end{aligned} \quad (1.28)$$

The values of R_G and X_G that maximize the power delivered to the load, is found by

1. Taking the partial derivative of P with respect to R_L .
2. Taking the partial derivative of P with respect to X_L .
3. Setting both of the above solutions equal to zero and solving for R_G and X_G (two equations with two unknowns).

$$\frac{\partial P}{\partial R_L} = 0 \quad (1.29)$$

$$\frac{\partial P}{\partial X_L} = 0 \quad (1.30)$$

Doing so, yields the following solution,

$$\begin{aligned} R_{G,\max} &= R_L \\ X_{G,\max} &= -X_L \end{aligned} \quad (1.31)$$

or $Z_{G,\max} = Z_L^*$; the maximum power is transferred to the load when the generator impedance is the complex conjugate of the load impedance. In this situation, the generator is said to be *matched* to the load. Generally, the generator and the load would be connected through a transmission line with the characteristic impedance Z_0 , so the maximum power transfer from generator to load will occur when both generator and load are matched to Z_0 .

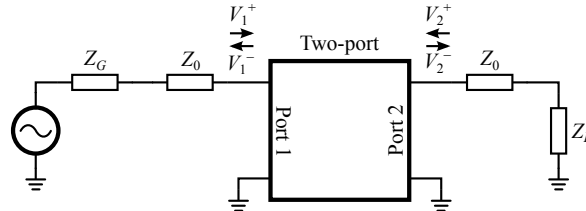


Figure 1.10: *S*-parameters of a two-port system.

The reflection coefficient, Γ , can more generally be described as an *S-parameter*. The *S*-parameters describe the ratio between the reflected and incident wave at a given port in a system. Consider a two-port as shown in Figure 1.10. Its four *S*-parameters are defined as follows:

$$\begin{aligned} S_{11} &= \left. \frac{V_1^-}{V_1^+} \right|_{V_2^+=0} = \Gamma_1 & S_{12} &= \left. \frac{V_1^-}{V_2^+} \right|_{V_1^+=0} \\ S_{21} &= \left. \frac{V_2^-}{V_1^+} \right|_{V_2^+=0} & S_{22} &= \left. \frac{V_2^-}{V_2^+} \right|_{V_1^+=0} = \Gamma_2 \end{aligned} \quad (1.32)$$

It is seen that S_{11} and S_{22} indicate the reflection due to the incident wave on the same port, when no contribution is made from the opposite port, i.e. these are the reflection coefficients of port 1 and 2, respectively. The parameter S_{21} indicates how much of the incident wave on port 1 is coming out of port 2 when no wave is incident on port 2, i.e. this indicates the *transmission coefficient* from port 1 to port 2. Likewise, S_{12} is the transmission coefficient from port 2 to port 1.

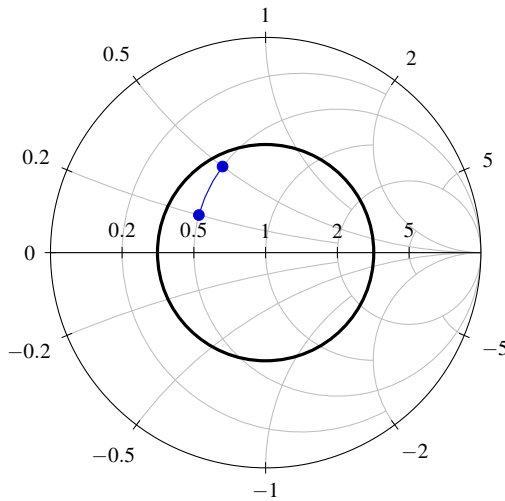


Figure 1.11: Smith chart. The circle illustrates the limit for which all points within the circle have a reflection coefficient below $\Gamma = 0.5$ (or -6 dB). Two points – $0.5 + j0.2$ and $0.5 - j0.5$ – are shown.

The S -parameters are easily measured using a vector network analyzer. The advantage of measuring S -parameters over, e.g., Y -parameters is that all ports are matched during the measurement instead of some being shorted, making odd behavior (like oscillations) less likely [26].

An important tool when doing matching, and designing antennas, to a certain Z_0 is the smith chart. The smith chart is used for plotting complex, normalized impedances and makes it easy to visually analyze the performance of a matched circuit. A smith chart is shown in Figure 1.11.

The smith chart maps the entire right complex half-plane into a circle, having $0 + j0$ all the way to the left and $\infty + j0$ all the way to the right. The y -axis (crossing $x = 0$) makes up the circumference of the circle. An impedance is plotted by first finding the resistive (real) part of the impedance on the horizontal line and then following the circular grid-lines up or down for positive or negative reactances, respectively. The smith chart shown in Figure 1.11 is a normalized smith chart. When matching to Z_0 , any impedance, Z , plotted in the smith chart, must be normalized by Z_0 ,

$$Z_n = \frac{Z}{Z_0} \quad (1.33)$$

This means that Z_0 will always appear at $1 + j0$ – in the center of the smith chart – and the goal of the matching is to get the impedance of the antenna (or other circuitry) as close to the center as possible for the desired frequency range.

The impedance bandwidth of an antenna is often given as the bandwidth for which the reflection coefficient, Γ , is below 0.5 (or -6 dB ; when denoting the reflection coefficient in (positive) decibels, it is commonly called *return loss*, $RL = -20\log_{10}|\Gamma|$ [17]). It may therefore be advantageous to plot this requirement. In the smith chart, this is plotted as a circle around the center and any point within the circle, is within the bandwidth of the circuit. The -6 dB circle is also shown in Figure 1.11. This type of circle is also known as an VSWR (Voltage Standing Wave Ratio) circle. The connection between the VSWR and the reflection coefficient is [17]

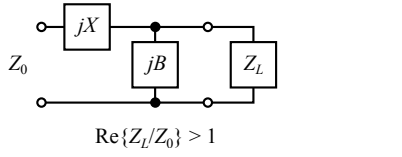
$$\text{SWR} = \frac{1 + |\Gamma|}{1 - |\Gamma|} \quad (1.34)$$

At $\Gamma = -6 \text{ dB}$, the SWR is 3.

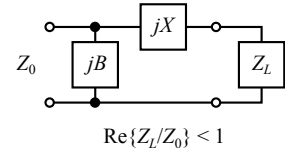
1.3.1 The L Network

In case the antenna is not designed to resonate exactly at the desired frequency or to the exact impedance bandwidth required, a tuning network can be placed immediately before the antenna.

The simplest matching network is the L-network which is made from two components – one in series and one in shunt – as shown in Figure 1.12. The values of X and B correspond to the reactance of the chosen component at the frequency of interest. The values of X and B (and their corresponding component values) can be derived through circuit theory, as done by [17]. The results are shown in Table 1.2.



(a) Real part of normalized load impedance greater than one.



(b) Real part of normalized load impedance less than one.

Figure 1.12: L-network. The series/shunt configuration depends on the value of the load impedance.

Variable	Description	Figure 1.12a	Figure 1.12b
Z_n	Normalized load = $R_n + jX_n$	Z_L/Z_0	
b	Normalized shunt susceptance = BZ_0	$\frac{X_n \pm \sqrt{R_n \sqrt{R_n^2 + X_n^2} - R_n}}{R_n^2 + X_n^2}$	$\pm \sqrt{(1 - R_n)/R_n}$
x	Normalized series reactance = X/Z_0	$\frac{1}{b} + \frac{X_n}{R_n} - \frac{1}{bR_n}$	$-X_n \pm \sqrt{R_n(1 - R_n)}$
C_p	Shunt capacitance in farad (for $b > 0$)	$\frac{b}{2\pi f Z_0}$	
L_p	Shunt inductance in henry (for $b < 0$)	$\frac{-Z_0}{2\pi b}$	
C_s	Series capacitance in farad (for $x < 0$)	$\frac{-1}{2\pi f x Z_0}$	
L_s	Series inductance in henry (for $x > 0$)	$\frac{x Z_0}{2\pi f}$	

Table 1.2: Formulas for computing the values of matching components for the two matching networks shown in Figure 1.12. These L-networks match a load (or antenna) impedance, Z_L ohm to a transmission line, Z_0 ohm at the frequency f hertz. There are two solutions: One for choosing $\pm = +$ and one for choosing $\pm = -$ [17].

1.3.2 Q-Factor

The Q -factor describes the ratio between the reactive and the resistive part of a component is [17]

$$Q = \frac{X}{R} \quad (1.35)$$

where

X = Reactance of the component.

R = Resistive part of the component.

Ideal capacitors and inductors are purely reactive and therefore, no power is lost in them (the average power $P = \text{Re}\{VI^*\} = |V|^2/\text{Re}\{Z\}$ only depends on the real part of Z [27]). However, practical components also have a small resistive part called the equivalent series resistance (ESR) which causes power to be delivered to the component, increasing the power loss. From Equation 1.35, it is therefore seen that a *large* Q -factor is desired for capacitors and inductors. The Q -factor of an antenna should, however, not necessarily be large as it is desired to lose power due to radiation, but a low Q -factor is not necessarily a good thing either, as the power loss may be caused by resistive loss in the antenna and not radiation.

1.3.3 Bode-Fano Criterion

The Bode-Fano criterion is a relation between the reflection coefficient and the obtainable bandwidth. In fact, this criterion provides a theoretical limit to the magnitude of the reflection coefficient over a specific bandwidth using a passive lossless matching network [17]. The criterion is inherently dependent on the type of load impedance, but for general passive serial or parallel RC or RL loads, the criteria can be expressed as [28]

$$\int_0^\infty \ln\left(\frac{1}{|\Gamma(\omega)|}\right) d\omega \leq \frac{\pi\omega_0}{Q_0} \quad (1.36)$$

where

Γ = Frequency dependent reflection coefficient.

Q_0 = Q -factor of the load.

ω_0 = Center frequency.

For the ideal reflection coefficient response, the reflection coefficient is $|\Gamma| = 1$ everywhere but in the required band $\Delta\omega$. Inside the band, the reflection coefficient is given by a maximum accepted value $|\Gamma| = \Gamma_m$. This ideal response is illustrated in Figure 1.13. For this case, the Bode-Fano criterion reduces to [29]

$$\frac{\Delta\omega}{\omega_0} Q_0 = \frac{\pi}{\ln\left(\frac{1}{\Gamma_m}\right)} \quad (1.37)$$

This leads to the following conclusions [17]:

- For a fixed load (Q_0 is constant) the bandwidth can only be increased at the cost of a higher reflection coefficient in the passband Γ_m .
- Perfect matching in the passband ($\Gamma_m = 0$), can only occur at discrete frequencies when $\Delta\omega = 0$.
- High- Q circuits are harder to match than low- Q circuits.

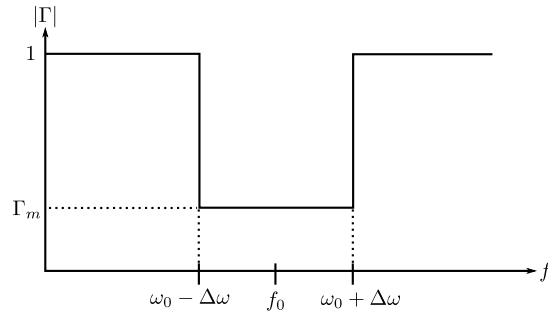


Figure 1.13: An ideal reflection coefficient response [29]

1.3.4 Tuners

From the description above, it is seen that the resonance frequency of an antenna can be altered by changing the matching network. By replacing a fixed capacitor with a variable capacitor, it is possible to cover a broader total bandwidth by tuning the resonance frequency. As the achievable bandwidth is generally proportional to the size of the antenna (see Section 1.2), it will be possible to cover a large bandwidth using a physically smaller antenna by having a variable matching network. This is desirable for mobile phones where the physical size of the antenna is limited and multiple bands must be covered [7].

Variable Capacitors

Three basic types of variable capacitors will now be described briefly.

Barium strontium titanate (BST) varactors are voltage controlled components where the bias voltage determines the amount of capacitance provided by the component. The Q -factor is dependent on the tuning range, η . For a tuning range of $\eta = 2\text{--}4$ at around 3 GHz, the Q -factor is around 30–65 [7].

A downside of the BST varactor is that it is quite nonlinear, having a typical third order intercept point (IIP₃) of around 32–40 dBm [7]. Also, an external power supply is necessary to bias the varactor.

Another type of variable capacitor is a SOI/SOS digitally tunable capacitor (SOI = silicon on isolator switches, SOS = silicon on sapphire switches). These consist of metal-isolator-metal (MIM) capacitors which are digitally switched using CMOS SOI or SOS switches as shown in Figure 1.14.

The Q -factor around 2 GHz of SOS/SOI digitally tunable capacitors (DTC) is typically 40–50 at minimum capacitance and ≥ 15 at maximum capacitance [7]. This is generally worse than the BTS varactors. The linearity, however, is generally better than for the BTS varactors with an IIP₃ of around 44 dBm [7].

A big advantage of the SOI/SOS DTCs is that their control voltage is less than 5 V and that they are quite low cost [7].

The last type of capacitor described is a MEMS tunable capacitor, which is the type used for this project. The MEMS tunable capacitor cell is shown in Figure 1.15.

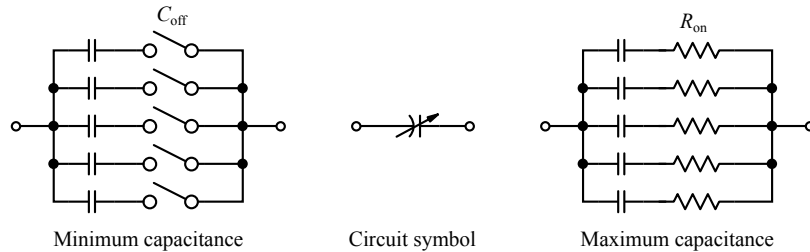


Figure 1.14: Circuit showing the operation of a SOS/SOI digitally tunable capacitor. To the left, the minimum capacitance situation is shown, where only parasitic capacitance from the switches is present. To the right, the maximum capacitance situation is shown where the on-resistance of the switches degrades the Q -factor.

A MEMS tunable capacitor consists of several of the cells shown in Figure 1.15. By applying a voltage on one or more of the cells, the top plate is pulled toward the bottom electrode, increasing the overall capacitance.

The Q -factor of a MEMS tunable capacitor is much higher than that of the BTS varactor and the SOI/SOS DTS – typically higher than 200 at minimum capacitance and above 100 at maximum capacitance, at 2 GHz [7]. The linearity is also better, having an achievable IIP₃ of greater than 68 dBm at 2.5 GHz.

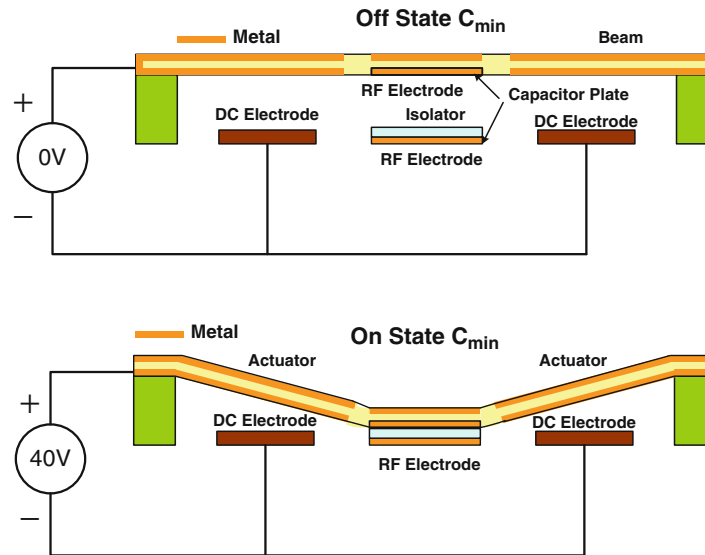


Figure 1.15: MEMS tunable capacitor cell in the on and off state [7].

Tuner Modeling

A tunable capacitor as described above would ideally have a purely imaginary impedance (infinite Q) and a reactance only made up of capacitance. As it happens, the ideal capacitor is impossible to come by in real life. Real capacitors have an equivalent series resistance (ESR) and parasitic capacitance and inductance determined by the physical layout of the component. To use a tunable capacitor in simulation, an equivalent circuit for the capacitor is therefore more accurate than using an ideal capacitor.

Two types of equivalent networks are common to represent a two-port network:

1. The π -network, with two shunt impedances and one series impedance in between. This is used for modeling a *series tunable capacitor*.
2. The T-network, with two series impedances and one shunt impedance in between. This is used for modeling a *shunt tunable capacitor*.

The two networks are shown in Table 1.3. The values of the components in the networks can be determined by measuring the S-parameters of a tunable capacitor at two frequencies. The two frequencies are necessary to obtain both capacitive and inductive parasitics. For the result to be accurate, the S-parameter measurements must be made very accurate [7]. The conversion formulas from S-parameters to component values are likewise shown in Table 1.3.

Based on the knowledge from this section, it is possible to accurately model a MEMS tunable capacitor from S-parameter measurements of it. It is also clear how a matching circuit can be designed, using the smith chart, to maximize the power delivered to the

	Series capacitor (π)	Shunt capacitor (T)
Circuit		
ω_L		$2\pi f_{\text{low}}$
ω_H		$2\pi f_{\text{high}}$
$X_1(\omega)$	$Z_0 \text{Im} \left\{ \frac{1 + S_{11} + S_{22} + (S_{11}S_{22} - S_{21}^2)}{1 + S_{22} - S_{11} - 2S_{21} - (S_{11}S_{22} - S_{21}^2)} \right\}$	$Z_0 \text{Im} \left\{ \frac{1 + S_{11} - S_{22} - 2S_{21} - (S_{11}S_{22} - S_{21}^2)}{1 - S_{11} - S_{22} + (S_{11}S_{22} - S_{21}^2)} \right\}$
$X_S(\omega)$	$Z_0 \text{Im} \left\{ \frac{1 + S_{11} + S_{22} + S_{11}S_{22} - S_{21}^2}{2S_{21}} \right\}^\dagger$	$Z_0 \text{Im} \left\{ \frac{2S_{21}}{1 - S_{11} - S_{22} + S_{11}S_{22} - S_{21}^2} \right\}$
$X_2(\omega)$	$Z_0 \text{Im} \left\{ \frac{1 + S_{11} + S_{22} + (S_{11}S_{22} - S_{21}^2)}{1 + S_{11} - S_{22} - 2S_{21} - (S_{11}S_{22} - S_{21}^2)} \right\}$	$Z_0 \text{Im} \left\{ \frac{1 - S_{11} + S_{22} - 2S_{21} - (S_{11}S_{22} - S_{21}^2)}{1 - S_{11} - S_{22} + (S_{11}S_{22} - S_{21}^2)} \right\}$
L_k	$\frac{\omega_L X_k(\omega_L) - \omega_H X_k(\omega_H)}{\omega_L^2 - \omega_H^2}^\dagger$	
C_k	$\frac{\omega_L^2 - \omega_H^2}{\omega_L \omega_H} \frac{1}{\omega_H X_k(\omega_L) - \omega_L X_k(\omega_H)}$	
R_1	$Z_0 \text{Re} \left\{ \frac{1 + S_{11} + S_{22} + (S_{11}S_{22} - S_{21}^2)}{1 + S_{22} - S_{11} - 2S_{21} - (S_{11}S_{22} - S_{21}^2)} \right\}$	$Z_0 \text{Re} \left\{ \frac{1 + S_{11} - S_{22} - 2S_{21} - (S_{11}S_{22} - S_{21}^2)}{1 - S_{11} - S_{22} + (S_{11}S_{22} - S_{21}^2)} \right\}$
L_1	$L_k \Big _{k=1}$	$\frac{Z_0}{\omega} \text{Im} \left\{ \frac{1 + S_{11} - S_{22} - 2S_{21} - (S_{11}S_{22} - S_{21}^2)}{1 - S_{11} - S_{22} + (S_{11}S_{22} - S_{21}^2)} \right\}$
C_1	$C_k \Big _{k=1}$	
R_s	$Z_0 \text{Re} \left\{ \frac{1 + S_{11} + S_{22} + S_{11}S_{22} - S_{21}^2}{2S_{21}} \right\}$	$Z_0 \text{Re} \left\{ \frac{2S_{21}}{1 - S_{11} - S_{22} + S_{11}S_{22} - S_{21}^2} \right\}$
L_s	$L_k \Big _{k=s}$	$\frac{\omega_H X_s(\omega_H) - \omega_L X_s(\omega_L)}{\omega_H^2 - \omega_L^2}$
C_s	$C_k \Big _{k=s}$	$\frac{\omega_L^2 - \omega_H^2}{\omega_L \omega_H} \frac{1}{\omega_H X_s(\omega_L) - \omega_L X_s(\omega_H)}$
R_2	$Z_0 \text{Re} \left\{ \frac{1 + S_{11} + S_{22} + (S_{11}S_{22} - S_{21}^2)}{1 + S_{11} - S_{22} - 2S_{21} - (S_{11}S_{22} - S_{21}^2)} \right\}$	$Z_0 \text{Re} \left\{ \frac{1 - S_{11} + S_{22} - 2S_{21} - (S_{11}S_{22} - S_{21}^2)}{1 - S_{11} - S_{22} + (S_{11}S_{22} - S_{21}^2)} \right\}$
L_2	$L_k \Big _{k=2}$	$\frac{Z_0}{\omega} \text{Im} \left\{ \frac{1 - S_{11} + S_{22} - 2S_{21} - (S_{11}S_{22} - S_{21}^2)}{1 - S_{11} - S_{22} + (S_{11}S_{22} - S_{21}^2)} \right\}$
C_2	$C_k \Big _{k=2}$	

Table 1.3: Formulas for computing the equivalent circuit components from S -parameters measured at two frequencies, f_{low} and f_{high} [7, 17]. Here ω with no index indicated the angular frequency of calculation. The resistance values may change depending on the frequency of the S -parameter measurement. † Mistakes in [7] have been corrected here.

antenna.

The next sections will describe some of the important terms and metrics used in a link budget. The next section describes basic propagation models, which are used to connect a maximum allowed path loss with a certain communication distance for different environments.

1.4 Basic Propagation Models

This section will describe some simple propagation models and terms that can be used to establish the maximum obtainable communication range given the maximum path loss computed in a link budget.

The simplest propagation model is the free-space path loss, which is given in Equation 1.19. The free-space path loss is, however, rarely appropriate, since it does not take trees, buildings, etc. into account [18]. There are, however, a myriad of empirical models which are based on actual measurements. The drawback is that these empirical models tend not to be general and a given model might not be suited for two different cities. This results in that empirical models often are grouped into three main branches: Foliage, terrain, and city models [30]. For foliage areas models such as the Weissbergers model and the ITU Vegetation model can be used [30]. For terrain areas, models such as the Egli or Longley-Rice model are used [30]. To model the path loss in cities, the Young, Okumura, Hata, or the COST 231 models can be used [30]. It should be noted that some of these models are not usable in upper LTE frequency range, and thus care should be taken when applying these models.

1.4.1 Multipath

The multipath effect exists when a wave and/or multiple waves are scattered, such that the receiver experiences multiple copies of the same wave coming from different directions. In areas where there is no ground or other obstacles (free-space) the multipath effect does not exist. The simplest multipath case is the two-ray case, where the surface of the earth is included, in this case there will be a single reflection from the earth and thus multiple paths from the transmitter to the receiver [31]. This scenario is illustrated in Figure 1.16a.

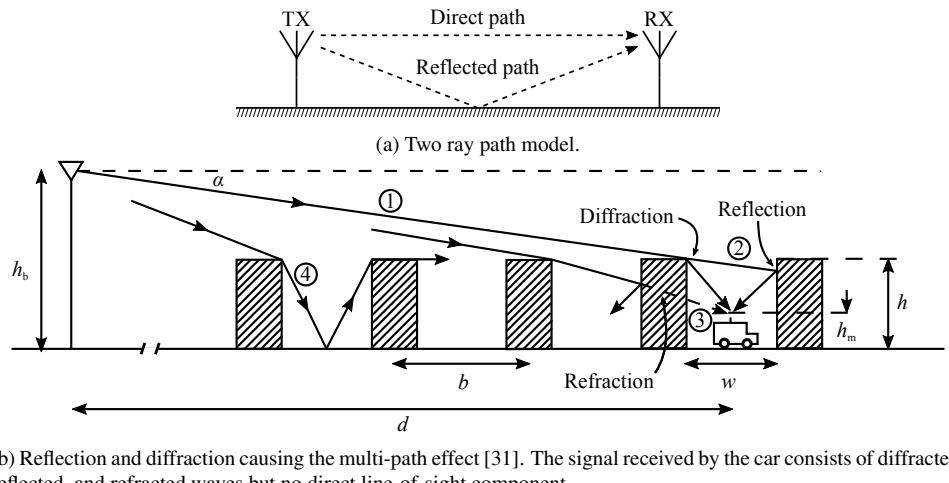


Figure 1.16: Two ray model and different multipath effects.

The multipath effect will be greatest in urban environments, where several buildings and other obstacles are present. If the surface is rough, scattering will also take place. This is the phenomenon where a single incoming wave scatters into multiple reflections. In addition to this there is also diffraction where a wave front is “bend” at the edges of buildings, which is illustrated in Figure 1.16b. Multipath results in a negative effect on the throughput. However, with MIMO, the multipath effects are now exploited positively to increase throughput and channel stabilization [31].

1.4.2 Fading

The signal strength in a wireless channel is constantly fluctuating. These variations are represented by fading. The variations can be caused by scattering, reflections, blockage etc. Based on the type of variation, the fading is grouped in *small scale fading* and *large scale fading*. Large scale fading is typically caused by large objects, such as hills and buildings, where small scale fading occurs over small travel distances due to constructive or destructive adding of the multipath waves [31].

By superimposing the path loss with small scale fading and large scale fading, the combined model, which represents the total propagation and path loss, is obtained. This is illustrated in Figure 1.17.

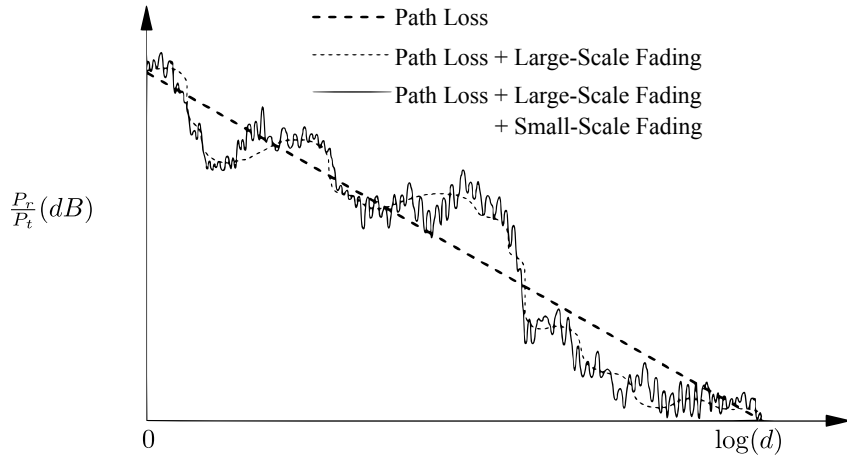


Figure 1.17: Combined path loss model with large- and small-scale fading [30].

1.4.3 Empirical Models

This section will describe some of the city-models that are often used in estimating the path loss.

Hata Model

The Hata model is a mathematical model derived from the graphical Okumura model, which is based on measurements from Tokyo in 1960 in the frequency range 200 MHz to 1920 MHz. The model is divided into three groups: Urban, suburban, and open areas which are defined in dB in Equation 1.38, Equation 1.41, and Equation 1.42, respectively [32].

$$L_{50} = L_{50}(\text{urban}) = 69.55 + 26.12 \log(f_c) - 13.82 \log(h_t) - a(h_r) + [44.9 - 6.55 \log(h_t)] \log(d) \quad (1.38)$$

where

f_c = Center frequency in MHz and in the range: $150 < f_c < 1500$.

h_t = Height in meters, which must satisfy $30 < h_t < 200$.

d = Distance in km which must satisfy $1 < d < 20$.

$a(h_r)$ = The mobile antenna height correction factor. Defined in Equation 1.39 [32] for small and medium sized cities. Defined in Equation 1.40 [32] for a large city.

$$a(h_r) = (1.1 \log(f_c) - 0.7)h_r - [1.56 \log(f_c) - 0.8] \quad \text{if } 1 \text{ m} \leq h_r \leq 10 \text{ m} \quad (1.39)$$

$$a(h_r) = \begin{cases} 8.29(\log(1.54h_r))^2 - 1.1 & \text{if } f_c \leq 200 \text{ MHz}, \\ 3.2(\log(11.75h_r))^2 - 4.97 & \text{if } f_c \leq 400 \text{ MHz} \end{cases} \quad (1.40)$$

$$L_{50}(dB) = L_{50}(\text{urban}) - 4.78(\log(f_c))^2 + 18.33 \log(f_c) - 40.94 \quad (1.41)$$

$$L_{50}(dB) = L_{50}(\text{urban}) - 2 \left(\log \left(\frac{f_c}{28} \right) \right)^2 - 5.4 \quad (1.42)$$

This extension to the Okumura model is often used in practical applications since it is easier to apply than the Okumura model. However, it only handles frequencies up to 1500 MHz, which lead to the COST 231 model being developed.

COST 231 Model

The COST 231 model is an extension of the Hata model. It includes the PCS bands 1800 MHz to 1900 MHz which makes it an ideal model for many wireless personal communication systems (GSM etc.). The path loss is given by Equation 1.43 in dB [32] and the model is valid in the frequency range of 1500 MHz to 2000 MHz, link distance from 1 km to 20 km, a transmitter antenna height of 30 m to 200 m, and a receiver height of 1 m to 10 m [32]. It should also be stated that the model is restricted to applications where the base station antenna is above adjacent roof tops [33].

$$L_{50}(dB) = 46.3 + 33.9 \log(f_c) - 13.82 \log(h_t) - a(h_r) + [44.9 - 6.55 \log(h_t)] \log(d) + C \quad (1.43)$$

where

f_c = Frequency in MHz.

h_t = Transmitter height in m.

h_r = Receiver height in m.

$a(h_r)$ = Mobile antenna height correction factor from Equation 1.39 and Equation 1.40.

d = Distance of propagation.

C = 0 dB for suburban and medium cities with medium tree density, 3 dB for metropolitan centers.

Extended COST

An extension to the COST 231 model is described in a ITU (International Telecommunication Union) report [33] and this model extends the COST 231 such that it is accurate up to 3 GHz. The path loss model for an urban environment in the range of 2000 MHz to 3000 MHz is given by [33]

$$L = 46.3 + 33.9 \log(2000) + 10 \log\left(\frac{f_c}{2000}\right) - 13.82 \log(\max\{30, h_t\}) + [44.9 - 6.55 \log(\max\{30, h_t\})](\log(d))^\alpha - a(h_r) - b(h_t) \quad (1.44)$$

where

f_c = The frequency in MHz.

h_t = Transmitter height in m.

h_r = Receiver height in m.

$a(h_r)$ = The mobile antenna height correction factor given in Equation 1.45.

$b(h_t)$ = Transmitter height correction factor given in Equation 1.46.

α = Given in Equation 1.47.

$$a(h_r) = (1.1 \log(f) - 0.7) \min\{10, h_r\} - (1.56 \log(f) - 0.8) + \max\left\{0, 20 \log\left(\frac{h_r}{10}\right)\right\} \quad (1.45)$$

$$b(h_t) = \min\left\{0, 20 \log\left(\frac{h_t}{30}\right)\right\} \quad (1.46)$$

$$\alpha = \begin{cases} 1 & \text{if } (d \leq 20 \text{ km}) \\ 1 + (0.14 + 1.87 \times 10^{-4} f + 1.07 \times 10^{-3} h_t) & \text{if } (20 \text{ km} < d \leq 100 \text{ km}) \end{cases} \quad (1.47)$$

In this section, basic propagation models were described, making it possible to predict the communication distance given a certain maximum path loss. In the next section, the effect of having a user present in a mobile communication system will be described.

1.5 User Effects

In this section, the user's impact on mobile antenna performance will be described, including both effects of both the head and the hands. The user introduces a loss which can be used in the link budget to obtain an estimate of the total loss in a system.

Antenna parameters such as efficiency, radiation pattern, impedance, etc. will be effected by the user, as the body of the user will look like a lossy and large dielectric body from the antennas point of view [34]. The internal antennas that are implemented in most phones today, have a similar performance compared to external stubby antennas, which were used in a numerous older designs. However, this is only if the antennas are measured and compared in free-space or next to a phantom head. In practical use, a mobile phone with an internal antenna design will be much more vulnerable to head and hand impacts from the user. The negative performance impact will be there but will differ from user to user as things like head and hand size, hand position, whether the user is left or right handed, etc., varies. This is, of course, a drawback in switching from external to internal antennas but the development also comes with a lot of advantages. The internal antenna provides robust design and normally has higher performance in mechanical tests such as drop tests, wearing tests, etc., as the antenna is placed inside the phone, thus, making physical interaction impossible [34]. To counteract and minimize the user effect problem to the internal antennas, some basic design guidelines can be followed.

1.5.1 Design Guidelines

An antenna, that is placed in the top of the phone, will be more effected by the user in talk mode as the antenna will be closer to the head. To avoid this, a ground plane can be placed between the user and the head in order to create more isolation. However, placing the antenna on top of the ground plane decreases the bandwidth significantly, which leads to an increase in the antenna size to keep the required bandwidth. This is not a realizable solution in mobile phones, as the size requirement of the antennas are very strict as a result of recent smartphone designs with bigger screens and smaller cases. A way to solve this problem is to place the antenna in the bottom of the phone, hence lowering the user effect and making it possible to place the antenna without the ground plane as isolation. This solution provides a certain ground clearance, which makes it possible to decrease the volume and thickness of the antenna, saving space in the mobile phone [34].

The bottom-placed antenna design was proven to work by Motorola with their Motorola Razr V3 phone, which was the first phone to use the bottom placed antenna. There were some skeptics to this design, as the bottom of the phone would be placed in the middle of the hand in talk mode. However, Motorola proved that hypothesis wrong and therefore, many phone manufacturers are now using their own bottom placed antennas [35]. This solution, of course, only applies in talk mode as the head effect is close to zero when the phone is used in data mode. In data mode, the phone is usually held either in vertical mode with one hand (data mode) or in horizontal mode with two hands (play mode). In vertical mode, given the size of today's smartphones, the hand will be placed around the middle of the phone (depending on the individual user), clearing the top and bottom. This indicates that it does not matter whether the antenna is placed in the top or bottom of the phone. In the case of horizontal mode with two hands, the hands covers both the top and the bottom of the phone, so in this case it still makes no difference if the antenna is placed in the bottom or in the top of the phone [35].

In talk or data (vertical or horizontal) mode, there will still be some negative user effect on the performance. As long as the head or hand is within the near field of the phone, the impact of the user will be significant and needs some attention. Besides following the simple design guidelines, antenna tuning can be used to optimize the performance when the antenna's resonance frequency is detuned as a result of the user impact.

1.5.2 Simulation and Measurement Studies

A recent study has been carried out in 2014 at Aalborg University on user effects of MIMO LTE performance, which is also the antenna design goal of this project [36]. The study is based on time-domain simulations of the user effects of head and hand phantoms in a free-space scenario. The phantom hand used is modified such that the finger can move across the phone's backplane to give more realistic results. The simulations were done in CST Microwave Studio using the time-domain solver using FEM (Finite Element Method). Furthermore, the antenna is placed in different positions to evaluate on the user effect for different antenna positions. The different positions and the results of the simulation study can be seen in Table 1.4 and Table 1.5. In Table 1.4, the S -parameters S_{11} and S_{22} are the reflection coefficient for the antenna at port 1 and 2, respectively, and S_{21} indicates the isolation between the two antennas. From the results, it is clearly seen that the antennas are significantly detuned in the presence of a user. In the worst case, the reflection coefficient drops from -8.2 dB to -0.6 dB, which is the case for the side mounted antenna. The bottom mounted antenna is the best case where the reflection coefficient only drops around -2.5 dB which is still a noticeable drop. The transmission between the antennas drops as a result of the mismatch loss due to the user effects. This is an advantage of the user effect in this LTE MIMO system but is clearly not a reliable advantage as the goal is to improve the system and minimize the user effects. Overall, the results are sensitive and dependent on the finger position with the top mounted antennas as the most sensitive as the finger in this case is closest to the antenna [36].

In Table 1.5, the results of the radiation efficiencies and total efficiencies are presented for both the top/side and the bottom/side antennas as for the results of the S -parameters. T1 and T2 represents the total efficiencies and R1 and R2 the radiation efficiencies for the main and diversity antenna, respectively.

The results show close resemblance in comparison with the S -parameters and show that the efficiency is strongly influenced by the user effects. In this case, the strongest user effect of the finger is with the side antenna, as with the S -parameters [36].

In combination with the impact of user effects, a measurement on this topic was carried out at Aalborg University in 2008 [21]. The measurements were done for 44 different persons, where 6 persons were measured twice to check the ability to repeat measurements of the same person. The simulations and measurements are not fully comparable and in this case many factors such as, environment, test frequency, etc., are very different. From the measurements, the body loss was found to be 3 dB. The 6 test persons that were measured twice during the measurements, showed that the user effect were very dependent on the individual user. Some of the possible reasons for varying results between user are listed below:

- Position of the hand on the handset.
- Distance between the head and the handset.
- Tilt angle of the handset.
- The shapes of the head and the hand.

	Antennas: Top/Side			Antennas: Bottom/Side		
	S_{11}	S_{22}	S_{21}	S_{11}	S_{22}	S_{21}
FS	-7.9	-8.2	-8.4	-7.9	-8.2	-8.4
P1	-2.4	-1.2	-22.7	-5.5	-1.1	-21.0
P2	-4.8	-1.2	-22.5	-5.5	-0.6	-22.9
P3	-2.0	-1.2	-22.8	-5.1	-1.8	-19.7
P4	-4.8	-1.2	-22.2	-5.2	-1.9	-19.2
P5	-1.5	-1.1	-22.6	-4.8	-2.6	-19.4
P6	-4.3	-1.1	-22.5	-5.0	-2.0	-18.5

Table 1.4: S -parameter of the two MIMO antennas in free-space compared to the user effect of the hand in six different finger positions [36].

	Antennas: Top/Side				Antennas: Bottom/Side			
	R1	R2	T1	T2	R1	R2	T1	T2
FS	-0.2	-1.1	-1.0	-1.9	-0.2	-1.1	-1.0	-1.9
P1	-13.4	-9.2	-15.8	-14.8	-8.9	-10.9	-9.6	-17.0
P2	-14.1	-8.6	-14.7	-14.6	-8.6	-9.7	-9.0	-18.5
P3	-13.3	-9.3	-16.2	-14.9	-8.7	-14.4	-9.7	-18.5
P4	-14.3	-8.9	-14.9	-14.9	-8.6	-14.4	-9.6	-18.2
P5	-14.0	-9.6	-17.6	-15.5	-8.9	-15.2	-9.9	-18.8
P6	-14.0	-8.8	-14.6	-15.0	-8.7	-15.4	-9.7	-18.1

Table 1.5: Radiation and total efficiency of the two MIMO antennas in free-space compared the user effect of the hand in six different finger positions [36].

- The size of the person.
- Variations in skin humidity.
- Many, possibly minor, parameters such as age, sex, amalgam teeth fillings, glasses, amount of hair, and so forth.

1.5.3 SAR – Specific Absorption Rate

SAR is a measure of how transmitted RF energy is absorbed by the body from the source being measured [37]. SAR is defined as [20]

$$\text{SAR} = \frac{\sigma}{2\rho} |E|^2 \quad (1.48)$$

where

σ = Conductivity of the tissue [S/m].

ρ = Material density [kg/m^3].

E = Electric field intensity.

The SAR value is averaged over a specific volume and have different requirement for the volume and max SAR dependent on region [35],

- Europe – Max SAR 2 W/kg averaged over 10 g of tissue.
- US – Max SAR 1.6 W/kg averaged over 1 g of tissue.

The SAR requirements and testing is standardized by the Federal Communications Commission (FCC) and is tested at the highest power level in all the frequency bands. Standardized head and body models filled with liquid is used and specific holding positions is tested. Pinpoint measurements are done at specific locations within the head and body models and the highest SAR value is used to verify the requirements. The SAR value does not tell anything about the general exposure to RF emission but only the highest SAR from that specific phone. Therefore, buying a phone with a low measured SAR value is not equal to low SAR exposure in general. A phone with a high measured SAR value can have a lower averaged SAR exposure than a phone with a low measured SAR value and vice versa [37].

The negative influence of the user effect has been a known issue for quiet some time and is confirmed by the resent studies from 2014 [36]. The results presented for both the S -parameters, the total efficiency, and the radiation efficiency show very varying results dependent on the position of the finger and the antenna placement. However, the noticeable part of the results is that even

in the best case, the user still has a significant effect on the performance of the antenna, which needs attention. In the case of the GSM specifications, the body loss is taken as 3 dB, which is close to the best case simulation scenario. From the simulation and measurement studies it is seen that a body loss of 10 dB is more common, which also implies that the user effect needs more attention when used in a link budget.

In the next section, the effect of MIMO in an LTE system will be described.

1.6 MIMO in Handsets

Multiple antennas in both transmitter and receiver in wireless systems, which is better known as MIMO, has become a widespread technology and used in many applications today, due to its ability to increase performance. Most wireless systems are limited by the channel in which they propagate, due to phenomena such as multi-path fading. Multi-path happens when the transmitted signal travels through multiple different paths, which influences the time it takes for the signal to reach the receiver, the angle of arrival, and even frequency shifts due to Doppler. This creates random fluctuation in the received signal level, affecting the performance of the wireless communication. MIMO is an effective way of dealing with the challenges in delivering more throughput and cope with the multipath effects from buildings. MIMO exploits the multi-path phenomenon to transmit several different data streams simultaneously, also referred to as spatial multiplexing. This can help in both single user or in multi-user scenarios. For the single user, it allows for faster data rates without increasing the transmit power or allocating more frequency resources. In the multi-user scenario, the base station can effectively create beams to individual users while using the same shared frequency. This is also known as Space Division Multiple Access (SDMA). The purpose of this section is to explain what is understood by such a system, how it relates to the antenna design, and how it makes a difference. The principal mechanisms and performance metrics are explained. This section will not describe the statistical channel models but rather focus on the antenna related perspectives.

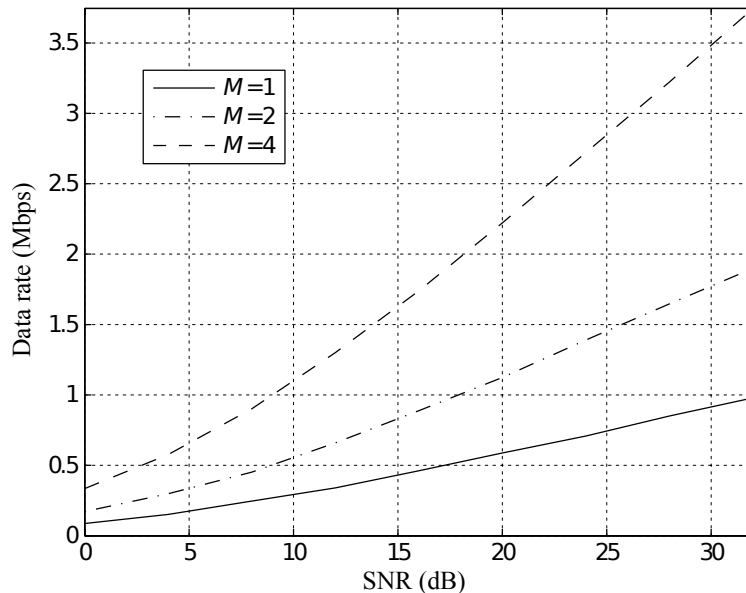


Figure 1.18: Throughput versus SNR given a specific M -ary MIMO-setup [38].

1.6.1 Perks of MIMO

As shown in the introduction to this section, the use of MIMO results in enhanced performance. Figure 1.18 shows the general performance increase, however this is gained by the addition of multiple different performance gains. The performance gains are spatial diversity gain, multiplexing gain, array gain, and interference reduction [38], which will be described briefly in the following.

Spatial Diversity Gain

The spatial diversity gain improves the resistance to fading in the receiver. This is done by providing the receiver with multiple different copies of the same transmitted signal. Ideally, the copies are independent from another. A diversity technique is required to combine the signals at the receiver [38]. Some examples could be equal gain combining, maximal-ratio combining, or selection combining. The spatial diversity is also quite intuitive since the probability that one of the signals are not in a fade increases per added element, given that they are somewhat independent.

Spatial Multiplexing Gain

Spatial multiplexing can be used in scatter rich channels where the received signals are independent. Instead of transmitting the same signal, as done in diversity gain, the spatial multiplexing transmits multiple independent data streams. This allows for a linear increase in the data rate, thus the capacity of the wireless network is increased. Generally, the number of independent streams that can be supported is limited by the number of receive antennas [4].

Array Gain

The array gain is the result of coherent combining of the wireless signals at the receiver, which results in an increase in the receive SNR. The array gain is improved linearly as the number of receive antennas increases [39]. This gain improves the resistance to noise and thus also the coverage [4].

Interference Gain

By using MIMO, the interference from different users and base stations can be avoided by exploiting extra spatial degrees of freedom, such as array gain. Furthermore, beam-steering could be implemented such that the signal could be directed towards the designated receiver. Obviously, all of the above can not be used at the same time. However, using a combination allows for improved coverage, capacity, and reliability [4].

1.6.2 Channel Capacity

The capacity of a channel is the maximal transmission rate for which a reliable communication can be achieved, and if the transmission rate exceeds this, the system breaks down [4]. The channel capacity is one of the primary performance measures to characterize the performance of MIMO systems [4]. This section will focus on the capacity for time-invariant SISO, SIMO, MISO, and MIMO channels. The main assumptions for the time-invariant channel is the following [4]:

- The channel is time-invariant.
- A codeword spans over an asymptotic long data block, which averages out the noise.
- Channel state information is available at both the transmitter and receiver.

Time-Invariant SISO Channel

A simple SISO channel, as illustrated in Figure 1.19, is given by the input-output relation:

$$y(k) = h x(k) + n(k)$$

Here h describes the channel, which is time *independent*. The signal power is $\bar{P}|h|^2$, which is the power in $h x(k)$ and the noise power of $n(k)$ is σ_n^2 . Thus, the SNR is given by the ratio [4]

$$\text{SNR}_{\text{AWGN}} = \frac{\bar{P}|h|^2}{\sigma_n^2} \quad (1.49)$$

This yields a channel capacity of [4]

$$C_{\text{AWGN}} = \log_2 (1 + \text{SNR}_{\text{AWGN}}) \quad (1.50)$$

It is seen that the SNR is an important factor for the AWGN channel capacity.

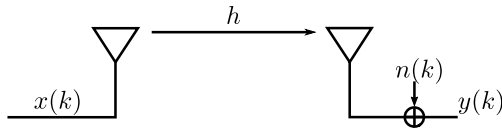


Figure 1.19: The time-invariant SISO channel

Time-Invariant SIMO Channel

The channel capacity for a SIMO system, where a symbol $x(k)$ is sent from a single antenna and received at M_R antennas, is illustrated in Figure 1.20. In a SIMO system, the signal is coherently combined at the receiver. When including this post-processing, the system transforms into an equivalent SISO channel [4].

The system model changes from a scalar equation to a vector notation due to the multiple antennas. The channel coefficients are denoted as h_j , j, \dots, M_R and are known at the transmitter. At a given antenna, j , the received signal $y_j(k)$ is given by [4]:

$$y_j(k) = h_j x(k) + n_j(k) \quad (1.51)$$

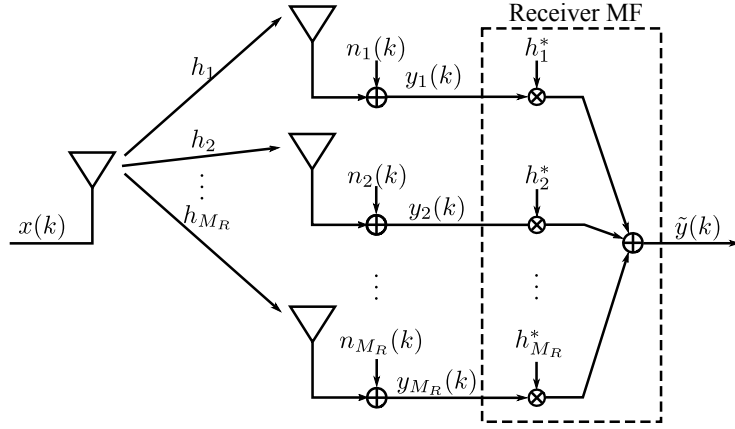


Figure 1.20: The time-invariant SIMO channel.

The multiple antennas receive multiple distorted copies of the transmitted symbol. Each received signal has different parts of the signal depending on the channel. To recover most of the original message, the different symbols are combined. This combination can be done in multiple ways: Matched filtering, maximum ratio combining, or equal-gain combining. Matched filtering requires the most amount of post-processing since it requires the signals to be aligned in phase, so they can be added constructively and scaled. This maximizes the post-processing SNR of the SIMO system. Mathematically the received signal at antenna j is first multiplied with a scalar coefficient h_j^* matched to the channel. This yields $|h_j|^2 x(k) + h_j^* n_j(k)$. The processed signals are then added up, resulting in a processed signal [4]

$$\tilde{y}(k) = \|\mathbf{h}\|^2 x(k) + \tilde{n}(k) \quad (1.52)$$

The SIMO system becomes equivalent to a scalar AWGN channel, with a potentially larger SNR due to the post-processing [4]. This leads us to an SNR and a channel capacity given by [4]

$$\text{SNR}_{\text{SIMO}}^{\text{TI}} = \frac{\bar{P} \|\mathbf{h}\|^2}{\sigma_n^2} \quad (1.53)$$

$$C_{\text{SIMO}}^{\text{TI}} = \log_2 \left(1 + \frac{\bar{P} \|\mathbf{h}\|^2}{\sigma_n^2} \right) \quad (1.54)$$

Time-Invariant MISO Channel

In the MISO case, the system consists of multiple antennas at the transmitter and a single antenna at the receiver. This is illustrated in Figure 1.21. Given that the channel is known at the transmitter, it is possible to perform pre-processing on the transmitted

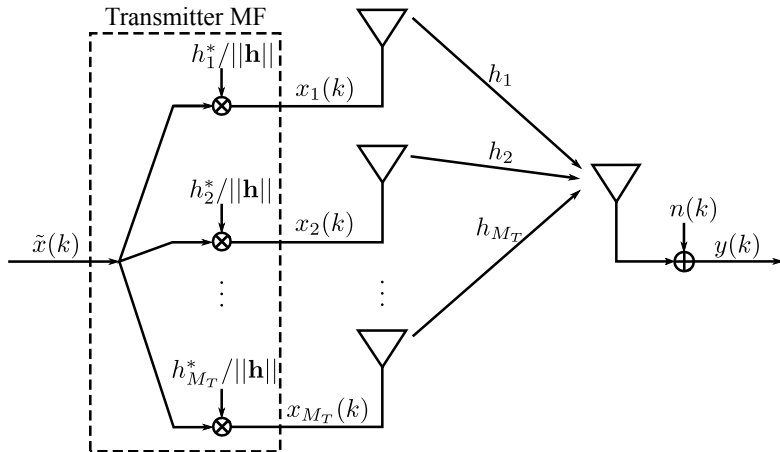


Figure 1.21: The time-invariant MISO channel.

signals. This transforms the MISO case into an equivalent SISO channel. The pre-processing consists of scaling each version of the

transmitted symbol to insure that the signals are added up constructively at the receiver. The pre-processing must take the channel for each antenna into account when doing this scaling.

A signal $x_i(k)$ is sent from the i th antenna in the array. This signal travels through the channel h_i and this channel is known at the transmitter. The received signal is then given as [4]:

$$y(k) = \sum_{i=1}^{M_T} h_i x_i(k) + n(k) = \mathbf{h}^T \mathbf{x}(k) + n(k) \quad (1.55)$$

where

M_T = The number of transmitter antennas.

$$\mathbf{h} = [h_1 \cdots h_{M_T}]^T.$$

$$\mathbf{x}(k) = [x_1(k) \cdots x_{M_T}(k)]^T.$$

The MISO becomes an equivalent SISO channel. The pre-processing that is often used is transmit spatial matched filtering or transmit MRC, where the transmitted signal is matched to the channel h_i before being sent from antenna i . The weights applied in the transmit MF are the exact same as the receiver MF due to perfect knowledge of the channel [4]. The output of the pre-processing is under the power constraint $\sum_{i=1}^{M_T} E|x_i(k)|^2 \leq \bar{P}$. The signal x_i sent from the antenna is then [4]

$$x_i(k) = \frac{h_i^*}{\|\mathbf{h}\|} \tilde{x}(k) \quad (1.56)$$

On the receiving side, the signals are phase-aligned and added constructively. It is obvious that more power is allocated to the stronger channels, thus maximizing the SNR. The SNR and channel capacity then becomes [4]:

$$\text{SNR}_{\text{MISO}}^{\text{TI}} = \frac{\bar{P} \|\mathbf{h}\|^2}{\sigma_n^2} \quad (1.57)$$

$$C_{\text{MISO}}^{\text{TI}} = \log_2 \left(1 + \frac{\bar{P} \|\mathbf{h}\|^2}{\sigma_n^2} \right) \quad (1.58)$$

Thus, it is seen that for time-invariant channels with perfect channel knowledge for both transmitter and receiver, the capacity for SIMO and MISO systems are the same. This is, however, not the case for fading channels when the channel state is unknown for the transmitter. This leads to performance degradation in the MISO case [4].

Time-Invariant MIMO Channel

When multiple antennas are available at both transmitter and receiver, the capacity can be increased by sending multiple symbols per transmission period. This relies on pre- and post-processing which is matched to singular value decomposition of the channel [4], illustrated in Figure 1.22. This processing extracts independent spatial routes for the communication. MIMO can be interpreted as multiple pairs of independent SISO channels where the capacity simply becomes the sum of these independent SISO channels [4].

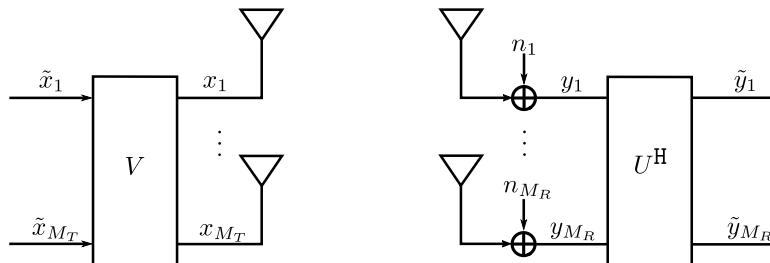


Figure 1.22: The time-invariant MIMO channel.

The singular value decomposition of the channel matrix is fundamental in understanding the underlying concepts of MIMO systems. The SVD extracts the equivalent independent AWGN channels, gives the maximum number of streams that can be multiplexed, and it provides a simple way to compute the capacity. The SVD of the channel matrix \mathbf{H} is [4]

$$\mathbf{H} = \mathbf{U} \Lambda \mathbf{V}^H \quad (1.59)$$

Both \mathbf{U} ($M_R \times M_R$) and \mathbf{V} ($M_T \times M_T$) are unitary matrices, and Λ is a $M_R \times M_T$ diagonal matrix with non-negative singular values λ_k with $k = 1, \dots, M_{\min}$ where $M_{\min} = \min(M_T, M_R)$. The λ_k 's are called the eigenmodes of the channel and are often ordered decreasingly for convenience.

Another important quantity is the channel matrix rank \mathbf{H} , which is denoted r_H . This is defined as the number of nonzero singular values of \mathbf{H} , which determines the maximum number of independent streams that can be multiplexed at the same time [4]. The singular value and channel energy relationship is also useful. This is given as

$$\text{tr}(\mathbf{HH}^H) = \sum_{i=1}^{M_T} \sum_{j=1}^{M_R} |h_{ji}|^2 = \sum_{k=1}^{r_H} \lambda_i^2 \quad (1.60)$$

Each channel is called an eigenchannel. The entire MIMO channel is equivalent to the set of eigenchannels, each with a different SNR. Looking at the input-output relation [4]

$$\tilde{\mathbf{y}} = \Lambda \tilde{\mathbf{x}} + \tilde{\mathbf{n}} \quad (1.61)$$

From each input-output relation $\tilde{y}_k = \lambda_k \tilde{x}_k + \tilde{n}_k$ it is obvious that this describes an AWGN channel as seen previously in the SISO case. Since the noise are all independent, each AWGN subchannel are all independent as well. This forms a set of parallel AWGN channels, which leads to the conclusion that the capacity of the MIMO system is the sum of individual channel capacities. Finally, it is needed to include the transmit power allocation to fully calculate the channel capacity.

The power allocation is done using the water-filling algorithm [4]. For each eigenchannel we define:

$$\gamma_k = \frac{\lambda_k^2}{\sigma_n^2}, \text{ where } k = 1, \dots, r_H \quad (1.62)$$

The transmitted power of eigenchannel k is given by P_k . Then $P_k \gamma_k$ can be interpreted as the SNR of the k th eigenchannel. The capacity of each eigenchannel with transmit power P_k becomes $\log_2(1 + P_k \gamma_k)$. Now, this becomes a maximization problem, in which the SNR or channel capacity should be maximized with respect to the power constraint: $\sum_{k=1}^{r_H} P_k \leq \bar{P}$. The channel capacity of the MIMO system is then the sum of the individual capacities with optimized transmit power per eigenchannel [4]

$$\begin{aligned} C_{\text{MIMO}}^{\text{TI}} &= \underset{P_k}{\text{maximize}} \quad \sum_{k=1}^{r_H} \log_2(1 + P_k \gamma_k) \\ &\text{subject to} \quad \sum_{k=1}^{r_H} P_k \leq \bar{P} \end{aligned} \quad (1.63)$$

This optimization problem can be solved using the Lagrangian multipliers method, which gives the capacity of the time-invariant MIMO channel as [4]

$$C_{\text{MIMO}}^{\text{TI}} = \sum_{k=1}^{r_H} \log_2(1 + P_k^o \gamma_k) \quad (1.64)$$

where the transmit power is allocated as

$$P_k^o = \left(\frac{1}{\gamma_0} - \frac{1}{\gamma_k} \right)^+ \quad (1.65)$$

Here, γ_0 is the cut-off value and it is determined using the power constraint

$$\sum_{k=1}^{r_H} P_k^o = \sum_{k=1}^{r_H} \left(\frac{1}{\gamma_0} - \frac{1}{\gamma_k} \right)^+ = \bar{P} \quad (1.66)$$

From this it is seen that the power allocation and channel matrix rank are key elements to MIMO. The major advantage for MIMO systems is the fact that multiple streams of data can be sent simultaneously. The MISO and SIMO systems only experience an increase in SNR which allows for a more robust channel and the use of higher order modulation schemes. However, this is only true for independent AWGN channels, and in reality, the channel capacity has to be expressed stochastically using complex channel models.

1.6.3 Antenna Design in MIMO Applications

The three most important factors in MIMO antenna design are: Near-field coupling, the envelope correlation ρ_e , and total efficiency η_{total} . The near-field coupling is a measure of the coupled power towards the second antenna when the first antenna is excited. The coupling is evaluated by the S_{21} parameter and is often referred to as the *isolation*. This isolation affects the efficiency and envelope correlation coefficient [40]. The envelope correlation coefficient is a measure of how independent the antenna radiation patterns are, so if the two radiation patterns are pointing in two different directions, the correlation coefficient is zero, and if the radiation patterns are exactly the same, the correlation coefficient will be one. As a rule of thumb, a correlation coefficient of 0.5 is assumed to be sufficient, and 0.3 is generally seen as good for MIMO applications [4].

The total efficiency is simply given by Equation 1.67 [40], where η_{rad} is the radiation efficiency, which takes dielectric and conductive losses into account.

$$\eta_{\text{total}} = \eta_{\text{rad}}(1 - |S_{11}|^2 - |S_{21}|^2) \quad (1.67)$$

In practice, the total efficiency may be found directly by supplying a known amount of power to the antenna and observing the power radiated by the antenna. The total efficiency is then the ratio of the radiated power to the supplied/total power [18]

$$\eta_{\text{total}} = \frac{P_{\text{rad}}}{P_{\text{total}}} \quad (1.68)$$

The radiated power is proportional to the spherical integral of the farfield obtained in an anechoic chamber [18]

$$P_{\text{rad}} \propto \int_0^{2\pi} \int_0^\pi |F_\theta|^2 + |F_\phi|^2 \sin \theta d\theta d\phi \quad (1.69)$$

where F is the complex field sampled for each polarization. The total power, P_{total} , can be found (relatively) by rearranging Equation 1.68 and using Equation 1.69 *on a reference antenna* with known total efficiency, η'_{total} (here, ' denotes the reference antenna)

$$P_{\text{total}} \propto \frac{P'_{\text{rad}}}{\eta'_{\text{total}}} \quad (1.70)$$

As both the radiated power and the total power is now found using the same relative power measure (the same radiated-power formula, Equation 1.69), the total efficiency can be found using Equation 1.68.

The envelope correlation coefficient can be calculated by Equation 1.71 [41]. The far-field radiation pattern, F for each polarization, needs to be measured in order to reliably calculate the envelope correlation coefficient.

$$\rho = \left| \frac{\int_0^{2\pi} \int_0^\pi A_{12}(\theta, \phi) \sin \theta d\theta d\phi}{\sqrt{\int_0^{2\pi} \int_0^\pi A_{11}(\theta, \phi) \sin \theta d\theta d\phi \int_0^{2\pi} \int_0^\pi A_{22}(\theta, \phi) \sin \theta d\theta d\phi}} \right|^2 \quad (1.71)$$

where

$$A_{mn} = \text{XPR}_{mn} \cdot E_{\theta,m}(\theta, \phi) E_{\theta,n}^*(\theta, \phi) P_\theta(\theta, \phi) + E_{\phi,m}(\theta, \phi) E_{\phi,n}^*(\theta, \phi) P_\phi(\theta, \phi).$$

$E_{x,m}(\theta, \phi)$ = The recorded complex farfield in the polarization x of antenna m .

$P_x(\theta, \phi)$ = The distribution of incoming waves for polarization x . If the distribution is assumed to be isotropic, this can be set to $1/4\pi$.

XPR_{mn} = Cross polarization ratio = $P_{v,m}/P_{h,n}$ for the antenna set mn .

$P_{v,m}$ = Relative power in the θ polarization of antenna m ,

$$P_{v,m} = \int_0^{2\pi} \int_0^\pi |E_{\theta,m}|^2 \sin \theta d\theta d\phi$$

$P_{h,n}$ = Relative power in the ϕ polarization of antenna n ,

$$P_{h,n} = \int_0^{2\pi} \int_0^\pi |E_{\phi,n}|^2 \sin \theta d\theta d\phi$$

The envelope correlation coefficient can also be estimated by the S -parameters, as given in Equation 1.72 [42]. However, the use of this is often discouraged since it assumes very high radiation efficiency [42].

$$\rho_e \approx |\rho_c|^2 = \frac{|S_{11}^* S_{12} + S_{21}^* S_{22}|^2}{(1 - |S_{11}|^2 - |S_{21}|^2)(1 - |S_{22}|^2 - |S_{12}|^2)} \quad (1.72)$$

Thus, when designing antenna for the purpose of MIMO, the antennas need to be designed in a way such that the elements receives decorrelated signals. This can be done in different ways, such as changing the angular patterns, changing the polarization of the elements, or spatially separating the antennas, which are the most used methods. However, there are also other techniques such as decoupling networks, parasitic elements, active antenna cancellation, eigenmodes, and balanced currents.

Spatial Correlation

The spatial correlation between two antennas is given by the radiated E-field patterns as given in Equation 1.71. There, it is seen that the correlation is a comparison between the radiated E-field patterns and the incident E-fields arriving at the antenna, which is given by the probability P_θ and P_ϕ .

From the Equation 1.71 it can also be deduced that the spacing, polarization, and radiation patterns effects the correlation between two antennas. In order to investigate only the effects of spacial separation, we consider the case with two omnidirectional antennas which are both vertically polarized. This is described by Equation 1.73 [4].

$$\rho = \oint e^{j\beta\sqrt{d^2+l^2}\cos\zeta} p_\theta(\theta, \phi) \sin\theta d\theta d\phi \quad (1.73)$$

d = is the horizontal spacing

l = is the vertical spacing

$\cos\zeta = \sin(\phi + \tan^{-1}(l/d) \operatorname{sgn}\phi) \sin\phi$

In Figure 1.23, two cases of Equation 1.73 are shown: One where only the horizontal spacing is considered and another where only the vertical spacing is considered. The AoA (angle of arrival) is given by Taga and assumes that the AoA in azimuth is uniform and Gaussian in the elevation plane [4]. The mean angle, $\bar{\theta}$, is at 70° and the standard deviation σ_θ is 20° . From the plot it can be seen that the vertical spacing required for a certain correlation is larger than that of the horizontal spacing. This comes from the Taga-model used for the angle of arrival, since its distribution is nonuniform. This can, however, not be used to argue that the antennas should be spaced horizontally since smartphones are often operated both horizontally and vertically [4].

It is also possible to make the array in other topologies such as planar, circular, or random. This is, however, not very practical for mobile devices given the current usage of low frequencies in telecommunication (500 MHz to 2700 MHz) as described in Section 1.1.

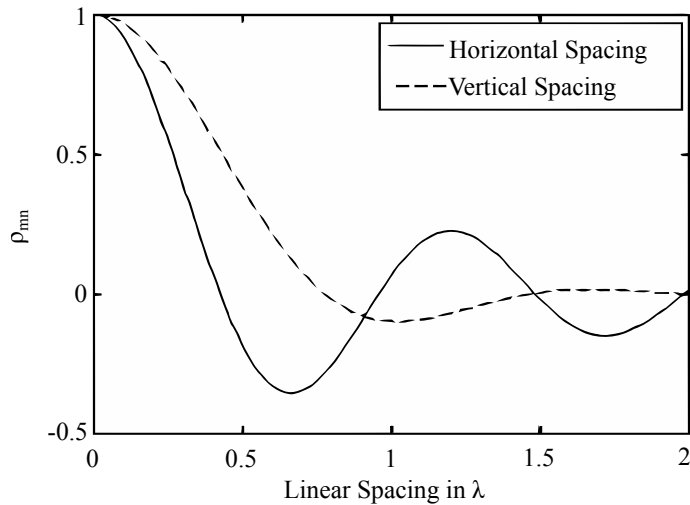


Figure 1.23: Spacing versus wavelength for the horizontal and vertical case [4]

Polarization and Radiation Patterns

In addition to the spatial separation to decorrelate antennas, polarization and different radiation patterns can also be used to decorrelate elements. This is very often used in small mobile devices where the physical size limits the spacing between elements.

In theory, using a perfectly polarized dipole and loop antenna, it would be possible to create totally decorrelated elements because they have opposite polarization. This is hard to implement in practice, but it is possible to lower the correlation of two elements by having a difference in polarization. However, using different polarization to get a lower correlation requires a suitable XPR in the channel. The XPR should be around 6 dB or lower [4].

Multiplexing Efficiency

Multiplexing efficiency is a measure of total efficiency for an antenna system, taking into account the total efficiency for each antenna *and* the correlation between antenna elements. In this way, it is a single parameter that describes the total loss in SNR (or power) when using a MIMO antenna system [43].

For a 2×2 MIMO system, relevant to this project, and assuming high SNR, the multiplexing efficiency, η_{mux} , is computed as [43]

$$\eta_{\text{mux}} = \sqrt{\eta_1 \eta_2 (1 - |\rho|^2)} \quad (1.74)$$

where

η_n = Total efficiency of the n th antenna.

ρ = Correlation between antenna 1 and 2.

In the rest of the report, efficiency and correlation will mostly be treated separately to see more details between the antennas. However, the metric of multiplexing may be useful when evaluating the antennas performance in a link budget.

In this section, the basic principles of MIMO have been described. Important terms such as correlation and capacity have been described and multiplexing efficiency has been discovered as a usable term for modeling MIMO into a link budget. An example link budget will be given next.

1.7 Example LTE Link Budget

In this section, an example link budget is given to show what parts of the link is affected by the antenna design. The link shows the total path loss expected in a link. Using the path loss models from Section 1.4, this path loss can be used to estimate the possible communication distance.

The presented link budget is for typical values and is largely based on [3]. The maximum path loss is computed as

$$\begin{aligned} \text{max path loss} = & \text{power + gains} \\ & - \text{SNR requirement} - \text{noise} - \text{losses} - \text{margin} \end{aligned} \quad (1.75)$$

where all quantities are given in dB.

The values for the link budget are shown in Table 1.6. The entries dependent on the antenna design are described below.

TX Antenna Gain The antenna gain is defined as the product of the directivity and the total efficiency of an antenna [18]. However, for a MIMO system, the multiplexing efficiency is a better metric than total efficiency as it also takes the correlation between antennas into account (see Section 1.6.3).

Body Loss The body loss is caused partially by the user absorbing power and partially by the user detuning the antennas. The detuning may be helped using a digital tuner to retune the antenna in the presence of a user.

It is desired to have as low a maximum path loss as possible. The antennas developed in the report will therefore aim to fulfill the following criteria:

- Increase the antenna gains by increasing the total efficiency.
- Increase the effective antenna gain (multiplexing efficiency or diversity gain) by lowering the farfield correlation between the two antennas.
- Lower the effect of body loss by using a digitally tunable capacitor to re-tune the antenna in the presence of a user.

In this section, a basic link budget for LTE was given. The important parameters, which can be optimized through antenna design, have been clarified.

In the following sections, the theory behind simulations and measurements will be described. This includes the basics of FDTD, the vector network analyzer, and the Satimo anechoic chamber. The following section describes FDTD which is the basis for the simulations in the report.

Power			
Maximum TX power	[3]	23	dBm
Antenna gains			
TX antenna gain	†	0	dBi
RX antenna gain	[3]	18	dBi
SNR			
SNR requirement	[3]	-7	dB
Noise			
eNode B noise figure	[3]	2	dB
Thermal noise	[3]	-119	dBm
Losses			
Body loss	†	0	dB
Cable loss	[3]	2	dB
Margins			
Interference margin	[3]	2	dB
Maximum path loss (Equation 1.75)		161	dB

Table 1.6: Example uplink link budget for LTE. †Dependent on/may be improved by the antenna design.

1.8 Finite Difference Time Domain

This section will describe the finite difference time domain method. This is a method for solving Maxwell equations in time domain. A brief introduction to Maxwell's Equations is given in order to understand the methodology of FDTD. After this, the techniques and ideas behind FDTD are presented and used on the 1D scalar wave-equation. An introduction to the Yee Algorithm, Yee cells, and Yee notation is presented and applied on the 3D Maxwell curl equation. Lastly, the key parameters of FDTD are discussed and related to CST Microwave Studio.

1.8.1 Introduction to Maxwell's Equations

Maxwell's equations are a set of equations that describe how electric and magnetic fields propagate. The set of equations consists of Gauss' law, Gauss' Magnetism law, Faraday's law, and finally Ampere's law.

Gauss' Law

Gauss' law describes how the electric field behaves around electric charges. Below is Gauss' law written in point-differential form. The equation states that the divergence of the electric flux density \mathbf{D} is equal to the volume electric charge density ρ_V [44]. This states that the field around a point \mathbf{D} is equal to the electric charge density ρ_V . From this, it is found that, if there exists an electric charge, the divergence of \mathbf{D} is nonzero, and only zero when there is no charge present.

$$\nabla \cdot \mathbf{D} = \rho_V \quad (1.76)$$

Gauss' Magnetism Law

Gauss' magnetism law, is much like the previous formula, but for magnetic fields. Basically, Gauss' law for magnetism states that a magnetic charge does not exist. This is given in the Equation below [44].

$$\nabla \cdot \mathbf{B} = 0 \quad (1.77)$$

From this, it is clear, that there are no magnetic monopoles. The divergence of \mathbf{B} or \mathbf{H} fields is always zero and the magnetic fields always flows in closed loops.

Faraday's Law

Faraday's law states that the curl of the \mathbf{E} , is equal to the rate of change of a magnetic field. This is very important in the way that electric waves propagate. This is given in the Equation below [44].

$$\nabla \times \mathbf{E} = -\frac{\partial \mathbf{B}}{\partial t} \quad (1.78)$$

From this equation, it can be seen that a time changing magnetic field gives rise to an E-field circulating around it. Likewise, a circulating E-field causes a time changing magnetic field.

Ampere's Law

Ampere's law, is much like Faraday's law, but for curling magnetic fields. In simple words, the Equation below states that the curl of a magnetic field \mathbf{H} , and is given by the rate of change of a electric field \mathbf{D} termed displacement current density and the electric current density [44].

$$\nabla \times \mathbf{H} = \frac{\partial \mathbf{D}}{\partial t} + \mathbf{J} \quad (1.79)$$

This is symmetric to Faraday's law, with an additional term. However the outcome is the same, i.e. that a time changing electric field gives rise to an H-field circulating around it and likewise a circulating H-field causes a time changing electric field. From Faraday and Ampere's law it is seen how waves can actually propagate, since a change in an electric field causes a curling magnetic field, which then gives rise to a curling electric field and so on.

Constitutive relations

Before doing any mathematical manipulations or calculations, it is necessary to have an idea on how the different terms and variables are connected through physical constants. E.g. how the electric flux density is connected to the electric field, which can lead to simplification of calculations later on.

Electric Flux Density The electric flux density \mathbf{D} is related to the electric field \mathbf{E} by the permittivity measured in Farads per meter. Permittivity is a fundamental parameter of a given material, which affects the propagation of an electric field. Typically, it is denoted by ϵ . The relation is given by [44]

$$\mathbf{D} = \epsilon \mathbf{E} \quad (1.80)$$

Magnetic Flux Density The magnetic flux density \mathbf{B} is related to the magnetic field \mathbf{H} by the permeability measured in Henry per meter. Permeability is a fundamental parameter of a given material, which affects the propagation of a magnetic field. Typically it is denoted by μ . The relation is given by [44]

$$\mathbf{B} = \mu \mathbf{H} \quad (1.81)$$

Electric Current Density The electric current density \mathbf{J} is related to the electric field \mathbf{E} by the conductivity measured in Siemens per meter. Conductivity is a fundamental parameter of a given material, which affects the current flow in a conductor. Typically it is denoted by σ . The relation is given by [44]

$$\mathbf{J} = \sigma \mathbf{E} \quad (1.82)$$

1.8.2 The 1D Wave Equation

The wave equation is one of the most basic partial differential equation which describes how waves propagate. This section will use the 1-dimension wave to describe the method of FDTD. Furthermore it is assumed that

- The region is free of charge and current: $\mathbf{J} = \mathbf{M} = 0$.
- The medium is linear (field-independent).
- The medium is isotropic (direction-independent).
- The medium is non-dispersive (frequency-independent).

Given these assumptions, Ampere's and Faraday's law can be rewritten as

$$\frac{\partial \epsilon \mathbf{E}}{\partial t} = \nabla \times \mathbf{H} - 0 \implies \frac{\partial \mathbf{E}}{\partial t} = \frac{1}{\epsilon} \nabla \times \mathbf{H} \quad (1.83)$$

$$\frac{\partial \mu \mathbf{H}}{\partial t} = -\nabla \times \mathbf{E} - 0 \implies \frac{\partial \mathbf{H}}{\partial t} = -\frac{1}{\mu} \nabla \times \mathbf{E} \quad (1.84)$$

Expanding E- and H-field into the Cartesian components,

$$\frac{\partial E_x}{\partial t} = \frac{1}{\epsilon} \left(\frac{\partial H_z}{\partial y} - \frac{\partial H_y}{\partial t} \right) \quad \frac{\partial H_x}{\partial t} = \frac{1}{\mu} \left(\frac{\partial E_z}{\partial y} - \frac{\partial E_y}{\partial t} \right) \quad (1.85)$$

$$\frac{\partial E_y}{\partial t} = \frac{1}{\epsilon} \left(\frac{\partial H_x}{\partial z} - \frac{\partial H_z}{\partial t} \right) \quad \frac{\partial H_y}{\partial t} = \frac{1}{\mu} \left(\frac{\partial E_x}{\partial z} - \frac{\partial E_z}{\partial t} \right) \quad (1.86)$$

$$\frac{\partial E_z}{\partial t} = \frac{1}{\epsilon} \left(\frac{\partial H_y}{\partial x} - \frac{\partial H_x}{\partial t} \right) \quad \frac{\partial H_z}{\partial t} = \frac{1}{\mu} \left(\frac{\partial E_y}{\partial x} - \frac{\partial E_x}{\partial t} \right) \quad (1.87)$$

which for the 1D case $\partial/\partial z = \partial/\partial y = 0$ simplifies to

$$\frac{\partial E_x}{\partial t} = 0 \quad (1.88)$$

$$\frac{\partial E_y}{\partial t} = -\frac{1}{\epsilon} \frac{\partial H_z}{\partial x} \quad (1.89)$$

$$\frac{\partial E_z}{\partial t} = \frac{1}{\epsilon} \frac{\partial H_y}{\partial x} \quad (1.90)$$

The same steps can be used to get an expression for the H-field. For each direction the E and H expressions can be combined to get the 1D scalar wave equation, e.g. the z -direction [44],

$$\frac{\partial^2 E_z}{\partial t^2} = c^2 \frac{\partial^2 E_z}{\partial x^2} \quad (1.91)$$

where c is the speed of light. This equation tells us that an electric field moving in the z -direction will propagate along the x -axis in time, with a speed of c . Going back to the general wave-equation [44]

$$\frac{\partial^2 u}{\partial t^2} = c^2 \frac{\partial^2 u}{\partial x^2} \quad (1.92)$$

Since the wave-equation is a second order partial differential equation, it is known to have two linearly independent solutions [44]

$$u(x, t) = F(x + ct) + G(x - ct) \quad (1.93)$$

Both F and G are known as propagating-wave solutions, where an argument of the form $x + ct$ is a wave moving towards decreasing x and an argument of the form $x - ct$ is a wave moving towards increasing x [44]. In order to compute this numerically, finite differences are used. Thus, the following needs to be approximated using finite-differences

$$\frac{\partial^2 u(x, t)}{\partial t^2}, \frac{\partial^2 u(x, t)}{\partial x^2} \quad (1.94)$$

Taylor series expansion is used to approximate the expression at a point x_i using finite differences: $u(x_i) = u(x_i + \Delta x) + u(x_i - \Delta x)$ which then is used to solve the wave-equation by substituting the two central differences into the 1D wave equation. This gives the solution for the latest time step as [44]

$$u_i^{n+1} = \left(\frac{c\Delta t}{\Delta x} \right) [u_{i+1}^n - 2u_i^n + u_{i-1}^n] + 2u_i^n - u_i^{n-1} \quad (1.95)$$

$$+ O[(\Delta t)^2] + O[(\Delta x)^2] \quad (1.96)$$

1.8.3 Dispersion

Whenever discrete numerical methods are used, dispersion must be taken into account. Dispersion, in this case, can be seen as a variation in wavelength. For the wave equation, this depends on the chosen time and space steps [44]:

- **Magic time-step:** $c\Delta t = \Delta x$. No dispersion.
- **Very fine mesh:** $\Delta t \rightarrow 0, \Delta x \rightarrow 0$. No dispersion.
- **Difference 1:** $c\Delta t < \Delta x$. Wavelength smaller in sampled space than in reality.
- **Difference 2:** $c\Delta t > \Delta x$. Unstable as ω is complex. Exponential growth.

Generally the magic time-step is only an exact solution in 1D. It exists for all dimensions but only for one incident angle [44]. It is also seen that finer mesh cells reduces the error term.

1.8.4 The Yee Algorithm

The Yee algorithm is a set of finite difference equations for Maxwell's curl equation system derived by Kane Yee [44]. This algorithm solves both E- and H-fields in space and time using coupled curl equations instead of solving for one field at a time using the wave equation. Some of the key features of the Yee Algorithm are the following [44]:

- Both E- and H-field boundaries can be used.
- Solving both E- and H-fields is more robust.

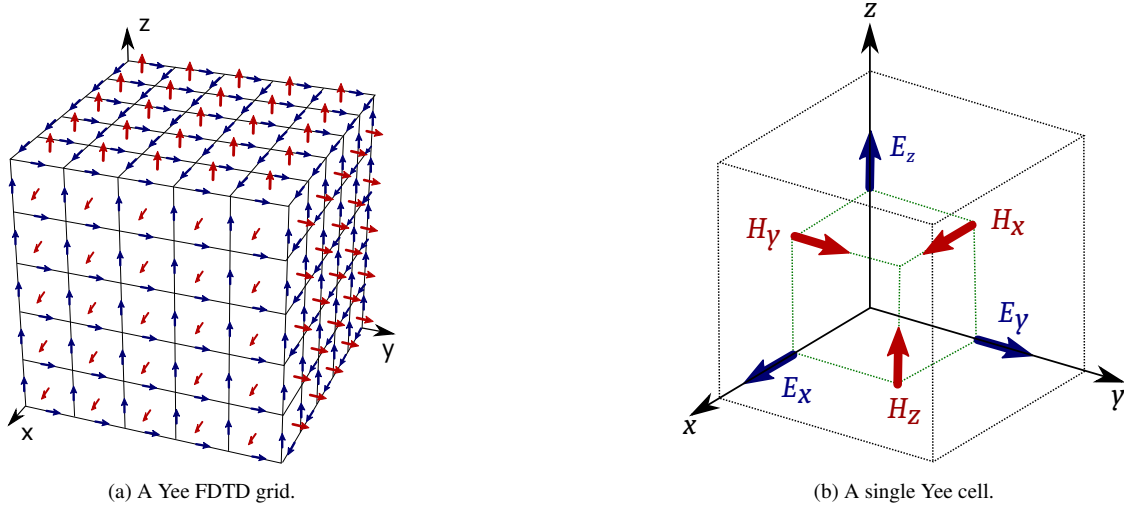


Figure 1.24: Spatial interpretation of the Yee Algorithm.

- Electric and magnetic material properties can be modeled easily.
- Unique field features, e.g. singularities.

The Yee algorithm centers the E- and H-fields in 3D, such that every E-field is surrounded by four curling H-fields and every H-field is surrounded by four curling E-fields. This is illustrated on Figure 1.24a, each cell referred to as the Yee-cell. A single Yee cell is shown in Figure 1.24b. The arrangement of the electric and magnetic fields implicitly enforces Gauss' Law and Gauss' Magnetic Law, which makes the Yee mesh divergence free, with respect to the E- and H-fields [44].

The centering of the E- and H-fields in time is often termed the leapfrog method. This time stepping is fully explicit, and thus avoids problems with simultaneous equation and matrix inversions. This leapfrog method is shown in Figure 1.25.

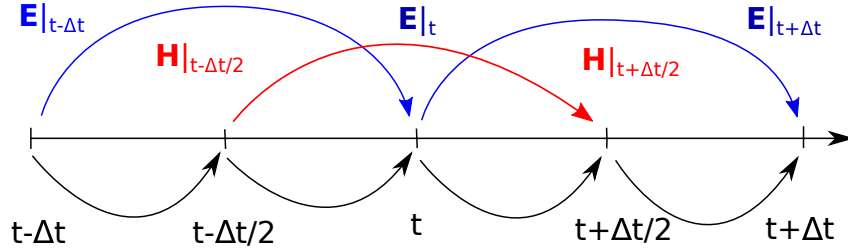


Figure 1.25: Leap-frog method illustrated on the time line

To keep an overview, Yee created the following notation which is useful when considering 3D FDTD equations

$$u_X(i\Delta x, j\Delta y, k\Delta z, n\Delta t) = u_{X_{i,j,k}}^n \quad (1.97)$$

Finite Difference of Maxwell's Equations in 3D

For completeness the previous ideas and notation can now be used to derive a numerical approximation of Maxwell's Curl Equations in 3D. The derivations will not be shown here, and only the solution for a single Cartesian component will be given here, due to its complexity. As an example, the approximation for E_x is shown below [44],

$$E_x|_{i,j+1/2,k+1/2}^{n+1/2} = \left(\frac{1 - \frac{\sigma_{i,j+1/2,k+1/2}\Delta t}{2\epsilon_{i,j+1/2,k+1/2}}}{1 + \frac{\sigma_{i,j+1/2,k+1/2}\Delta t}{2\epsilon_{i,j+1/2,k+1/2}}} \right) E_x|_{i,j+1/2,k+1/2}^{n-1/2} + \quad (1.98)$$

$$\left(\frac{\frac{\Delta t}{\epsilon_{i,j+1/2,k+1/2}}}{1 + \frac{\sigma_{i,j+1/2,k+1/2}\Delta t}{2\epsilon_{i,j+1/2,k+1/2}}} \right) \left(\frac{H_z|_{i,j+1,k+1/2}^n - H_z|_{i,j,k+1/2}^n}{\Delta y} - \frac{H_y|_{i,j+1/2,k+1}^n - H_y|_{i,j+1/2,k}^n}{\Delta z} - J_{source}|_{i,j+1/2,k+1/2}^n \right) \quad (1.99)$$

As seen, the equations quickly become large and hard to handle. However, to fully extend this to 3D, this would have to be done for all the Cartesian coordinates for both E- and H-fields.

1.8.5 Absorbing Boundary Conditions

Many geometries of interest are defined in open regions, e.g. antennas, where the spatial domain is unbounded. Since computers have limited storage, it is needed to find a suitable boundary condition on the outer perimeter of the domain Ω in order to simulate to infinity. Thus, it is needed to find a boundary condition that allows outward propagating numerical wave to exit the outer perimeter of Ω without spurious reflections from the outgoing waves.

One way of achieving the absorbing boundary condition is by terminating the outer boundary with an absorbing material, which is analogous to the method used in anechoic chambers. For this, a perfectly matched layer (PML) is used, which is derived by Berenger [44]. This allows plane waves of arbitrary incidence, polarization, and frequency to be matched at the boundary. PML usually gives a back-reflection in the order of $\approx 10^{-6}$ – 10^{-8} [44].

1.8.6 FDTD Parameters and Relation to CST

CST Microwave Studio is used for all simulations in this report. The following will try to connect the FDTD theory to the parameters in CST. Even though CST uses Finite Integration Technique (FIT) instead of finite differences [45], FIT share the structure of FDTD, but uses the Maxwell's Equations on integral form. The advantage of FIT is that it uses less memory and it allows for easier code implementation of some features. Besides this, most of the basic parameters are the same.

Cell Size and Meshing

The choice of cell size is very important when doing FDTD simulations. A general rule of thumb is that a cell should be much less than the smallest wavelength. As a rule of thumb, 10 cells per wavelength is sufficient, that is the cell size should be $\lambda/10$. In advanced FDTD simulations, an adaptive meshing is often used where even smaller cells are used in dense materials with strong-field locations, and large cells outside these areas. When doing this, it is also very important not to change the cell size too much compared to the neighbor cells. It is also necessary that the cell size are small enough to approximate the geometry, which is to be modeled accurately. Geometries such as circles are being approximated with rectangular cells, this causes a “staircase effect” on the object, and the representation can be inaccurate if the cell sizes used are too large.

Another rule of thumb, which can help assessing the right cell size, is that the smallest mechanical item of the structure is to be approximated by at least two cells. The rule of thumb says that [46]:

$$\Delta = \frac{d_{\min}}{N_d} \quad (1.100)$$

where

Δ = Is the length/width/height of the cell.

d_{\min} = Smallest physical dimension.

N_d = Oversampling factor – should be ≥ 1 .

Time Step Size

The time step size is another parameter that has to be chosen with care when doing FDTD simulations. The time step should be small enough, such that at any point, a wave should not pass through more than one cell. Calculating the time step is dependent on the cell size, dimensions, and the propagation speed. The time step for the 3D rectangular grid can be calculated as [46]:

$$\Delta t = \frac{1}{c \sqrt{\frac{1}{(\Delta x)^2} + \frac{1}{(\Delta y)^2} + \frac{1}{(\Delta z)^2}}} \quad (1.101)$$

$$= \frac{1}{c \sqrt{\frac{3}{\Delta^2}}} \quad (1.102)$$

$$= \frac{\Delta}{c\sqrt{3}} \quad (1.103)$$

where:

c = Speed of light.

$\Delta = \Delta x = \Delta y = \Delta z$ = Size of the cell side for rectangular cell.

Accuracy and Time Limit

These terms are taken directly from CST Microwave Studio, and are values that limit the simulation either when a certain accuracy criteria has been met or when it has been simulated for a certain amount of time. In practice, it is undesirable that a simulation is stopped due to a given time limit. Therefore, this limit is often set to a very large number. In CST, accuracy is a measure that describes how much energy is left in the system. The accuracy setting makes the simulation stop when a certain energy level, within the structure, has decreased to a chosen level.

In this section, the basics of FDTD has been covered. This clarifies some of the underlying principles of the CST Microwave Studio software used for simulations in this project. The next chapter covers the vector network analyzer, which is used for measuring S-parameters.

1.9 Vector Network Analyzer

In this section, a description will be given of the vector network analyzer, which is a very important tool in characterizing antennas. The VNA is able to sweep through a wide frequency range and measure the response of the device under test (DUT). The application for network analyzers is not only antennas. VNAs are used in the characterization for almost every passive RF component such as cables, switches, and attenuators [47]. It is also possible to measure the performance of active devices such as amplifiers, tuners, etc. Fundamentally, the VNA measures the incident, reflected, and transmitted waves, which can be used to determine the S-parameters [47], Figure 1.26 illustrates this.

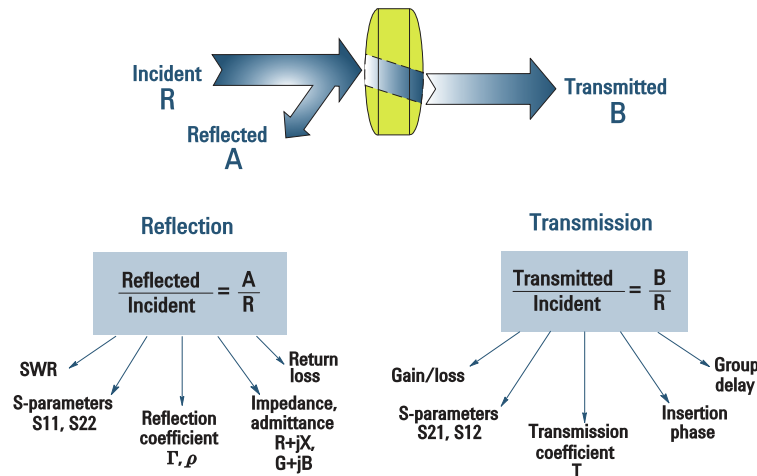


Figure 1.26: Fundamental Network Analyzer measurement [48].

The essential component behind the Network Analyzer is the signal-separation hardware. This is used to separate the incident wave from the reflected wave in the test ports. The two separated waves can then be measured independently to get the phase and magnitude information [47].

1.9.1 Calibration

In order to accurately measure the phase and magnitude of the incident and reflected waves, the VNA needs to be properly calibrated. Even though some elements of the VNA are calibrated at manufacturing, not everything can be accounted for. Different cables and connectors can have a large effect on the phase and magnitude and even a difference room temperature can affect the measurements [47]. Due to all these variables, it is important to calibrate the VNA before a measurement.

Sources of Error

There are generally four inherent sources of error in the VNA. These are often referred to as systematic source of error due to their presence at all time, however they can all be greatly suppressed by calibration [47]. These systematic sources of error are listed below:

- Port match.
- Directivity.
- Frequency response.

- Isolation.

Port match Ideally, the VNA ports would have an input impedance of exactly 50Ω . This is, however, hard to realize in reality and a small loss will be present at each port of the VNA due to mismatch [47].

Directivity This source of error has its origin in the signal-separation hardware. The imperfections in these allow for a small portion of the reflected wave to leak into the reverse direction. Due to this finite isolation between the paths, the waves will not be perfectly separated. This can be compensated by the calibration [47].

Frequency Response Due to the multiple receivers which are inherently present in VNAs, lies a source of error. This is due to small differences in the frequency response in the receivers. The calibration of this is referred to as reflection and transmission tracking [47].

Isolation Ideally, the VNA ports would be totally isolated, which is hard to realize in practice. This causes some of the measured signal at one port to leak into the other. This is also called cross-talk, and can be compensated by the calibration [47].

1.9.2 Calibration Types

There are multiple methods that can be used to calibrate a VNA. These depend on the number of ports, frequency range, and the device under test. However, for a two-port VNA, the following types are the most common:

- Frequency response calibration.
- One-path two-port calibration.
- Full S-parameter calibration.

Frequency Response Calibration is the simplest method of calibration. It is sometimes termed transmission normalization. This only corrects the frequency response of the VNA, and should only be used when a rough measurement of S_{12} and S_{21} is sufficient.

One-path Two-Port Calibration allows for accurate forward S-parameter measurement. This type of calibration assumes that port two of the VNA is perfectly matched, and can therefore only be used for accurate S_{11} and S_{21} .

Full S-Parameter Calibration is the most complete calibration type since it takes all ports into account during the calibration. This allows for accurate measurements of all four S-parameters. There are multiple ways of doing a full two-port calibration, and the most common are the Short-Open-Load-Through (SOLT) method. For modern VNAs, electronic calibration standards are often used.

Short-Open-Load-Through

This is a cheap and easy way of accurately calibrating a VNA. Basically, a set of known connectors with known values, which consist of a connector that is shorted, a connector that is open, a connector with a 50Ω load, and lastly, the two cables are connected together with a female-female connector. The short and open circuit will create fully reflected voltage and current waves on the transmission line. The 50Ω will result in full absorption, such that all the incident power is absorbed [48]. Generally, the 50Ω load is the source of error in these types of calibrations, since it is hard to get a perfect 50Ω load in reality [47].

Electronic Calibration

The electronic calibration kits are generally made by having a range of different known impedance states that are electronically switchable [49]. The characteristics are often stored in the calibration kit and can be read by the VNA. The calibration is similar to the SOLT method, but can support more complex impedance states [49].

In this section, the basic functionality of a VNA and the importance of calibrating has been described. This makes it possible to make accurate S-parameter measurements on the prototypes which will be designed in this project. In the next section, the functionality of the Satimo StarLab anechoic chamber will be described in order to show how efficiency and farfield measurement can be made as well.

1.10 Satimo StarLab Anechoic Chamber

The farfield measurements for this project will be carried out in a StarLab anechoic chamber by Satimo. In this section, the basic principles of doing measurements in this chamber will be described.

The Satimo chamber is shown in Figure 1.27a. It consists of fifteen dual-polarized probes arranged in a circle with 22.5° between each. The probes are located in a circle of absorbing cones and the whole machine is placed in a shielded room.

The measurements used in this project are passive measurements. This means that the power is supplied from outside the chamber to the Device Under Test, which then radiates. The source is a user defined frequency sweep. For each frequency, the real

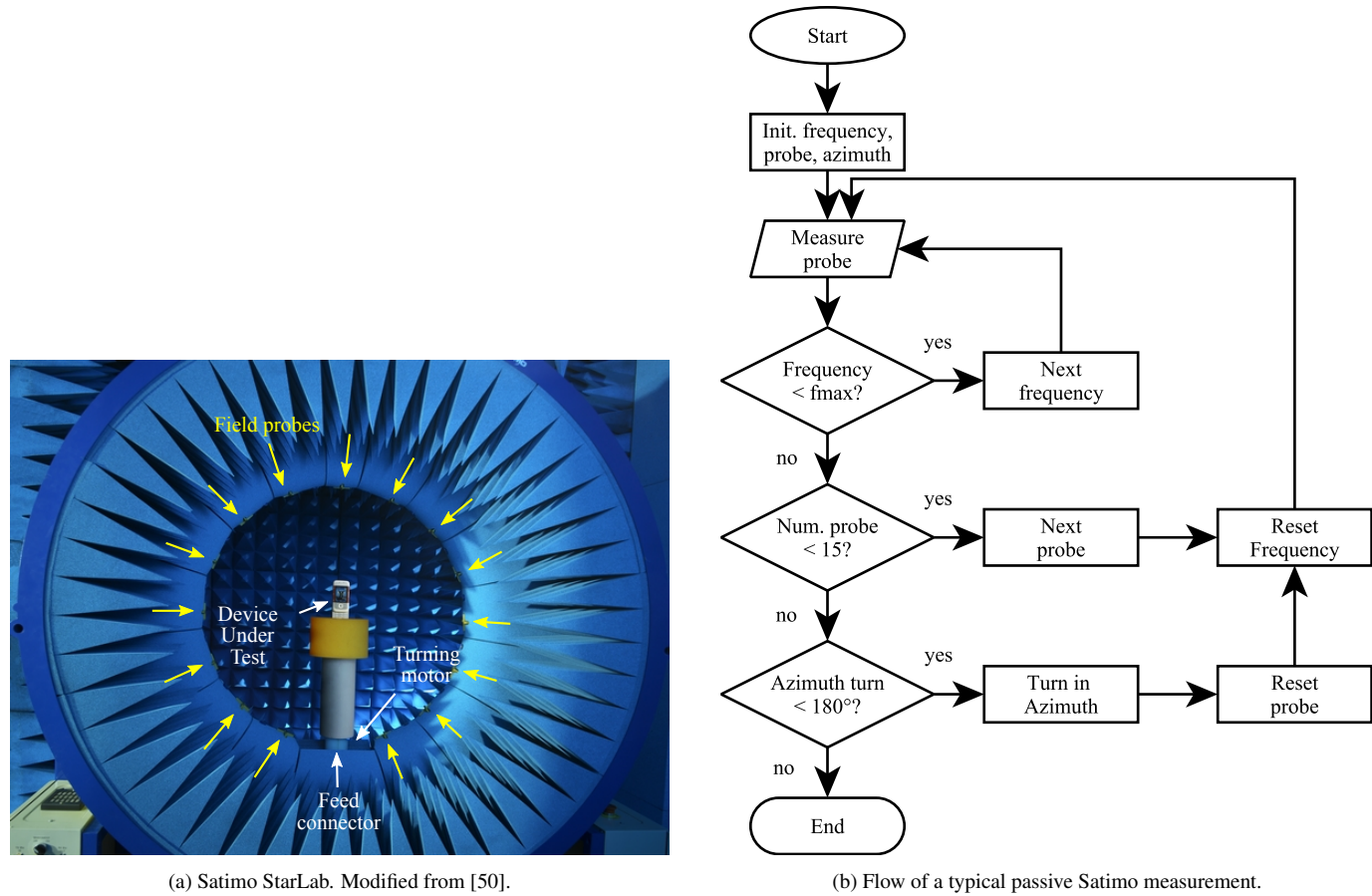


Figure 1.27: Satimo StarLab passive measurement procedure.

and imaginary field at each probe for each polarization is sampled and recorded to a PC. After all frequencies for all probes have been recorded, the bed of the DUT turns, e.g. 22.5° , and the procedure repeats. The flow is shown in Figure 1.27b. The output is stored in a `trx` file in the order described by the flow chart. The post processing of the `trx` files is described thoroughly in Appendix B.

The measurements used for this report will mainly be used to compute the total efficiency of the DUT. The efficiency can be computed by first calibrating the measurements by measuring a reference antenna with a known efficiency. The procedure for this is described in Section 1.6.3.

The Satimo chamber is quite a complex system, and there are many sources of error. However, some of them are the same as with the VNA, which was described in Section 1.9.1. Furthermore, there can be current flowing on the cable, bad connections, misaligned probes and inaccuracy in the motor rotations.

In this section, the Satimo StarLab chamber has been described. Based on this, the farfields can be measured of the antennas. By measuring reference antennas, the total efficiency can be computed. This section concludes the problem analysis, and the fundamental theorems and theories behind this project have been described. This leads to the final problem statement, which will briefly sum up the problem investigated throughout the rest of the report.

1.11 Problem Statement

The problem statement, which will be investigated in this report, is formulated as the following:

How can a pair of MIMO antennas for LTE handsets be designed so that all bands from 700 MHz to 960 MHz and from 1710 MHz to 2650 MHz are covered with a total efficiency above 50 % using a tunable MEMS capacitor, and how does a small ground clearance – the distance between the antenna element and the ground plane – affect the performance?

The further specifications for the design will be described next in the requirement specification.

Chapter 2

Requirements Specification

The requirement specification sums up requirements, definitions, and guidelines for designing the antennas in the following chapters. Not all the requirement are hard requirements but guidelines for the design process.

2.1 Functional Requirements

ID	Requirement
F1	The antenna system must consist of two single-feed dual-band antennas covering the bands described in Requirement S1.
F2	Each antenna must cover both uplink and downlink at the same time for each required LTE band.
F3	Must have a simple matching network, containing a variable capacitor for tuning inside the specified bands.
F4	Must use a WiSpry WS1040 MEMS variable capacitor chip in the matching network.

2.2 Specific Requirements

ID	Specification	Requirement
S1	Frequency bands/tunable range	700–960 MHz, 1710–2170 MHz, 2300–2400 MHz, 2550–2650 MHz
S2	Minimum tunable bandwidth (700–960 MHz)	80 MHz (band 8)
S3	Minimum tunable bandwidth (1710–2650 MHz)	720 MHz (band 15)
S4	Physical dimensions	External: $70 \times 140 \times 7 \text{ mm}^3$, PCB: $55 \times 120 \times 1.6 \text{ mm}^3$ (FR-4)
S5	Ground plane copper thickness	0.035 mm
S6	In-band return loss (impedance bandwidth)	$\text{RL} > 6 \text{ dB}$
S7	In-band correlation between antenna elements (correlation bandwidth)	$\rho_e < 0.5$
S8	In-band total efficiency in free-space (efficiency bandwidth)	> 50 %
S9	Maximum SAR	2 W/kg averaged over 10 g of tissue
S10	Tunable capacitor range (WS1040)	0.3 pF to 2.9 pF in steps of 0.2 pF (0.1 pF minimum)
S11	Reference power level	23 dBm (0.2 W)

In this chapter, the functional and specific requirements for the antennas have been listed. The next chapter contains a test specification for the above specific requirements, describing how each requirement will be tested.

Chapter 3

Test Specification

In this chapter, it will be described how the specific requirements from Chapter 2 will be tested.

Test of Requirement S1 – Frequency Bands/Tunable Range The frequency bands are chosen according to the LTE bands [14]. This specification determines what is “in-band” for other requirements, below, and is not tested by itself.

Test of Requirement S2 – Minimum Tunable Bandwidth in the Low Band The return loss, correlation, and efficiency is measured within the low band for the capacitance range specified in Requirement S10. The specified bandwidth must be obtained for a minimum of one capacitance value. See Requirements S6, S7, and S8.

Test of Requirement S3 – Minimum Tunable Bandwidth in the High Band The return loss, correlation, and efficiency is measured within the high band for the capacitance range specified in Requirement S10. The specified bandwidth must be obtained for a minimum of one capacitance value. See Requirements S6, S7, and S8.

Test of Requirement S4 – Physical Dimensions The physical dimensions of the PCB, antenna, and the external limitations are measured with a measuring tape.

Test of Requirement S5 – Copper Thickness The PCB is chosen to have a copper thickness according to the requirement.

Test of Requirement S6 – In-band Return Loss The return loss is determined by measuring the S -parameters on a vector network analyzer. The return loss is then $RL_1 = -|S_{11}|$ for the top antenna and $RL_2 = -|S_{22}|$ for the side antenna [17].

Test of Requirement S7 – In-band Correlation Between Antenna Elements The correlation between antennas is determined from the farfield pattern, measured in the Satimo StarLab, assuming isotropic distribution of incoming waves. The correlation is then found according to Equation 1.71.

Test of Requirement S8 – In-band Total Efficiency in Free-Space The total efficiency is determined from the farfield pattern, measured in the Satimo StarLab. The total efficiency is then found according to Equation 1.68.

Test of Requirement S9 – Maximum SAR The maximum SAR is simulated in CST with a phone case, modeled around the PCB, and a PEC screen. The SAR is only simulated – not measured.

Test of Requirement S10 – Tunable Capacitor Range The tunable capacitor is chosen according to this requirement and is not tested.

Test of Requirement S11 – Reference Power Level The specified power level is used for SAR simulations and is not tested.

The test specifications will be used to evaluate the antennas designed in the next chapter, where three initial antennas are designed and simulated.

Part II

Technical Solution

Chapter 4

Preliminary Design and Simulation

In this chapter, the design of three antenna designs will be documented. The antennas are developed from the requirement specification in Chapter 2. The documentation will contain the following:

Technical drawing A technical drawing with all dimensions of the antennas.

Circuit and component values A schematic showing the matching circuit and component values.

Description and surface currents A description of how the antenna works and the surface currents are distributed at different frequencies.

S-parameters A figure of all S-parameters at the minimum capacitance values.

S-parameter sweep A sweep of S-parameters. For one antenna, the tunable capacitor is swept from 0.3 pF to 2.9 pF in 0.2 pF steps. The other antenna has a fixed capacitance of 0.3 pF. Four plots are shown

1. S_{11} , sweeping the capacitor of antenna 1 and keeping the capacitor for antenna 2 fixed.
2. S_{21} , sweeping the capacitor of antenna 1 and keeping the capacitor for antenna 2 fixed.
3. S_{21} , sweeping the capacitor of antenna 2 and keeping the capacitor for antenna 1 fixed.
4. S_{22} , sweeping the capacitor of antenna 2 and keeping the capacitor for antenna 1 fixed.

Tunable bandwidth A table of the maximum obtained bandwidth for each antenna for the low and the high band. The maximum bandwidth is found from the S-parameter sweep at the capacitor value yielding the best bandwidth.

Correlation sweep A sweep of the envelope correlation between the two antennas. One sweep for each antenna, keeping the capacitance value of the opposite antenna fixed at 0.3 pF.

Efficiency sweep A sweep of the total efficiency of each antenna keeping the capacitance value of the opposite antenna fixed at 0.3 pF.

The simulations in this chapter are performed in free-space, i.e. with no user near the antennas.

4.1 Monopole Antenna

The antenna design, for both antennas, is shown in Figure 4.1a. Both antennas are designed from a basic folded monopole structure with two arms – one for the low band and one for the high band. The antennas are almost identical with a few changes as a result of the restrictions on the ground clearance. The antennas are designed to take full advantage of the ground clearance requirements in both height, length, and width. This is done in order to obtain the highest possible bandwidth in both bands.

Going from the top antenna to the side antenna, the ground clearance decreases from 10 mm to 7 mm. To compensate for the decrease in ground clearance the length of both the low band and high band arms are adjusted. This is done to obtain the highest bandwidth within the low band and high band.

The surface currents of the top antenna are shown in Figure 4.2. In the low band, the left arm is excited and, as the frequency increases, the short arm becomes more excited. This illustrates the different operation modes of the two arm folded monopole structure.

The S-parameter for both antennas can be seen in Figure 4.3. Both antennas are simulated with the tuning capacitors at 0.3 pF. In this state, both antennas cover the highest frequencies in the low and the high band. From the figure, it can be seen that both antennas almost covers the entire high band. However, some tuning is needed for the side antenna in the lower band.

The tuned S-parameters for both antennas can be seen in Figure 4.4. The return losses, S_{11} and S_{22} , show that both antennas almost cover the desired bandwidth. However, from 2500 MHz to 2650 MHz, both antennas are 1 dB to 3 dB lower than required.

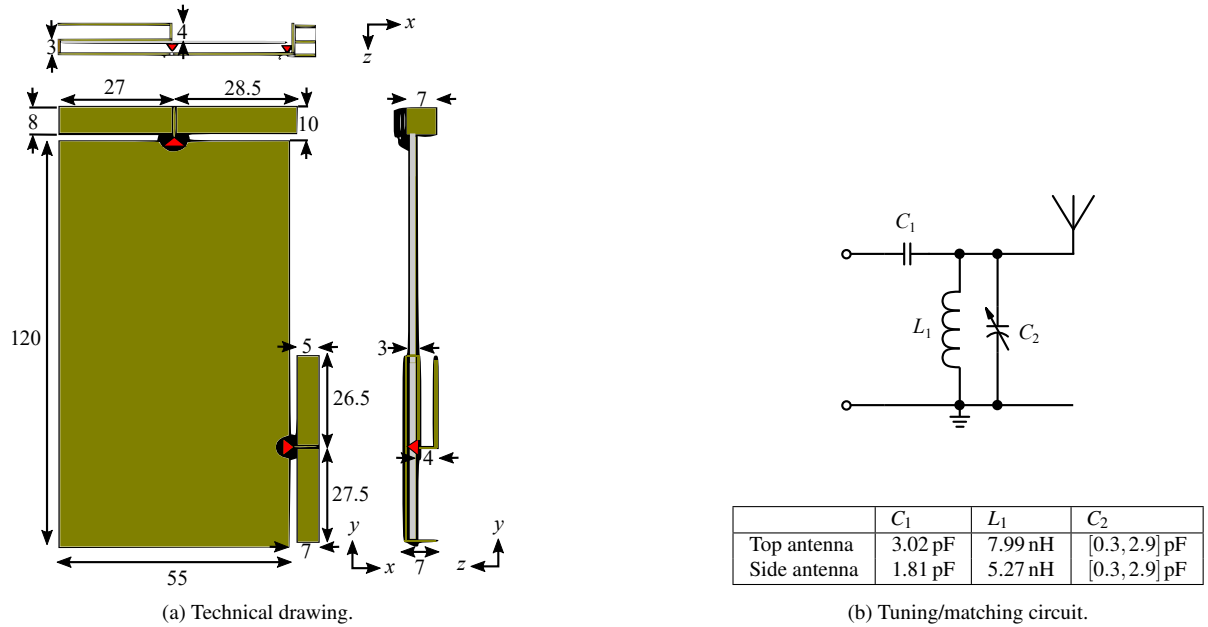


Figure 4.1: Technical drawing and tuning circuit for the antenna. The matching circuit is applied for both the top and the side antenna.

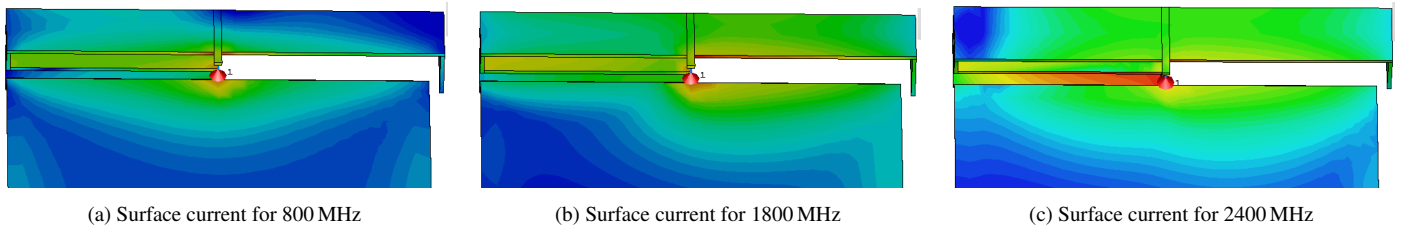


Figure 4.2: Surface currents at each resonance with $C_2 = 0.3 \text{ pF}$.

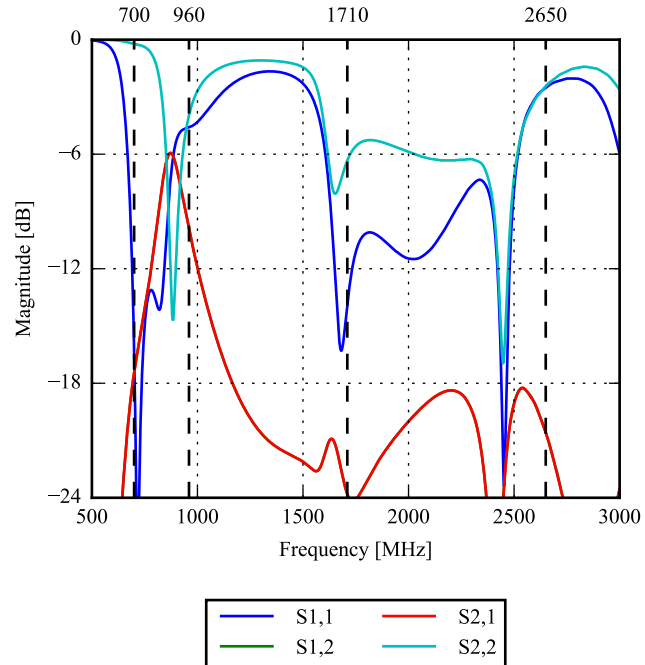


Figure 4.3: S-parameters with $C_2 = 0.3 \text{ pF}$ for both antennas.

Antenna	Band	Start [MHz]	Stop [MHz]	Bandwidth [MHz]
Top Side	Low	680	1011	331
	Low	818	909	91
Top Side	High	1590	2527	937
	High	1850	2533	683

Table 4.1: Maximum bandwidth obtained in the low and high band for the top and the side antenna, respectively.

The side antenna also shows a lower level than desired at 1750 MHz and in the low band limits. During the S -parameter simulation sweep of one antenna, the variable capacitor of the other antenna is set to the initial fixed value of 0.3 pF.

The isolation, S_{21} , is shown in Figure 4.4. The S_{21} sweep shows a low isolation at 5 dB in the low band. The surface current simulations, shown in Figure 4.2, show that the monopole antenna design excites the ground plane, which could cause the low isolation. This should be taken into consideration as the isolation can have a significant effect on the MIMO performance.

The channel bandwidth for both antennas are shown in Table 4.1. Both antennas fulfill the desired bandwidth requirement in the lower bands. However, only the top antenna complies with the bandwidth requirement in the high band where the side antenna lacks 37 MHz.

The correlation, between the antennas, is shown in Figure 4.5. The figure shows the correlation when sweeping the tuning capacitors from 0.3 pF to 2.9 pF. From the figure, it is seen that the correlation exceeds the requirement of 0.5 in the low band for both the top and side antenna with a maximum at 700 MHz. The surface currents at the different operation frequencies, seen in Figure 4.2, show a strong coupling to the ground plane, which could cause the high correlation in the low band.

The efficiency for both antennas is shown in Figure 4.6. The efficiency is plotted for each sweep of the tunable capacitors. The efficiency mostly covers the desired spectrum at an efficiency of -3 dB with a drop of 1.5 dB around 750 MHz for the side antenna.

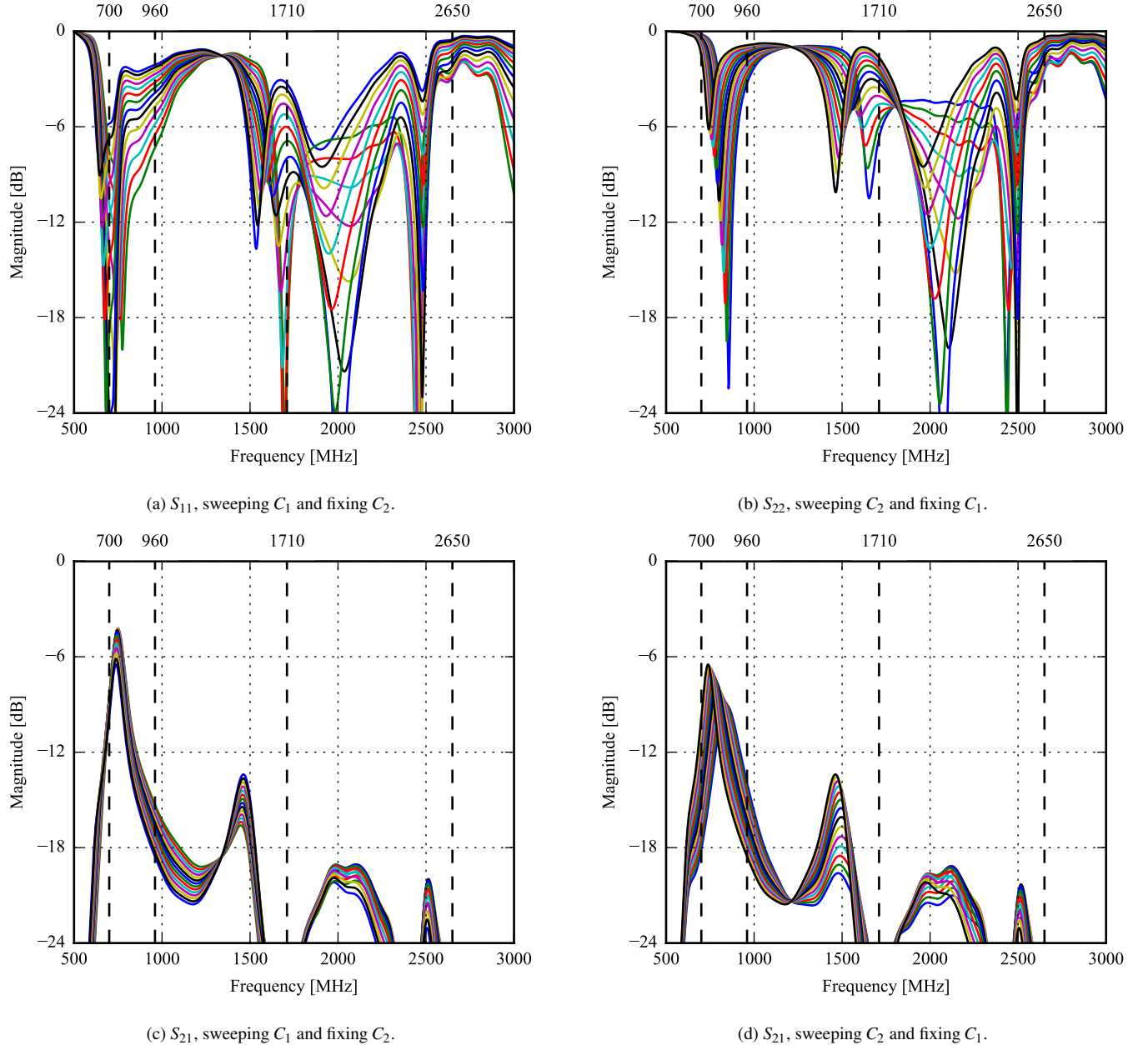


Figure 4.4: S -parameter sweep in free-space for tuning the shunt capacitor of each antenna, C_1 and C_2 for port 1 and 2, respectively. Port 1 is the top antenna and port 2 is the side antenna.

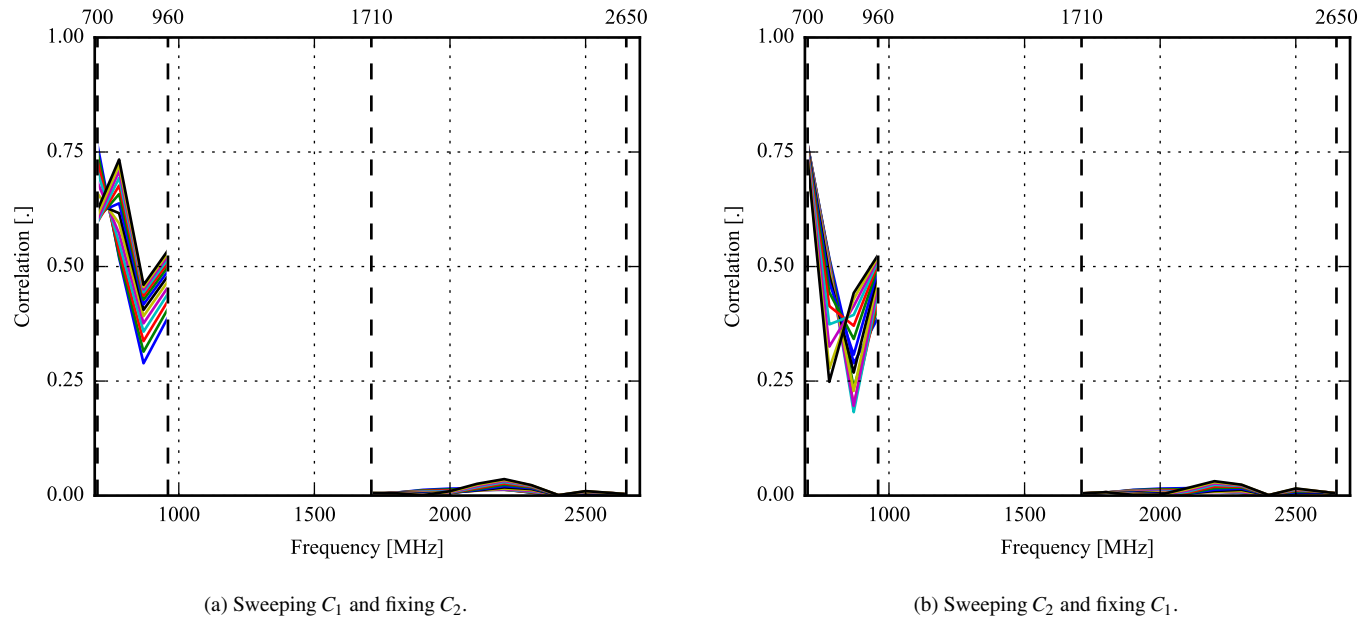


Figure 4.5: Correlation between the antennas when sweeping tuning capacitors. Here, C_1 and C_2 are the tuning capacitor for the top and side antenna, respectively.

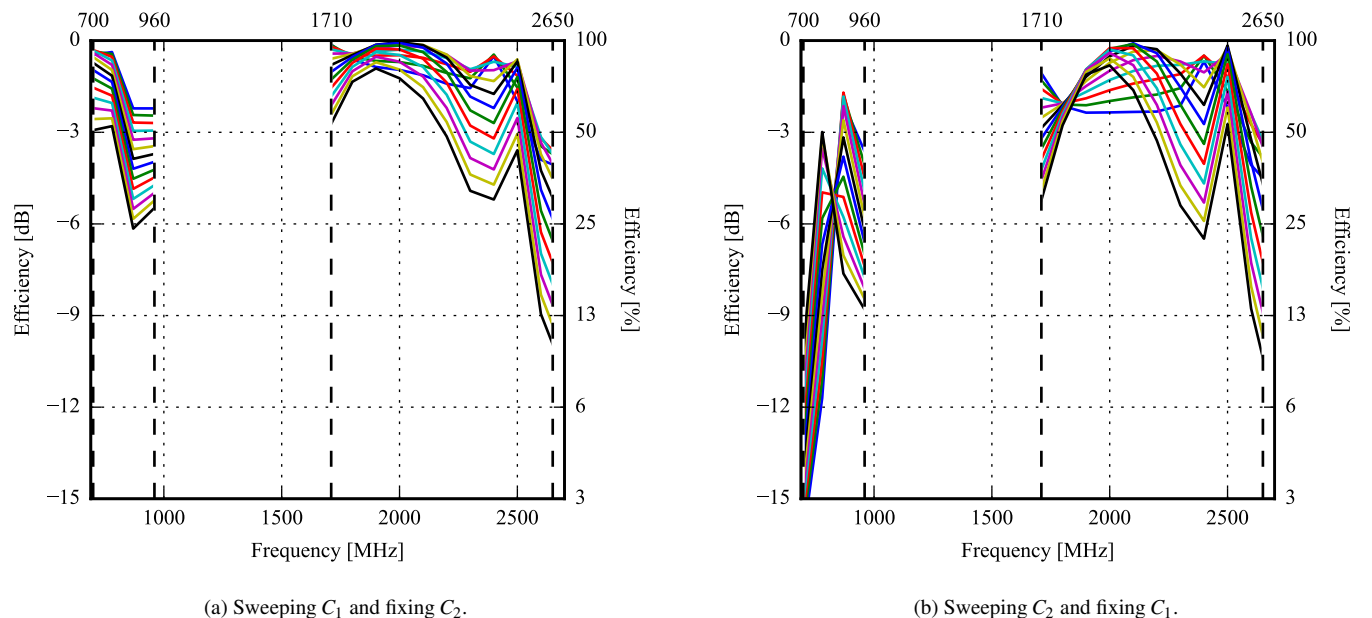


Figure 4.6: Efficiency for each antenna when sweeping the tunable capacitors. Here, C_1 and C_2 are the tuning capacitor for the top and side antenna, respectively.

4.2 Triangle-Feed Antenna

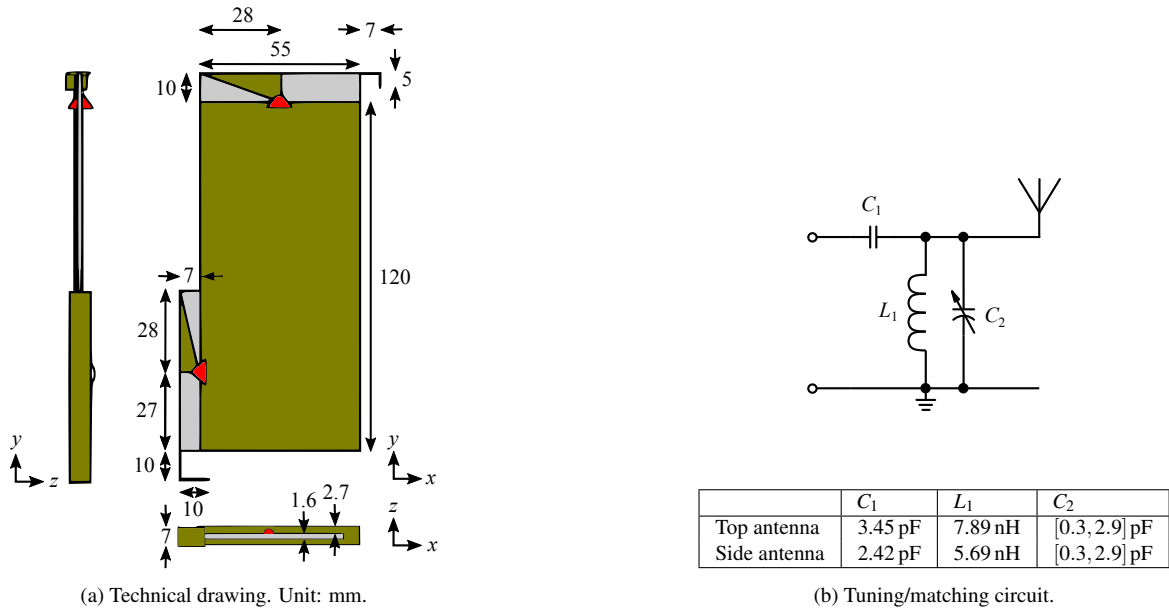


Figure 4.7: Technical drawing and tuning circuit for the antenna. The antennas are built on FR-4 board using 35 μm copper. There is a matching circuit as shown for each of the two feeds.

The antenna is shown in Figure 4.7. The two antennas each consist of a triangle-feed printed on FR-4 and the main element following the edge of this FR-4 block.

The low band element consists of a CCE (Capacitively Coupled Element) antenna which is inherently non-resonant [51, 52]. The resonance of this type of antenna is dependent on the matching circuit. For this design, the matching is performed by C_1 and L_1 to resonate at 960 MHz and C_2 is used to tune the resonance frequency down to 700 MHz.

The triangular feed creates two new resonances in the mid band (around 1800 MHz) and the high band (around 2400 MHz). Looking at the top antenna, the right-hand side from the feed line resonates at around 1800 MHz and the left-hand side resonates at around 2400 MHz. By determining the x -position of the triangle-feed, these two resonances can either be separated or joined, making it possible to cover all the required high LTE bands. The surface currents, illustrating how the structure resonates after matching, is shown in Figure 4.8.

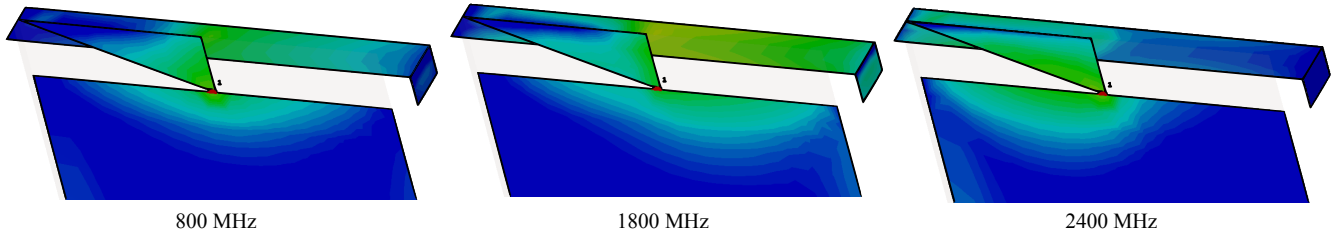


Figure 4.8: Surface currents around each resonance with $C_2 = 0.3 \text{ pF}$.

The S-parameters for both antennas are shown in Figure 4.9 with the tuning capacitors at their minimum values, 0.3 pF. At this position, the highest end of the low band, around 960 MHz, is covered. It is seen that the top antenna (port 1) covers the whole lower band whereas the side antenna only covers around half of the band and must be tuned to cover the whole band. The high band is almost covered at this capacitor setting for both antennas.

The tuned S-parameters are shown in Figure 4.10. Here is seen that the entire lower band can be covered by the side antenna (S_{22}) and that the entire high band is covered at $C_2 = 0.7 \text{ pF}$ to 0.9 pF for the top and side antenna respectively. It is noted that all three resonances are moved when C_2 is altered.

It is seen that the isolation at low frequencies is only around 5 dB. This may cause problems when using the antennas for MIMO operation. The bad isolation may be caused by the way the CCE antenna resonates. The CCE antenna couples to the chassis and uses this as a resonator [52]. This may cause high correlation when both antennas couple to the chassis.

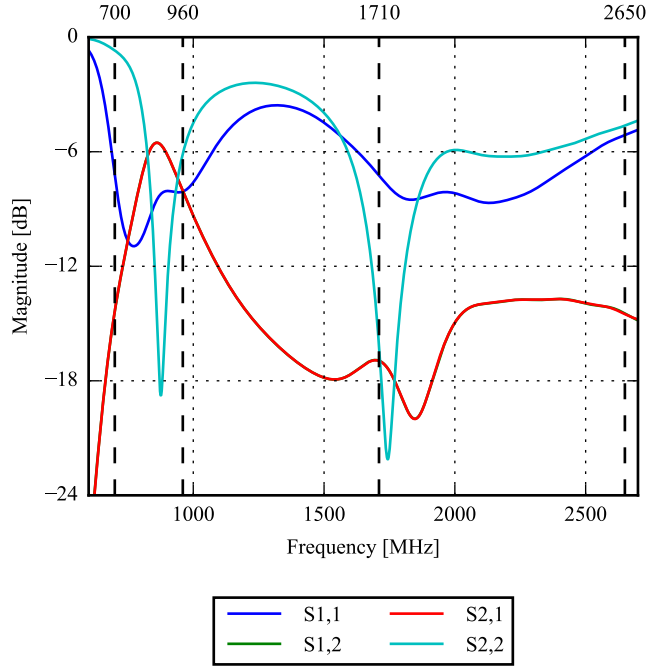


Figure 4.9: S -parameters with $C_2 = 0.3 \text{ pF}$ for both antennas.

This design provides high bandwidth, covering all desired bands for both antennas. However, the isolation between the two antennas is not the best. Additionally, building the antenna on lossy FR-4 may prove to decrease the efficiency bandwidth compared to an antenna with a less lossy isolator.

Antenna	Band	Start [MHz]	Stop [MHz]	Bandwidth [MHz]
Top	Low	688	1073	385
Side	Low	824	962	138
Top	High	1577	2637	1060
Side	High	1535	2654	1119

Table 4.2: Maximum bandwidth obtained in the low and high band for the top and side antenna, respectively.

The bandwidth in the high and low band for each antenna is shown in Table 4.2. It is clear that both antennas fulfill the requirements of tunable impedance bandwidth seen in the requirement specification, Section 2.

The correlation between the top and side antennas are shown in Figure 4.11 when sweeping the tuning capacitors. It is seen that the correlation in the high band is very low while the correlation in the low band is not the best. This may be caused by the fact that both antennas are coupling to the ground plane to radiate. A solution might be to use a different type of antenna design for the side.

The total system efficiency (i.e. including mismatch loss) is shown for a sweep of capacitance values in Figure 4.12. It is seen that, for the lowest capacitance setting, the top antenna has a total efficiency greater than -3 dB . The side antenna has a total efficiency greater than -3 dB in the high band for its low capacitance settings. In the low band, the antenna can be tuned to cover the whole band at a total efficiency above -4 dB .

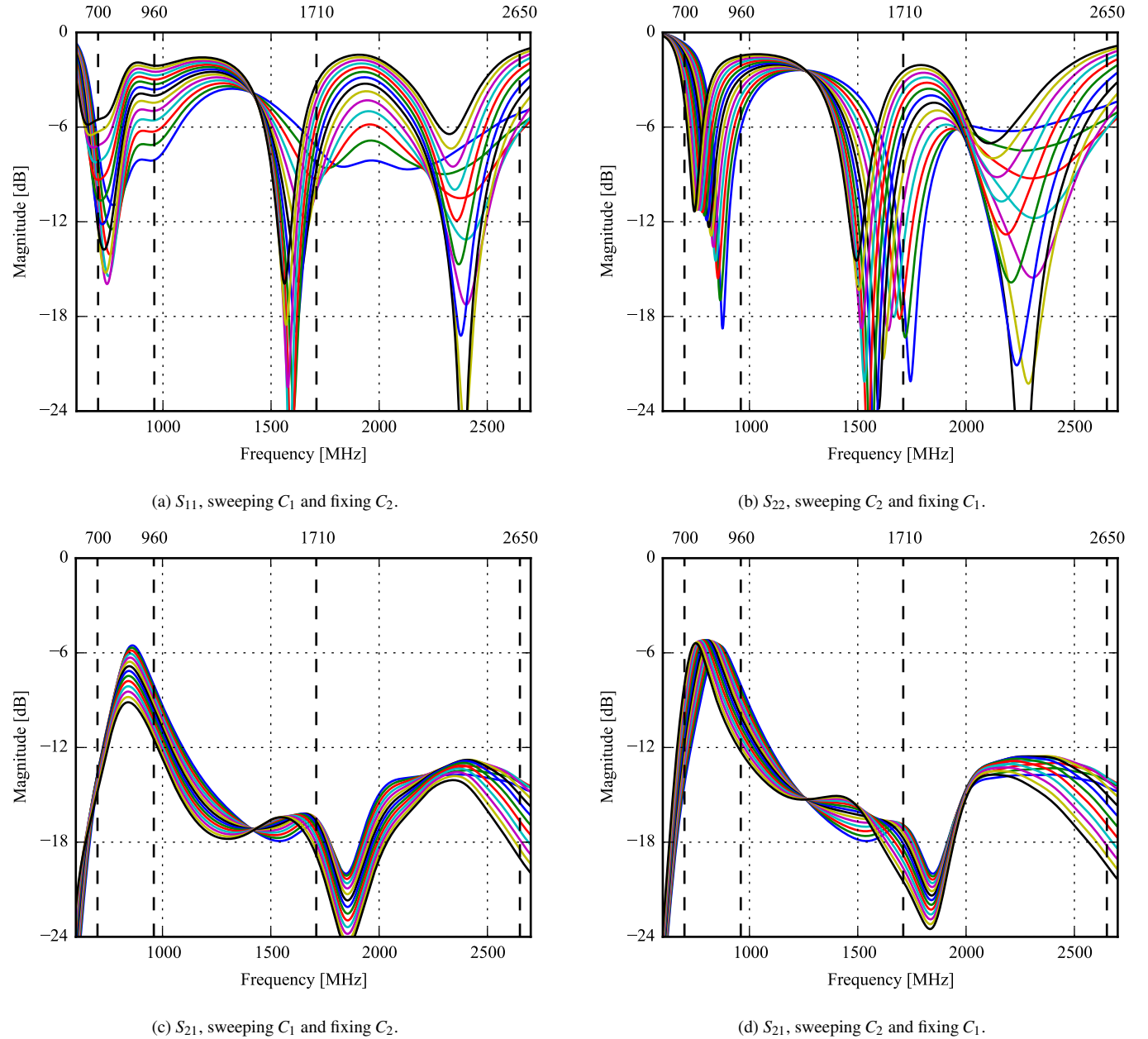


Figure 4.10: Parameter sweeps when tuning the shunt capacitor of each antenna, C_1 and C_2 for port 1 and 2, respectively. Port 1 is the top antenna and port 2 is the side antenna.

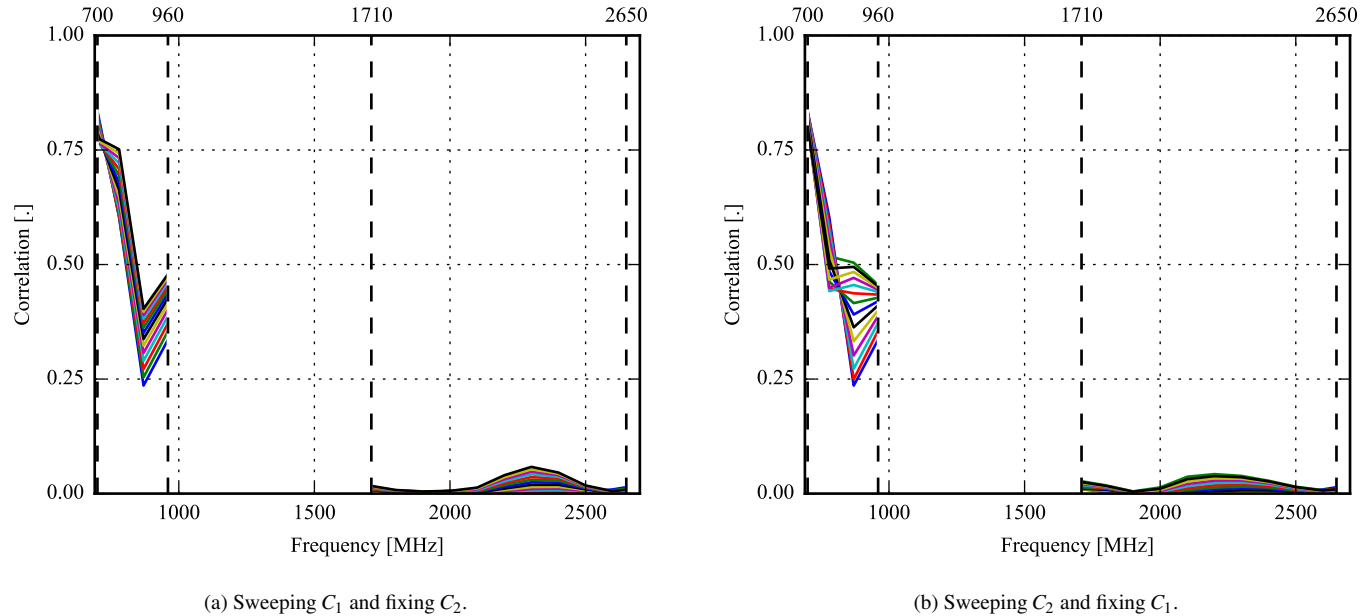


Figure 4.11: Correlation between the antennas then sweeping tuning capacitors. Here, C_1 and C_2 are the tuning capacitor for the top and side antenna, respectively.

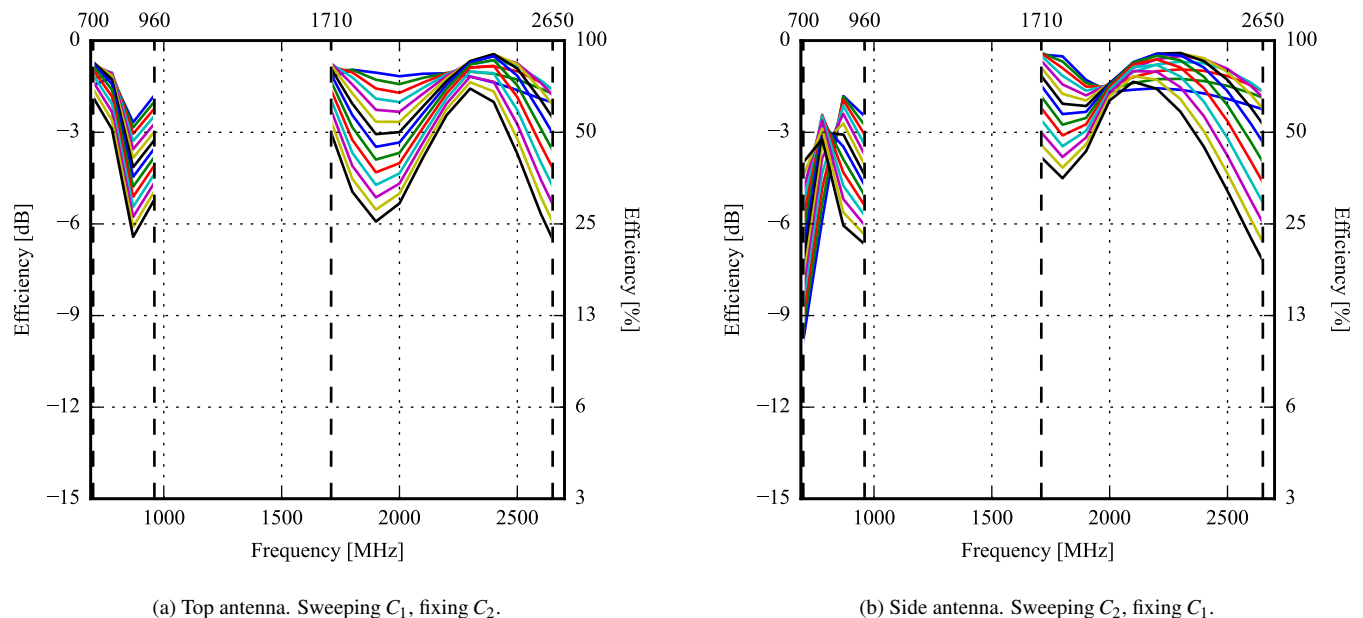


Figure 4.12: Efficiency for each antenna when sweeping the tuning capacitors. Here, C_1 and C_2 are the tuning capacitor for the top and side antenna, respectively.

4.3 Dual-Feed Antenna

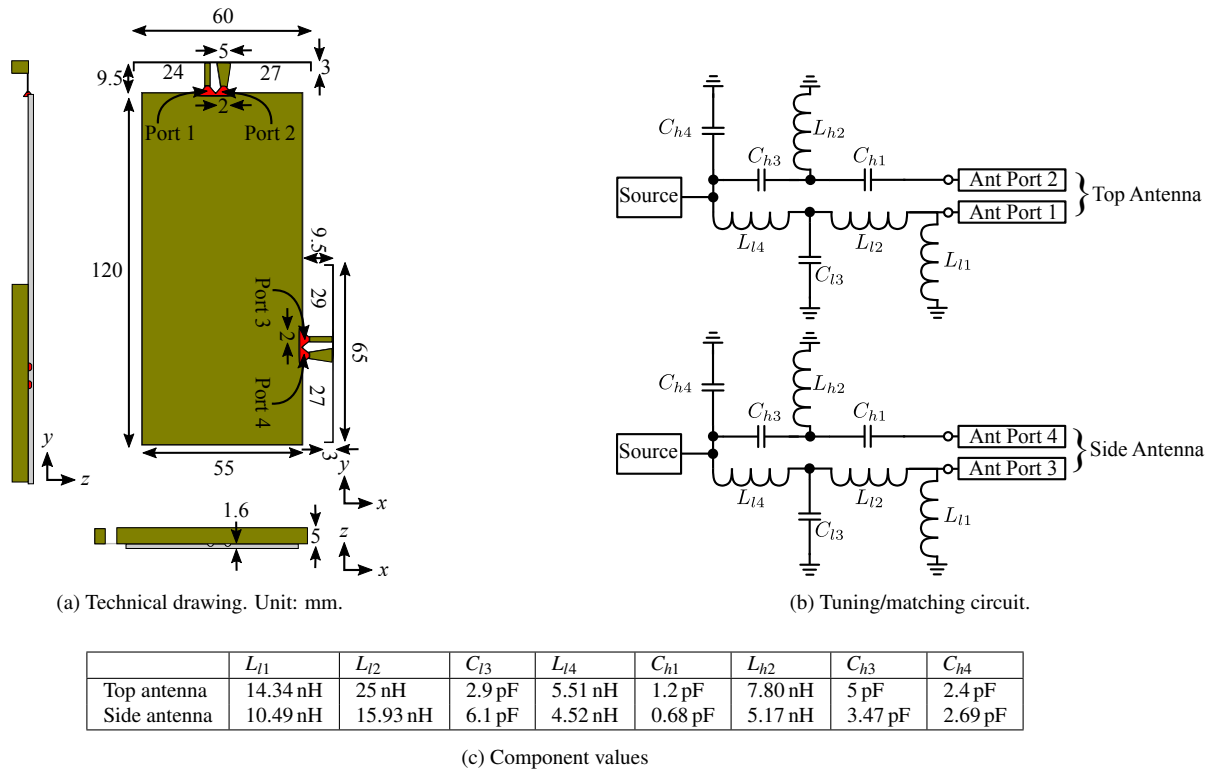


Figure 4.13: Technical drawing and tuning circuit for the antenna. The antennas are built on FR-4 board using $35\ \mu\text{m}$ copper. There is a matching circuit as shown for each of the two feeds.

This design is an inherently non-resonant capacitive coupling element antenna based on the one shown in [51]. The antenna presented in [51] does not have any tuning capabilities, nor is it designed for MIMO operation. The antenna is shown in Figure 4.13, as seen the antenna is , which enhances the bandwidth and efficiency. The antenna has two feeds, but only a single signal port is used. The signal is split into two branches at the matching network, one for the low band and one for the high band. The novel matching network is also based on [51].

As seen on Figure 4.13 the matching network is quite complex, this is usually the case for non-resonant CCE antennas, since the antenna structure is simplified greatly compared to other multi-resonant antennas, e.g. [53], [54] and [55].

The low band element consists of a non-resonant CCE, where the resonance is dependent on the matching circuit. For this design, the matching is *mostly* performed by L_{l1} , L_{l2} , L_{l3} , L_{l4} and C_{l3} . The higher-band is matched by C_{h1} , L_{h2} , C_{h3} and C_{h4} , furthermore there is a natural resonance at 2700 MHz, at the trapezoidal feed (Port 2), which extends the frequency of operation. It should also be noted that the low and high band are dependent on every part of the matching network, even though the components are denoted high (h) and low (l).

The surface currents, illustrating how the structure resonates after matching, is shown in Figure 4.14.

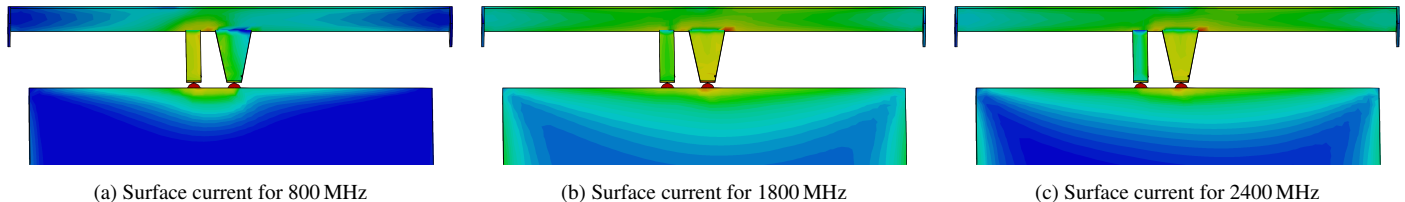


Figure 4.14: Surface currents

The S-parameters for both the top and the side antenna are shown in Figure 4.15. The tuning capacitors are chosen, for a maximum bandwidth with values: $C_{l3} = 2.9\ \text{pF}$ and $s_C_{h1} = 0.68\ \text{pF}$. At this position the top antenna (port 1) covers the entire low and high band. The side antenna covers much less and must be tuned to cover the whole low band. However, the high band is covered.

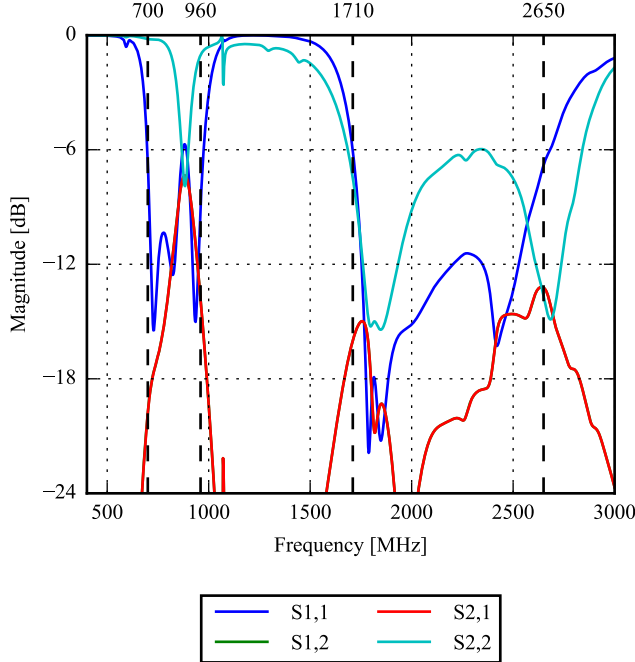


Figure 4.15: S -parameters with $C_{l3} = 2.9 \text{ pF}$ and $s_C_{h1} = 0.68 \text{ pF}$

It is seen that the isolation at low frequencies is only around 8 dB. This may cause problems when using the antennas for MIMO operation. The low isolation is most likely due to the way the CCE antenna resonates, since it uses the chassis as the resonator [52].

This design provides high bandwidth, covering most desired bands for both antennas. In this design, the top antenna would be used as the main antenna and the side antenna would be used for diversity, carrier aggregation, and MIMO operation.

Antenna	Band	Start [MHz]	Stop [MHz]	Bandwidth [MHz]
Top	Low	689	1087	398
Side	Low	670	911	241
Top	High	1714	2704	990
Side	High	1410	2845	1435

Table 4.3: Maximum bandwidth obtained in the low and high band for the top and the side antenna, respectively.

The bandwidth of each antenna is shown in Table 4.3. It is clear that both antennas fulfill the requirements of tunable impedance bandwidth seen in the requirement specification, Section 2. Below are the tuned S -parameters shown. The fixed antenna will be set to the maximum capacitor value, since this yields the best match.

The correlation between the top and side antennas are shown in Figure 4.17 when sweeping the tuning capacitors. Here it is seen that the correlation is low for the high band, while being quite high in the lowest part of the low band.

The total system efficiency sweep, is shown in Figure 4.18. It is seen that the top antenna is very efficient, where the lowest efficiency is around -3 dB for the low band and much higher for the high band. The side antenna has a total efficiency greater than -6 dB for the low band and higher than -3 dB for the high band, except for a single capacitor value.

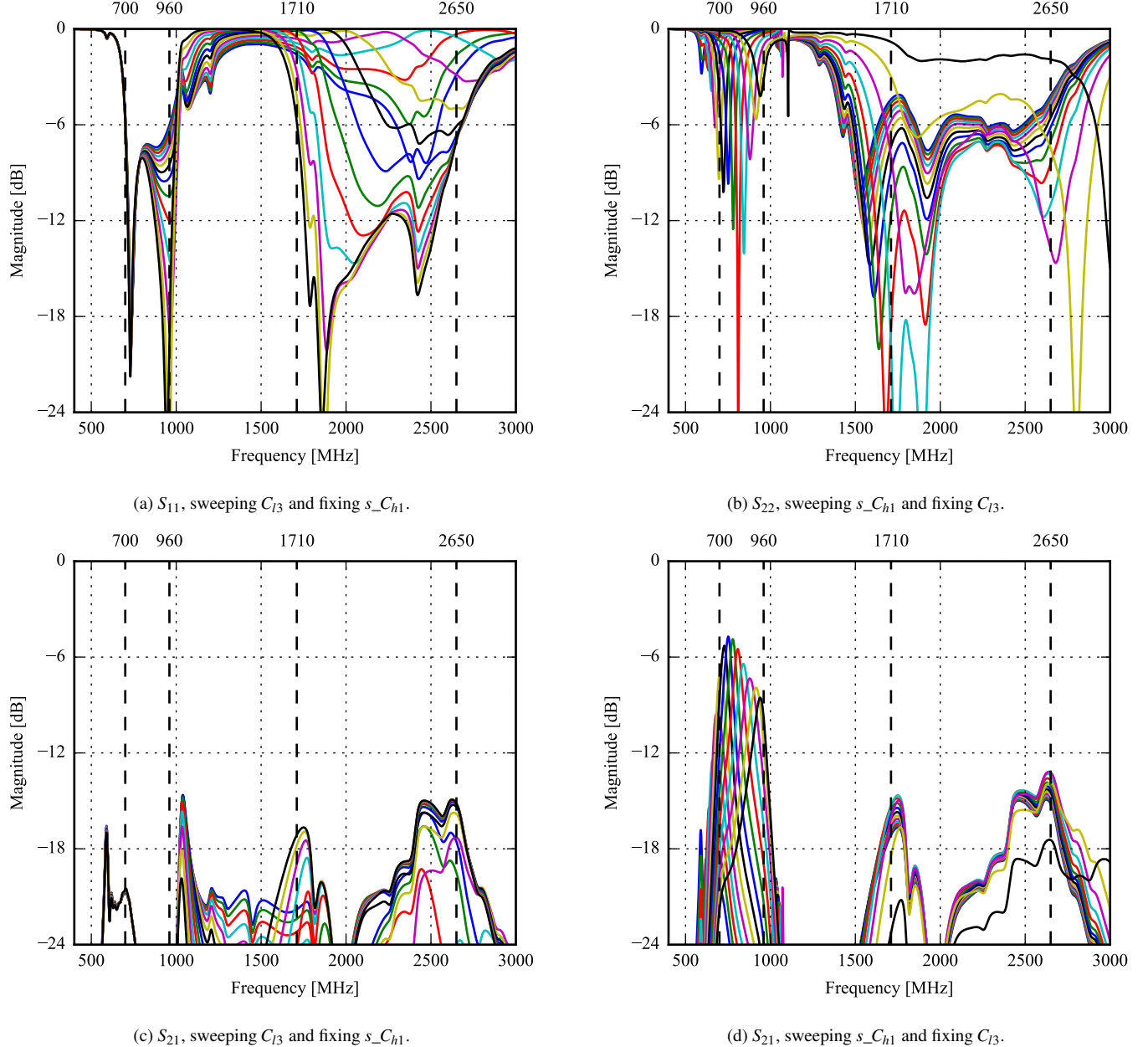


Figure 4.16: Parameter sweeps when tuning the shunt capacitor of each antenna, C_{l3} and s_C_{h1} for port 1 and 2, respectively. Port 1 is the top antenna and port 2 is the side antenna.

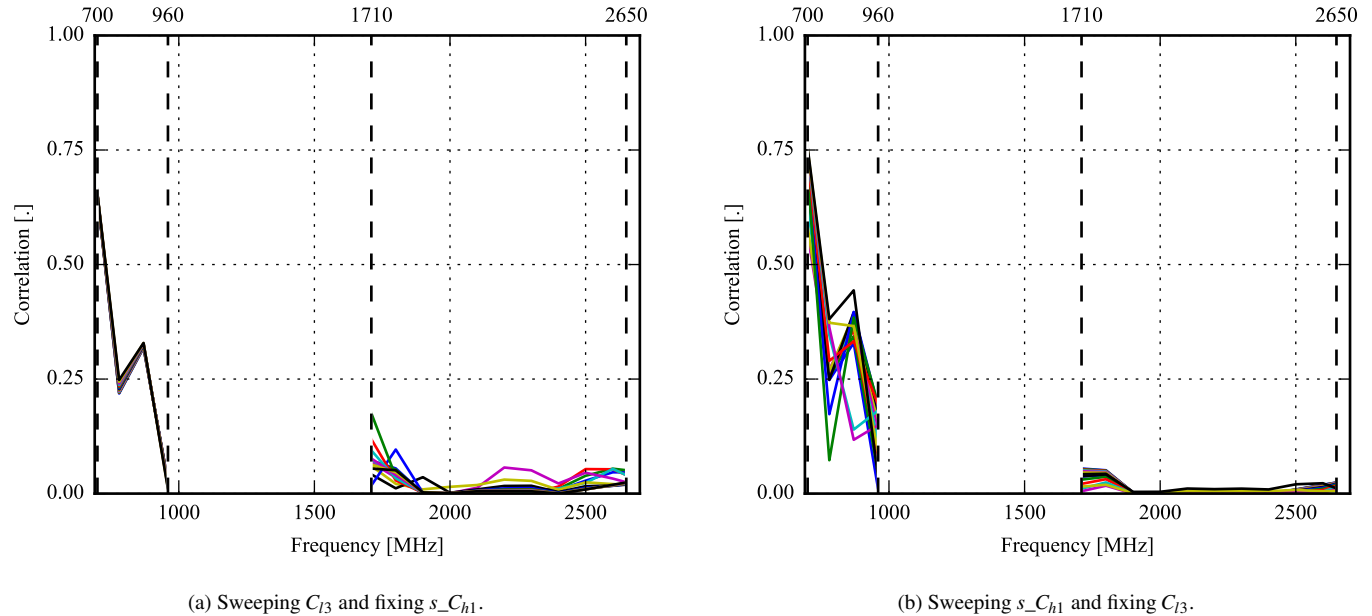


Figure 4.17: Correlation between antennas then sweeping tuning capacitors. Here, C_{l3} and s_C_{h1} are the tuning capacitor for the top and side antenna, respectively.

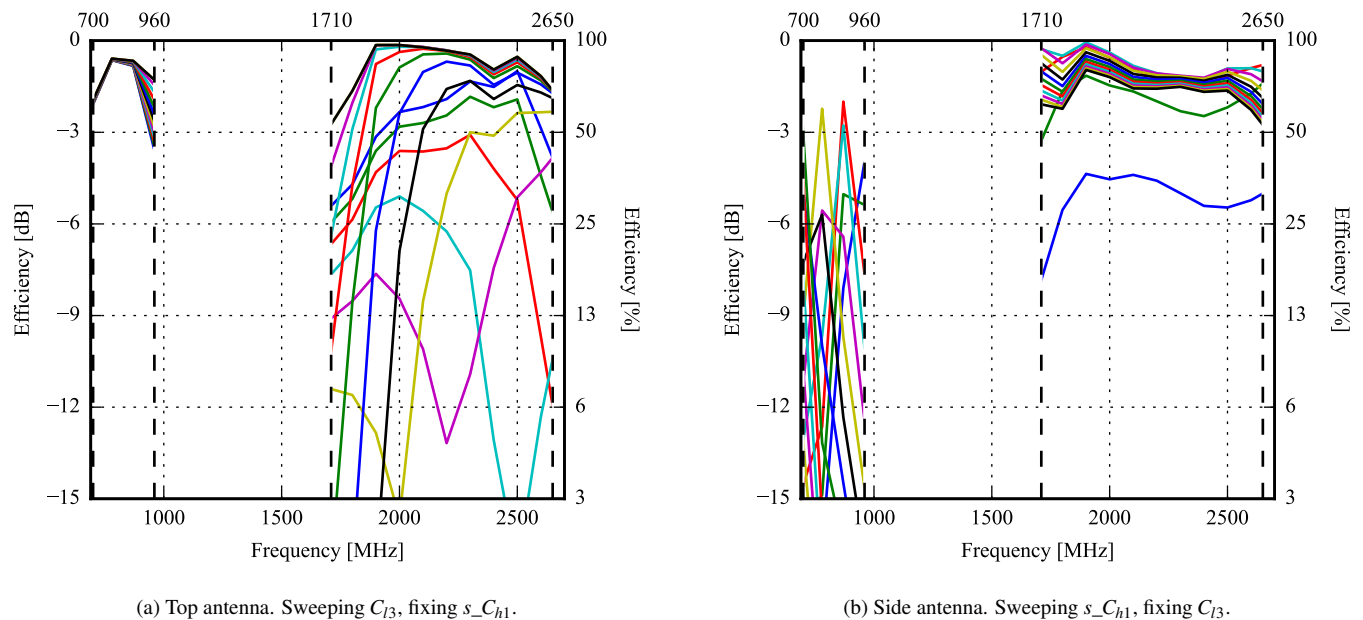


Figure 4.18: Efficiency for each antenna when sweeping the tuning capacitors. Here, C_{l3} and s_C_{h1} are the tuning capacitor for the top and side antenna, respectively.

4.4 Conclusion

The three simulated designs show very promising results. All three appear to be able to cover the entire low and high band at a reasonably high efficiency. The three designs are very different. The monopole is a copper-in-air design with a simple matching network, the triangle-feed antenna is partially made on FR-4, and the dual-feed design is very simple in its structure while having a more complex matching network.

Because the three designs are so different, they may respond very differently to user effects. The next chapter will cover the simulation of the three designs in three use cases as well as simulate the specific absorption rate of the designs.

Chapter 5

User Effect Simulations

In this chapter, the antennas from Chapter 4 are simulated in use. The four simulation models are shown in Figure 5.1. The SAR simulation is solely used to check the requirement for maximum SAR seen in the requirement specification, Chapter 2. For the other three simulations, the same types of results as in Chapter 4 are shown to see how the antennas perform when the phones are in use.

The simulations are done with a phone case in order to align the phone with the blue spacer as seen in Figure 5.1. The case used is made of thin 0.5 mm plastic and is customized to fit each antenna design. Furthermore, to make the SAR simulations more accurate and realistic, a screen model made of PEC is used.

The material types and constants can be seen in Table 5.1. The head, hand, and spacer is made accordingly to the CTIA test plan [56]. Second order permittivity dispersion model fits have been used for the head and hand models to gain more accurate results.

The below settings were used when simulating the user effect:

Accuracy –60 dB.

One hand (data mode) Approximately 7 500 000 mesh cells.

Two hands (play mode) Approximately 15 000 000 mesh cells.

Head and hand (talk mode, SAR) Approximately 15 000 000 mesh cells.

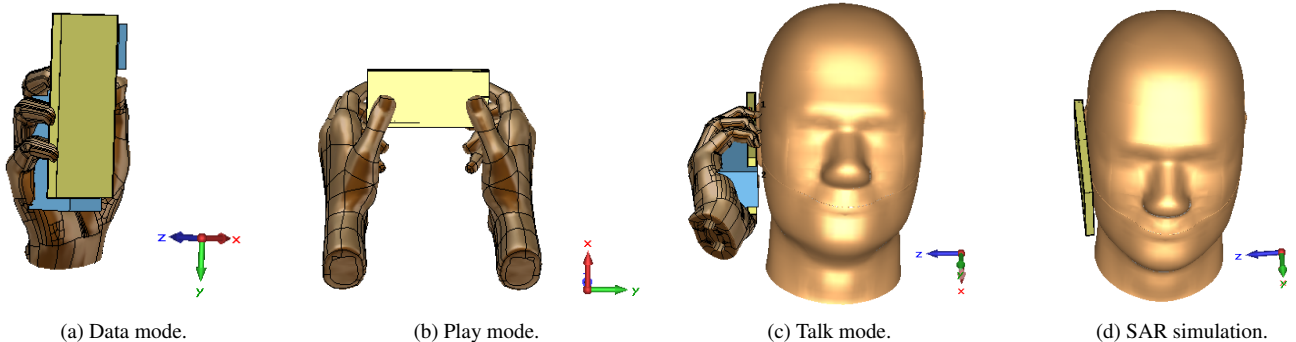


Figure 5.1: User effect simulation modes.

Type	Material	Permeability [μ]	Permittivity [ϵ]
Case	Plastic	1	3
Spacer	Vacuum	1	1
Hand	Shell and fluid	1	2nd order dispersion model
Head	Shell	1	3.7
Head	Fluid	1	2nd order dispersion model

Table 5.1: Material types and constants used in the user effect simulations.

5.1 Monopole Antenna

In this section, the antenna from Section 4.1 will be simulated in practice use with a user model. The antenna positions are shown in Figure 5.2.

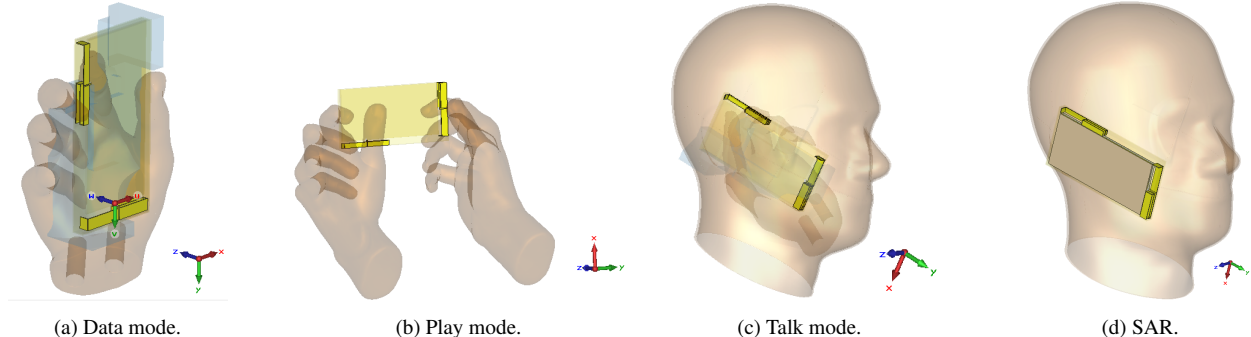


Figure 5.2: MIMO monopole antenna position for each user effect simulation.

5.1.1 Data Mode

The S-parameter sweeps for the data mode, can be seen in Figure 5.4. The highest obtainable bandwidth for both antennas is found from the S-parameter sweep and is listed in Table 5.2. The top antenna covers the required bandwidth in both the low and high band. However, as seen in the Table 5.2, the side antenna only covers the bandwidth in the high band and the low band needs additional tuning to fulfill the bandwidth requirements. The S-parameter sweeps, Figure 5.4, also show the S_{21} isolation loss. The lowest notable isolation is within the low band, at 10 dB and 8 dB for the top and side antenna, respectively.

The correlation between the top and side antenna can be seen in Figure 5.5. The correlation is plotted sweeping the tunable capacitors of each antenna, while the other antenna is fixed at 0.3 pF. The correlation for the top and side antenna is below 0.5 for both the low and high band as desired.

The efficiency in data mode for both antennas can be seen in Figure 5.6. The efficiency is plotted for each value of tunable capacitors. Comparing the efficiency in data mode with the free-space efficiency, the data mode generally decreases over the entire spectrum for both antennas. The different sweep modes of the tunable capacitor shows most significant efficiency drop in the low band with a maximum drop of 8 dB for the top antenna and 9 dB for the side antenna. Both antennas cover the free-space requirement of -3 dB efficiency within the frequency band 1710 MHz to 2200 MHz.

Antenna	Band	Start [MHz]	Stop [MHz]	Bandwidth [MHz]
Top	Low	677	1065	388
Side	Low	700	710	10
Top	High	1183	2127	944
Side	High	1765	2120	355

Table 5.2: Monopole antenna in data mode. Maximum bandwidth obtained in the low and high band for the top and the side antenna, respectively.

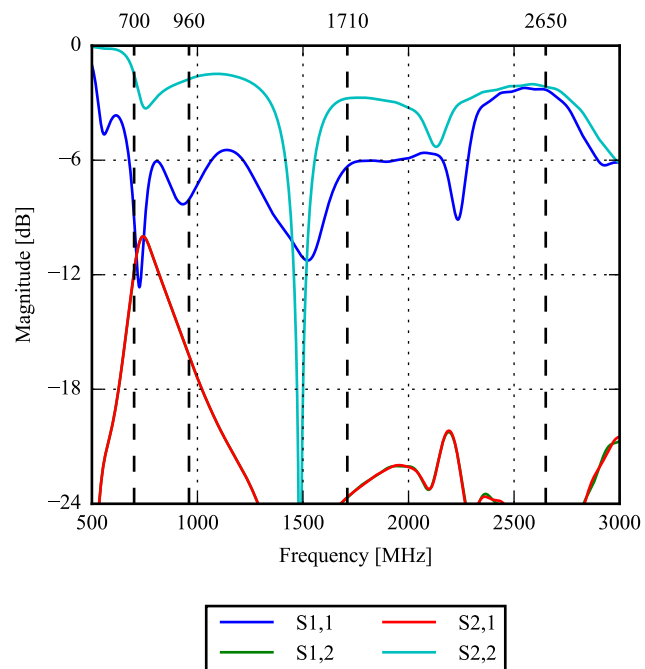


Figure 5.3: Monopole antenna in data mode. S-parameters with both tuning capacitors fixed at 0.3 pF.

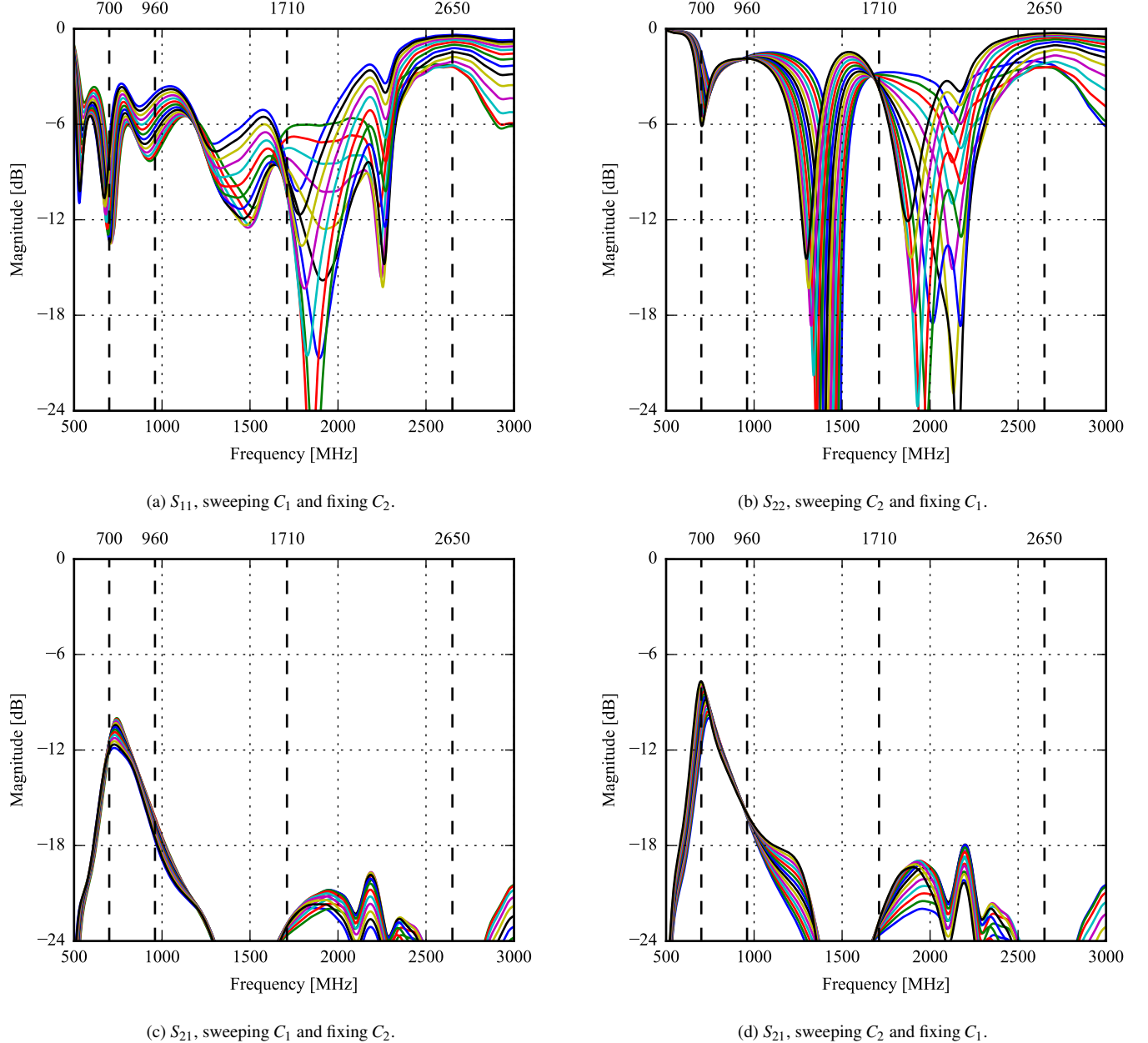


Figure 5.4: S -parameter sweep in data mode for tuning the shunt capacitor of each antenna, C_1 and C_2 for port 1 and 2, respectively. Port 1 is the top antenna and port 2 is the side antenna.

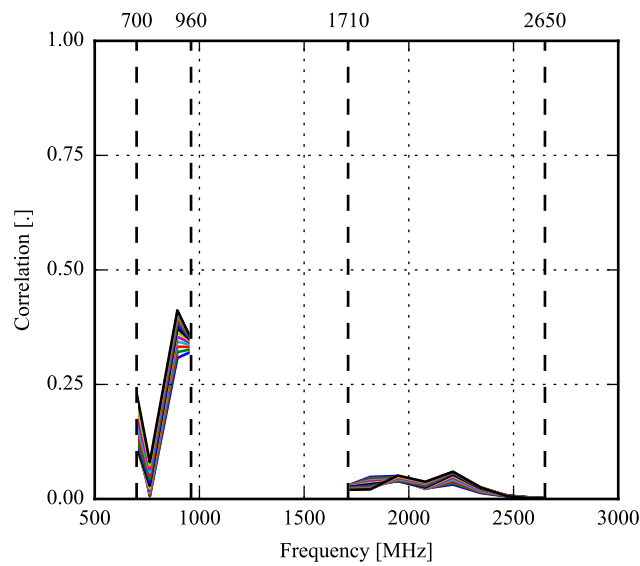
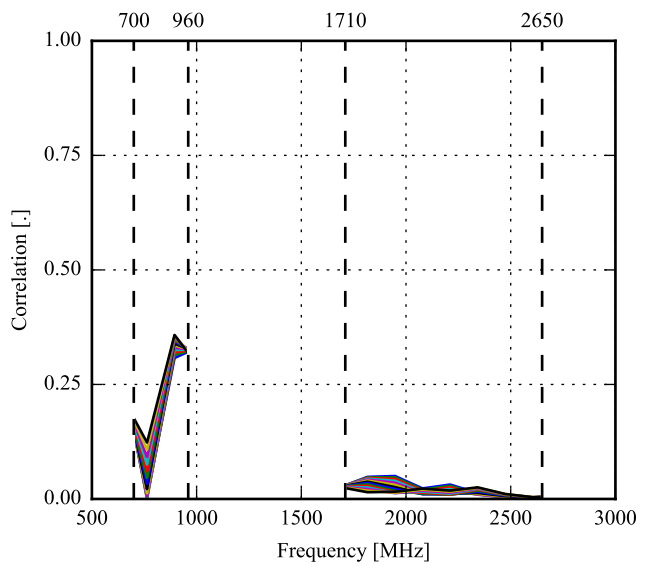
(a) Sweeping C_1 and fixing C_2 .(b) Sweeping C_2 and fixing C_1 .

Figure 5.5: Monopole antenna in data mode. Correlation between antennas when sweeping the tuning capacitors. Here, C_1 and C_2 are the tuning capacitor for the top and side antenna, respectively.

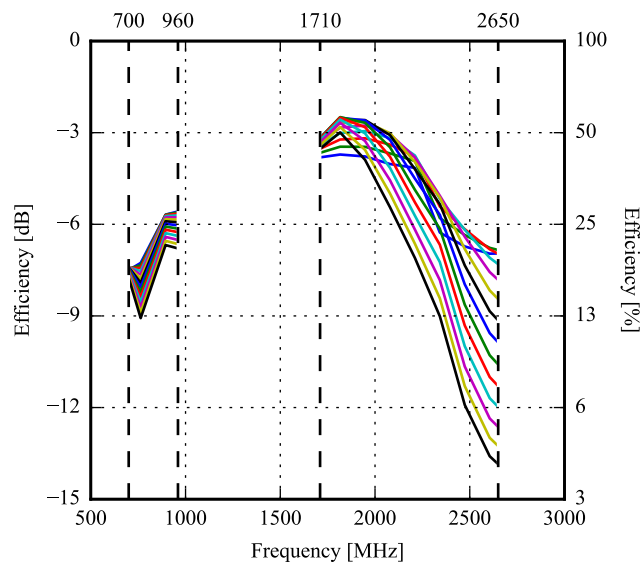
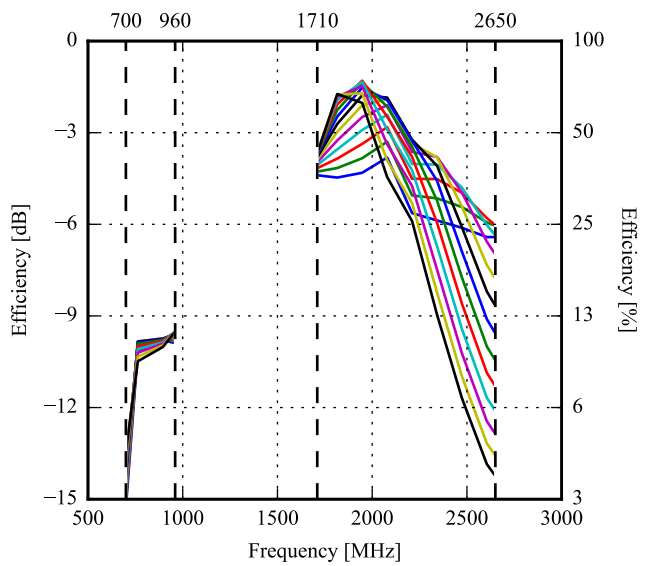
(a) Sweeping C_1 and fixing C_2 .(b) Sweeping C_2 and fixing C_1 .

Figure 5.6: Monopole antenna in data mode. Efficiency for each antenna when sweeping the tunable capacitors. Here, C_1 and C_2 are the tuning capacitor for the top and side antenna, respectively.

5.1.2 Play Mode

The S-parameter sweeps for the play mode, can be seen on Figure 5.8. The highest obtainable bandwidth for both antennas is found from the S-parameter sweep and is listed in Table 5.3. The top antenna covers the required bandwidth in the low band but lacks 87 MHz in the high band. The side antenna does not fulfill any of the bandwidth requirements and will need additional tuning. The S-parameter sweeps, Figure 5.8, also show the S_{21} isolation loss. The lowest notable isolation is within the low band, at 12 dB and 10 dB for the top and side antenna, respectively.

The correlation between the top and side antenna can be seen in Figure 5.9. The correlation is plotted sweeping the tunable capacitors of each antenna, while the other antenna is fixed at 0.3 pF. The correlation for the top and side exceeds the required correlation limit with 0.1 in the low band from 700 MHz to 880 MHz.

The efficiency in play mode for both antennas can be seen in Figure 5.10. The efficiency is plotted for each sweep of the tunable capacitors. Comparing the efficiency in play mode with the free-space efficiency, the play mode efficiency generally decreases over the entire spectrum for both antennas. The different sweep modes of the tunable capacitor show most significant efficiency drop in the low band. However, comparing the individual sweep modes, the highest efficiency drop for the top antenna is within the high band at 2500 MHz and within the low band at 960 MHz for the side antenna. The top antenna has a maximum drop of 10 dB for the top antenna and for the side antenna, the efficiency drop is greater than 14 dB.

Both antennas have the highest efficiency within the frequency band of 1800 MHz to 2200 MHz with an efficiency of approx -5 dB. The simulation results are as expected compared to the data mode, as the play mode introduces body losses from two hands.

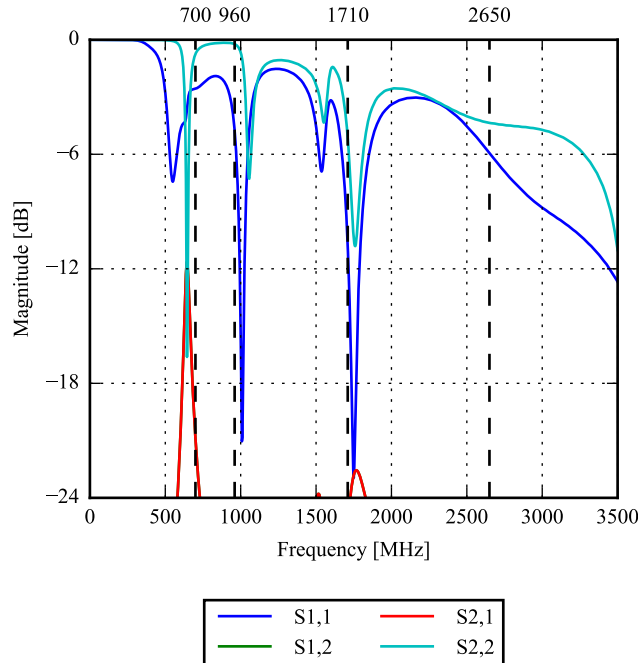


Figure 5.7: Monopole antenna in play mode. S-parameters with both tuning capacitors fixed at 0.3 pF.

Antenna	Band	Start [MHz]	Stop [MHz]	Bandwidth [MHz]
Top	Low	920	1000	80
Side	Low	1010	1060	50
Top	High	1420	2053	633
Side	High	1635	2180	545

Table 5.3: Monopole antenna in play mode. Maximum bandwidth obtained in the low and high band for the top and the side antenna, respectively.

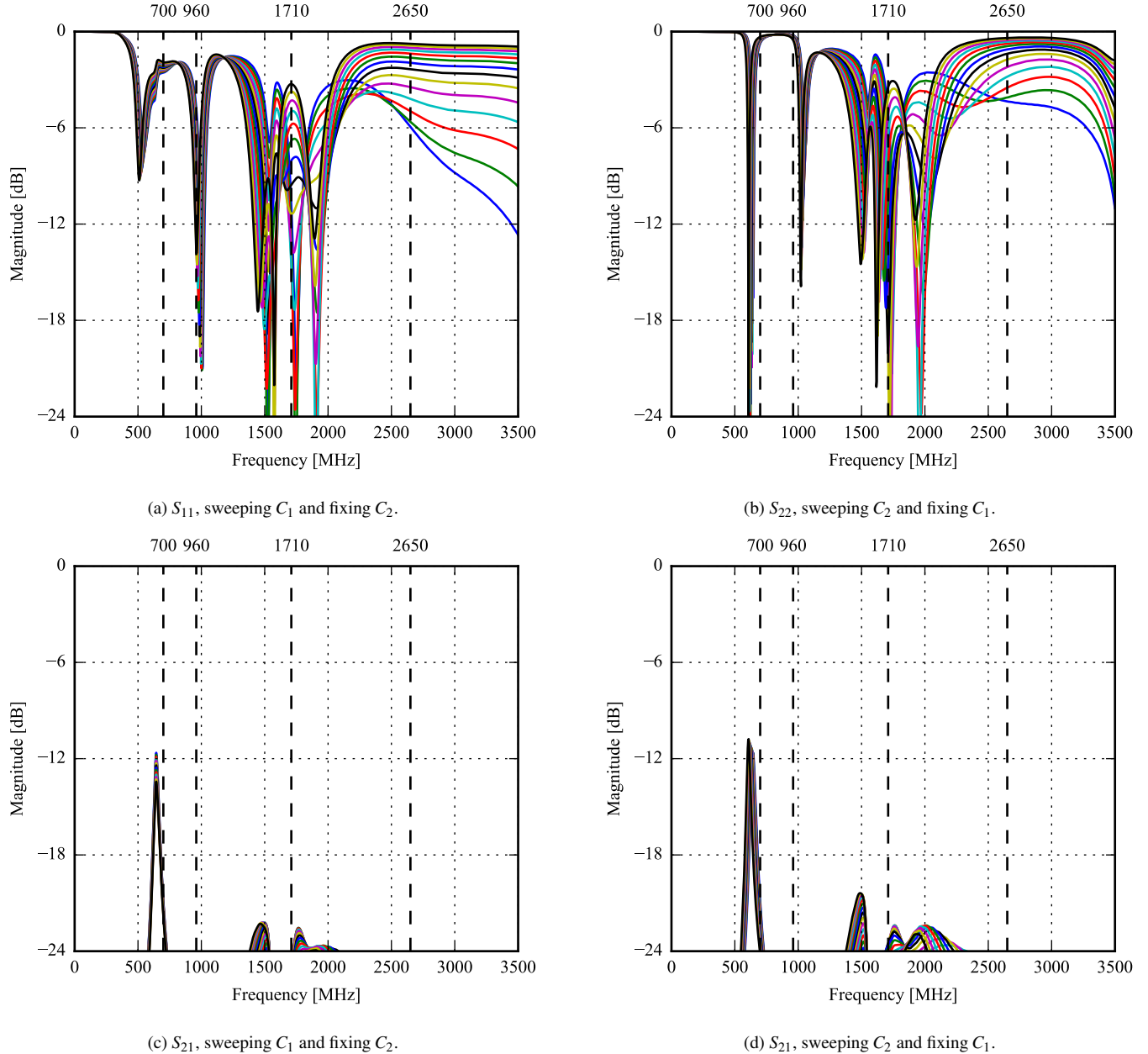


Figure 5.8: S -parameter sweep in play mode for tuning the shunt capacitor of each antenna, C_1 and C_2 for port 1 and 2, respectively. Port 1 is the top antenna and port 2 is the side antenna.

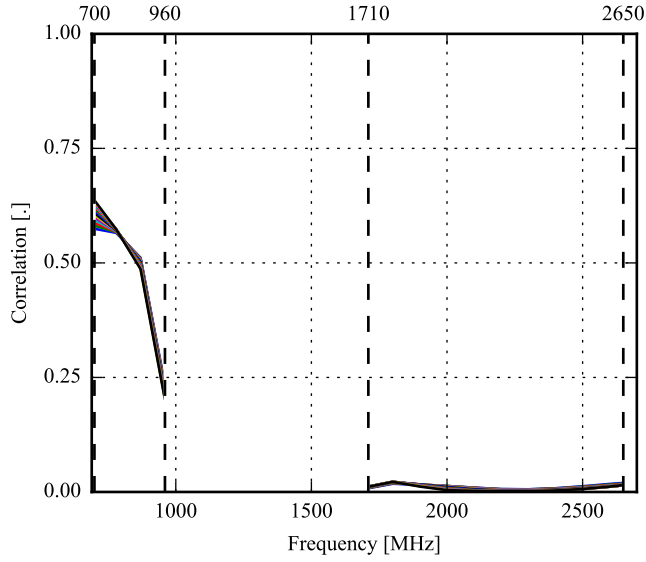
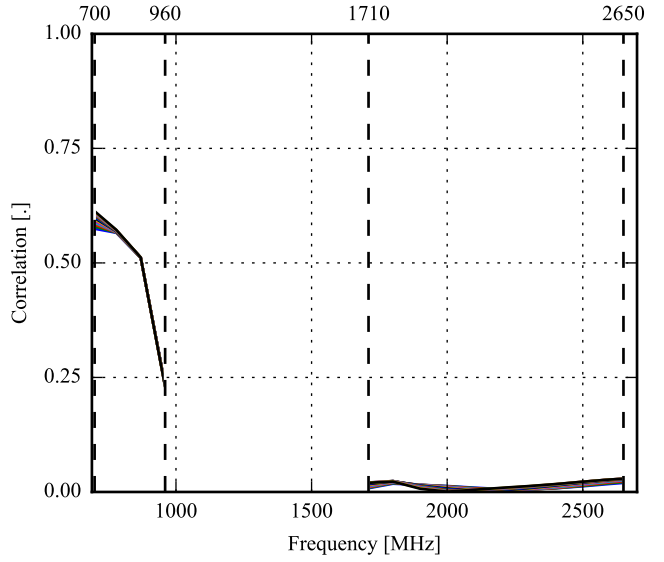
(a) Sweeping C_1 and fixing C_2 .(b) Sweeping C_2 and fixing C_1 .

Figure 5.9: Monopole antenna in play mode. Correlation between antennas when sweeping the tuning capacitors. Here, C_1 and C_2 are the tuning capacitor for the top and side antenna, respectively.

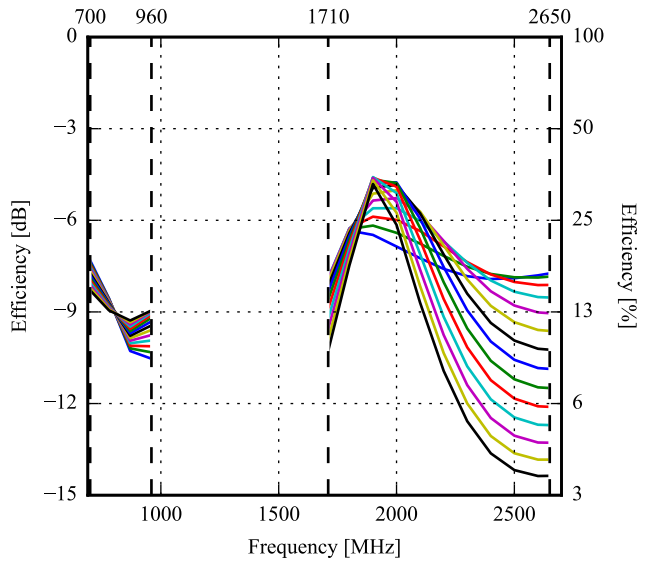
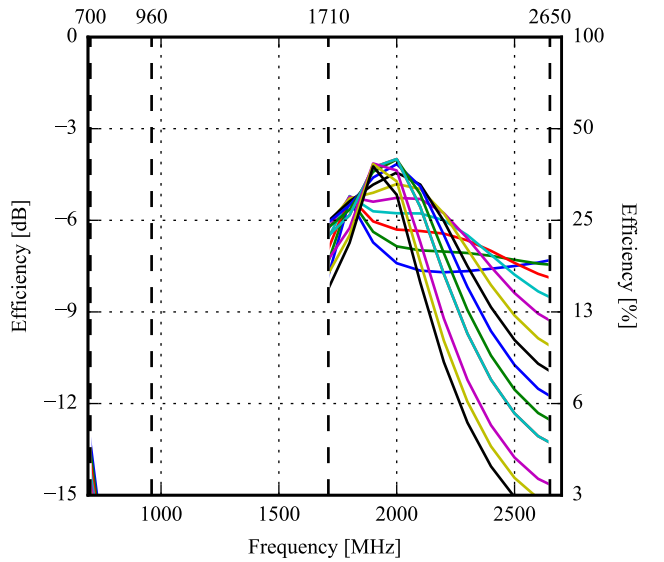
(a) Sweeping C_1 and fixing C_2 .(b) Sweeping C_2 and fixing C_1 .

Figure 5.10: Monopole antenna in play mode. Efficiency for each antenna when sweeping the tunable capacitors. Here, C_1 and C_2 are the tuning capacitor for the top and side antenna, respectively.

5.1.3 Talk Mode

The S-parameter sweeps for the talk mode, can be seen on Figure 5.12. The highest obtainable bandwidth for both antennas is found from the S-parameter sweep and is listed in Table 5.4. The top antenna covers the required bandwidth both in the low band and high band. The side antenna only covers the high band and will need some additional tuning in the low band. The S-parameter sweeps, Figure 5.12, also show the S_{21} isolation loss. The lowest notable isolation is within the low band at 12 dB and 8 dB both the top and side antenna, respectively.

The correlation between the top and side antenna can be seen in Figure 5.13. The correlation is plotted sweeping the tunable capacitors of each antenna while the other antenna is fixed at 0.3 pF. The correlation for the top and side exceeds the required correlation limit with 0.15 in the low band from 700 MHz to 750 MHz.

The efficiency in talk mode for both antennas can be seen in Figure 5.14. The efficiency is plotted for each value of the tunable capacitors. Comparing the efficiency in talk mode with the free-space efficiency, the talk mode efficiency generally decreases over the entire spectrum for both antennas. The different sweep modes of the tunable capacitor show most significant efficiency drop in the low band. However, comparing the individual sweep modes, the highest efficiency drop for the top antenna is within the low band at 960 MHz and within the high band at 2500 MHz for the side antenna. The top antenna efficiency drops more than 13 dB and the side antenna has a maximum drop of 12 dB.

Both antennas have the highest efficiency within the frequency band of 1710 MHz to 2300 MHz with an efficiency of approximately -8 dB for the top antenna and approximately -6 dB for the side antenna. The simulation results are as expected compared to the data mode, as the talk mode introduces both head and hand losses.

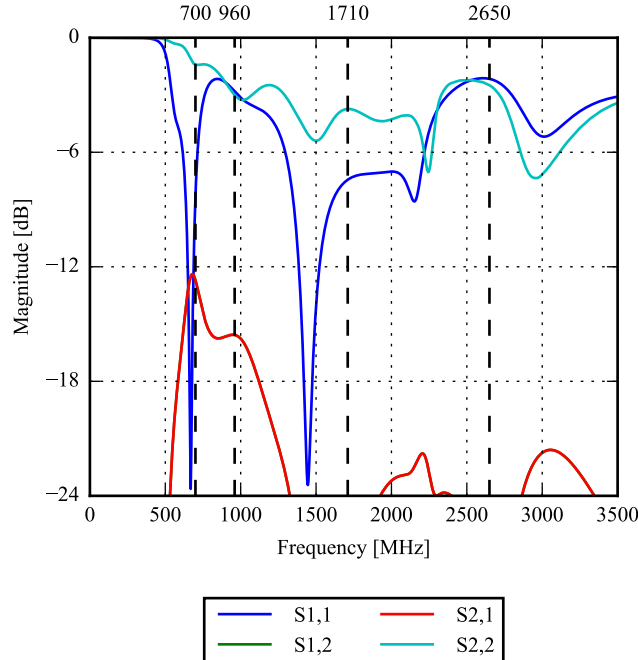


Figure 5.11: Monopole antenna in talk mode. S-parameters with both tuning capacitors fixed at 0.3 pF.

Antenna	Band	Start [MHz]	Stop [MHz]	Bandwidth [MHz]
Top	Low	510	645	135
Side	Low			0
Top	High	1092	2305	1213
Side	High	1335	2132	797

Table 5.4: Monopole antenna in talk mode. Maximum bandwidth obtained in the low and high band for the top and the side antenna, respectively.

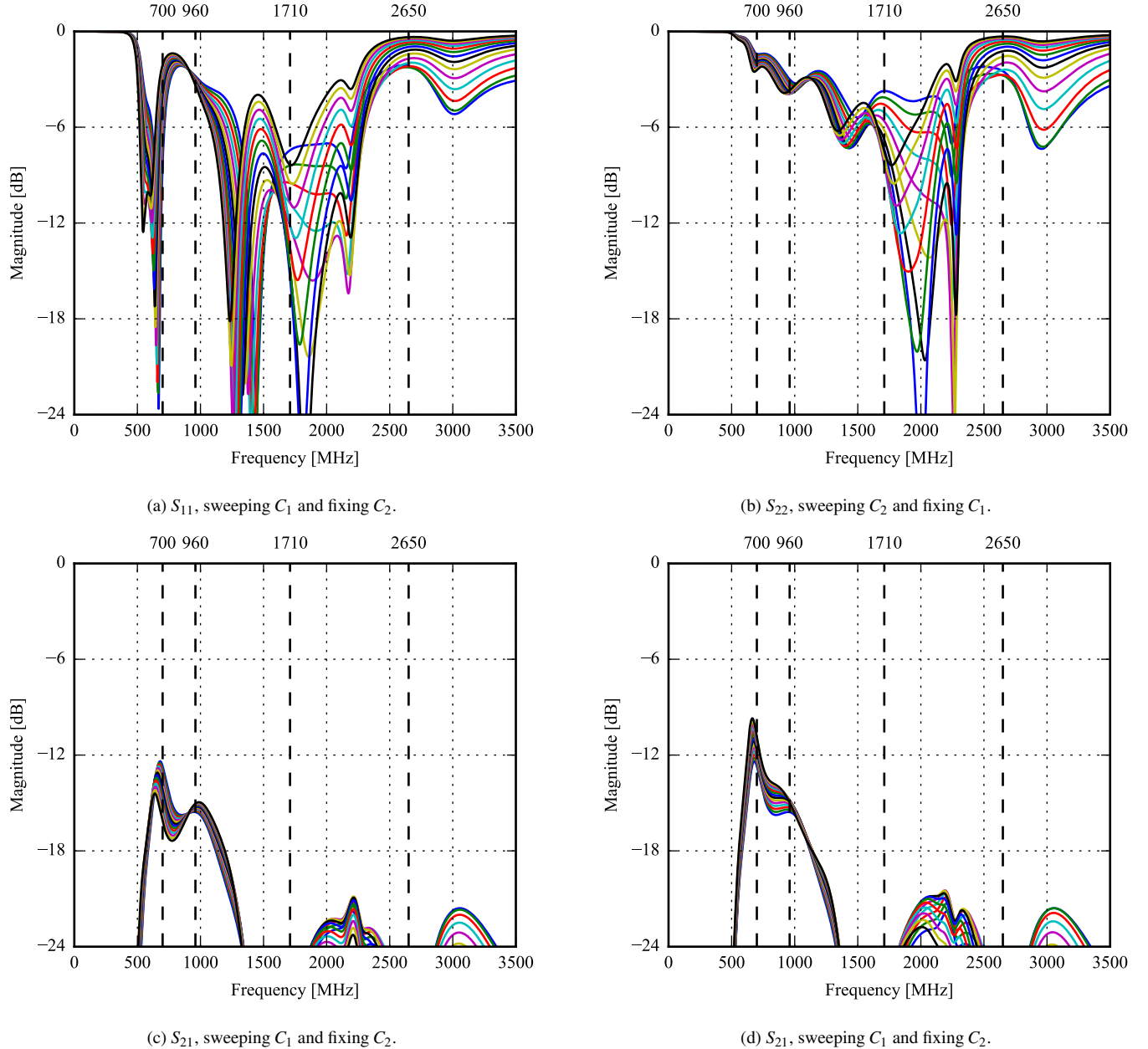


Figure 5.12: S -parameter sweep in talk mode for tuning the shunt capacitor of each antenna, C_1 and C_2 for port 1 and 2, respectively. Port 1 is the top antenna and port 2 is the side antenna.

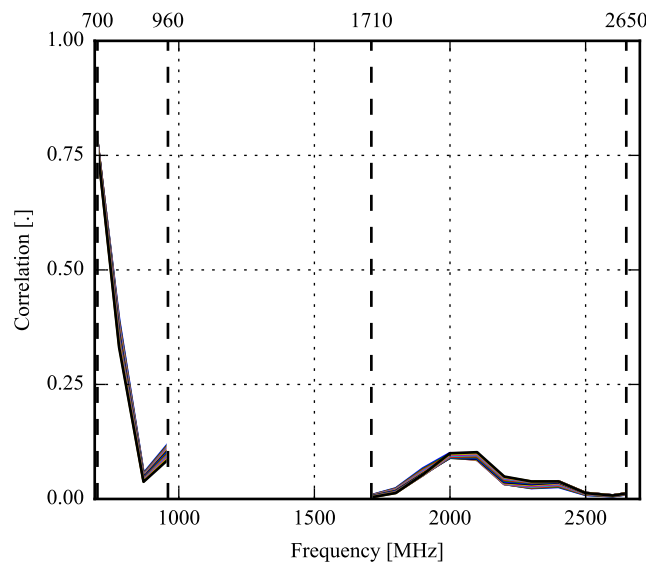
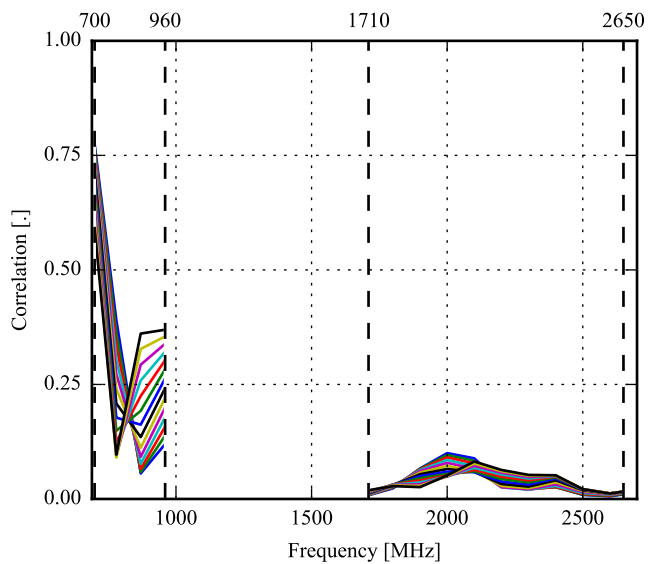
(a) Sweeping C_1 and fixing C_2 .(b) Sweeping C_2 and fixing C_1 .

Figure 5.13: Monopole antenna in talk mode. Correlation between antennas when sweeping the tuning capacitors. Here, C_1 and C_2 are the tuning capacitor for the top and side antenna, respectively.

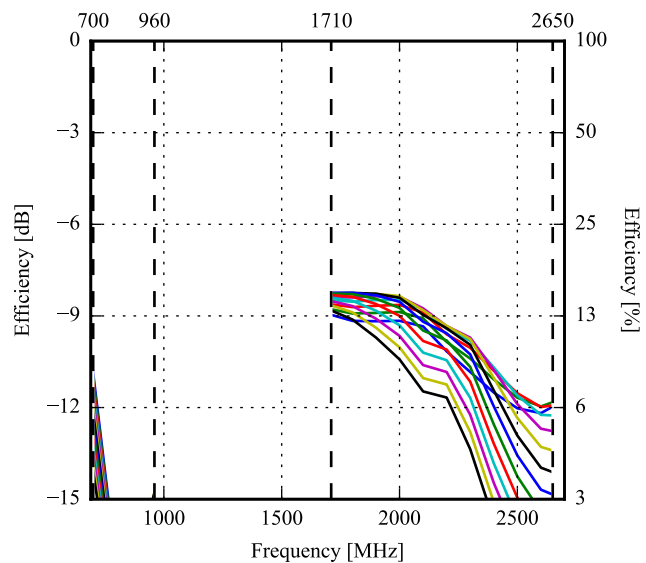
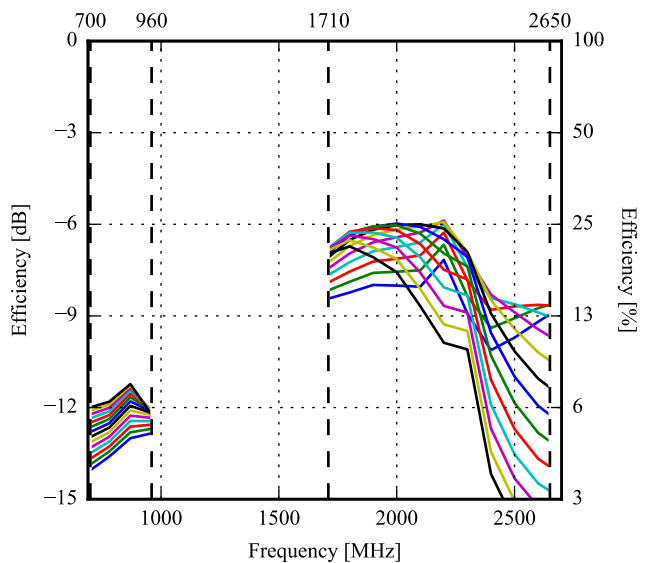
(a) Sweeping C_1 and fixing C_2 .(b) Sweeping C_2 and fixing C_1 .

Figure 5.14: Monopole antenna in talk mode. Efficiency for each antenna when sweeping the tunable capacitors. Here, C_1 and C_2 are the tuning capacitor for the top and side antenna, respectively.

5.1.4 SAR

The SAR simulation results for both antennas are shown in Figure 5.15. As seen from the figure, the SAR value for both antennas is within the requirement of 2 W/kg. The top antenna has a maximum SAR value of 1.4 W/kg at 1800 MHz and the side antenna 1.1 W/kg at 1700 MHz. Generally, the SAR values for both antennas comply with the requirement and are especially small in the low band.

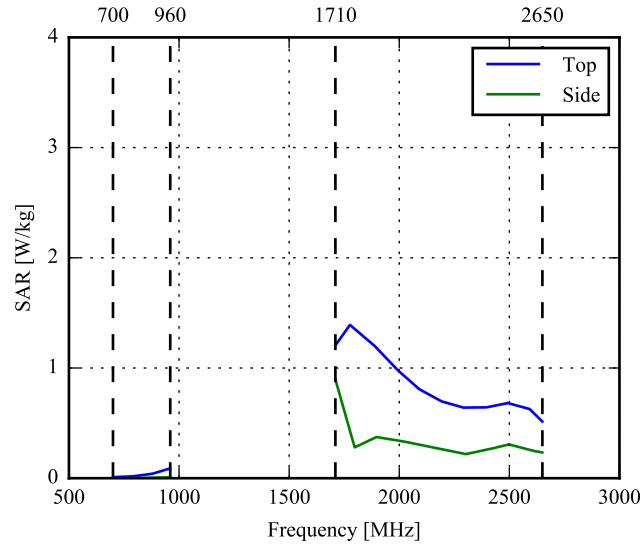


Figure 5.15: SAR simulation of the monopole antenna.

5.2 Triangle-Feed Antenna

In this section, the results from Section 4.2 will be repeated, having the phone in data mode, play mode, and talk mode. Additionally, the maximum SAR value, recorded in the users head, will be simulated. The antenna positions, for each use case, are shown in Figure 5.16.

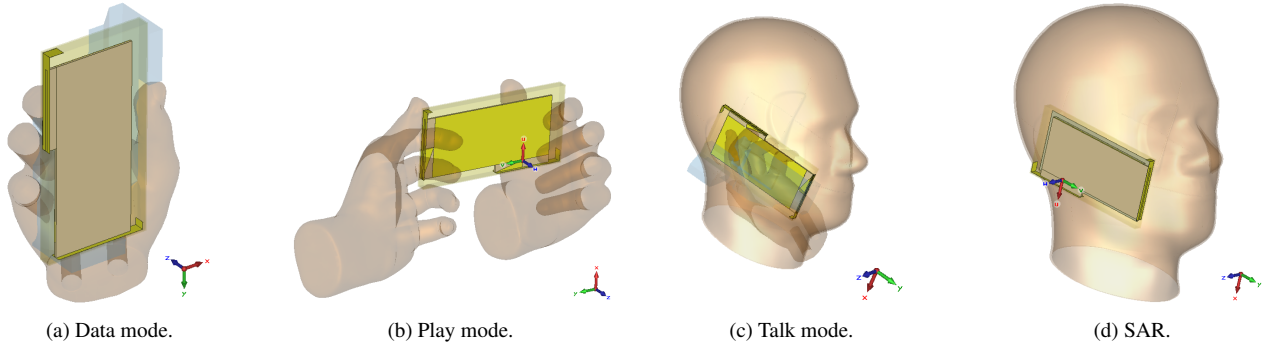


Figure 5.16: Antenna position for each user effect simulation.

5.2.1 Data Mode

The S-parameters, with the tunable capacitors set to their minima, are shown in Figure 5.17. It is seen that that the low band of the side antenna has been tuned down to around the middle of the low band. As it is not possible to tune the resonance further upwards, the bands around 960 MHz are not covered at greater than 6 dB return loss. The high band is still almost covered at around 5 dB return loss. The top antenna, on the other hand, almost covers both the low and the high band simultaneously.

The S-parameters, when sweeping the tunable capacitors, are shown in Figure 5.18. The maximum impedance-bandwidths are summed up in Table 5.5. From this, it is again clear that only the top antenna is able to cover the high end of the low band. None of the antennas can cover the high band at 6 dB return loss. However, as they can cover the high band at greater than 5 dB, this is not considered a problem.

The correlation between the antennas, when sweeping the tunable capacitors, are shown in Figure 5.19. The correlation is, for frequencies above 750 MHz, below 0.5 when sweeping the top antenna. When sweeping the side antenna, the correlation remains below 0.5 for all capacitor settings. The correlation has dropped significantly from the free-space simulation in Figure 4.11.

The efficiencies for each antenna, when sweeping the tuning capacitors, are shown in Figure 5.20. It is seen that the efficiency, generally, has decreased from the free-space simulation in Chapter 4. At -3 dB efficiency, there is no bandwidth left. At -6 dB, the most of the bands can be covered except at the lower part of the low band for the side antenna where the efficiency decreases to a maximum of -7 dB. The efficiency in the high band is generally higher than in the low band.

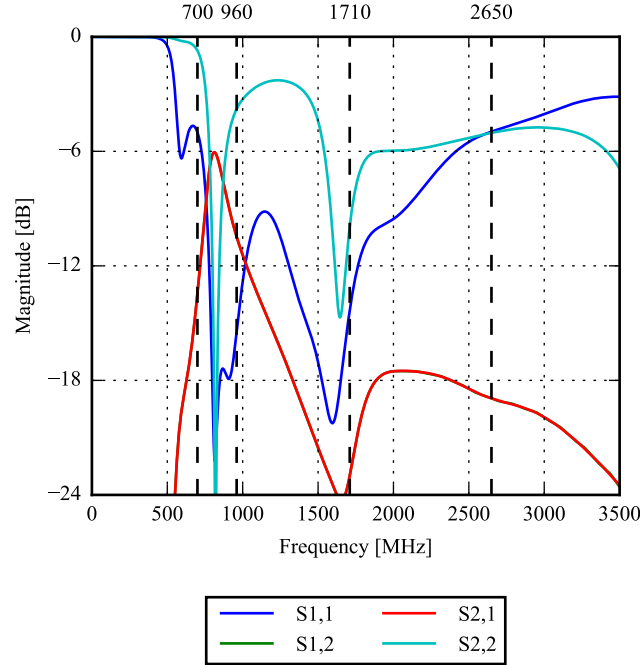


Figure 5.17: Triangle-feed antenna in data mode. S -parameters with both tuning capacitors fixed at 0.3 pF.

Antenna	Band	Start [MHz]	Stop [MHz]	Bandwidth [MHz]
Top	Low	570	2583	2013
Side	Low	779	891	112
Top	High	570	2583	2013
Side	High	1506	2623	1117

Table 5.5: Triangle-feed antenna in data mode. Maximum bandwidth obtained in the low and high band for the top and the side antenna, respectively. It is seen that, for the low capacitor settings on the top antenna, both the low and high band are covered at the same time.

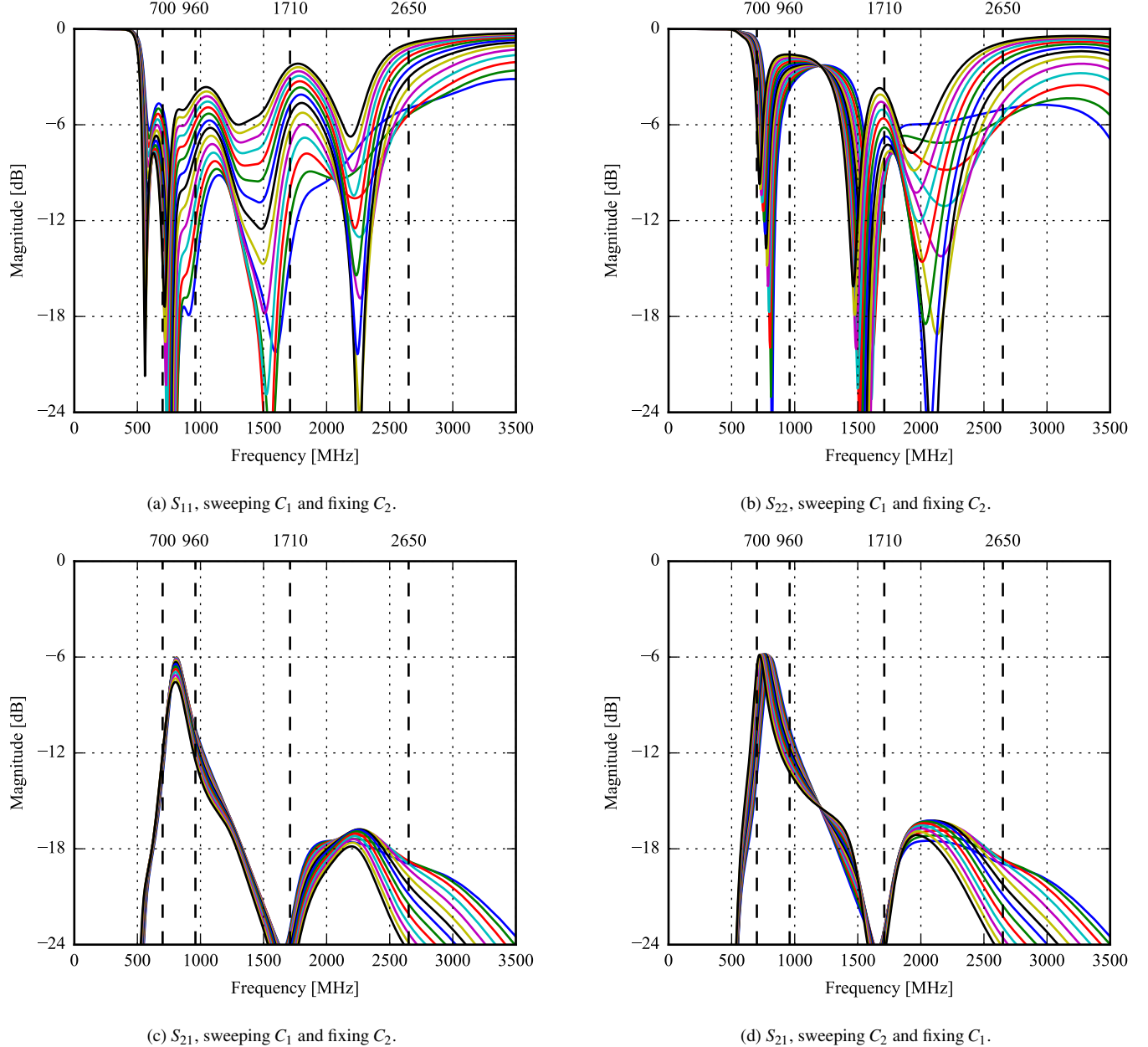


Figure 5.18: Triangle-feed antenna in data mode. Parameter sweep for tuning the shunt capacitor of each antenna, C_1 and C_2 for port 1 and 2, respectively. Port 1 is the top antenna and port 2 is the side antenna.

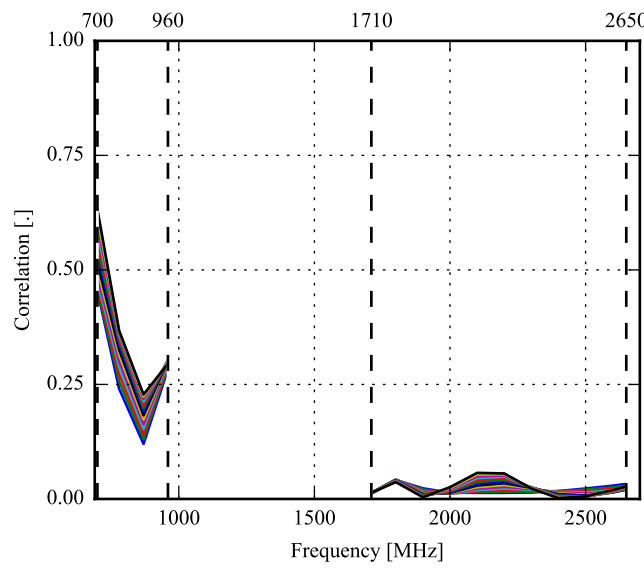
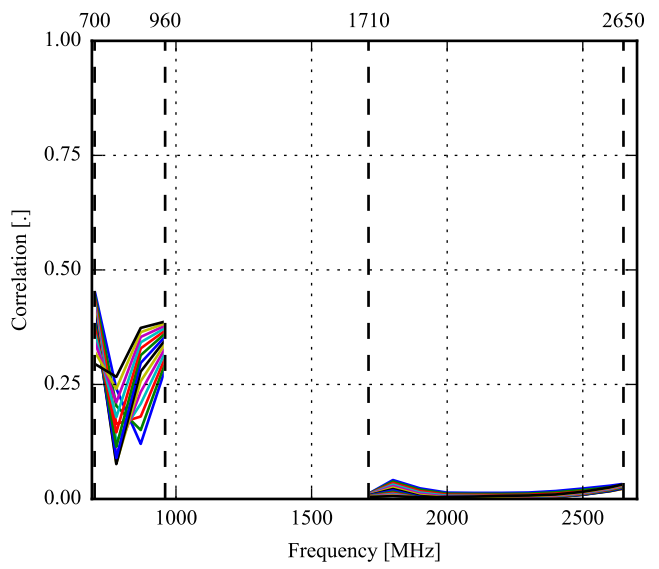
(a) Sweeping C_1 and fixing C_2 .(b) Sweeping C_2 and fixing C_1 .

Figure 5.19: Triangle-feed antenna in data mode. Correlation between antennas when sweeping the tuning capacitors. Here, C_1 and C_2 are the tuning capacitor for the top and side antenna, respectively.

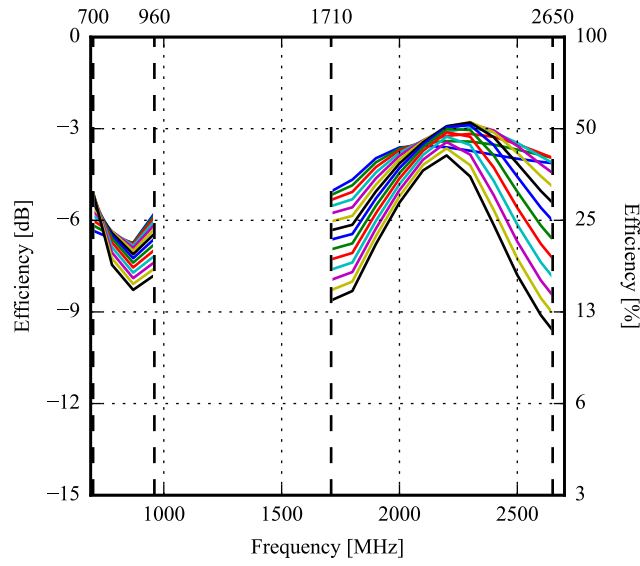
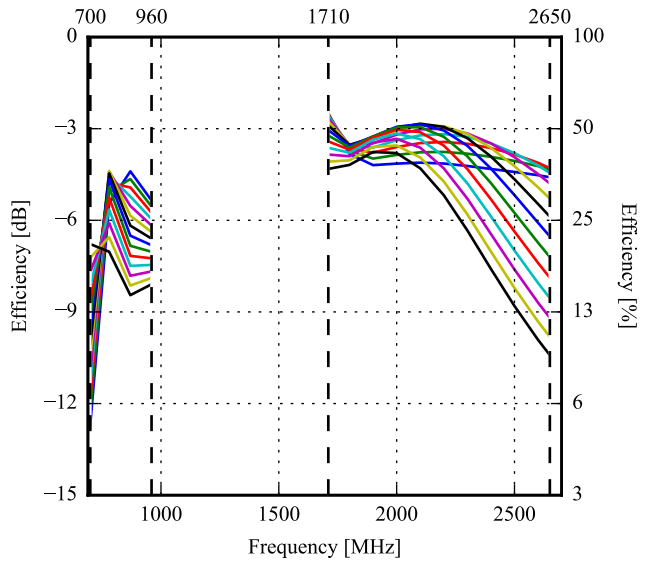
(a) Top antenna. Sweeping C_1 , fixing C_2 .(b) Side antenna. Sweeping C_2 , fixing C_1 .

Figure 5.20: Triangle-feed antenna in data mode. Efficiency for each antenna when sweeping the tuning capacitors. Here, C_1 and C_2 are the tuning capacitor for the top and side antenna, respectively.

5.2.2 Play Mode

The S-parameters, with the tunable capacitors set to their minima, are shown in Figure 5.21. Here, both the top and side antennas have been tuned down. As for data mode, the side antenna can only cover the lower half of the low band whereas the top antenna can cover the lower band at greater than 5 dB return loss.

The S-parameters, when sweeping the tunable capacitors, are shown in Figure 5.22. The maximum impedance-bandwidths are summed up in Table 5.6. It is seen, that both antennas almost cover the high band. The tunable bandwidth is still large enough to cover the LTE bands in the low band.

The correlation between the antennas, when sweeping the tunable capacitors, are shown in Figure 5.23. The correlation is similar to that of the data mode.

The efficiencies for each antenna, when sweeping the tuning capacitors, are shown in Figure 5.24. Compared to the data mode, the high band efficiency of the top antenna has decreased more than the low band efficiency. The side antenna is very similar to the data mode results.

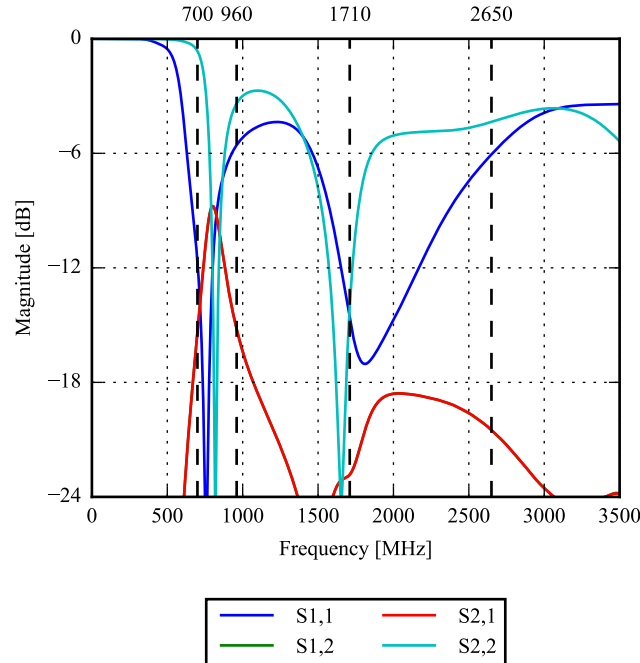


Figure 5.21: Triangle-feed antenna in play mode. S-parameters with both tuning capacitors fixed at 0.3 pF.

Antenna	Band	Start [MHz]	Stop [MHz]	Bandwidth [MHz]
Top	Low	629	928	299
Side	Low	780	881	101
Top	High	1379	2703	1324
Side	High	1388	2559	1171

Table 5.6: Triangle-feed antenna in play mode. Maximum bandwidth obtained in the low and high band for the top and the side antenna, respectively. The bandwidth for the side antennas high band is ignoring the slight rise above -6 dB in the middle of the high band.

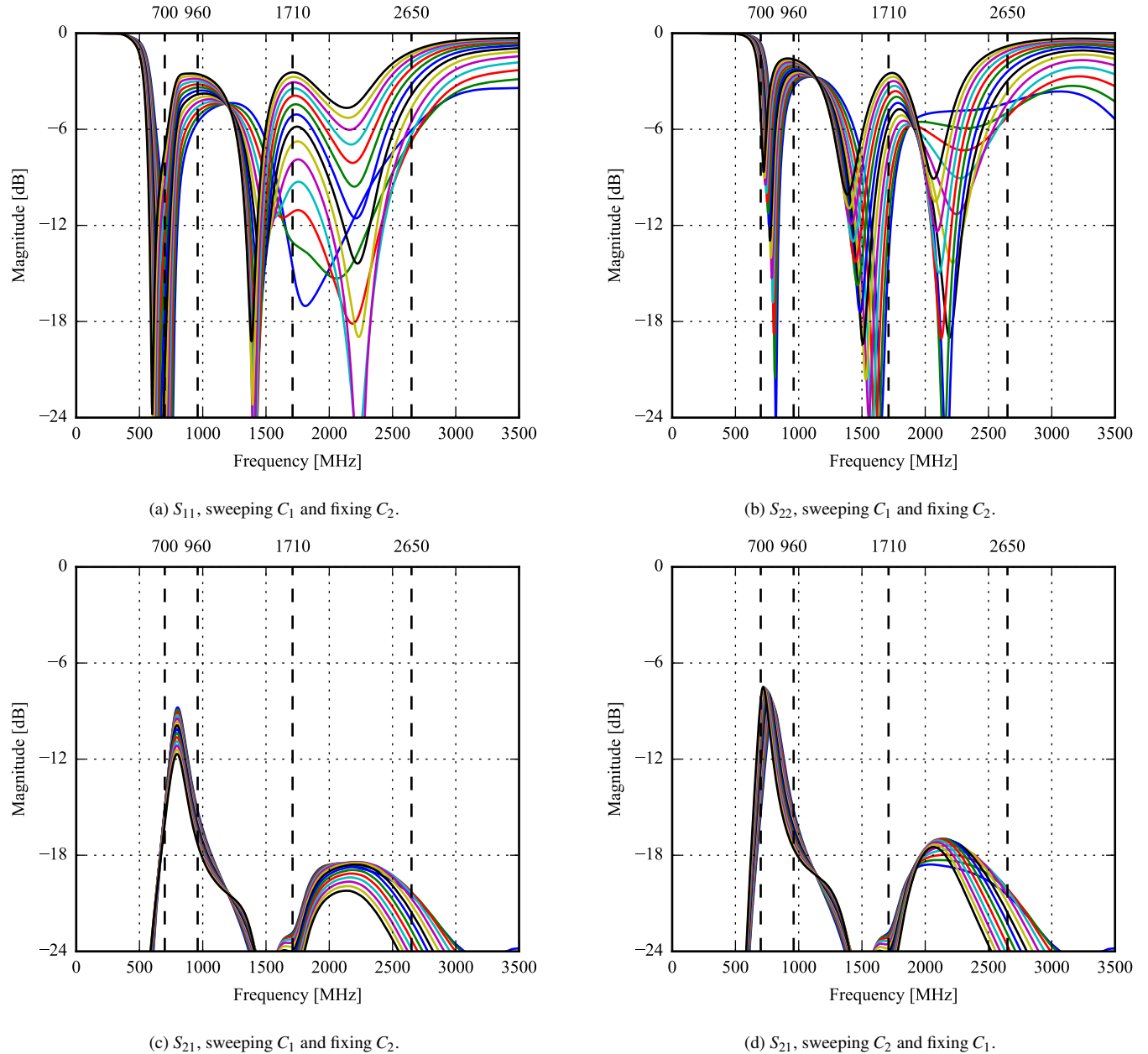


Figure 5.22: Triangle-feed antenna in play mode. Parameter sweep for tuning the shunt capacitor of each antenna, C_1 and C_2 for port 1 and 2, respectively. Port 1 is the top antenna and port 2 is the side antenna.

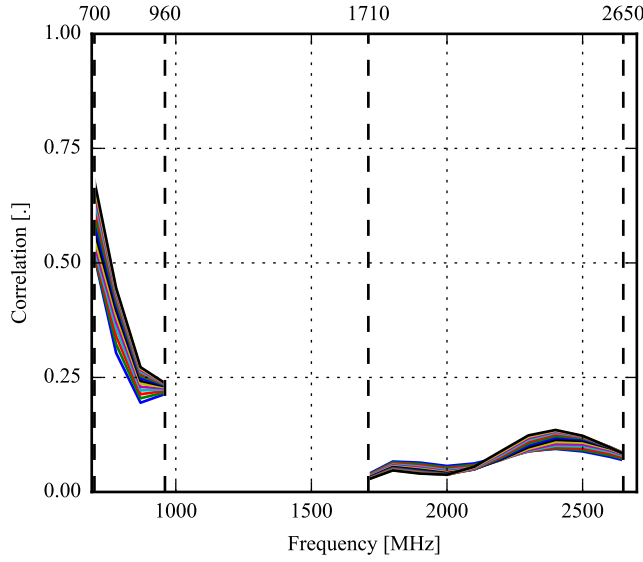
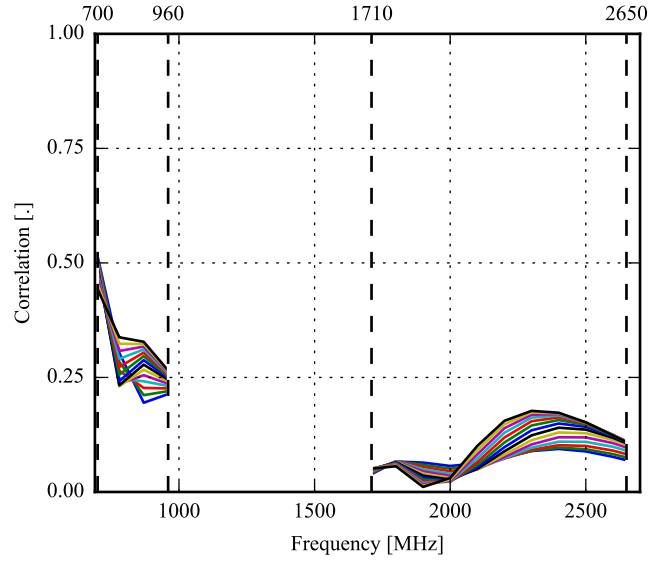
(a) Sweeping C_1 and fixing C_2 .(b) Sweeping C_2 and fixing C_1 .

Figure 5.23: Triangle-feed antenna in play mode. Correlation between antennas when sweeping the tuning capacitors. Here, C_1 and C_2 are the tuning capacitor for the top and side antenna, respectively.

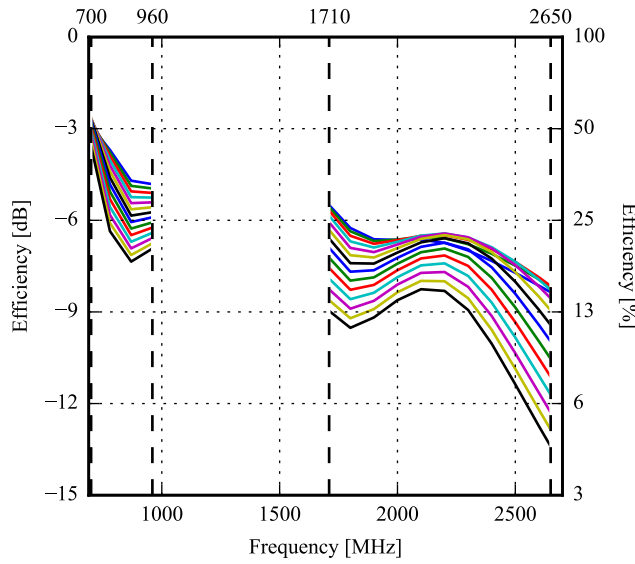
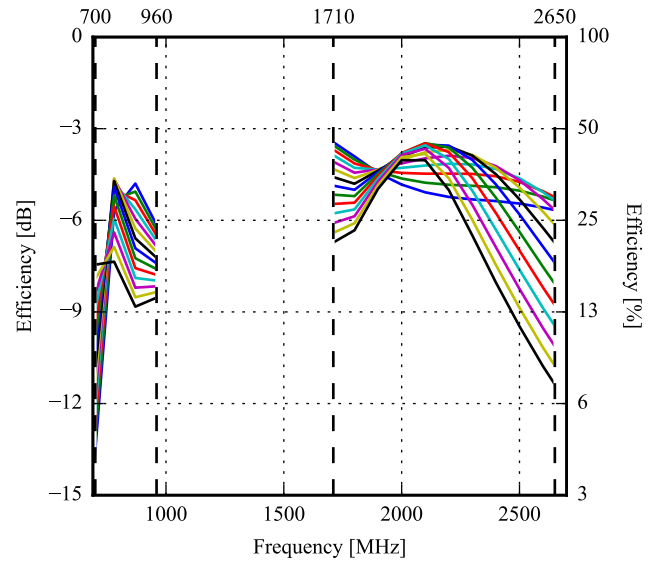
(a) Top antenna. Sweeping C_1 , fixing C_2 .(b) Side antenna. Sweeping C_2 , fixing C_1 .

Figure 5.24: Triangle-feed antenna in play mode. Efficiency for each antenna when sweeping the tuning capacitors. Here, C_1 and C_2 are the tuning capacitor for the top and side antenna, respectively.

5.2.3 Talk Mode

The S-parameters, with the tunable capacitors set to their minima, are shown in Figure 5.25. The top antenna is still able to cover both the low and the high band. The side antenna's resonance, however, has been shifted down even further than in data and play mode and now only covers the very lowest part of the low band.

The S-parameters, when sweeping the tunable capacitors, are shown in Figure 5.26. The maximum impedance-bandwidths are summed up in Table 5.7. The tunable bandwidths are still large enough to cover the low band LTE bands but the side antenna can not cover the bands up towards 960 MHz. The high band can still be covered quite well by both antennas.

The correlation between the antennas, when sweeping the tunable capacitors, are shown in Figure 5.27. The correlation is very low between the antennas for every capacitor setting.

The efficiencies for each antenna, when sweeping the tuning capacitors, are shown in Figure 5.28. In this mode, the efficiency drops very significantly. For the top antenna, the best efficiency is in the high band, peaking at around -6 dB. The low band efficiency of the top antenna peaks at around -9 dB. The side antenna performs even worse, peaking at around -8 dB in the high band and at -12 dB in the low band. Based on this, the phone would not be very usable in talk mode. As for the SAR results, described below, the results may change when a more realistic case and screen is added to the simulation, as this might lower the influence of the users head.

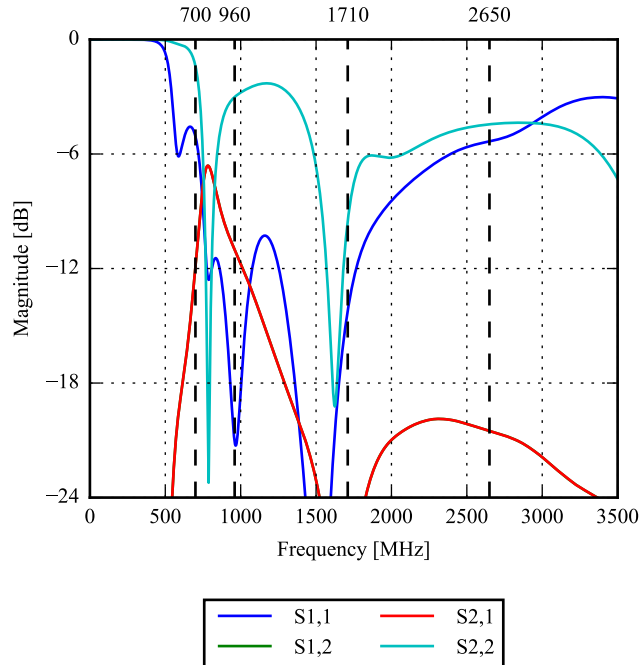


Figure 5.25: Triangle-feed antenna in talk mode. S-parameters with both tuning capacitors fixed at 0.3 pF.

Antenna	Band	Start [MHz]	Stop [MHz]	Bandwidth [MHz]
Top	Low	701	2597	1896
Side	Low	749	844	95
Top	High	701	2597	1896
Side	High	1439	2516	1077

Table 5.7: Triangle-feed antenna in talk mode. Maximum bandwidth obtained in the low and high band for the top and the side antenna, respectively. It is, again, seen that both the low and high band are covered at the same time for the top antenna.

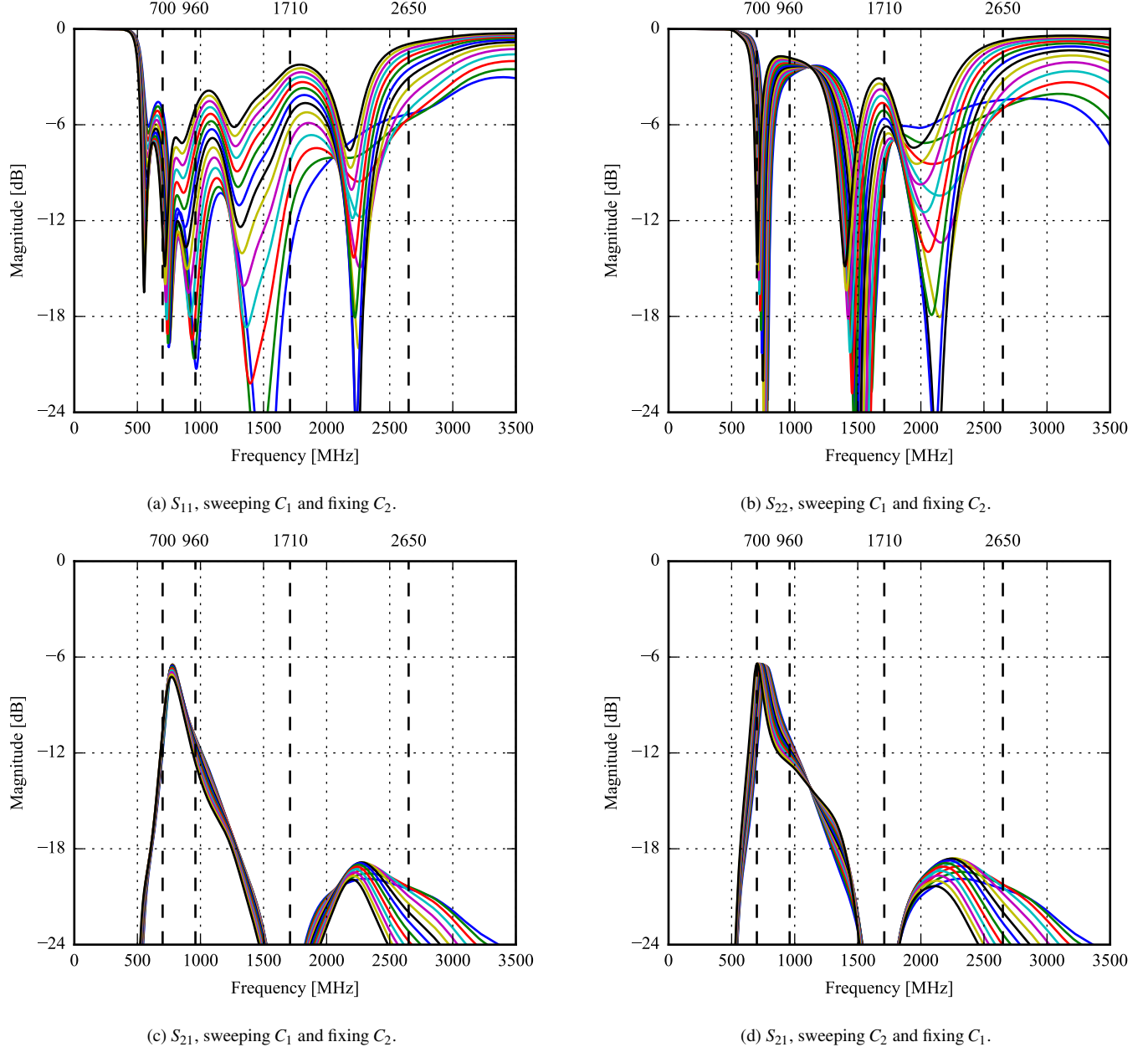


Figure 5.26: Triangle-feed antenna in talk mode. Parameter sweep for tuning the shunt capacitor of each antenna, C_1 and C_2 for port 1 and 2, respectively. Port 1 is the top antenna and port 2 is the side antenna.

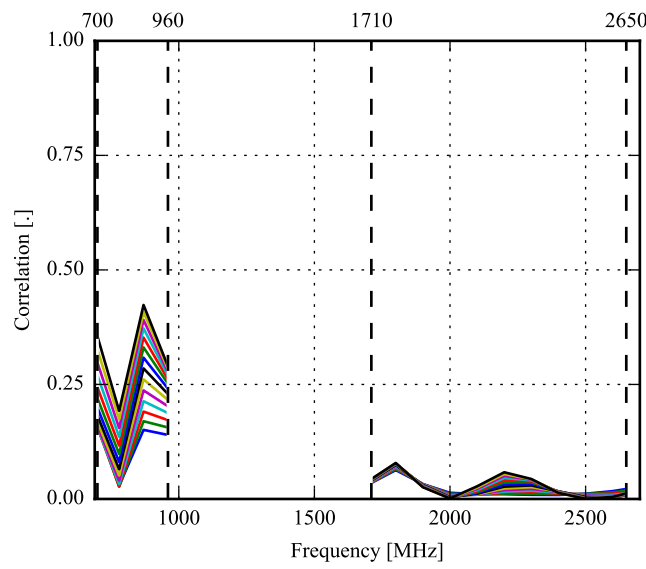
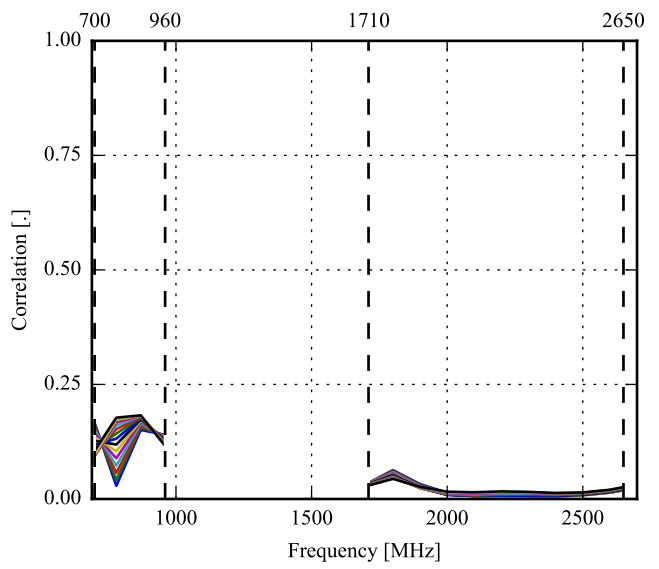
(a) Sweeping C_1 and fixing C_2 .(b) Sweeping C_2 and fixing C_1 .

Figure 5.27: Triangle-feed antenna in talk mode. Correlation between antennas when sweeping the tuning capacitors. Here, C_1 and C_2 are the tuning capacitor for the top and side antenna, respectively.

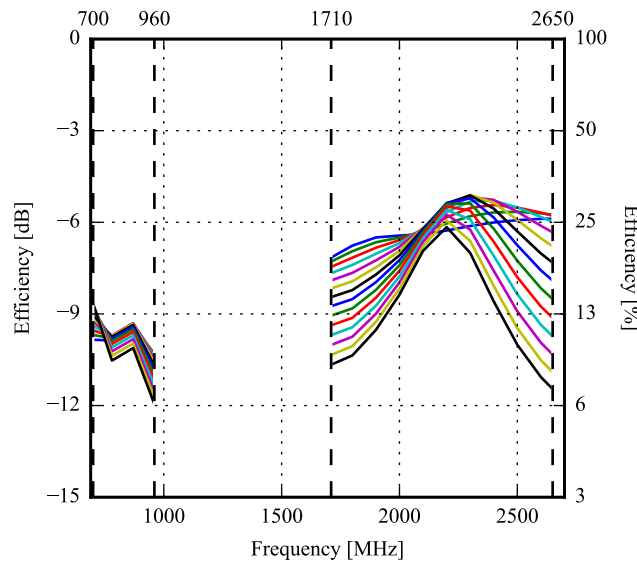
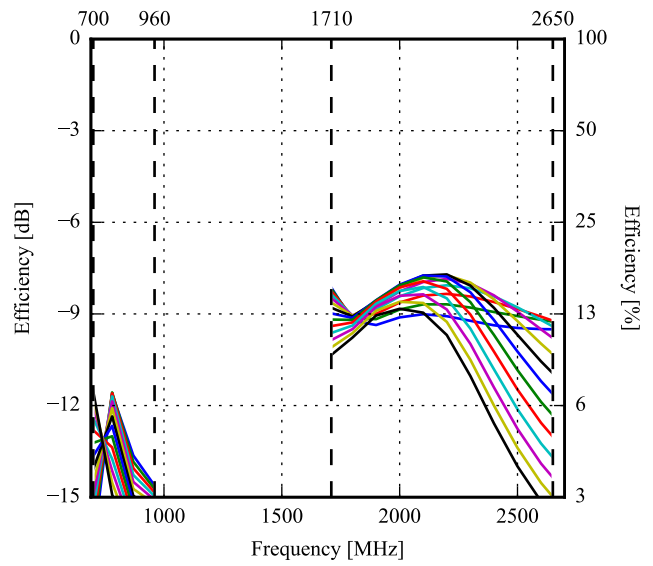
(a) Top antenna. Sweeping C_1 , fixing C_2 .(b) Side antenna. Sweeping C_2 , fixing C_1 .

Figure 5.28: Triangle-feed antenna in talk mode. Efficiency for each antenna when sweeping the tuning capacitors. Here, C_1 and C_2 are the tuning capacitor for the top and side antenna, respectively.

5.2.4 SAR

The result from the SAR simulation is shown in Figure 5.29. It is seen, that the maximum SAR is much lower than the required maximum of 2 W/kg for both antennas. Both antennas fulfill the requirement with a max SAR value of 0.8 W/kg at 2600 MHz and 1.3 W/kg at 2000 MHz for the top and side antenna respectively. Both in the low band and high band, the overall SAR value is quite low, with a few peaks in the high band.

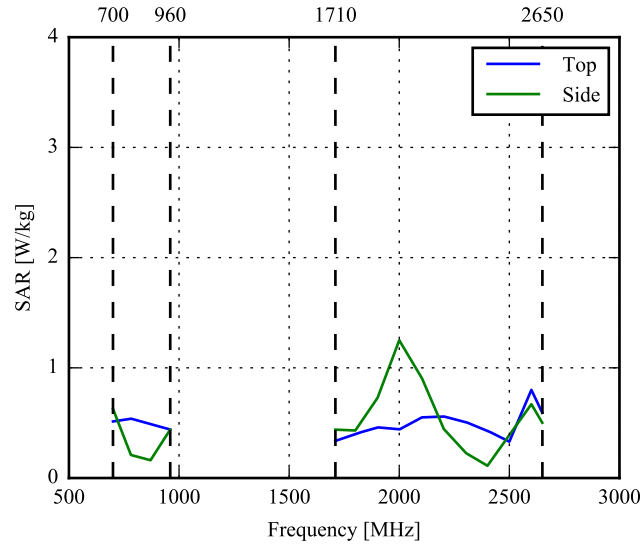


Figure 5.29: SAR simulation of the triangle-feed antenna.

5.3 Dual-Feed Antenna

In this section, the results from Section 4.3 will be repeated, having the phone in data mode, play mode, and talk mode. Furthermore, the maximum SAR value, recorded in the users head, will be simulated. The antenna positions, for each use case, are shown in Figure 5.30.

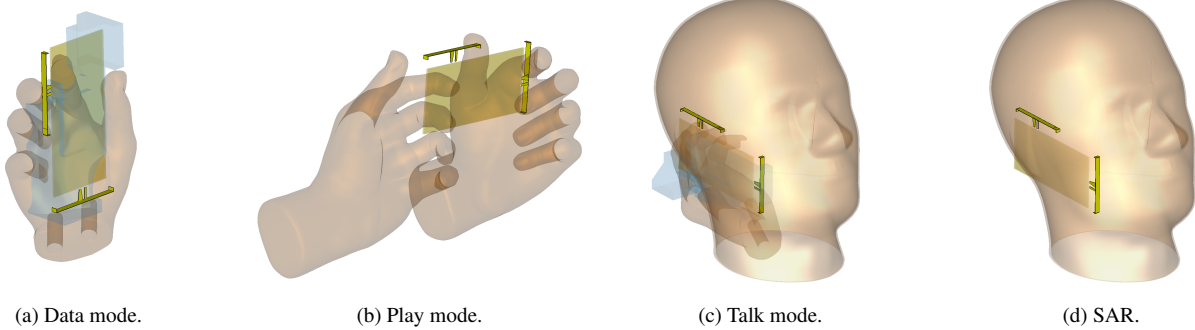


Figure 5.30: Antenna position for each user effect simulation.

5.3.1 Data Mode

Figure 5.31 shows the S-parameters with the tunable capacitors set to their maxima. As such, both the top and side antennas have been tuned down to the lowest possible frequency. It is seen that the top antenna covers most of the band from 700 MHz to 960 MHz with a return loss above 6 dB. The side antenna is, however, very narrowband and must be tuned in order to cover all the low bands. It is also seen that the side antenna does not cover the entire high band when tuned down to the lowest capacitor value.

The S-parameters, when sweeping the tunable capacitors, are shown in Figure 5.32. The maximum impedance-bandwidths are summed up in Table 5.8. From this, it is again clear that only the top antenna is able to cover the high end of the low band. Both antennas are able to cover the entire high band at 6 dB return loss, except for a drop of 1 dB at 2600 MHz to 2650 MHz for the top antenna.

The correlation between the antennas, when sweeping the tunable capacitors, are shown in Figure 5.33. The correlation is, for frequencies above 700 MHz, below 0.4 when sweeping the top and side antenna. For the high band, the correlation is significantly lower, which is also to be expected. The correlation has dropped a lot from the free-space simulation in Figure 4.17.

The efficiencies for each antenna, when sweeping the tuning capacitors, are shown in Figure 5.34. It is seen that the efficiency, generally, has decreased from the free-space simulation in Chapter 4. At -3 dB efficiency, there is no bandwidth left. At -6 dB all bands are covered. The efficiency in the high band is generally higher than in the low band.

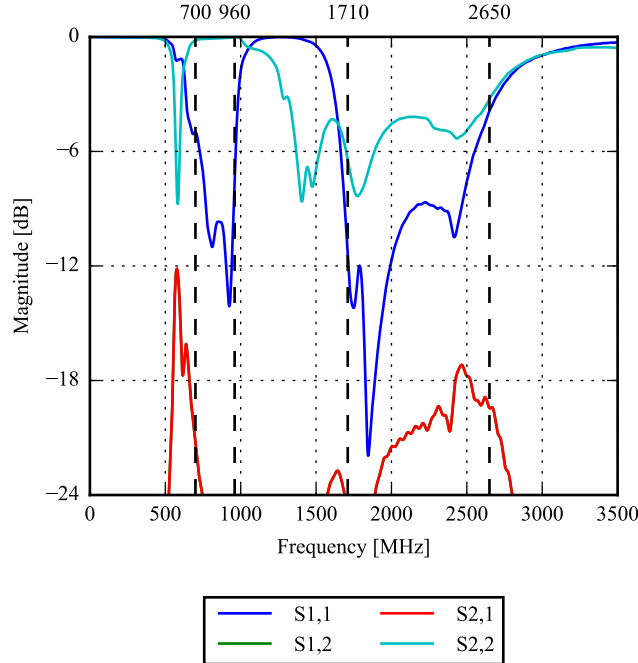


Figure 5.31: The antenna in data mode. S-parameters with both tuning capacitors fixed at 2.9 pF.

Antenna	Band	Start [MHz]	Stop [MHz]	Bandwidth [MHz]
Top	Low	713	963	250
Side	Low	717	765	48
Top	High	1635	2537	902
Side	High	1430	2582	1152

Table 5.8: The antenna in data mode. Maximum bandwidth obtained in the low and high band for the top and the side antenna, respectively.

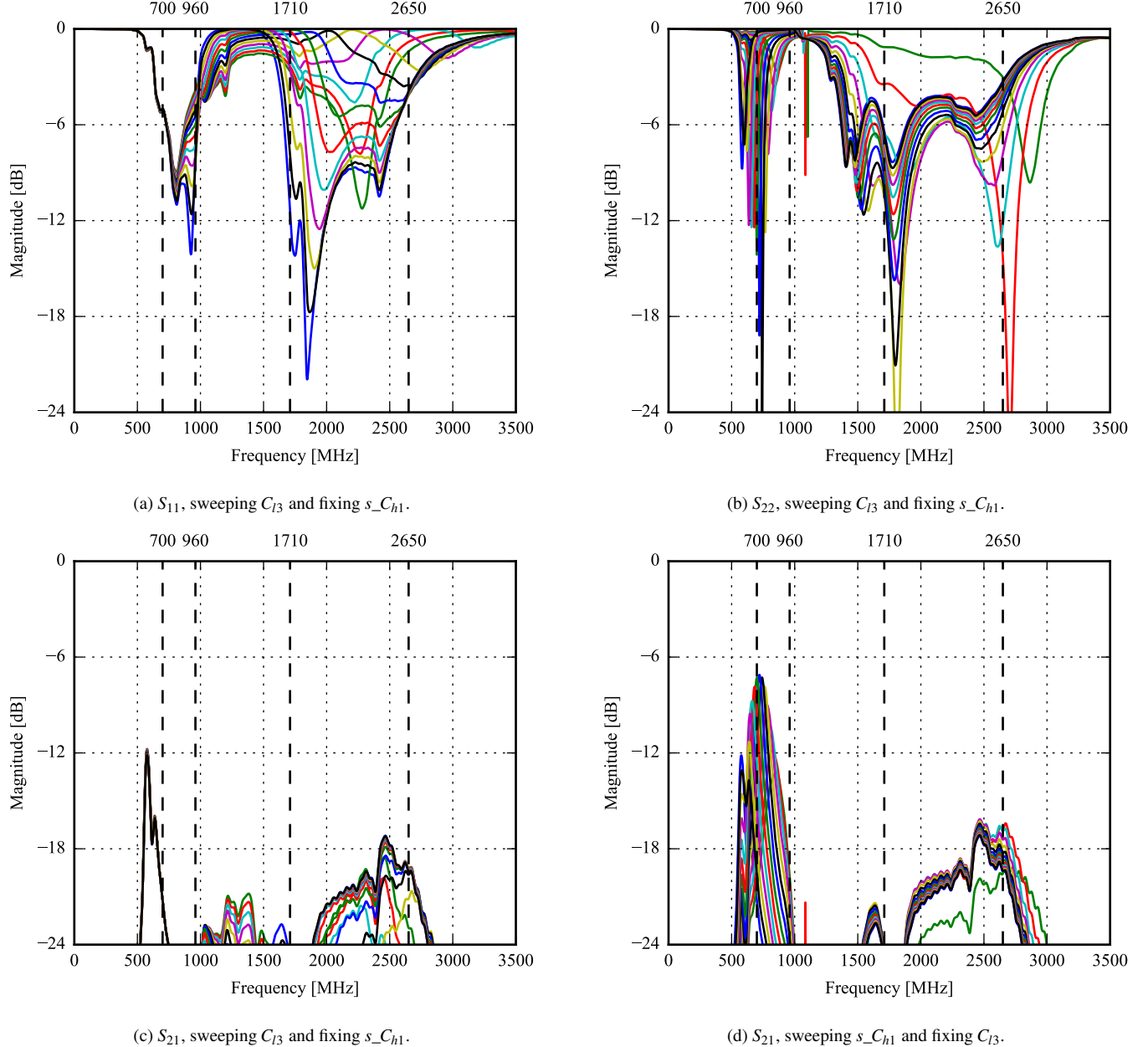


Figure 5.32: The antenna in data mode. S-parameter sweep for tuning the shunt capacitor of each antenna, C_{l3} and s_C_{h1} for port 1 and 2, respectively. Port 1 is the top antenna and port 2 is the side antenna.

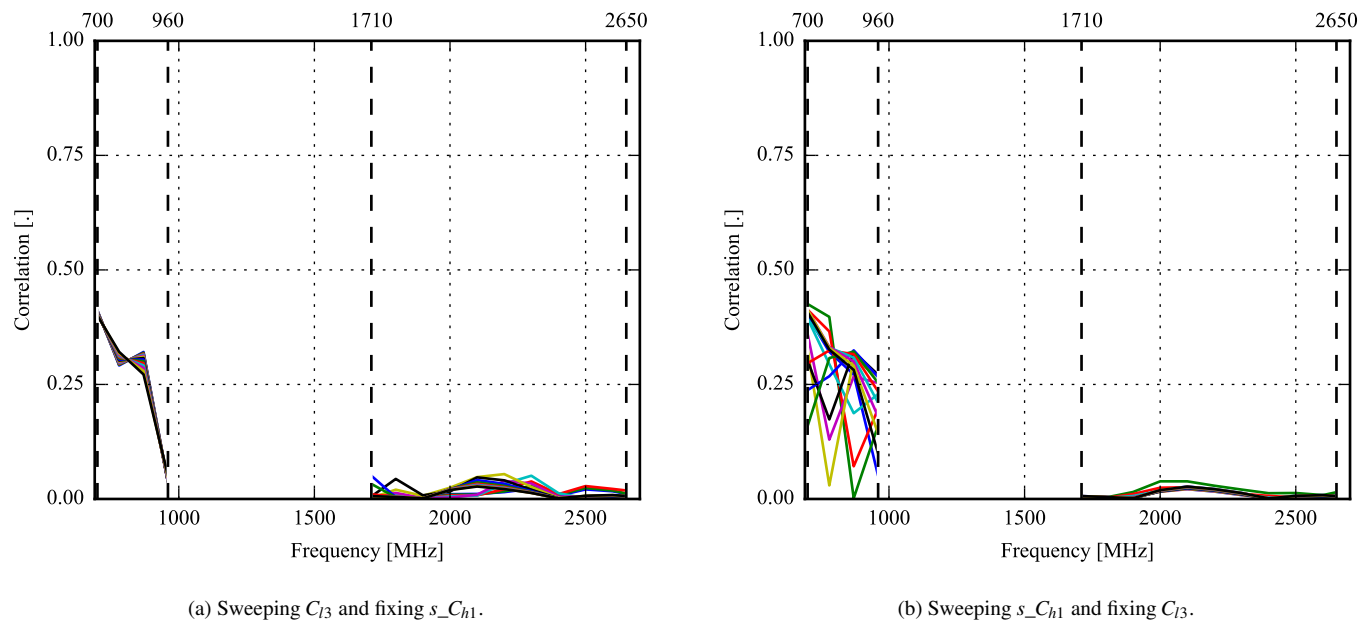


Figure 5.33: The antenna in data mode. Correlation between antennas when sweeping the tuning capacitors. Here, C_{l3} and s_C_{h1} are the tuning capacitor for the top and side antenna, respectively.

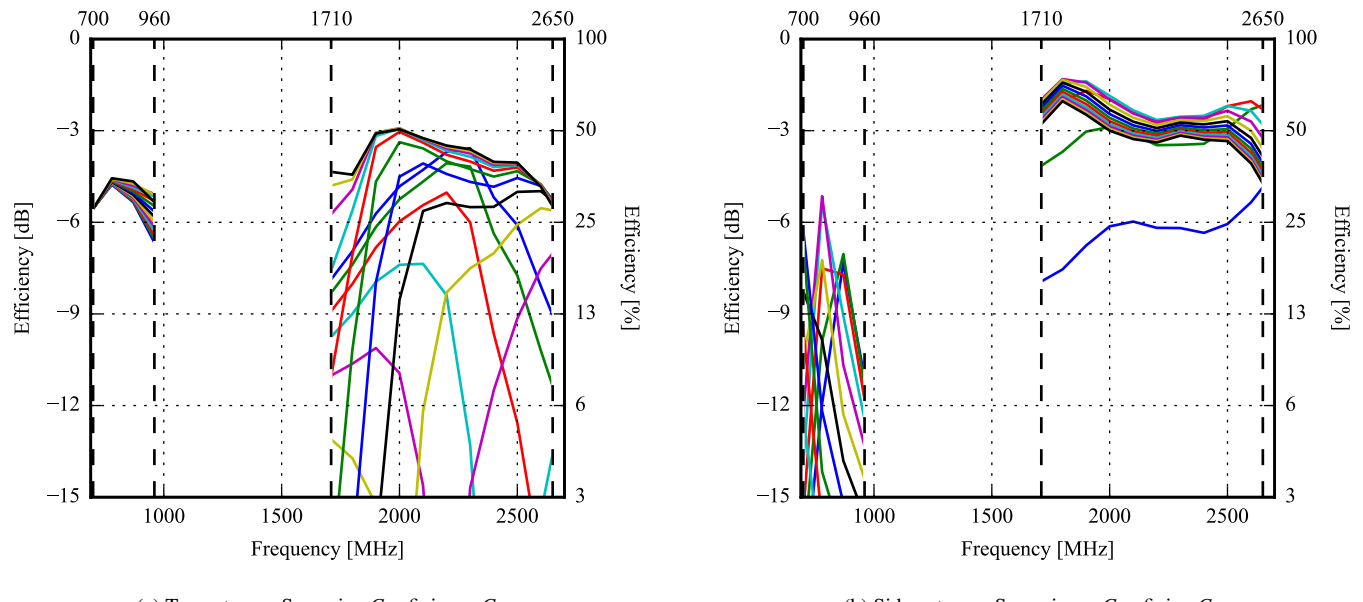


Figure 5.34: The antenna in data mode. Efficiency for each antenna when sweeping the tuning capacitors. Here, C_{l3} and s_C_{h1} are the tuning capacitor for the top and side antenna, respectively.

5.3.2 Play Mode

Figure 5.35 shows the S -parameters with the tunable capacitors set to their maxima. As such, both the top and side antennas have been tuned down to the lowest possible frequency. It is seen that the top antenna covers most of the band from 700 MHz to 960 MHz with a return loss above 4 dB. The side antenna is, however, very narrowband, and must be tuned in order to cover all the low bands. It is also seen that the side antenna does not cover the entire high band when tuned down to the lowest.

The S -parameters, when sweeping the tunable capacitors, are shown in Figure 5.36. The maximum impedance bandwidths are summed up in Table 5.8. From this, it is again clear that only the top antenna is able to cover the high end of the low band. Both antennas are able to cover the entire high band at 4 dB return loss.

The correlation between the antennas, when sweeping the tunable capacitors, are shown in Figure 5.37. The correlation is, for frequencies above 700 MHz, below 0.4 when sweeping the top and side antenna. For the high band, the correlation is significantly lower. Again, the correlation has dropped a lot from the free-space simulation in Figure 4.17.

The efficiencies for each antenna, when sweeping the tuning capacitors, are shown in Figure 5.38. It is seen that the efficiency, generally, has decreased from the free-space simulation in Chapter 4 and is also lower than the data mode. At -3 dB efficiency, there is no bandwidth left. At -6 dB most of the bands are covered.

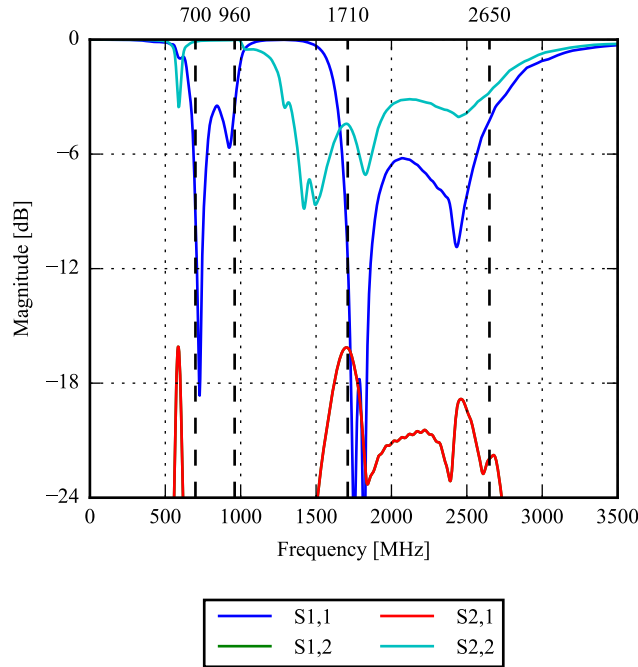


Figure 5.35: The antenna in play mode. S -parameters with both tuning capacitors fixed at 2.9 pF.

Antenna	Band	Start [MHz]	Stop [MHz]	Bandwidth [MHz]
Top	Low	690	791	101
Side	Low	780	803	23
Top	High	1676	2579	903
Side	High	1341	1919	578

Table 5.9: The antenna in play mode. Maximum bandwidth obtained in the low and high band for the top and the side antenna, respectively. The bandwidth for the antennas high band is ignoring the rise above -6 dB in the middle of the band.

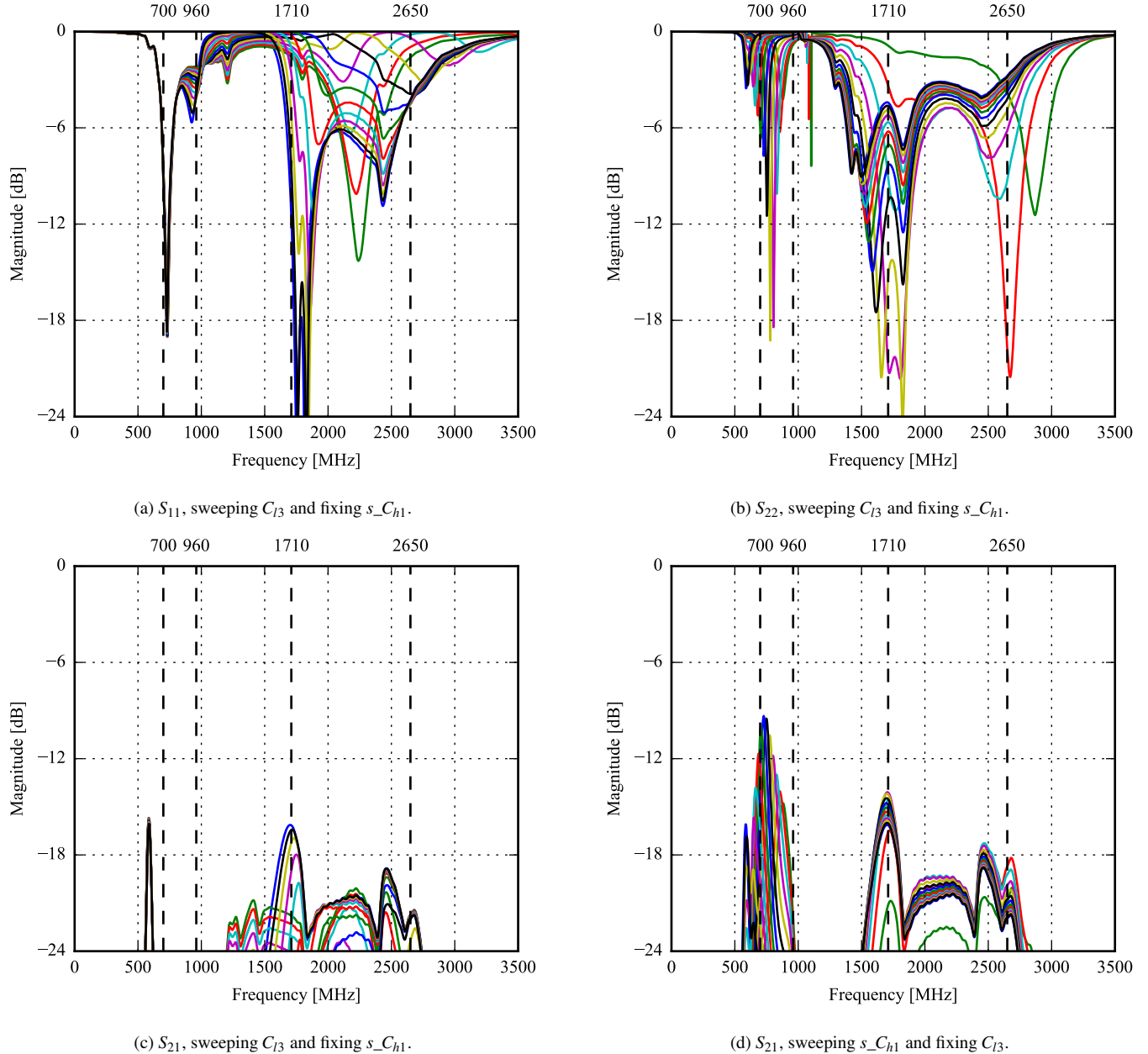


Figure 5.36: The antenna in play mode. Parameter sweep for tuning the shunt capacitor of each antenna, C_{l3} and s_C_{h1} for port 1 and 2, respectively. Port 1 is the top antenna and port 2 is the side antenna.

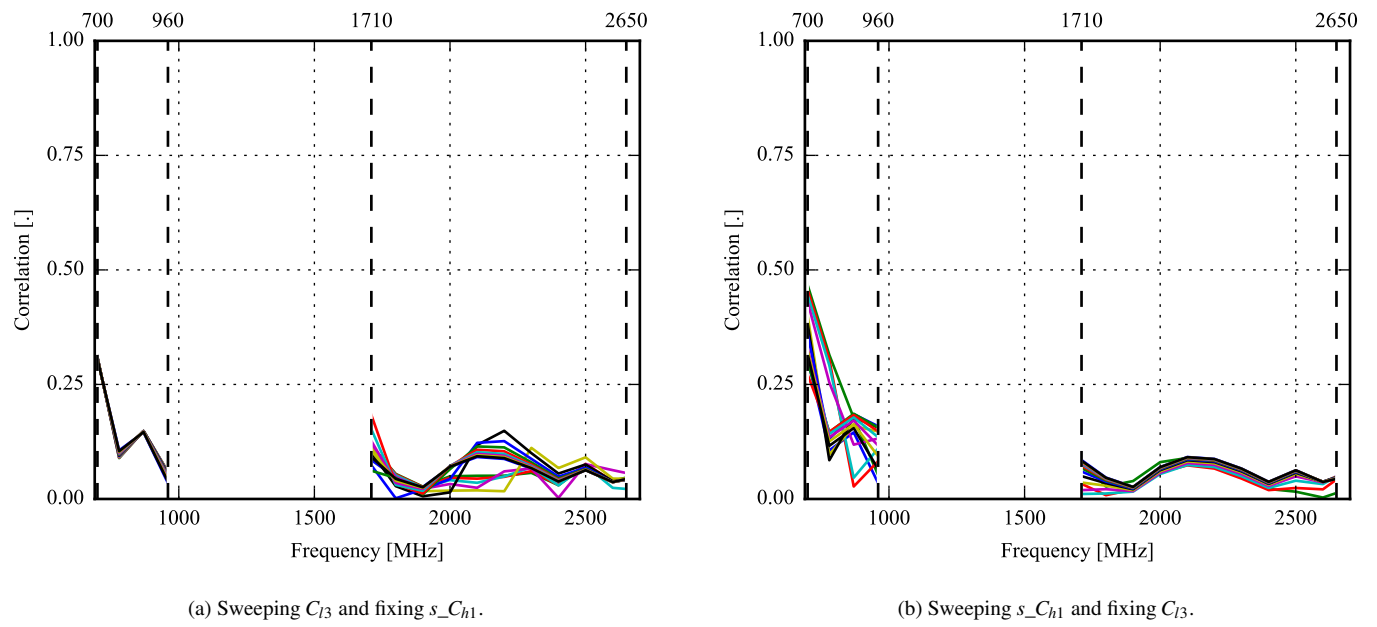


Figure 5.37: The antenna in play mode. Correlation between antennas when sweeping tuning the capacitors. Here, C_{l3} and s_C_{h1} are the tuning capacitor for the top and side antenna, respectively.

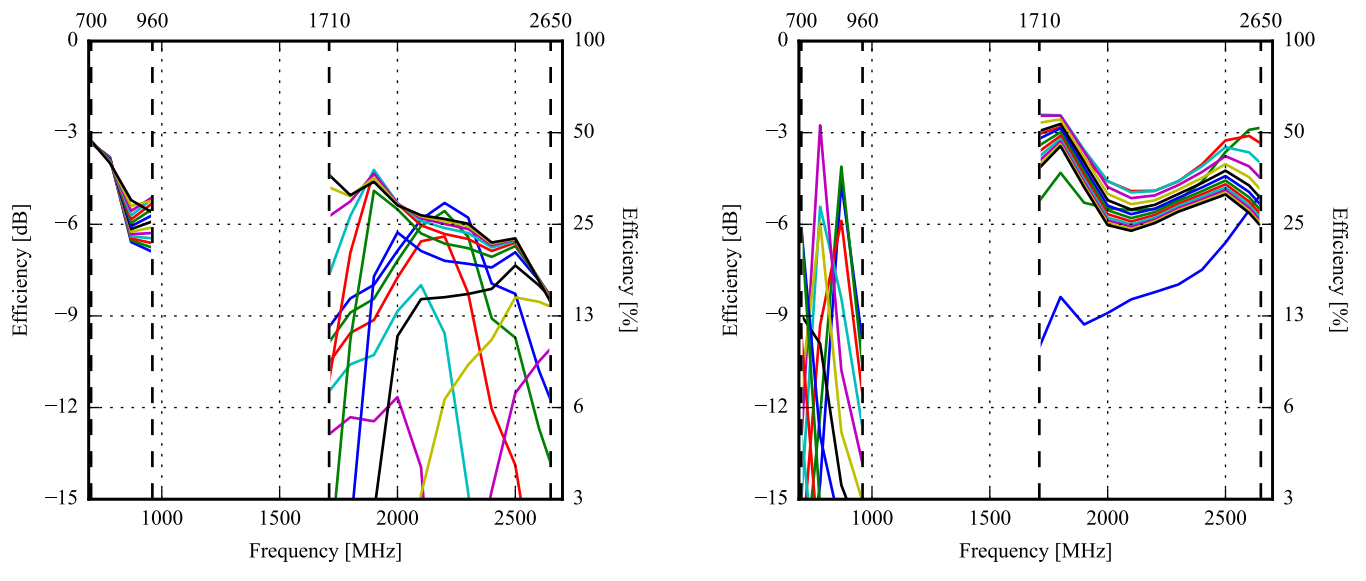


Figure 5.38: The antenna in play mode. Efficiency for each antenna when sweeping the tuning capacitors. Here, C_{l3} and s_C_{h1} are the tuning capacitor for the top and side antenna, respectively.

5.3.3 Talk Mode

Figure 5.39 shows the S -parameters with the tunable capacitors set to their maxima. As such, both the top and side antennas have been tuned down to the lowest possible frequency. It is seen that the top antenna covers most of the band from 700 MHz to 960 MHz, with a return loss above 6 dB. The side antenna is, however, very narrowband, and must be tuned in order to cover all the low bands. It is also seen that the side antenna does not cover the entire high band when tuned down to the lowest.

The S -parameters, when sweeping the tunable capacitors, are shown in Figure 5.36. The maximum impedance-bandwidths are summed up in Table 5.8. From this it is again clear that only the top antenna is able to cover the high end of the low band. Both antennas are able to cover the entire high band at 6 dB return loss, except for a small drop of 1 dB from 2600 MHz to 2650 MHz.

The correlation between the antennas, when sweeping the tunable capacitors, are shown in Figure 5.37. The correlation is, for frequencies above 700 MHz, below 0.7 when sweeping the top and side antenna. For the high band, the correlation is significantly lower. Again, the correlation has dropped a lot from the free-space simulation in Figure 4.17.

The efficiencies for each antenna, when sweeping the tuning capacitors, are shown in Figure 5.42. It is seen that the efficiency, generally, has decreased from the free-space simulation in Chapter 4 and is also lower than the data mode. At -3 dB efficiency, there is no bandwidth left. At -9 dB most of the bands are covered.

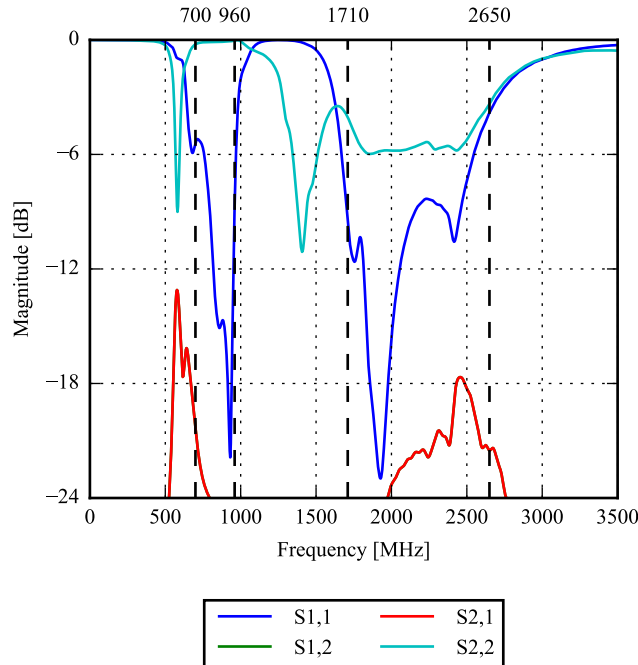


Figure 5.39: The antenna in talk mode. S -parameters with both tuning capacitors fixed at 2.9 pF.

Antenna	Band	Start [MHz]	Stop [MHz]	Bandwidth [MHz]
Top	Low	674	1055	381
Side	Low	576	617	41
Top	High	1658	2243	585
Side	High	1612	2784	1172

Table 5.10: The antenna in talk mode. Maximum bandwidth obtained in the low and high band for the top and the side antenna, respectively. It is, again, seen that both the low and high band are covered at the same time for the top antenna.

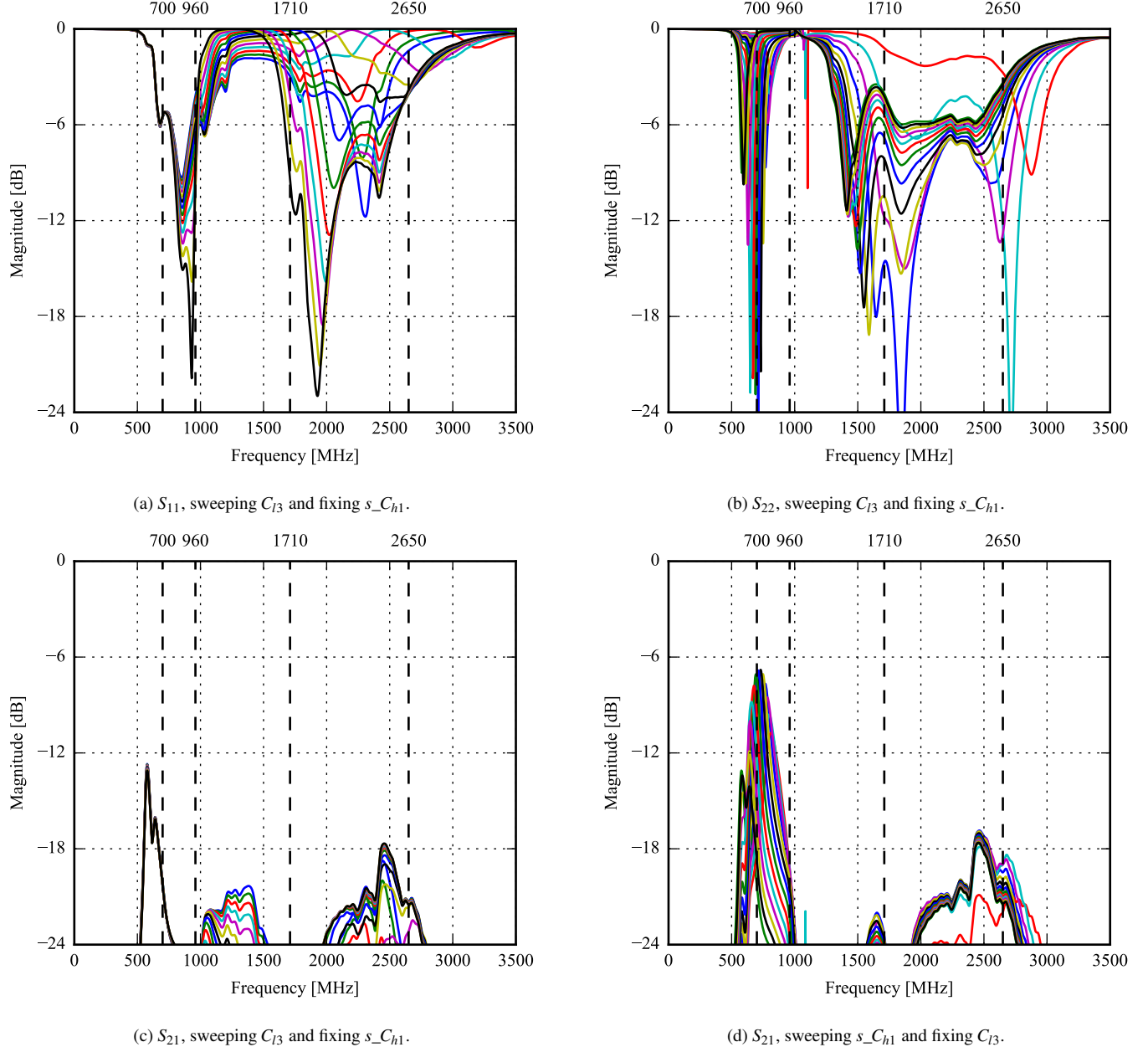


Figure 5.40: The antenna in talk mode. Parameter sweep for tuning the shunt capacitor of each antenna, C_{L3} and s_C_{h1} for port 1 and 2, respectively. Port 1 is the top antenna and port 2 is the side antenna.

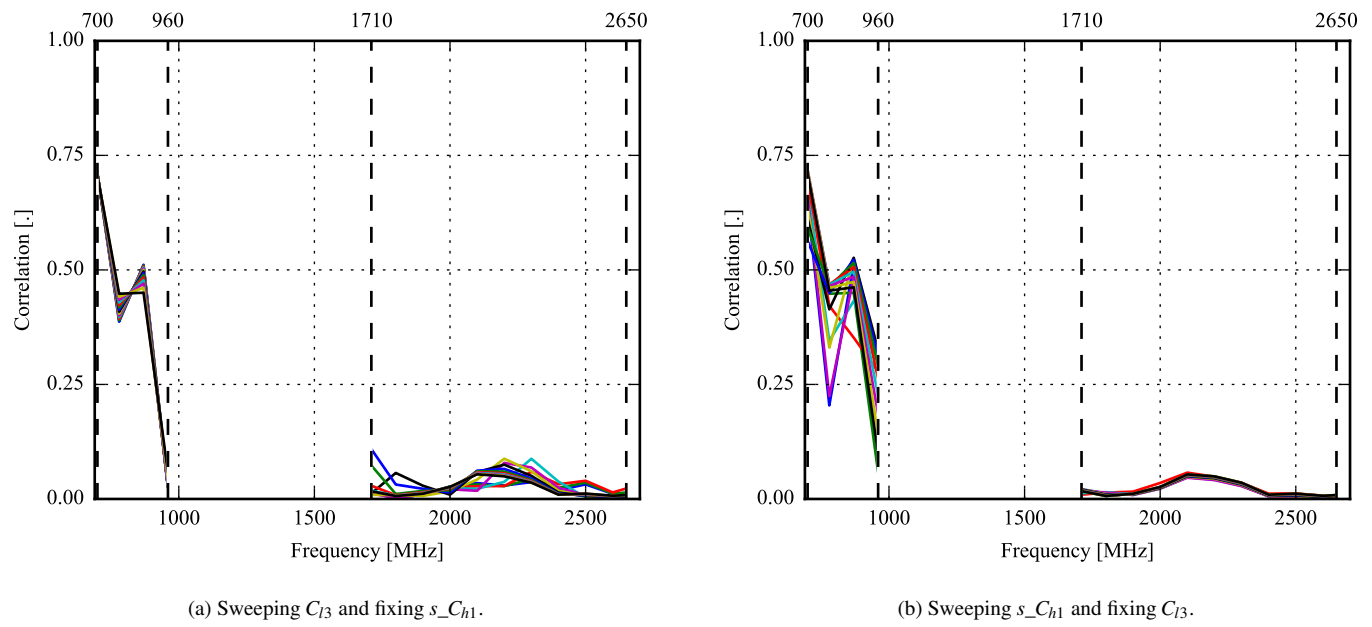


Figure 5.41: The antenna in talk mode. Correlation between antennas when sweeping the tuning capacitors. Here, C_{l3} and s_C_{h1} are the tuning capacitor for the top and side antenna, respectively.

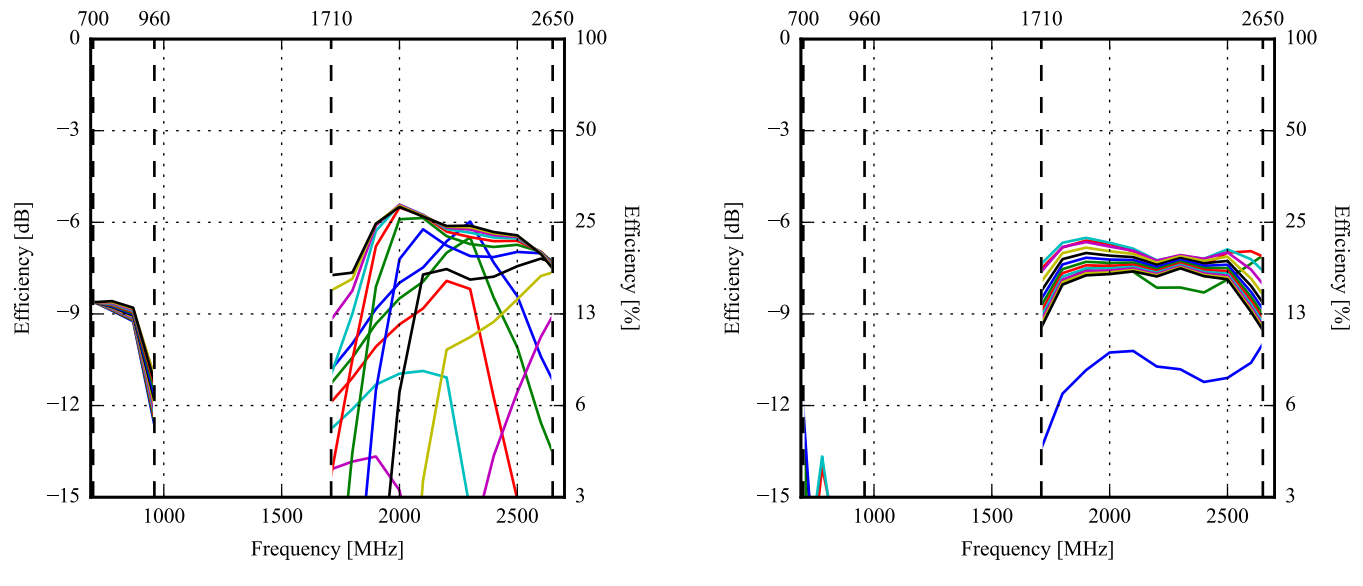


Figure 5.42: The antenna in talk mode. Efficiency for each antenna when sweeping the tuning capacitors. Here, C_{l3} and s_C_{h1} are the tuning capacitor for the top and side antenna, respectively.

5.3.4 SAR

The result from the SAR simulation is shown in Figure 5.43. It is seen, that the maximum SAR value is around 1.2 W/kg, which is within the maximum of 2 W/kg for the side antenna. A possible way to improve this may be to simulate the phone with a screen, which will be located between the antenna and the head. This may reflect some of the radiated power away from the user, lowering the maximum SAR. However, since it already complies with the requirements, this has not been done.

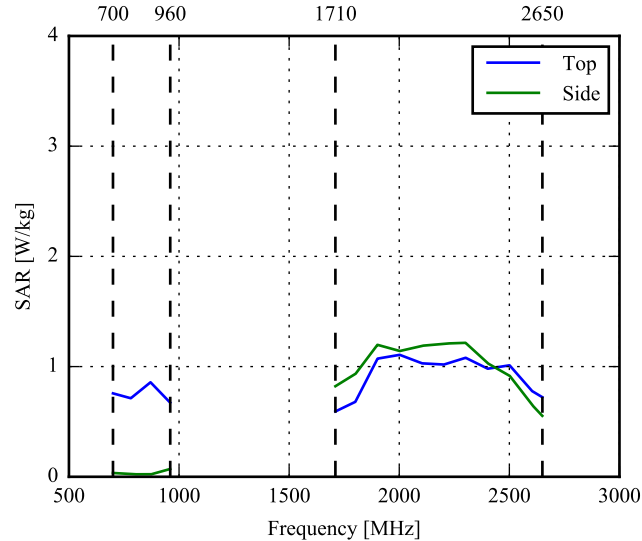


Figure 5.43: SAR simulation of the antenna.

5.4 Conclusion

The three preliminary designs have now been simulated in use cases where a user is present. All three designs appear to meet the requirements for SAR.

It is very clear from the simulations that the user has the effect of detuning the resonances of all antennas. The talk mode had the most severe effect on the antennas where the data and play modes were slightly more subtle.

The peak efficiencies are summarized in Table 5.11. Overall, the largest impact seems to be on the folded monopole antenna – especially in the low band. Both the triangle-feed antenna and the dual-feed design seem to hold up quite a bit better in data mode and play mode.

Design	Data mode		Play mode		Talk mode	
	L	H	L	H	L	H
Monopole top	-5.5	-2.5	-7.0	-4.5	-11.0	-8.0
Monopole side	-9.5	-1.5	-13.0	-4.0	-11.0	-6.0
Triangle-feed top	-5.0	-3.0	-3.0	-7.0	-8.5	-5.0
Triangle-feed side	-4.5	-3.0	-4.5	-3.5	-11.5	-7.5
Dual-feed top	-4.5	-3.0	-3.0	-4.5	-8.5	-5.5
Dual-feed side	-5.0	-1.5	-3.0	-2.5	-12.0	-6.5

Table 5.11: Peak efficiency (dB) in the low (L) and high (H) band for the three preliminary designs in different use cases (rounded to 0.5 dB).

Now all simulations of the preliminary designs have been finished. The simulations have been simplified compared to how the antennas would be built in real life (no transmission lines, no component losses, no component placement). In order to really verify the designs, the next step is therefore to prototype the designs on a PCB with discrete components.

Chapter 6

Prototypes

As the preliminary simulations have been finished, the next step is to show the real-life performance of the three antenna designs. The goal is to see, first of all, how the antennas perform with respect to efficiency and return loss but also to see how stable the designs are as the real-life components are very different than the ideal components used in the simulations.

A prototype of each of the three designs have been built and the results are documented in this chapter. The prototypes each consist of a single-sided ground plane with the matching networks located as close to the antenna feeds as possible. Both the matching components and the tuning capacitors are implemented with 0402 and 0603 surface mount components to take up as little space on the board as possible while still being hand-solderable. The tuning is performed by simply replacing the tuning capacitor for each measurement.

The following values are used for the tuning capacitor sweep:

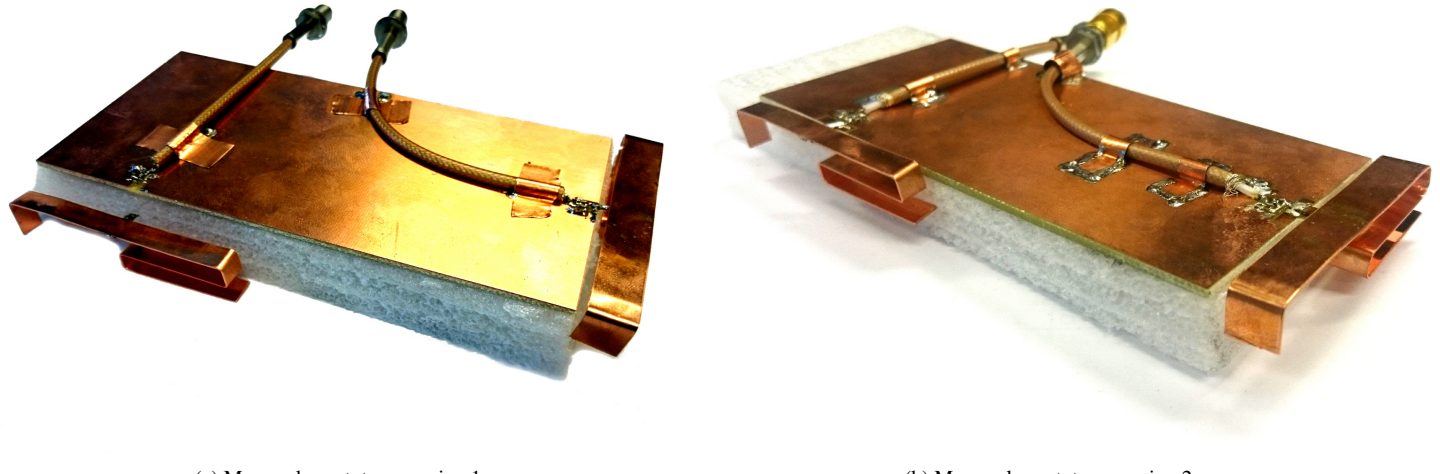
- 0.3 pF.
- 0.7 pF.
- 1.1 pF.
- 1.5 pF.
- 2.0 pF.
- 2.7 pF.
- 3.0 pF.

The antenna, which is not being swept, is terminated with a 0.3 pF tuning capacitor like in the simulations in Chapter 4 and 5.

6.1 Monopole Antenna

The first monopole prototype can be seen in Figure 6.1a. As seen on the figure, both monopole antennas were very fragile. The feed pads were too small and fragile, which caused them to break off, also as seen on the figure.

To solve the feed pad problem, a new prototype was made with $10\text{ mm} \times 2.5\text{ mm}$ feed pads. The pad size was chosen to match the final tuner PCB for the project, which can be seen in Figure 8.1. Furthermore, a FR-4 support was added under the antenna feeds to make it more robust. The new prototype can be seen in Figure 6.1b.



(a) Monopole prototype version 1.

(b) Monopole prototype version 2.

Figure 6.1: Monopole prototype comparison of version 1 and 2.

6.1.1 Simulation

The second prototype had some small changes of the feed pad and FR-4 support, as described above. As a result, the matching deviated a bit, compared to the first version matching simulations, which can be seen in Figure 4.4. To compensate for the design changes, the component values were changes accordingly. The new component values can be seen in Figure 6.2.



Figure 6.2: Matching circuit for the simulation prototype monopole antenna. These are the component values where the bandwidth is found to be the largest.

The S-parameter sweep for the new design can be seen in Figure 6.3. Compared to the S_{11} and S_{22} results, the spectrum coverage for the top antenna has been slightly improved. The improvement is significant in the high band, where the top antenna now covers from 1500 MHz to 3000 MHz, only with a small decrease of 1 dB around 2500 MHz. The side antenna also shows spectrum improvement in the high band, but lacks some coverage of approx 3 dB from 1710 MHz to 1800 MHz. Generally, the low band coverage for both antennas, compared to the first version, have decreased but still covers the band.

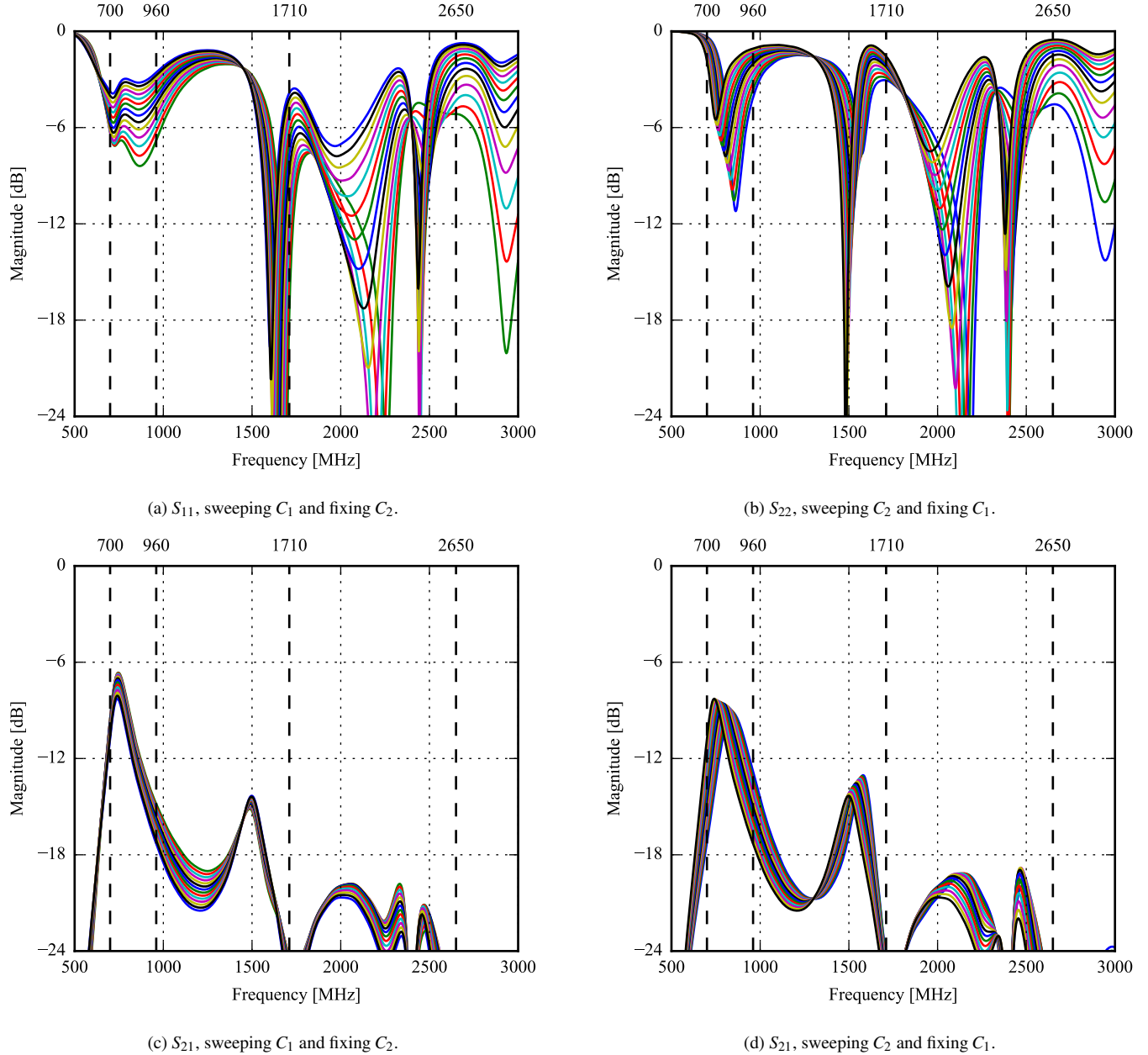


Figure 6.3: S -parameter sweep in free-space for tuning the shunt capacitor of each antenna, C_1 and C_2 for port 1 and 2, respectively. Port 1 is the top antenna and port 2 is the side antenna.

6.1.2 Measurements

A comparison between the simulated and measured S -parameters can be seen in Figure 6.5. The simulated and measured results are done with the tunable capacitor at 0.3 pF. Furthermore, some component values were changes, going from the simulation environment to the prototype. The prototype component values can be seen in Figure 6.4. Measuring the S -parameter and efficiency sweeps, it was found that the highest bandwidth was achieved with the tunable capacitor at 0.3 pF. The bandwidth results for the top and side antenna can be seen in Table 6.1. From the table it is seen, that both antennas cover the required bandwidth in the low band, but have some trouble in the high band.

The total efficiency, measured and simulated with the tunable capacitors at 0.3 pF, can be seen in Figure 6.5. Generally, the simulation results shows a higher efficiency, as expected. The lowest efficiencies are measured at 2400 MHz and from 700 MHz to 750 MHz with the lowest efficiency being -9 dB. Overall, the top antenna shows the best results although it still has some problems in the low band where the efficiency drops to -6 dB.

The S -parameter sweep for both antennas can be seen in Figure 6.3. The sweep is done accordingly to Chapter 6. From the



Figure 6.4: Matching circuit for the prototype monopole antenna. These are the component values where the bandwidth is found to be the largest.

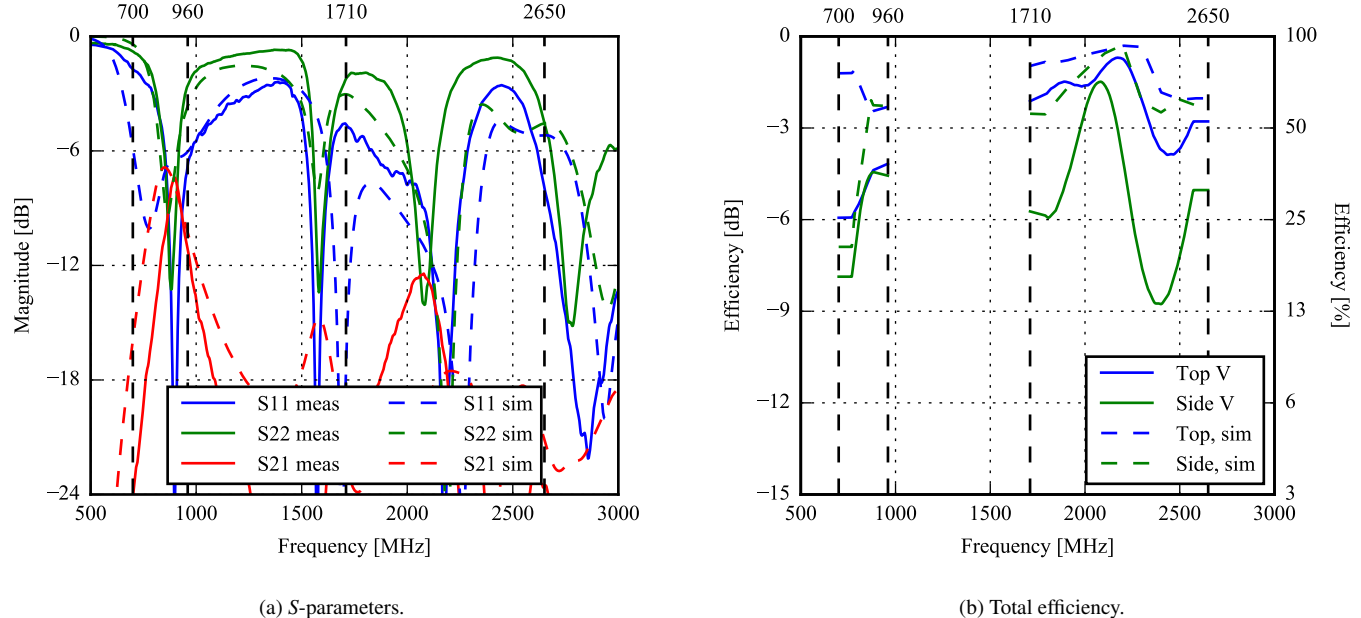


Figure 6.5: S -parameters and total efficiency of the monopole antenna prototype with the component values from Figure 6.2.

results, it is seen that by sweeping the tunable capacitors, the antennas are capable of covering most of the required bandwidth at 6 dB return loss. However, both the top and side antenna experience some problems in the high band. The top antenna is able to cover the required bandwidth except at 2300 MHz, where the return loss drops to 3 dB. The side antenna experiences a return loss drop in the high band around 2200 MHz and 2450 MHz. The side antenna also experiences some bandwidth problems in the low band, which makes it unable to sufficiently cover the band limit at 960 MHz. Some of the coverage problems, especially in the high band, are likely to disappear if the sweeps were done with the same number of component values as used in the simulation.

The isolation results show the lowest isolation in the low band, at approximately 800 MHz to 900 MHz for both the top and side antenna. This result is as expected when compared with the simulation results.

The efficiency sweep can be seen in Figure 6.7. The sweep is done accordingly to the introduction of Chapter 6 as with the S -parameter sweeps. Looking at the results, it is clear that none of the antennas completely fulfill the efficiency requirements. The top antenna is able to exceed -3 dB efficiency in the high band, at some of the capacitor values. The side antenna shows slightly lower efficiency results compared to the top antenna. The low band efficiency is above -4 dB for both antennas.

The correlation between the top and side antenna can be seen in Figure 6.8. The correlation is simulated and measured with the sweeping capacitor at the initial value of 0.3 pF for both the top and side antenna. From the figure, it is seen that the most

Antenna	Band	Start [MHz]	Stop [MHz]	Bandwidth [MHz]
Top	Low	830	1000	170
Side	Low	830	930	100
Top	High	1800	2300	500
Side	High	2650	3000	300

Table 6.1: Maximum bandwidth obtained in the low and high band for the top and side antenna, respectively.

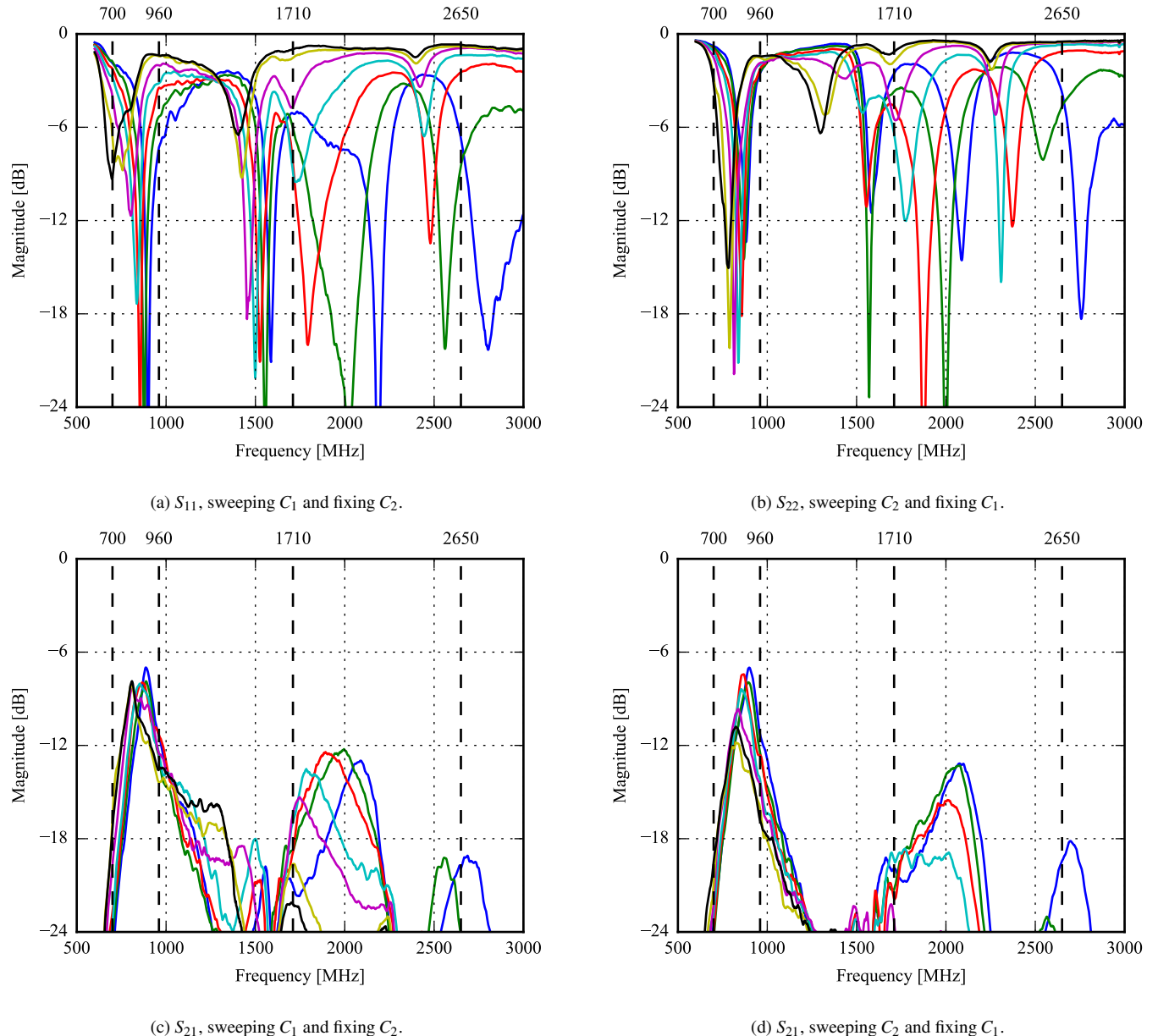


Figure 6.6: S -parameter sweep in free-space for tuning the shunt capacitor of each antenna, C_1 and C_2 for port 1 and 2, respectively. Port 1 is the top antenna and port 2 is the side antenna.

significant difference in the simulated and measured correlation is in the low band at approximately 830 MHz to 960 MHz. Within this frequency range, the simulated correlation is approximately 0.25 higher than the measured value.

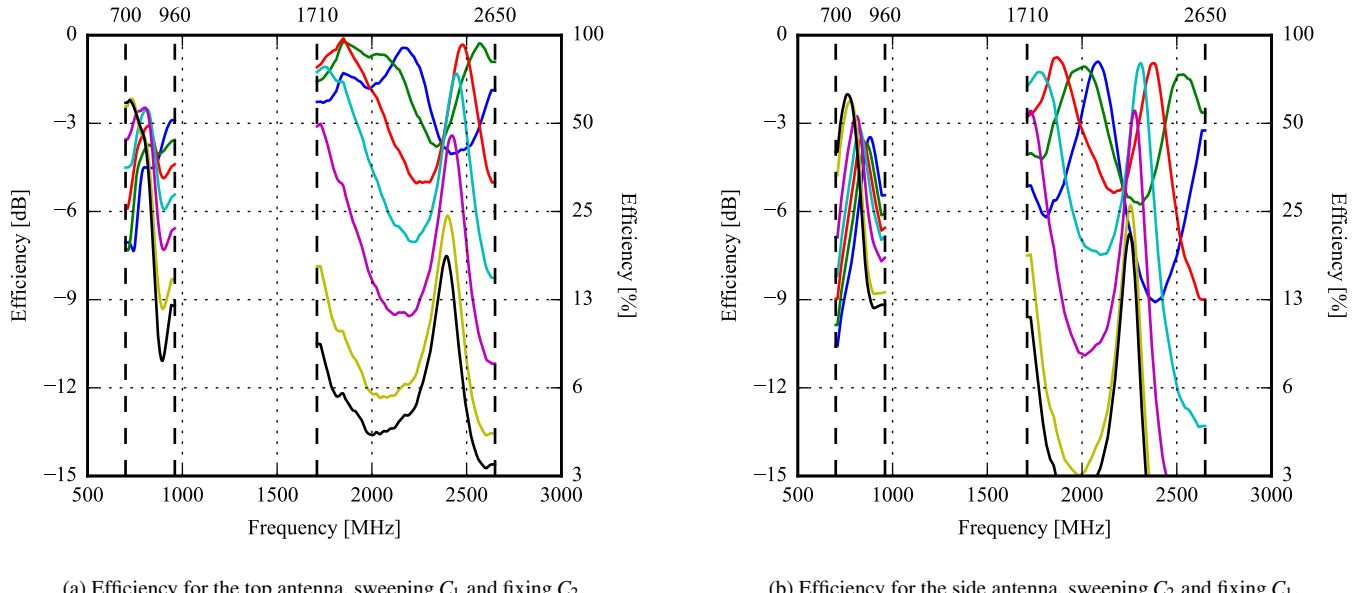
(a) Efficiency for the top antenna, sweeping C_1 and fixing C_2 .(b) Efficiency for the side antenna, sweeping C_2 and fixing C_1 .

Figure 6.7: Efficiency sweeps in free-space for tuning the shunt capacitor of each antenna, C_1 and C_2 for port 1 and 2, respectively. Port 1 is the top antenna and port 2 is the side antenna.

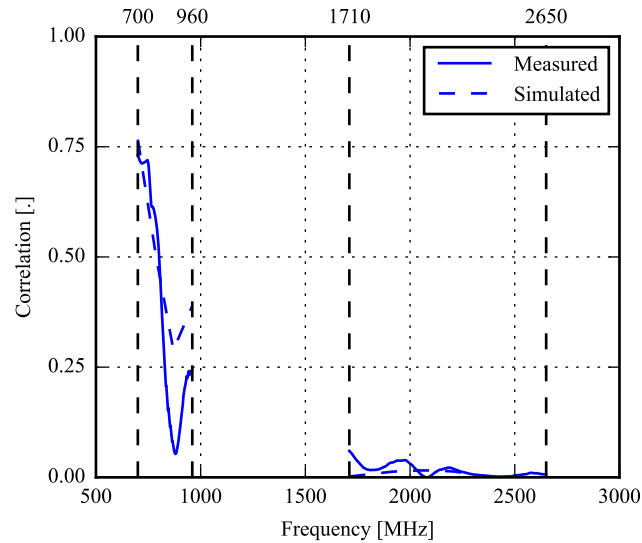


Figure 6.8: Correlation between the top and side antenna, with $C_2 = 0.3 \text{ pF}$ for both antennas.

6.2 Triangle-Feed Antenna

A prototype of the triangle-feed antenna has been built. The results will be described in this section.

The prototype is shown in Figure 6.9. Compared to the simulation, see Figure 4.7, a 5 mm strip of copper has been added next to the feed line. A free-space simulation has been made with the added copper strip for comparison.

6.2.1 Measurements

The measured and simulated S -parameters and total efficiency is shown in Figure 6.11. The component values used in the measurement are shown in Figure 6.10. From the S -parameters, it is seen that, in general, the resonances of the measurement correspond well with the resonances of the simulation – especially for the top antenna. The return loss level peaks are not the same but the antenna is nearly compliant with the impedance bandwidth requirement at 5 dB return loss. The isolation is better than the simulated, at a minimum of around 8 dB. The efficiency is generally slightly lower than the simulated. This is to be expected as real-life matching



Figure 6.9: Triangle-feed antenna prototype.

components are lossy due to their ESR. It is seen that the efficiency bandwidth of the side antenna in the low band is greater than the simulation. This is due to the more wide-band matching seen in the corresponding S -parameters, S_{22} , in the low band. Generally, the efficiency peaks correspond well with the return loss peaks and is quite good, peaking at above -3 dB in both the high and the low band.

The highest achievable bandwidth for both antennas can be seen in Table 6.2. From the table, it is seen that both antennas cover the required bandwidth quite well – especially at the low capacitance values.



Figure 6.10: Matching circuit for the triangle-feed antenna prototype. These are the component values where the bandwidth is found to be the largest.

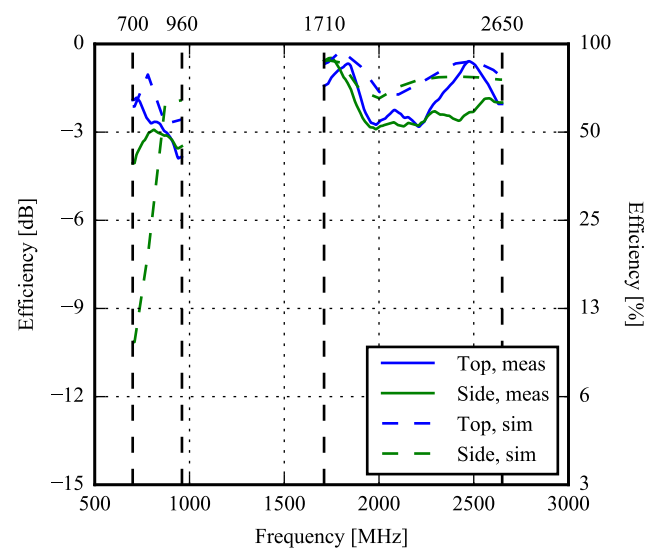
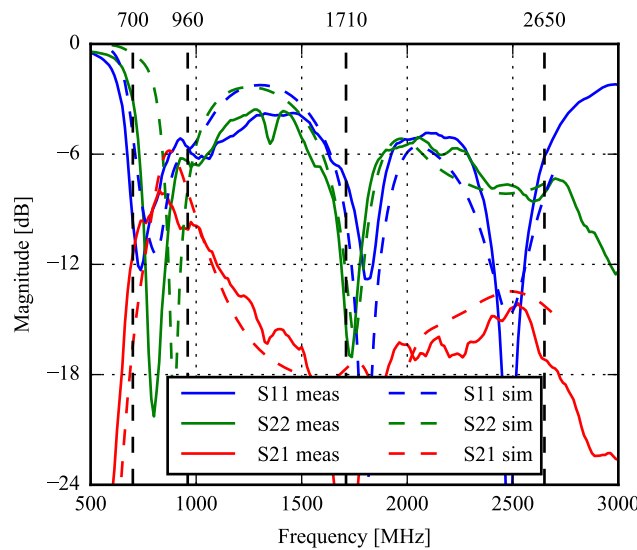


Figure 6.11: S-parameters and total efficiency of the triangle-feed antenna prototype with the component values from Figure 6.10.

Antenna	Band	Start [MHz]	Stop [MHz]	Bandwidth [MHz]
Top	Low	690	1300	610
Side	Low	720	1100	280
Top	High	1570	2780	1210
Side	High	1500	> 3000	> 1500

Table 6.2: Maximum bandwidth obtained in the low and high band for the top and the side antenna, respectively. The slight decrease in return loss is ignored for both the top and side antenna.

In addition to the S -parameters and the total efficiency, the envelope correlation coefficient has also been computed for the prototype. The result is shown in Figure 6.12, compared to the simulation. It is clearly seen that the simulated and measured correlation coefficients are very different. The reason for this is, most likely, that the antenna was not perfectly aligned when the top antenna and the side antenna were measured. To obtain realistic correlation results, the antenna should be located in the *exact* same position for every measurement.

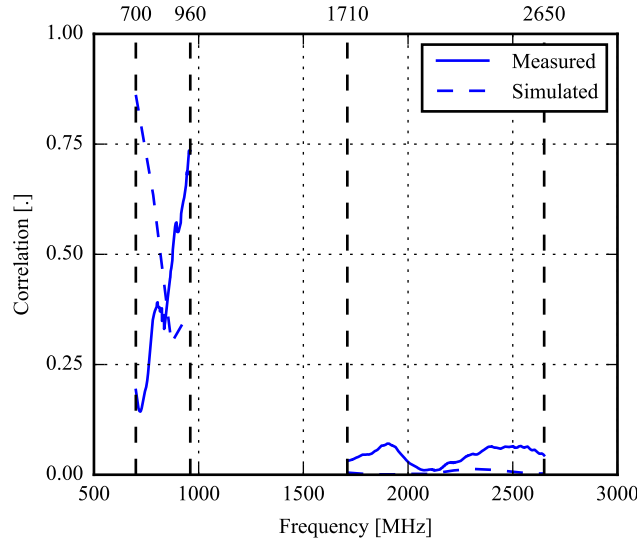


Figure 6.12: Measured and simulated envelope correlation coefficient for the triangle-feed antenna.

The shunt capacitor for each antenna has been swept to see the tuning ranges of the antennas. The S -parameters are shown in Figure 6.13. The efficiency-sweeps are shown in Figure 6.14. All component values, except the shunt capacitors, are the same values as in Figure 6.10.

From the S -parameters, it is seen that both the high and the low band for both antennas are covered at a return loss greater than 5 dB for the low capacitance settings. Both antennas can be tuned down using the shunt capacitor.

From the total efficiency, the same trend is seen. The efficiency can, generally, be tuned to be above -3 dB for both antennas in both the low and the high band.

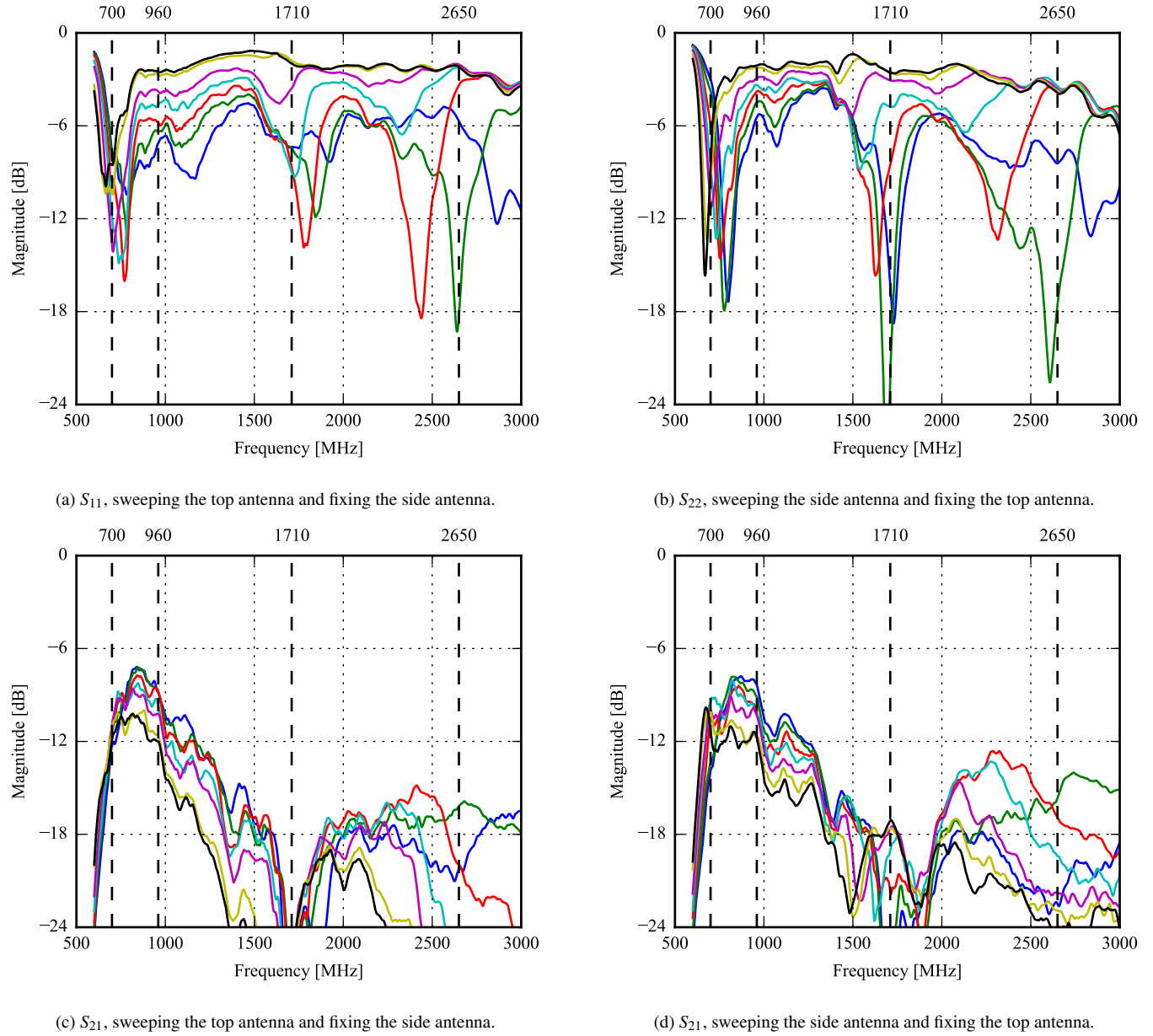
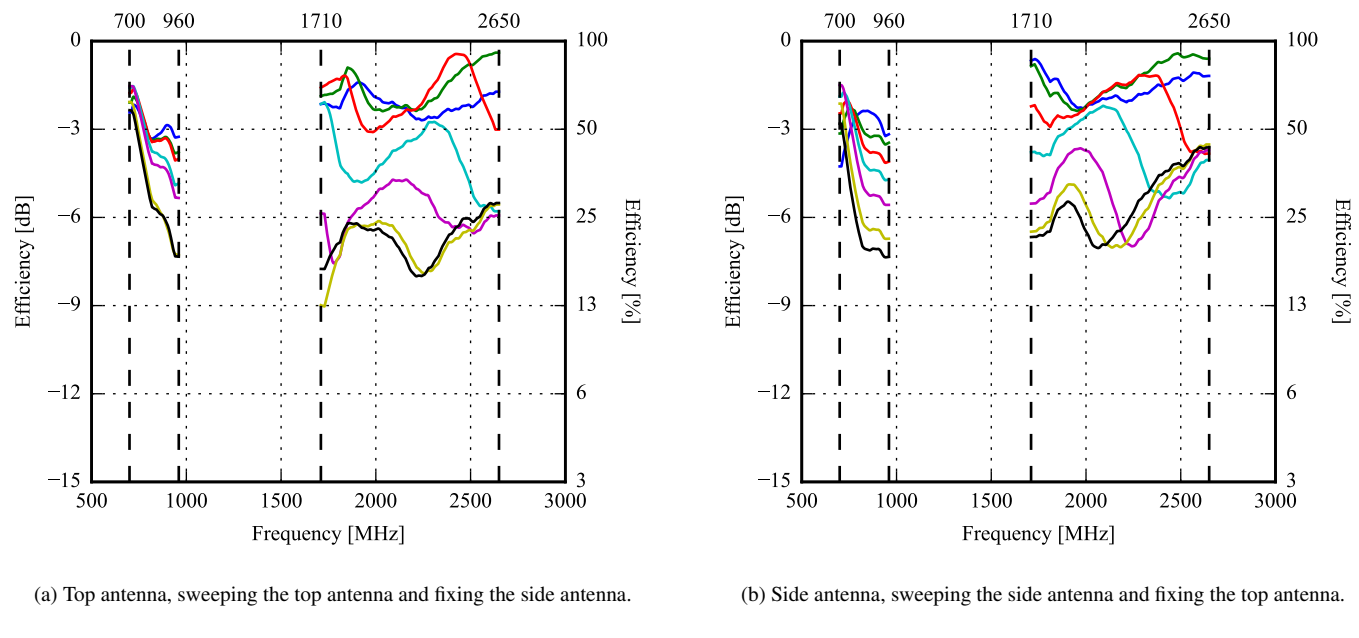


Figure 6.13: Triangle-feed antenna. S -parameters for different shunt-capacitor values.



(a) Top antenna, sweeping the top antenna and fixing the side antenna.

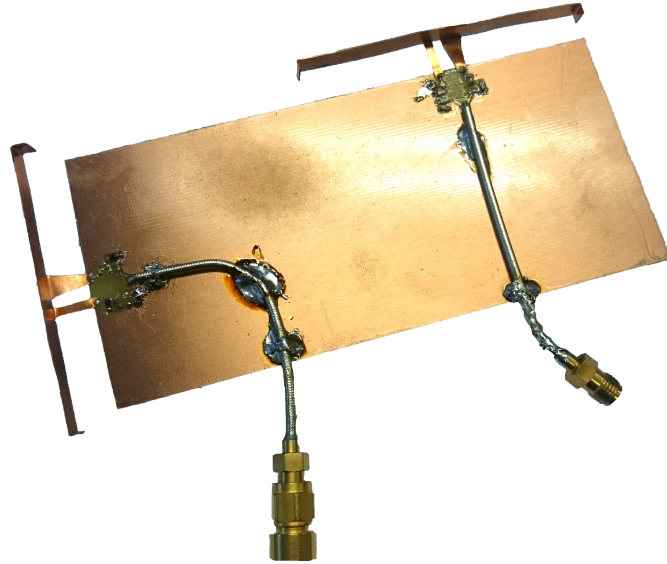
(b) Side antenna, sweeping the side antenna and fixing the top antenna.

Figure 6.14: Total efficiency for each of the antennas when sweeping the shunt-capacitor values.

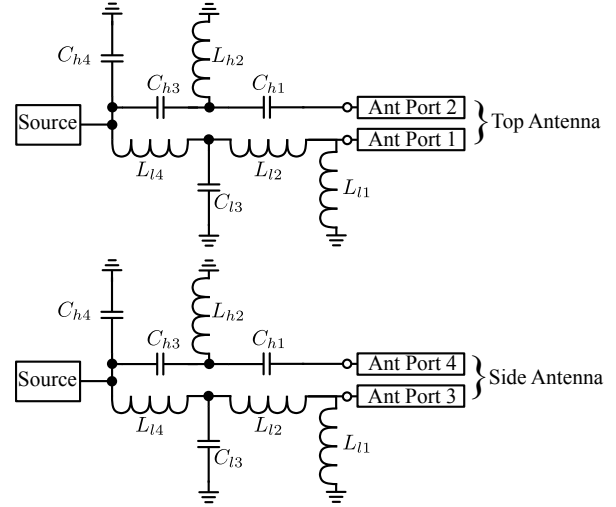
6.3 Dual-Feed Antenna

In this section, the prototype of the dual-feed antenna will be described.

The prototype and the used tuning circuit is shown in Figure 6.15. Both antennas are made on a CNC mill in the AAU metal workshop. This was done in order to have perfectly smooth edges and cut the two-feed design accurately.



(a) Dual-feed antenna prototype.



(b) Tuning/matching circuit.

Figure 6.15: Picture and tuning circuit for the prototype antenna. The antennas are built on FR-4 board using 35 μm copper. There is a matching circuit as shown for each of the four feeds.

6.3.1 Measurements

The simulated and measured S-parameters and total efficiency are shown in Figure 6.16. The results are done with the tunable capacitor at 0.3 pF. Furthermore, some adjustments were done to the component values. The current values are seen in Table 6.4.

From the S-parameters and the bandwidth table, it is seen that both antennas cover the required bandwidth in the lower band. The top antenna lacks 80 MHz in the high band, but this should not be a major problem as the antenna covers the remaining bandwidth at approximately 3 dB return loss. Comparing the simulated and the measured S-parameters, the results looks similar only with some detuning in the high band for both the side and top antenna.

The efficiency for the top antenna is approximately -1 dB, but drops to -7 dB from 2200 MHz to 2650 MHz. The side antenna covers the entire high band with approximately -2 dB to -1 dB efficiency. The low band efficiency is quite low compared to the high band, with an efficiency between -13 dB to -4 dB.

The measured and simulated envelope correlation coefficient can be seen in Figure 6.17. In the high band, the simulated and measured correlation is quite similar. However, for the low band, the simulated and measured results deviate. Comparing the correlation to the isolation in Figure 6.16 it is clear that correlation should be highest in the low band. The deviation in the low band results could be caused by the measurement placement of the antenna. The antenna should be placed in the exact same position for every measurement which can be hard to accomplish, also as mentioned in the triangle-feed prototype section, Section 6.2.

Antenna	Band	Start [MHz]	Stop [MHz]	Bandwidth [MHz]
Top	Low	700	960	260
Side	Low	830	910	80
Top	High	1710	2350	640
Side	High	1550	2645	1095

Table 6.3: Maximum bandwidth obtained in the low and high band for the top and the side antenna, respectively.

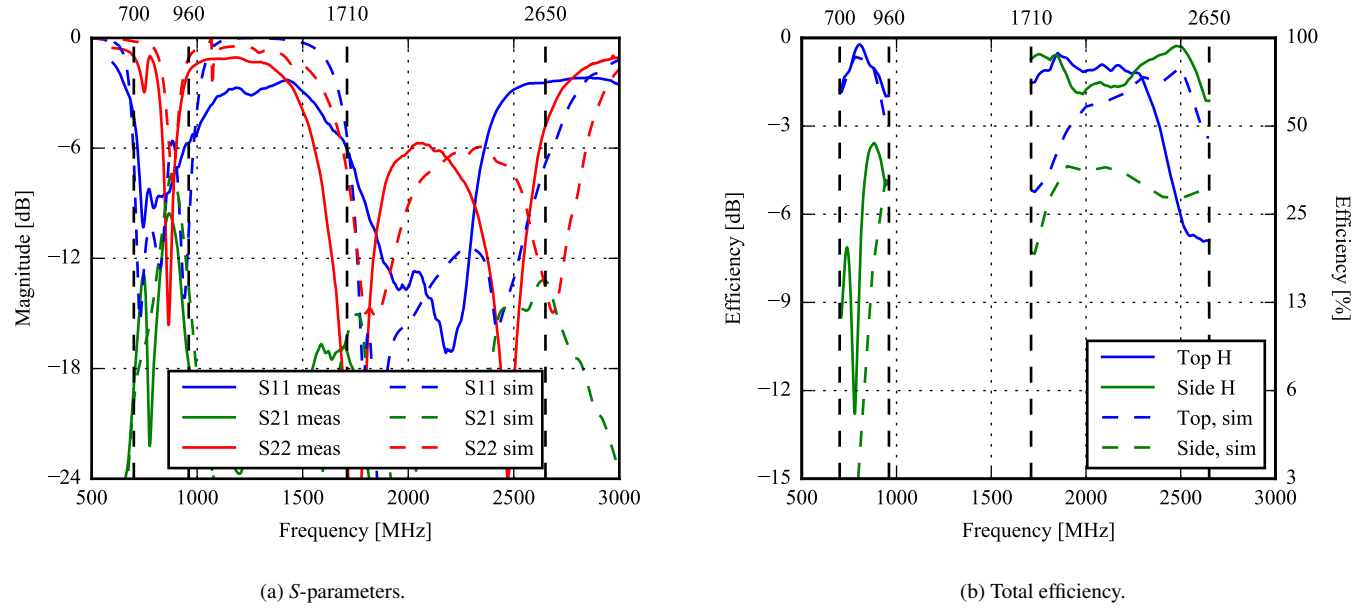


Figure 6.16: S -parameters and total efficiency of the dual-feed antenna prototype with the component values from Table 6.4.

	L_{l1}	L_{l2}	C_{l3}	L_{l4}	C_{h1}	L_{h2}	C_{h3}	C_{h4}
Top antenna	10 nH	15 nH	3 pF	5.6 nH	1.2 pF	7.5 nH	3 pF	0.1 pF
Side antenna	10 nH	16 nH	6.8 pF	4.3 nH	0.7 pF	5.1 nH	2.2 pF	1.2 pF

Table 6.4: Component values

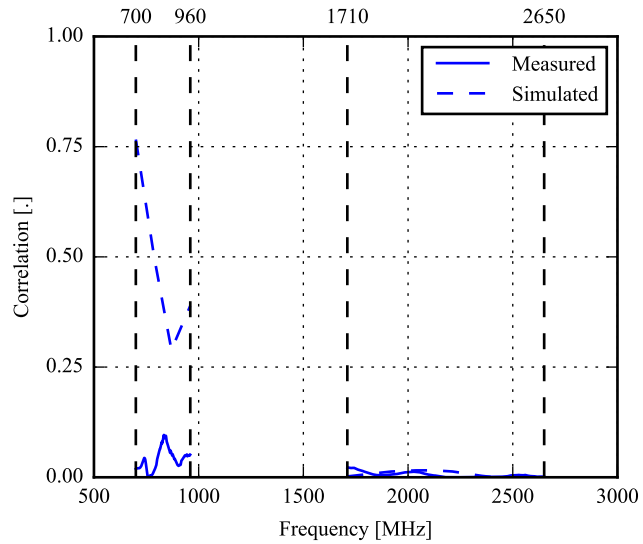


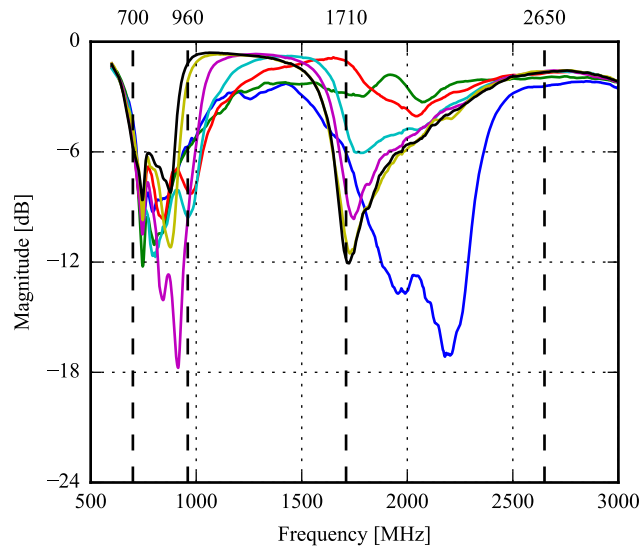
Figure 6.17: Measured and simulated envelope correlation coefficient for the dual-feed antenna.

The S-parameter sweep can be seen in Figure 6.18. The top antenna sweep of S_{11} shows that the antenna is capable of covering the entire low band and most of the high band. In the high band, the antenna has some problems from approximately 2400 MHz to 2650 MHz as the return loss drops to approximately 3 dB. The results of the side antenna S_{22} show that the antenna was unable to be tuned. Many component changes were made, having no effect on the ability to tune the antenna.

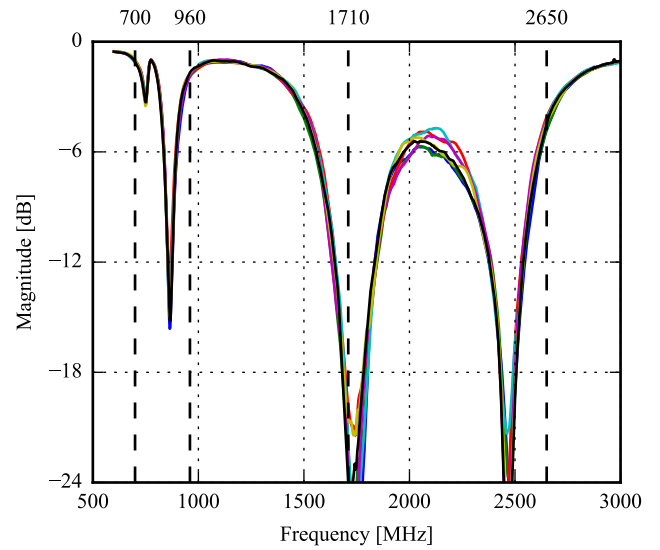
The lowest measured isolation is 9 dB in the low band. In the high band, the isolation is generally high with a maximum value of 14 dB.

The efficiency sweeps are shown in Figure 6.19. From the results, it is seen that the top antenna covers the low band quite well with an efficiency of approximately -2 dB. The top antenna, however, experiences some problems in the high end of the high band. The efficiency is approximately -2 % from 1710 MHz to 2200 MHz but drops to -6 dB from 2200 MHz to 2650 MHz. Generally, tuning the top antenna results in an overall efficiency drop that is most significant in the higher frequencies.

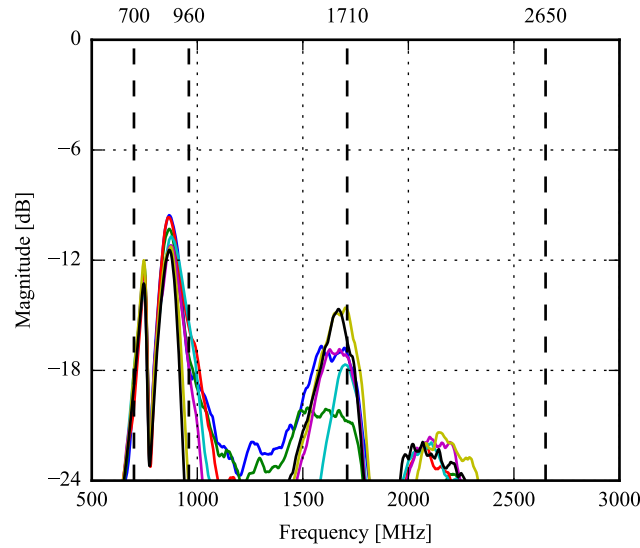
As mentioned earlier, the side antenna was unable to be tuned, so only a single measurement of the side antenna efficiency was made. The efficiency results for the side antenna is therefore as described above in the comparison of the simulated and measured results.



(a) S_{11} , sweeping the top antenna and fixing the side antenna.

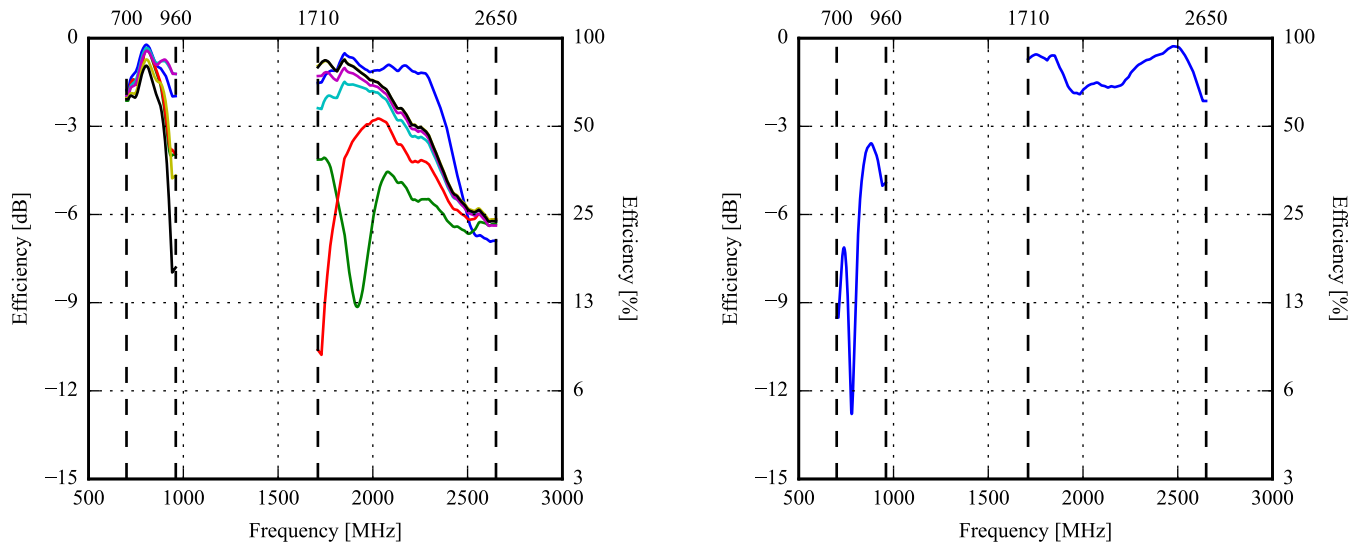


(b) S_{22} , sweeping the top antenna and fixing the side antenna.



(c) S_{21} , sweeping the top antenna and fixing the side antenna.

Figure 6.18: Dual-feed antenna. S-parameters for different shunt-capacitor values. The side antenna does not change resonance as desired when the shunt capacitor is changed. Therefore, only the top antenna is swept.



(a) Top antenna, sweeping the top antenna and fixing the side antenna.

(b) Side antenna, fixing both top and side antenna.

Figure 6.19: Total efficiency of both antennas when sweeping the top antenna. The side antenna does not sweep as desired when changing the capacitor. Therefore, no sweeps are made for the side antenna.

6.4 Conclusion

The three preliminary antenna designs have now been prototyped and measured for a range of discrete tuning capacitor values. As expected, the results from the simplified simulations did not exactly match the prototypes, but the general resonances of the three designs were distinguishable.

All designs did retune as the discrete shunt capacitor was changed, except for the dual-feed side antenna. The matching network only made it possible to match the antenna well, but no capacitors could be altered which would retune the antenna. Apart from this, the antenna did obtain a quite acceptable bandwidth in the high band and the high end of the low band.

The correlation has been computed but the positioning of the antennas in the Satimo chamber did not allow for all antennas to be located in exactly the same position for the top and side measurements so these results should *not* be trusted. An exception to this is the monopole for which a styrofoam jig was set up, allowing the positioning to be quite accurate. It is seen that the measured correlation for this antenna coincides well with the simulated. For the other two antennas, the correlation from the simulation should be trusted more than the measured.

	Top		Side	
	L	H	L	H
Monopole	-2.5	-0.2	-2.0	-1.0
Triangle-feed	-1.5	-0.5	-1.5	-0.5
Dual-feed	-0.2	-0.5	-3.5	-0.2

Table 6.5: Peak efficiency (dB) in the low/high band for the prototypes of the three preliminary designs.

The peak efficiencies of the three prototypes are summarized in Table 6.5. It is clear that the dual-feed design peaked very well with its top antenna. However, this antenna did not cover the whole high band and the side antenna was not tunable. Therefore, this design has not been chosen for later implementation on a PCB.

Both the monopole and the triangle-feed design were also quite efficient both in the low and the high band. The triangle-feed design, however, did preserve a higher efficiency during the sweep and had a higher minimum efficiency than the monopole did. For this reason, the triangle-feed design has been chosen as the first design to implement with the PCB in Chapter 8.

All the three preliminary designs have been designed to use up all the given space from the requirements in Chapter 2 and therefore have a ground clearance of 10 mm each. However, as the actual space in a mobile phone is limited, it may be desirable to go for less ground clearance. The next chapter will describe the design of an antenna with a smaller ground clearance. Here, it will be shown how the ground clearance affects the bandwidth of the antenna and another design for the PCB will be initiated.

Chapter 7

Minimized Antenna

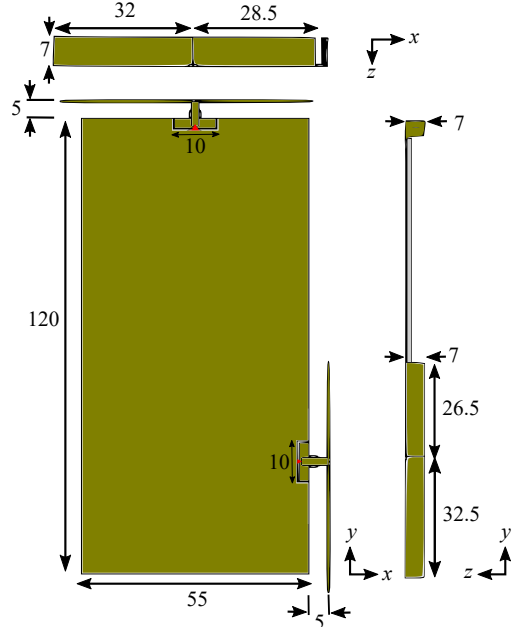
In this chapter, a second minimized design of the monopole antenna will be made. The antenna choice was based on the simple design and matching of the monopole antenna. A ground clearance simulation is carried out to investigate the effect on the bandwidth and the efficiency.

In the previous simulations and measurements, a tunable capacitor in the range 0.3 pF to 2.9 pF has been used. However, it has since been discovered that the tuner PCB, which will be described in Chapter 8, has two MEMS capacitors connected in parallel for the top antenna and four in parallel for the side antenna. This has here been exploited so that the minimized monopole is capable of tuning from 0.6 pF to 6 pF for the top antenna and from 1.2 pF to 12 pF for the side antenna. The higher tuning range makes it possible to make the antennas smaller and more resilient to user detuning.

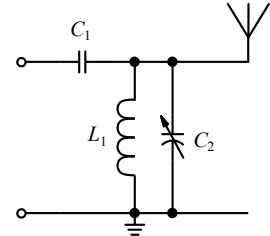
The board used for the measurements in this chapter will be described in greater detail in Chapter 8.

7.1 Ground Clearance Simulation

The minimized monopole design, developed for this chapter, and the tuning schematic can be seen in Figure 7.1. The design is still based on the first folded monopole design but is made smaller and simpler without any folding.



(a) Technical drawing. The ground clearance is here 5 mm.



	C_1	L_1	C_2
Top antenna	2.23 pF	3.94 nH	[0.6, 6] pF
Side antenna	2.15 pF	3.17 nH	[1.2, 12] pF

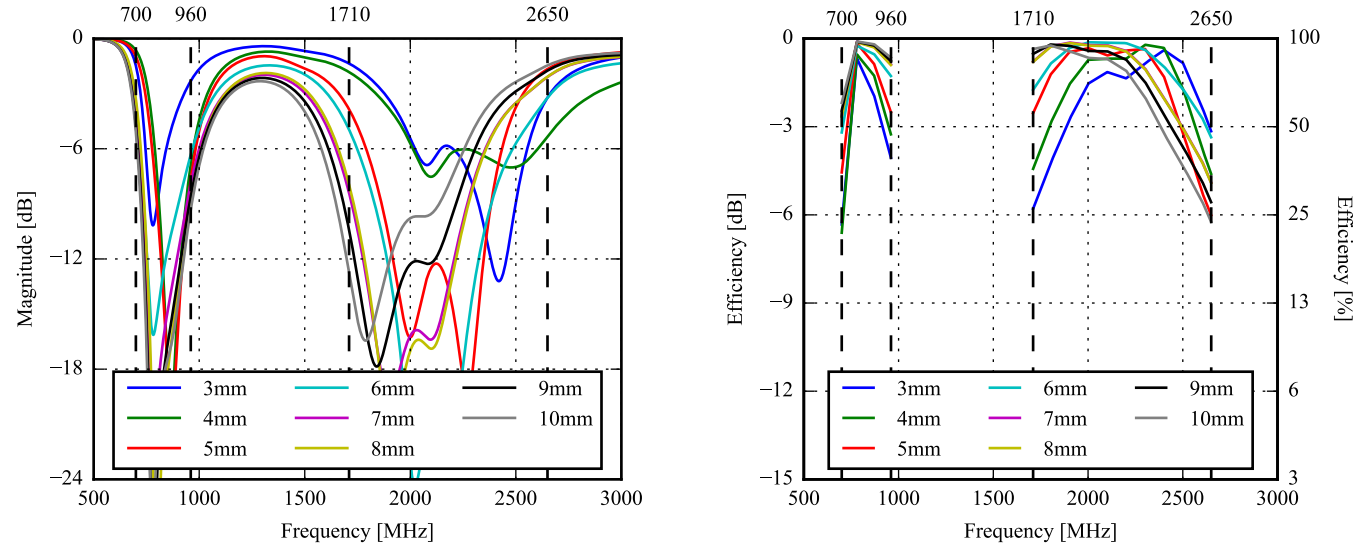
(b) Tuning/matching circuit.

Figure 7.1: Technical drawing and tuning circuit for the antenna. The matching circuit is applied for both the top and the side antenna.

The S_{11} and the efficiency, for different ground clearances, can be seen in Figure 7.2. The simulation sweep is done from 10 mm to 3 mm ground clearance in 1 mm steps and only for the top antenna. Each ground clearance simulation is matched and tuned independently to get the highest bandwidth possible in each case.

From the S_{11} results, it is clear that the bandwidth decreases as the ground clearance decreases. The most noticeable results is at 5 mm clearance as the bandwidth from this point does not increase significantly when increasing the ground clearance. However, decreasing the ground clearance further to 4 mm and 3 mm, the bandwidth drops significantly. Based on these results, it has been chosen to minimize the antenna design to a ground clearance of 5 mm.

The efficiency ground clearance comparison shows similar results. In the high band, it is clear that decreasing the ground clearance will also decrease the bandwidth. However, the high band results are hard to compare as the different simulations are matched at different frequencies to gain the highest bandwidth. The comparison is more noticeable in the low band where it is clear that the lower the clearance, the lower the efficiency. Generally, the efficiency does not drop that much when decreasing the ground clearance. It should be possible to increase the efficiency by compensating for the drop using tunable capacitors.



(a) S_{11} parameter for the top antenna, when sweeping the ground clearance.

(b) Efficiency for the top antenna, when sweeping the ground clearance.

Figure 7.2: S_{11} and efficiency for the top antenna, when sweeping the ground clearance from 3 mm to 10 mm

A sweep on the antenna height was also carried out from 7 mm to 4 mm with a ground clearance of 5 mm. The results are not included as the top antenna was unable to cover the high band at anything lower than 7 mm. To create a small-volume antenna it is therefore found that a trade-off between height and ground clearance must be made.

7.2 Simulation

The simulated S-parameter sweep for both the top and the side antenna can be seen in Figure 7.3. The bandwidth results can be seen in Table 7.1. Both antennas fulfill the requirement for the low band, but in the high band, the top antenna experiences some problems. The top antenna lacks 76 MHz of bandwidth in the high band. The lack of 76 MHz bandwidth is acceptable as it covers close to the 720 MHz requirement. From the results, it is seen that both antennas cover the entire low band. In the high band, both the top and the bottom antenna experiences some problems at the band limits where the return loss decreases to 5 dB and 4 dB, respectively. The isolation has improved a bit compared to the results from the first design but is still significant in the lower band.

The tuned efficiency for both antennas can be seen in Figure 7.4. From the results, it is seen that both antennas are capable of covering the high band with an efficiency greater than -3 dB. In the low band, a lot of tuning is needed to achieve an efficiency around -3 dB. Generally, the efficiency drops as the capacity increases as expected.

Antenna	Band	Start [MHz]	Stop [MHz]	Bandwidth [MHz]
Top	Low	964	1128	164
Side	Low	990	1118	128
Top	High	1908	2574	666
Side	High	1829	2559	1270

Table 7.1: Maximum bandwidth obtained in the low and high band for the top and the side antenna, respectively.

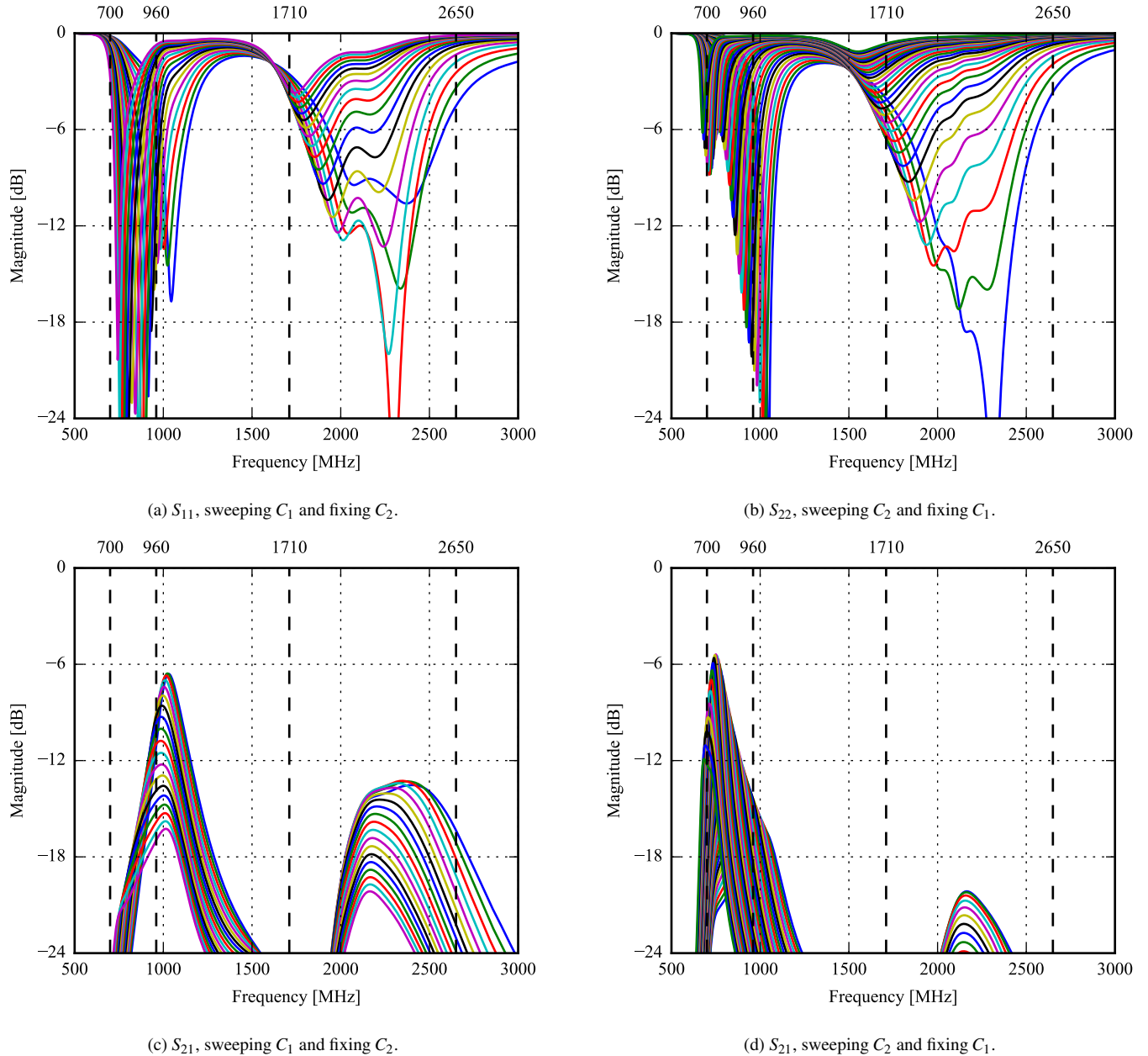


Figure 7.3: S -parameter sweep in free-space for tuning the shunt capacitor of each antenna, C_1 and C_2 for port 1 and 2, respectively. Port 1 is the top antenna and port 2 is the side antenna.

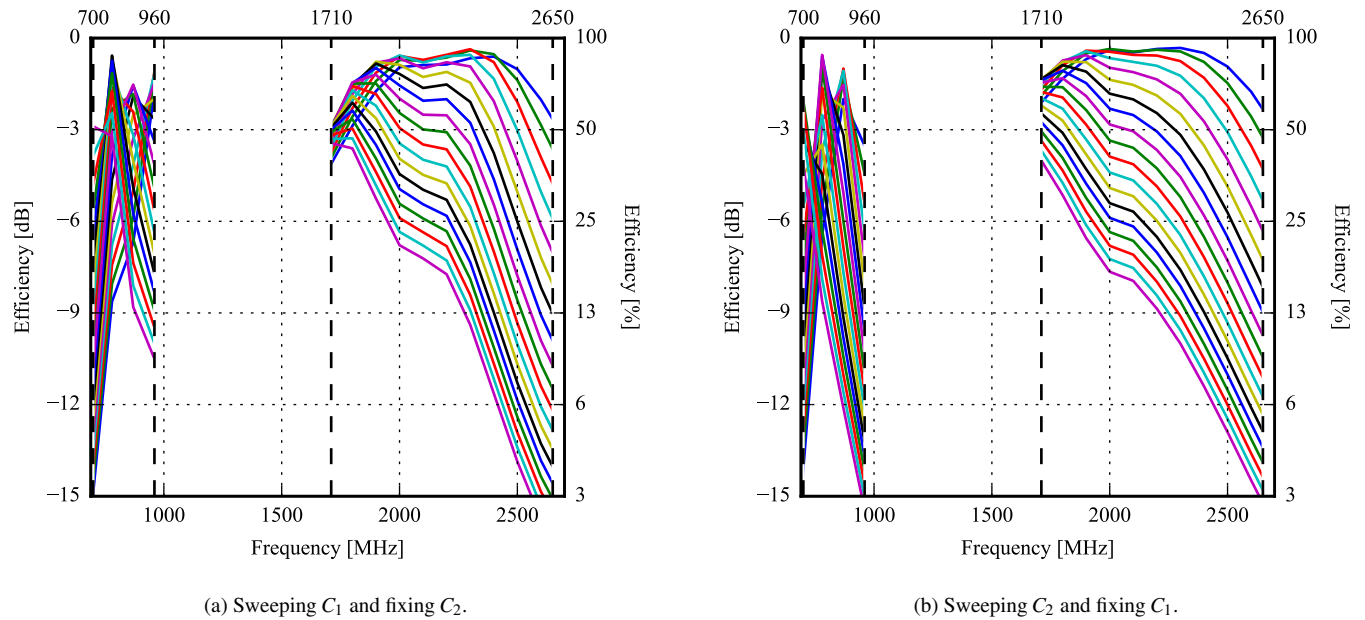


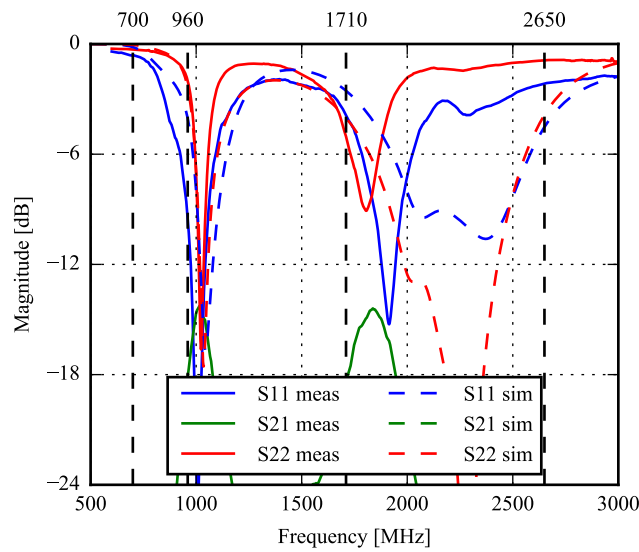
Figure 7.4: Efficiency for each antenna when sweeping the tunable capacitors. Here, C_1 and C_2 are the tuning capacitor for the top and side antenna, respectively.

7.3 Measurements

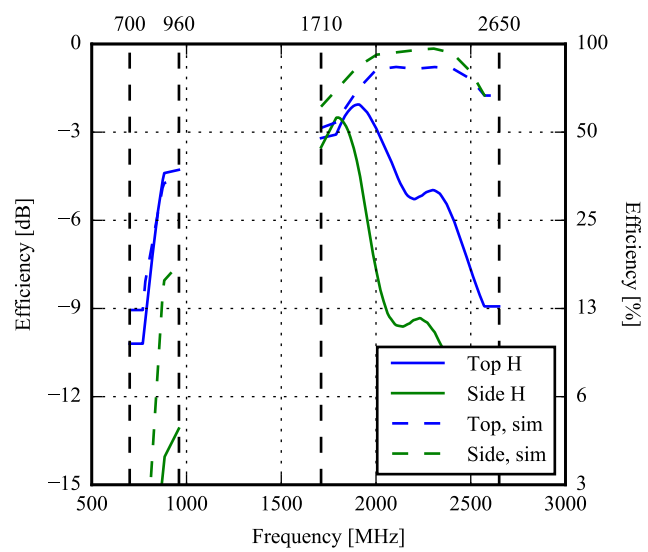
A comparison between the simulated and measured S -parameters and efficiencies can be seen in Figure 7.6. The component values used in the measurements can be seen in Table 7.5. From the S -parameters, it is seen that both antennas are detuned and have poor performance from 2000 MHz to 3000 MHz. The maximum bandwidth from the measurements can be seen in Table 7.2. Both antennas cover the bandwidth requirements in the low band but experiences some problems in the high band. The top antenna and the side antenna lack 500 MHz and 620 MHz bandwidth, respectively. The efficiency is also quite low as a result of the poor return loss of the high band.



Figure 7.5: Matching circuit for the minimized monopole prototype. These are the component values where the bandwidth is found to be the largest.



(a) S -parameters.



(b) Total efficiency.

Figure 7.6: S -parameters and total efficiency of the minimized monopole antenna prototype with the component values from Figure 7.5.

The S -parameter sweep for both the top and the side antenna can be seen in Figure 7.7. From the S_{11} and S_{22} sweeps, it is seen that sweeping the capacitors does not improve the high band coverage. However, it is possible to cover the low band quite well but the high band needs some improvements for both antennas. The minimum isolation is measured in the low band at 13 dB.

The efficiency sweep is seen in Figure 7.8. The top antenna almost covers the entire low band with an efficiency of -6 dB but as expected, it experiences poor performance from 2000 MHz to 2650 MHz. The side antenna covers the low band with an efficiency going from -8.5 dB to -4.6 dB and has an efficiency above -6 dB from 1710 MHz to 1850 MHz where it drops below -9 dB.

Antenna	Band	Start [MHz]	Stop [MHz]	Bandwidth [MHz]
Top	Low	920	1100	180
Side	Low	1000	1080	80
Top	High	1800	2020	220
Side	High	1710	1810	100

Table 7.2: Maximum bandwidth obtained in the low and high band for the top and the side antenna, respectively.

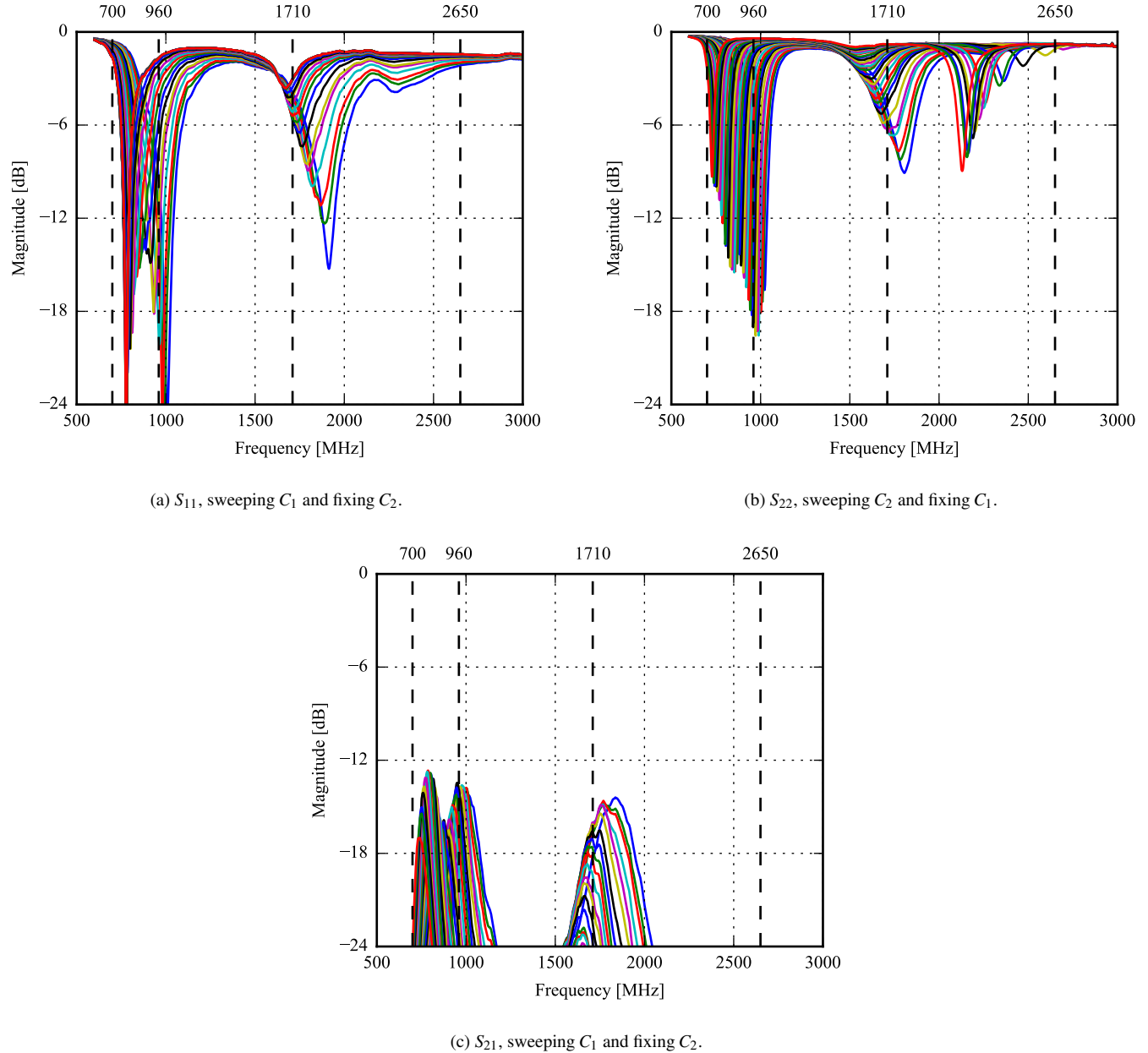


Figure 7.7: S -parameter sweep in free-space for tuning the shunt capacitor of each antenna, C_1 and C_2 for port 1 and 2, respectively. Port 1 is the top antenna and port 2 is the side antenna.

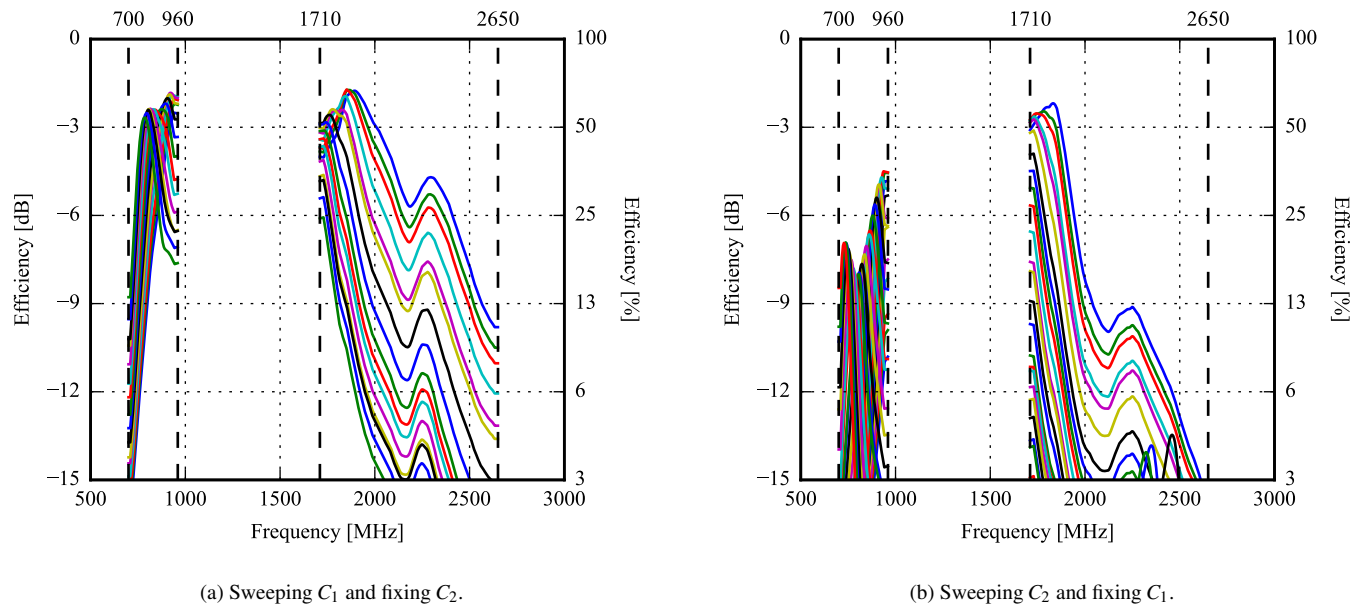


Figure 7.8: Efficiency for each antenna when sweeping the tunable capacitors. Here, C_1 and C_2 are the tuning capacitor for the top and side antenna, respectively.

7.4 Conclusion

It is found, as expected, that a larger ground clearance makes it possible to get a larger bandwidth. However, it has been found that even with only 5 mm ground clearance, a decent design can be made for a digitally tunable antenna.

A very simple antenna has been designed, simulated, and measured on a PCB with a MEMS tuner. It appears to be on a par with the preliminary design during the simulation phase. However, the measurement results showed a significant detuning and drop in efficiency and return loss when the PCB with MEMS tuner was used. Especially, the high band was hard to get resonating on the board. The design will therefore be modified to resonate better at high frequencies before it is used for the final measurements.

The next chapter will first describe the implementation of the triangle-feed antenna with the PCB and MEMS tuner as well. The design from this chapter will, at the same time, be revised to cover the high band better. The development, simulations, measurements, and refinements of this antenna will also be covered in the following.

Chapter 8

Printed Circuit Board

In this chapter, the triangle-feed prototype from Chapter 6 is moved from a simplified ground plane PCB to a PCB with a WiSpry WS1040 tuner for each antenna. Apart from this, the minimized design from Chapter 7 will be elaborated and measured.

On the board, each tuner has four capacitors where each has a range from approximately 0.3 pF to 3.0 pF. In the matching network for the top antenna, two capacitors are used in parallel making the range approximately 0.6 pF to 6.0 pF. The tuner for the side antenna has all four capacitors connected in parallel making the range approximately 1.2 pF to 12 pF. The two first capacitors are tuned simultaneously (“tracking”). The side antenna then has an additional two individual capacitors for extending its tunable range while not affecting the top antenna.

The PCB used in this chapter is shown in Figure 8.1.

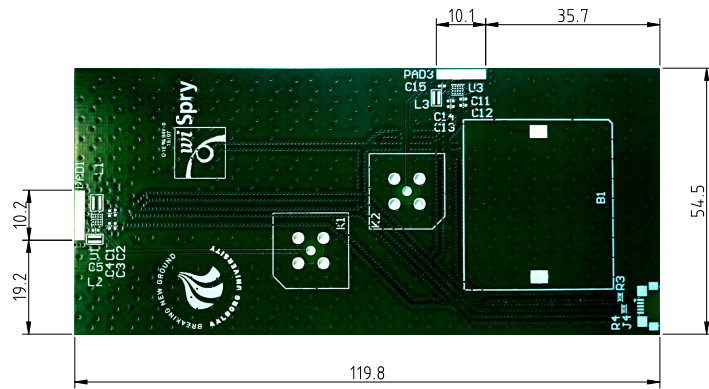


Figure 8.1: Tuner PCB used for measurements.

8.1 Triangle-Feed Antenna

In Chapter 6, it was found that the triangle-feed antenna design had the highest efficiency and was the most sweepable of the designs. For this reason, the triangle-feed design has been chosen as the first design to move to the printed circuit board with the WiSpry tuners installed.

The antennas are shown in Figure 8.2. The side antenna has been moved further towards the top to align with the feed. Extra length has been added by the end of the triangle, as this results in a greater bandwidth around 1800 MHz.

The antenna is tuned using the fiber-optic RFFE adapter described in Appendix A.1.

The S-parameters sweeps are shown in Figure 8.3. As it is seen, the high end of the high band – near 2.6 GHz – does not resonate as good as the prototype. However, the low band can be covered quite well for both the top and the side antenna.

The total efficiency is plotted in Figure 8.4. The efficiency, likewise, reflects that resonance is lacking near 2.6 GHz, so the mismatch loss is quite severe – especially for the side antenna. The low band looks acceptable for both antennas as the top antenna has a total efficiency above -3.1 dB and the side antenna has a total efficiency above -5.5 dB.

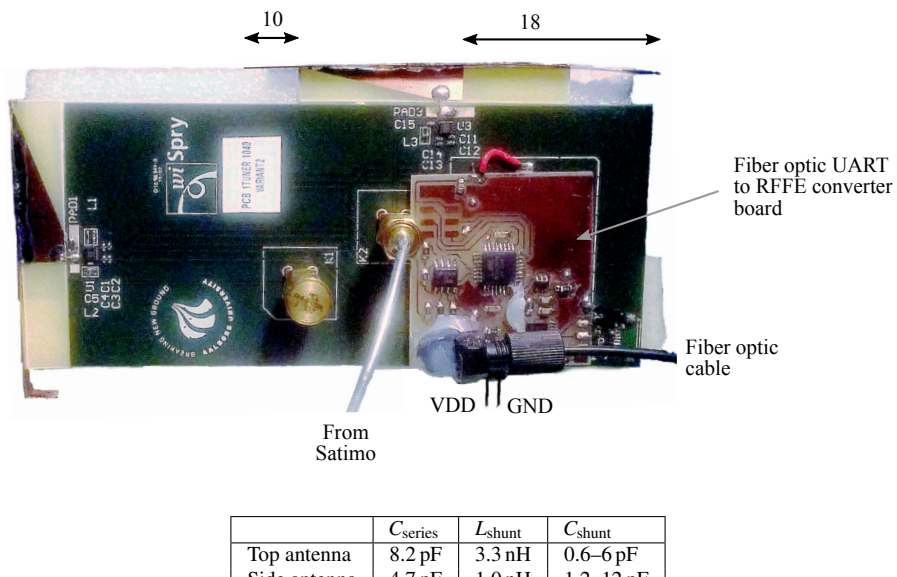


Figure 8.2: Triangle-feed antenna on a PCB with two WiSpry tuners. The location of the side-feed is different from the prototype and for this reason, the side antenna has slightly different dimensions. The changes from Figure 4.7a is noted on the figure.

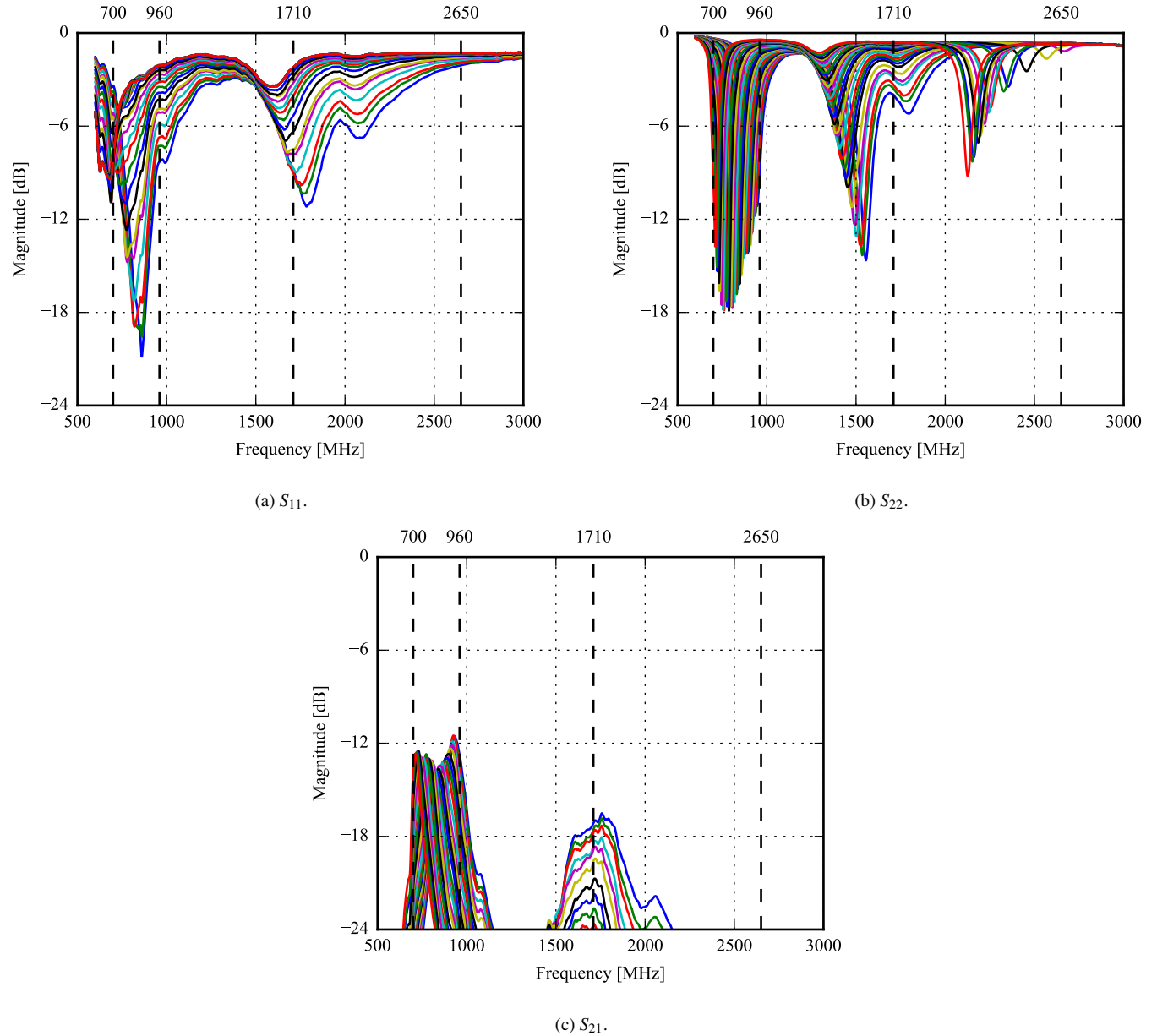


Figure 8.3: S -parameters of the triangle-feed antenna with tuners. The first sixteen values, the two tuners are tracking. After this, only the side tuner is altered.

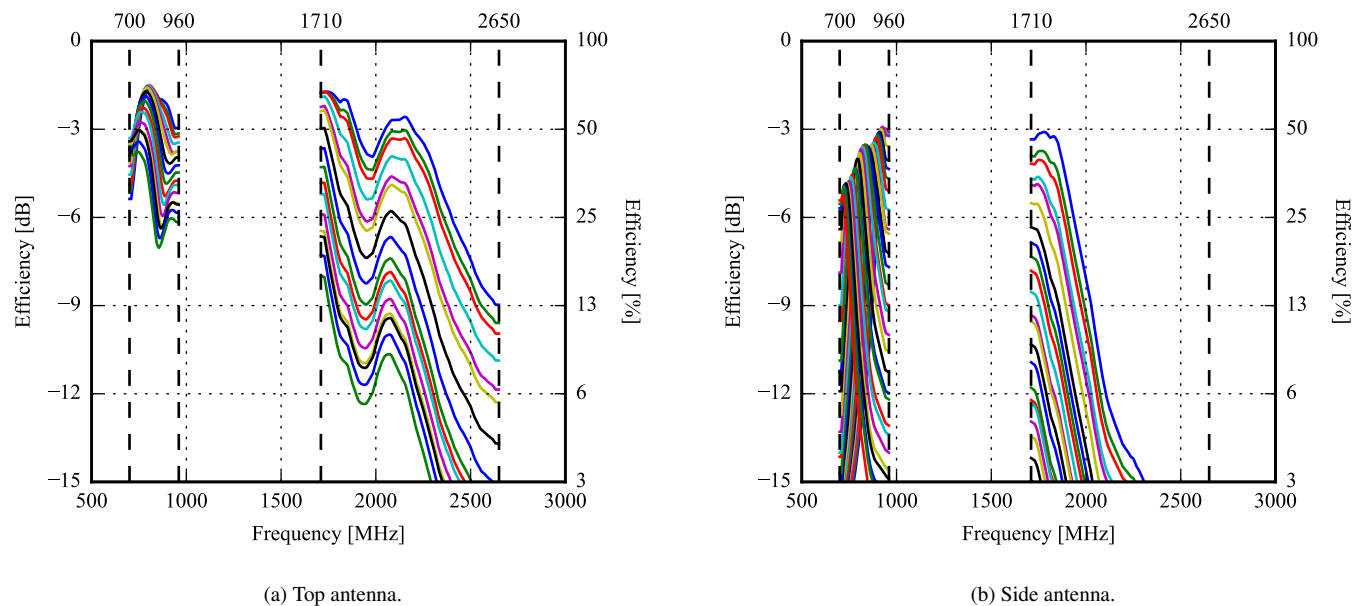


Figure 8.4: Total efficiency of the triangle-feed antennas with tuners.

8.2 Modified Minimized Antenna

From the S -parameter measurements of both the triangle-feed antenna and the minimized monopole antenna, it is clear that both antennas are experiencing problems in the high band when going from the simulation to the tuner PCB.

It has been chosen to elaborate on the minimized monopole antenna design and improve the high band. In order to do so, a second set of arms has been added to the antennas as shown in Figure 8.5. As previous experience has shown that the simplified simulations will detune in practice, the matching components in Figure 8.5 have been chosen to resonate slightly higher than desired.

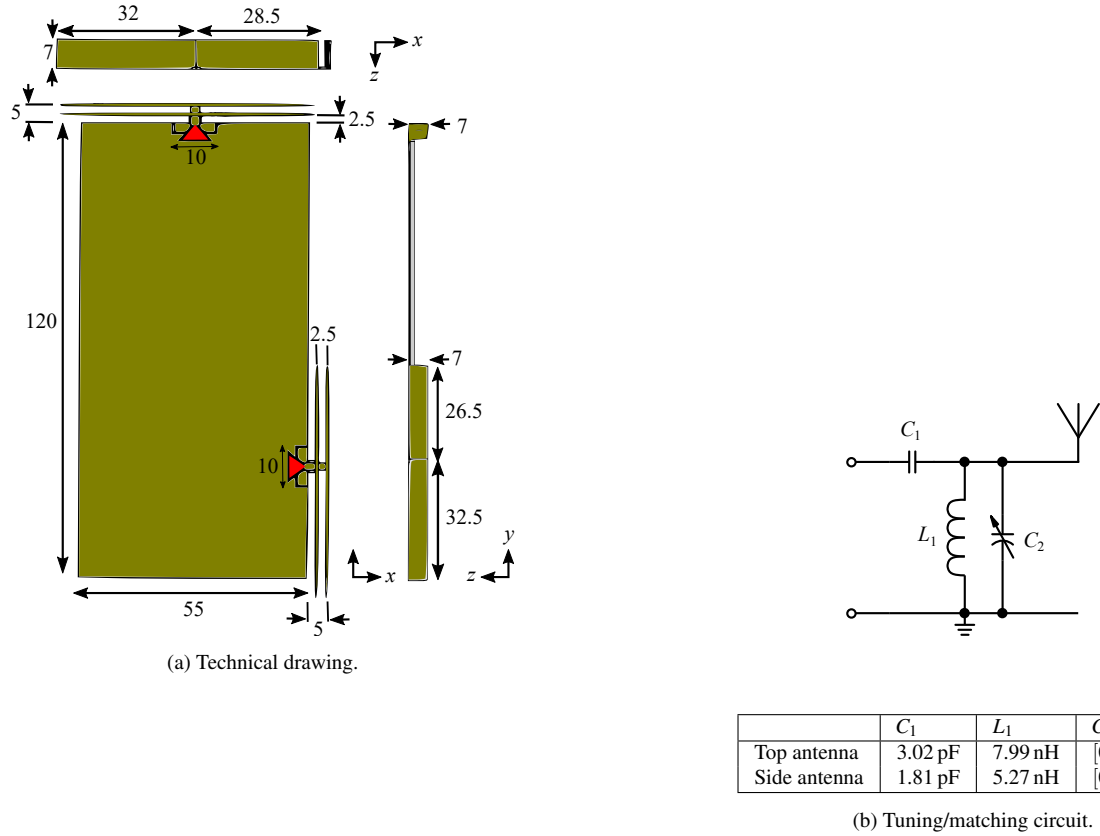


Figure 8.5: Technical drawing and tuning circuit for the antenna. The matching circuit is applied for both the top and the side antenna.

8.2.1 Free-Space Simulation

The new antenna design, presented in Figure 8.5, has been simulated. The resulting S -parameter sweep can be seen in Figure 8.6. The low band of both antennas can be covered by sweeping the tuning capacitor. The high band resonates higher than desired but is likely to detune when the antennas are added to the PCB. The maximum bandwidth for both antennas can be seen in Table 8.1. Both antennas cover the required bandwidth in the low band, but experiences some problems in the high band. The top antenna lacks 393 MHz and the side antenna 515 MHz. As a side effect of the extra added resonance, the bandwidth has dropped. It should, however, be able to cover both bands during the sweeps, as the bandwidth on the tuner PCB is expected to get detuned.

The isolation is rather low for the free-space simulation with a minimum isolation of 6 dB in the low band. The isolation in the high band is generally high with a isolation above 13 dB.

Antenna	Band	Start [MHz]	Stop [MHz]	Bandwidth [MHz]
Top	Low	938	1065	127
Side	Low	933	1031	98
Top	High	2291	2218	327
Side	High	2128	2433	205

Table 8.1: Modified monopole antenna in free-space. Maximum bandwidth obtained in the low and high band for the top and the side antenna, respectively.

The correlation sweep results can be seen in Figure 8.7. The high band correlation shows to be very low in the high band. In the

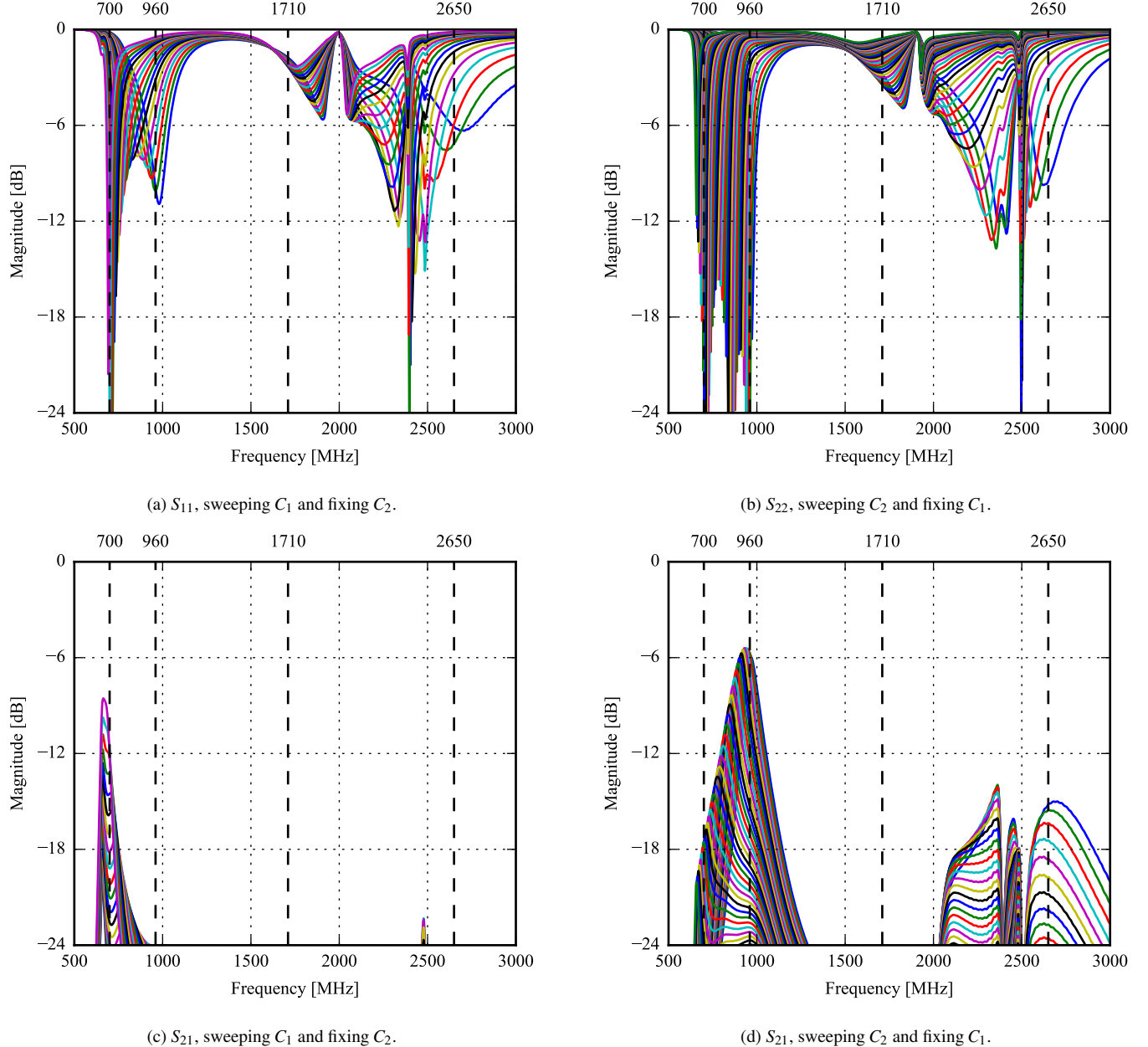
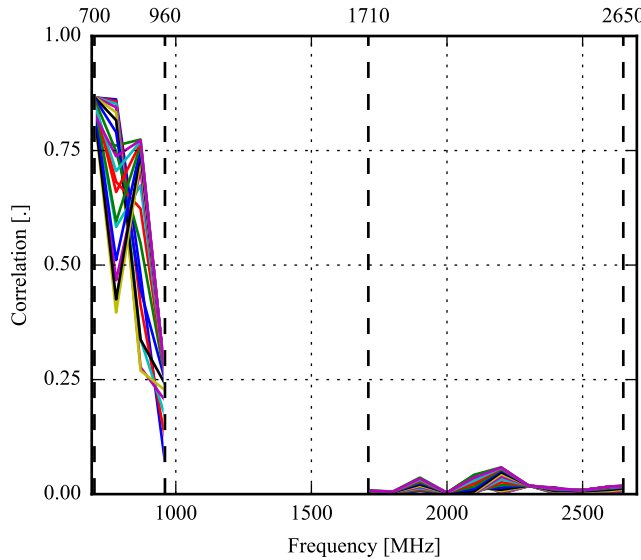
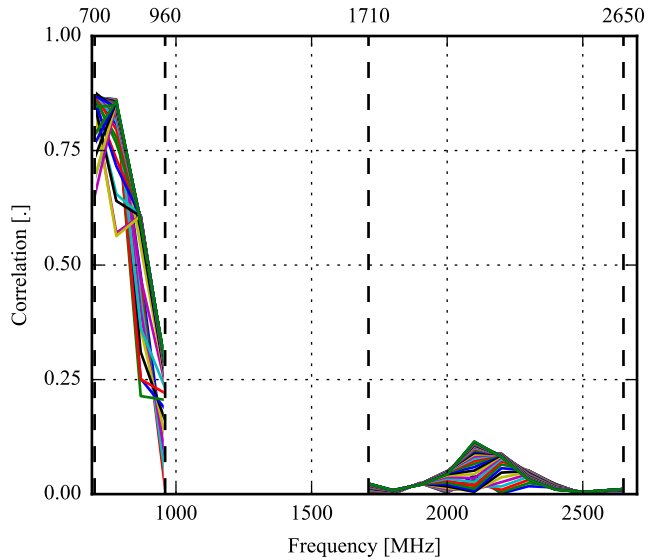
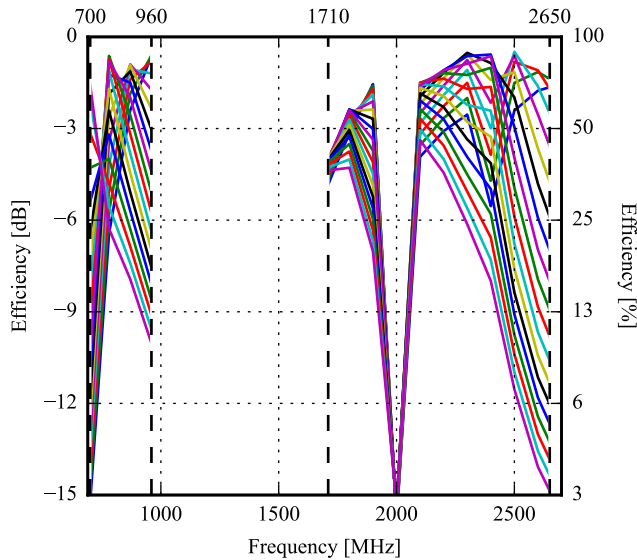
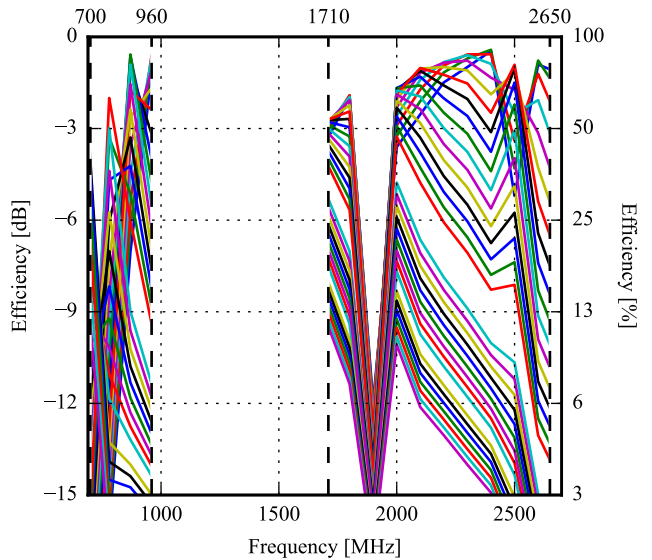


Figure 8.6: S -parameter sweep in free-space for tuning the shunt capacitor of each antenna, C_1 and C_2 for port 1 and 2, respectively. Port 1 is the top antenna and port 2 is the side antenna.

low band, the correlation is above the required 0.5 in most of the band. This is both when sweeping the top and the side tuners.

The efficiency sweep results can be seen in Figure 8.8. For the top antenna, the low band can almost be covered totally at -3 dB efficiency which is very good. The high band has a notch from 1905 MHz to 2089 MHz but apart from this, the entire high band can be covered at an acceptable efficiency. The side antenna can be tuned to cover the high end of the low band at an efficiency above -3 dB while the lower part does only reach between -9 dB and -6 dB. The high band has a notch from 1825 MHz to 2010 MHz but has a good efficiency outside this band.

(a) Sweeping C_1 and fixing C_2 .(b) Sweeping C_2 and fixing C_1 .Figure 8.7: Correlation between antennas when sweeping tuning capacitors. Here, C_1 and C_2 are the tuning capacitor for the top and side antenna, respectively.(a) Sweeping C_1 and fixing C_2 .(b) Sweeping C_2 and fixing C_1 .Figure 8.8: Efficiency for each antenna when sweeping the tunable capacitors. Here, C_1 and C_2 are the tuning capacitor for the top and side antenna, respectively.

8.2.2 User Effect Simulations

In this section, the modified monopole antenna will be simulated in practice use with an user. The antenna position for each simulation is shown in Figure 8.9.

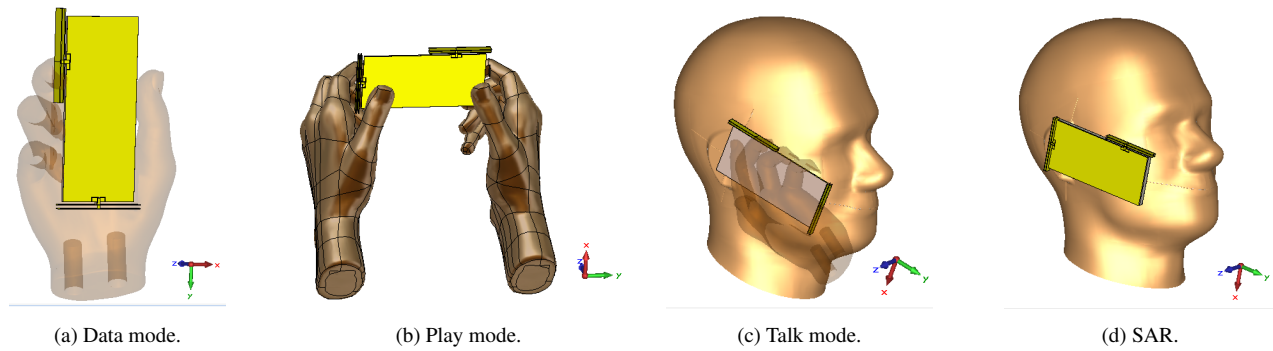


Figure 8.9: MIMO modified monopole antenna position for each user effect simulation.

Data Mode

The S-parameter sweeps can be seen in Figure 8.10. As seen from the sweep, both antennas are able to cover most of the bands. In the low band both antennas are able to cover the entire band at a 4 dB return loss. The high band is covered quite well for both antennas with an exception at 1848 MHz where the return loss drops to 2 dB. In the previous user effect simulations, it was observed that user effects caused detuning. However, this does not seem to be the case with this antenna when simulated in data mode. The maximum obtainable bandwidth can be seen in Table 8.2. Generally, the bandwidth is low for both antennas with only the top antenna fulfilling the low band bandwidth requirement. The results are as expected, as the user causes the return loss to drop. This, however, should not be a problem as the bandwidth is significantly higher at 4 dB return loss. The lowest isolation simulated is at 6 dB in the low band. Generally, the isolation is high in the high band but could cause some capacity problems in the low band.

Antenna	Band	Start [MHz]	Stop [MHz]	Bandwidth [MHz]
Top	Low	826	908	82
Side	Low	712	747	35
Top	High	2151	2471	320
Side	High	1977	2269	292

Table 8.2: Modified monopole antenna in data mode. Maximum bandwidth obtained in the low and high band for the top and the side antenna, respectively.

The S-parameter sweeps can be seen in Figure 8.10.

The correlation between the top and side antenna can be seen in Figure 8.11. It is seen that the correlation is slightly better than in free-space but is still quite high in the low band.

The efficiency sweep can be seen in Figure 8.12. The low band efficiency has dropped, for both antennas, to between -9 dB and -6 dB. In the high band, the both antennas generally have an efficiency above -6 dB although both have a notch where the efficiency drops.

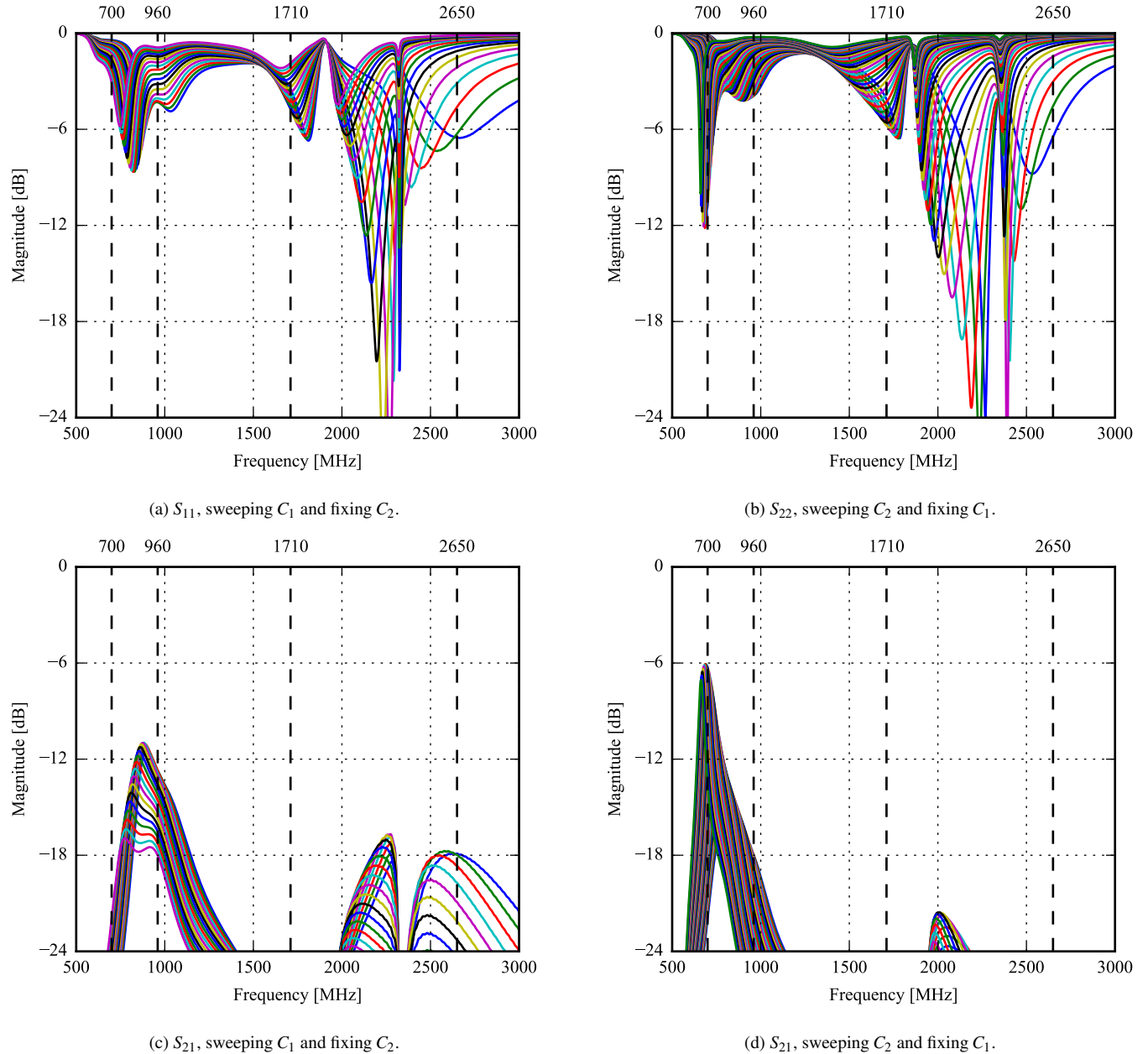


Figure 8.10: S-parameter sweep in data mode for tuning the shunt capacitor of each antenna, C_1 and C_2 for port 1 and 2, respectively. Port 1 is the top antenna and port 2 is the side antenna.

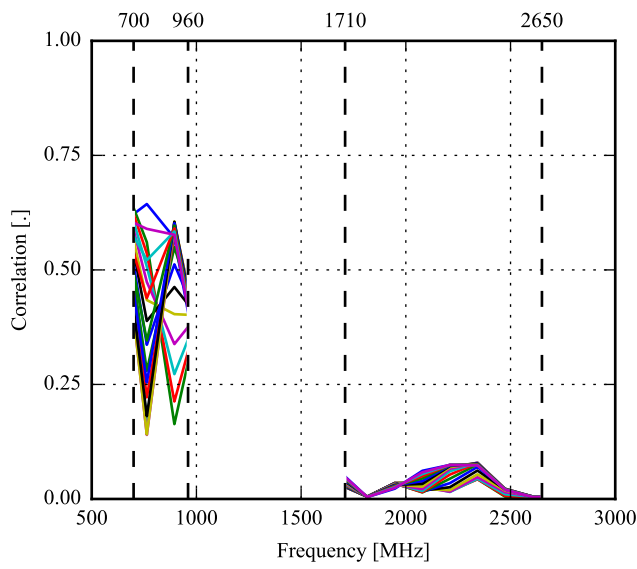
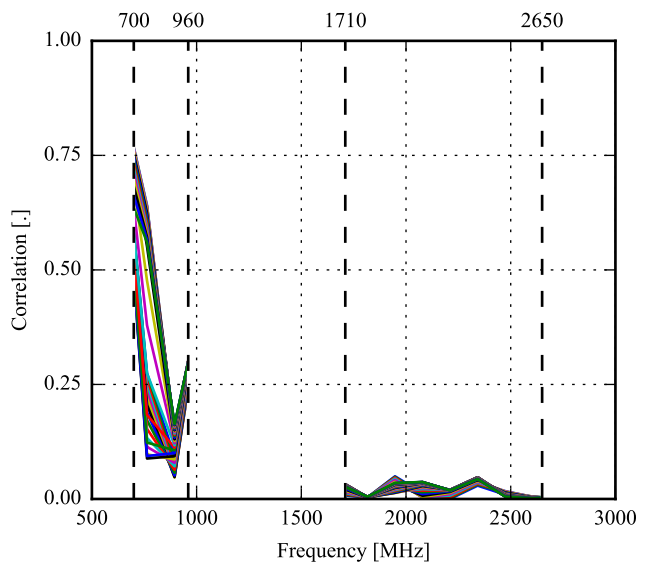
(a) Sweeping C_1 and fixing C_2 .(b) Sweeping C_2 and fixing C_1 .

Figure 8.11: Modified monopole antenna in data mode. Correlation between antennas when sweeping tuning capacitors. Here, C_1 and C_2 are the tuning capacitor for the top and side antenna, respectively.

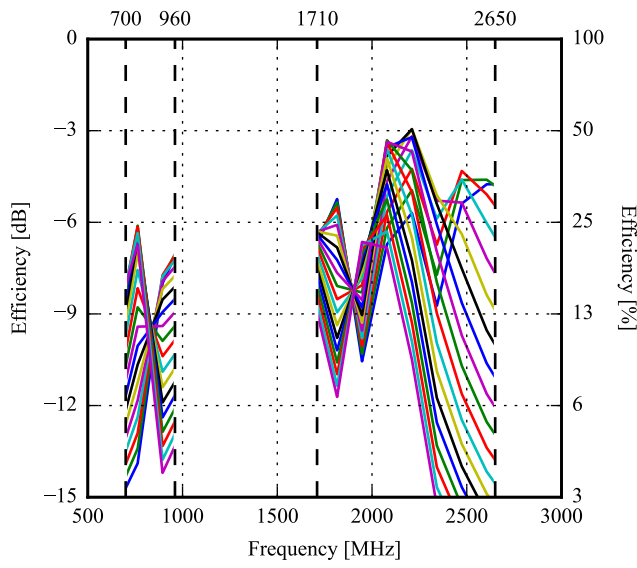
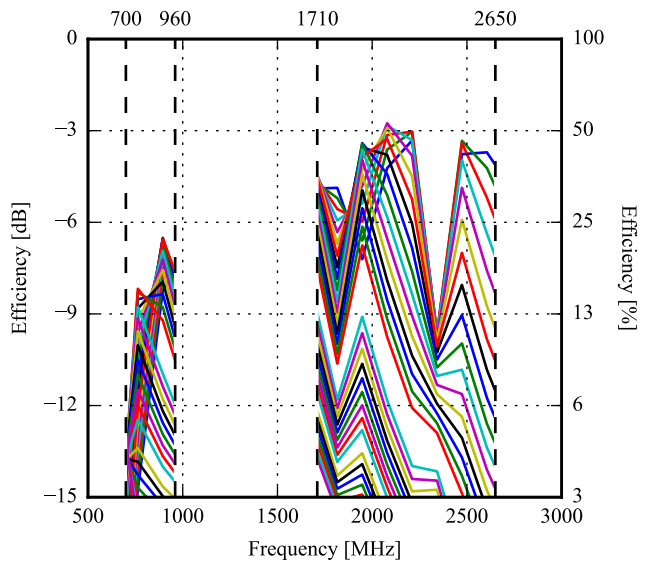
(a) Sweeping C_1 and fixing C_2 .(b) Sweeping C_2 and fixing C_1 .

Figure 8.12: Modified monopole antenna in data mode. Efficiency for each antenna when sweeping the tunable capacitors. Here, C_1 and C_2 are the tuning capacitor for the top and side antenna, respectively.

Play Mode

The S-parameter sweeps can be seen in Figure 8.13. The maximum bandwidth can be seen in Table 8.3. Compared to the data mode, the play mode has a slightly higher bandwidth in general but is more detuned. Both antennas almost cover the required bandwidth but are having some trouble at 1800 MHz where the return loss drops to 2 dB. The side antenna is unable to cover the low band at 6 dB return loss, but covers the band at 4 dB. The isolation is slightly higher than the data mode, with a minimum isolation of 7 dB in the low band. In the high band, the isolation is above 14 dB and should not cause any problems.

Antenna	Band	Start [MHz]	Stop [MHz]	Bandwidth [MHz]
Top	Low	876	965	89
Side	Low	804	913	111
Top	High	2177	2536	303
Side	High	2022	2325	359

Table 8.3: Modified monopole antenna in play mode. Maximum bandwidth obtained in the low and high band for the top and the side antenna, respectively.

The correlation between the top and side antenna can be seen in Figure 8.14. The correlation is still quite high in the low band – especially when sweeping the top tuner. The high band correlation is generally low.

The efficiency sweep can be seen in Figure 8.15. For the top antenna, both the low band and high band efficiencies have dropped below -3 dB. The efficiency for the side antenna has also dropped in both the low band and high band and is, in general, 3 dB lower compared to the free-space efficiency. As expected, both antennas have a drop in efficiency around 1800 MHz.

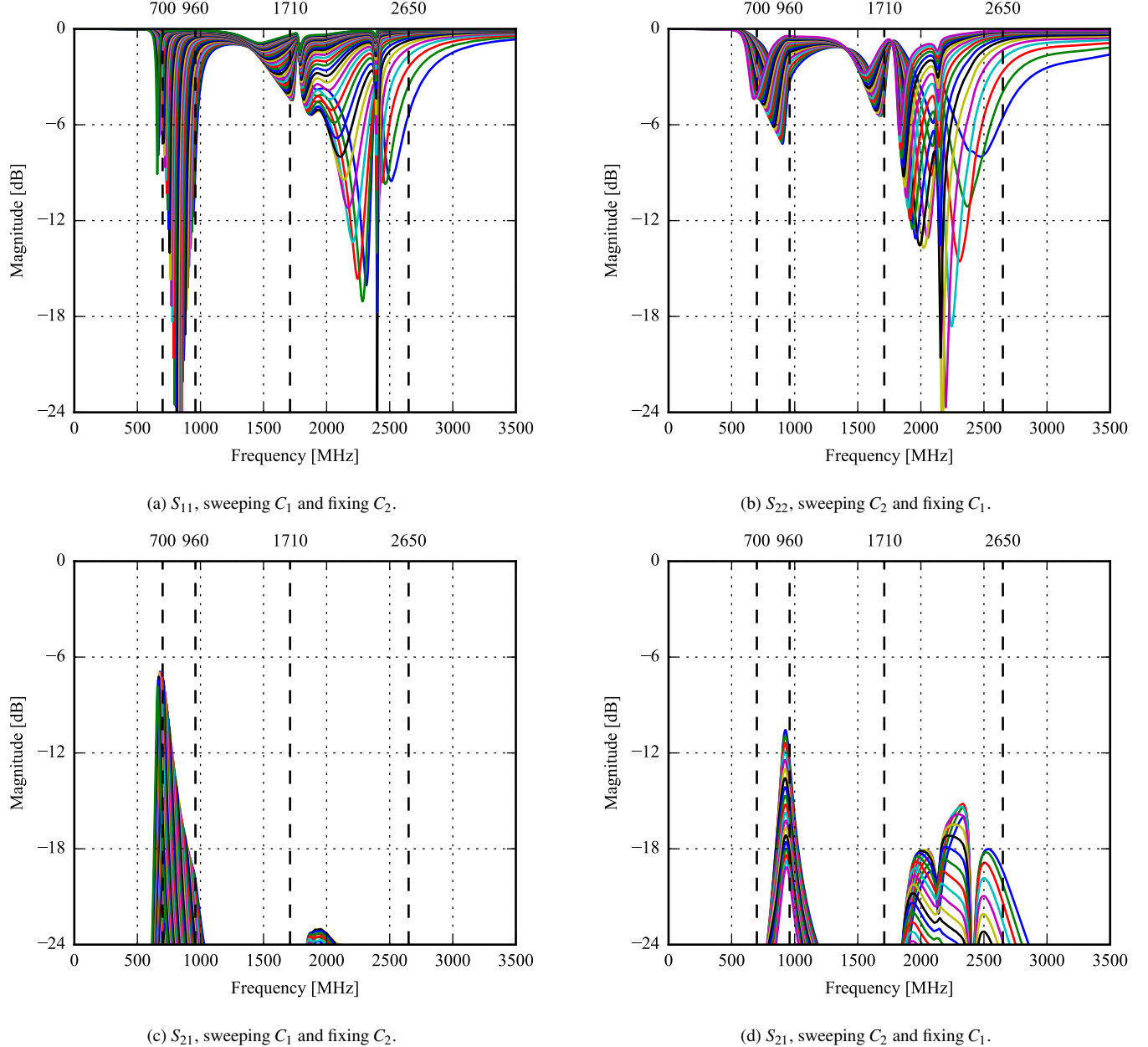


Figure 8.13: S -parameter sweep in play mode for tuning the shunt capacitor of each antenna, C_1 and C_2 for port 1 and 2, respectively. Port 1 is the top antenna and port 2 is the side antenna.

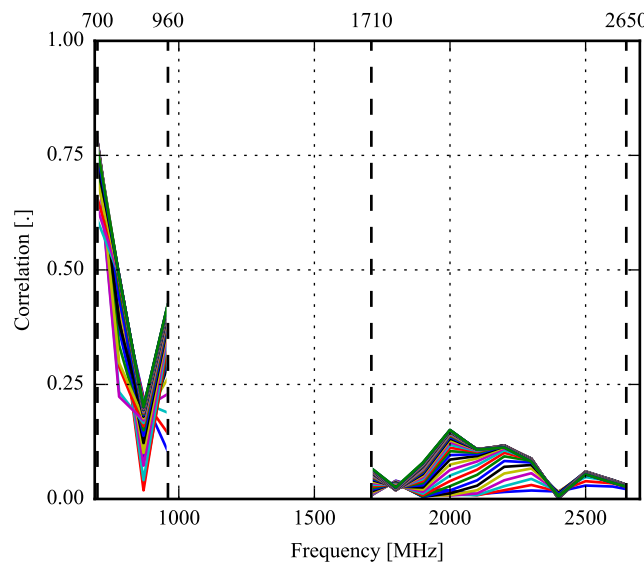
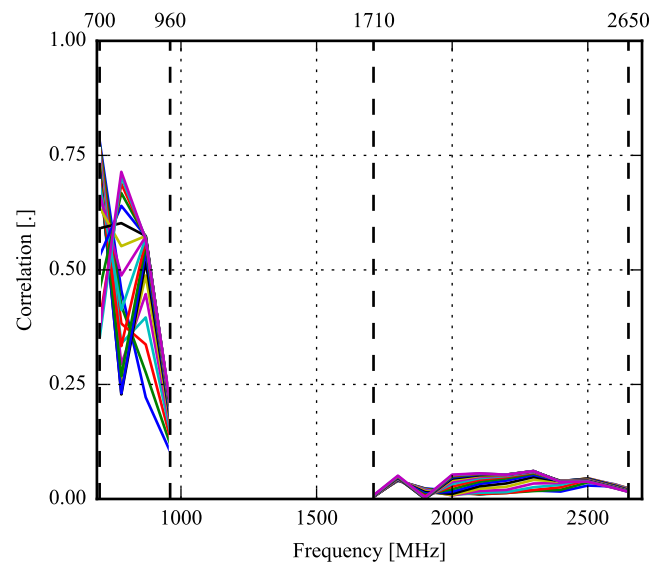
(a) Sweeping C_1 and fixing C_2 .(b) Sweeping C_2 and fixing C_1 .

Figure 8.14: Modified monopole antenna in play mode. Correlation between antennas when sweeping tuning capacitors. Here, C_1 and C_2 are the tuning capacitor for the top and side antenna, respectively.

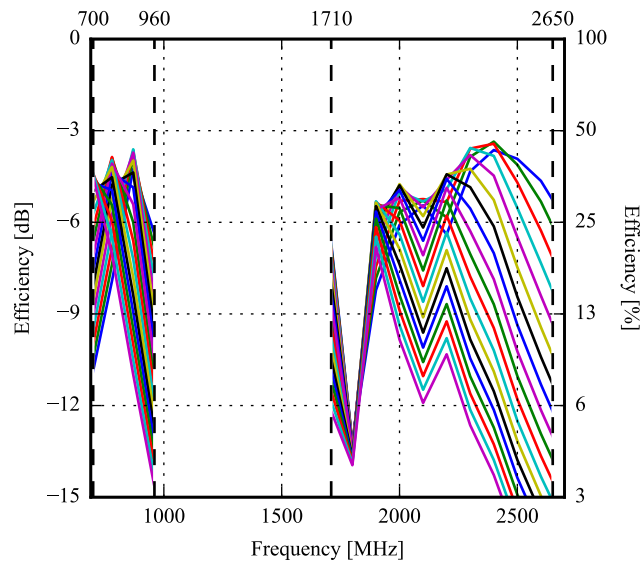
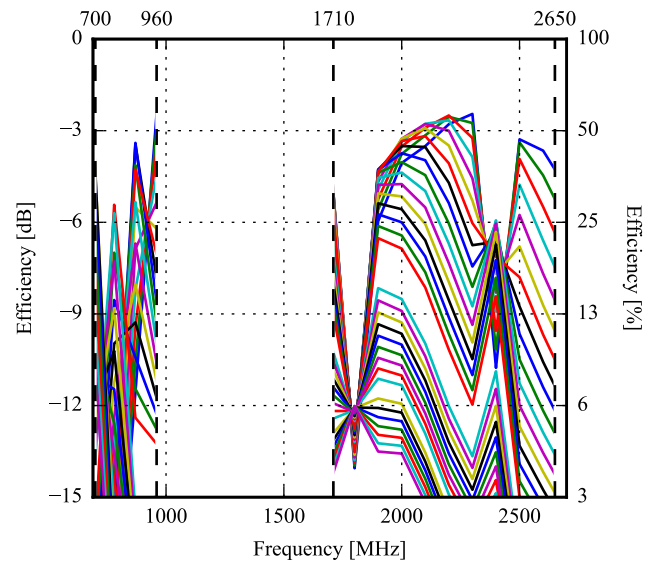
(a) Sweeping C_1 and fixing C_2 .(b) Sweeping C_2 and fixing C_1 .

Figure 8.15: Modified monopole antenna in play mode. Efficiency for each antenna when sweeping the tunable capacitors. Here, C_1 and C_2 are the tuning capacitor for the top and side antenna, respectively.

Talk Mode

The S-parameter sweeps can be seen in Figure 8.16. The maximum obtainable bandwidth can be seen in Table 8.4. The talk mode has the lowest bandwidth compared to the other user effect simulations. This is expected, as the talk mode experiences loss from both the head and the hand. Compared to the previous user effect simulations, the talk mode also has the highest detuning for both antennas. The sweep shows that both antennas are able to cover most of the required bandwidth but experiences some problems in the low band. The top antenna is able to cover the entire low band at 4 dB return loss, but the side antenna has some trouble covering the frequencies around 900 MHz to 960 MHz where the return loss drops to 2 dB.

As a result of the loss from both the head and the hand, the isolation is generally high for both antennas. The minimum isolation is within the low band at 13 dB which is quite high compared to the data and play mode.

Antenna	Band	Start [MHz]	Stop [MHz]	Bandwidth [MHz]
Top	Low	796	825	39
Side	Low	726	770	44
Top	High	2303	2519	219
Side	High	1958	2262	304

Table 8.4: Modified monopole antenna in talk mode. Maximum bandwidth obtained in the low and high band for the top and the side antenna, respectively.

The correlation between the top and side antenna can be seen in Figure 8.17. The correlation is very poor in this scenario, exceeding 0.5 in many parts of the low band. The high band the correlation is below 0.2, which is acceptable.

The efficiency sweep can be seen in Figure 8.18. For the low band, the efficiency has dropped to less than -10 dB for both antennas. In the high band, both antennas generally have an efficiency above -10 dB except for a notch at around 1900 MHz to 2000 MHz. Compared to the data and play mode, the talk mode has the lowest efficiency which also should be expected, considering the loss from both the head and the hand.

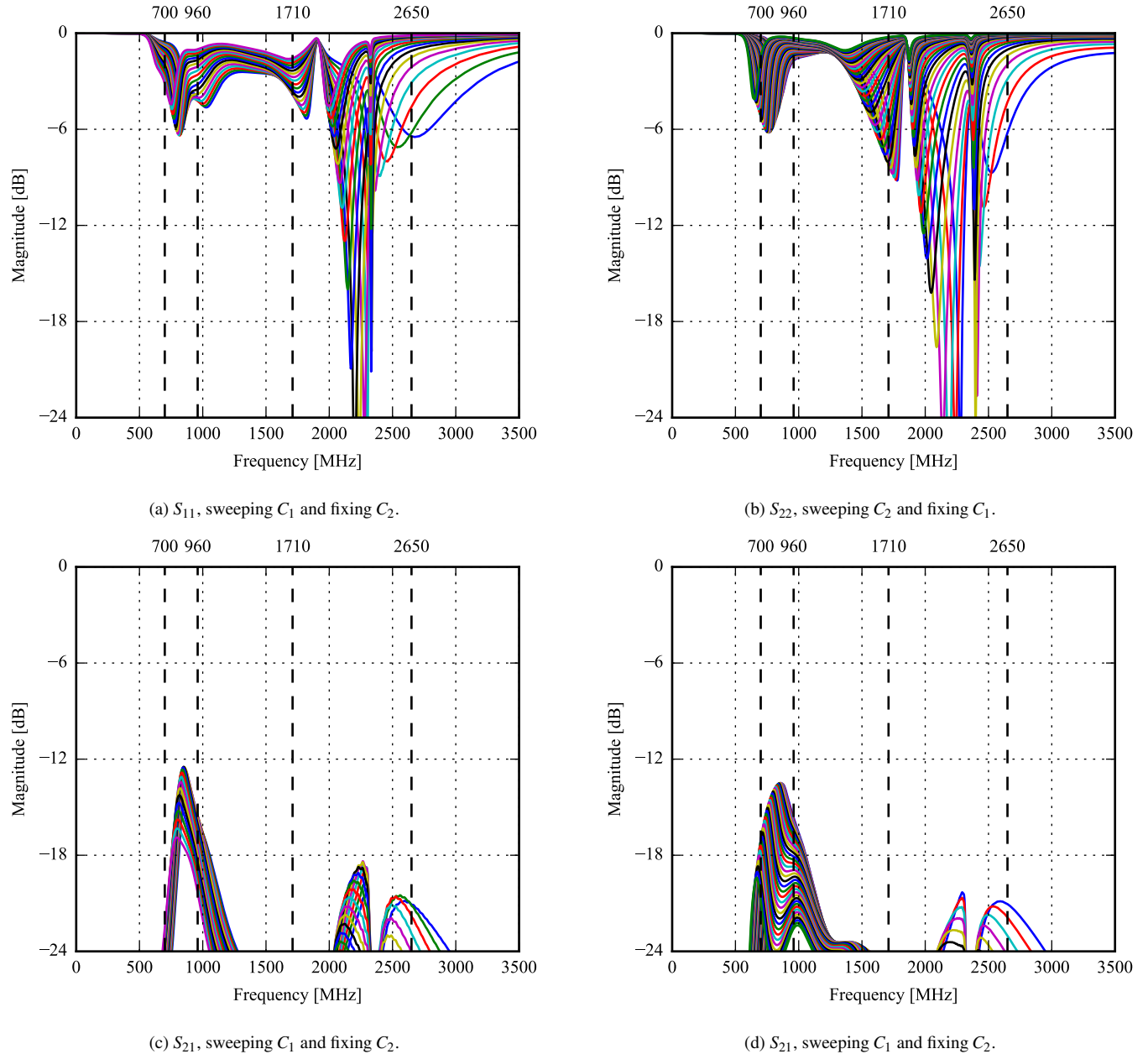


Figure 8.16: S-parameter sweep in talk mode for tuning the shunt capacitor of each antenna, C_1 and C_2 for port 1 and 2, respectively. Port 1 is the top antenna and port 2 is the side antenna.

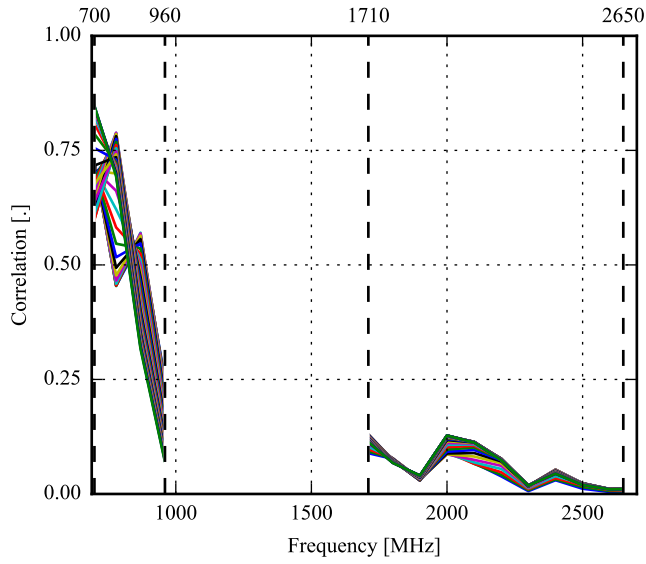
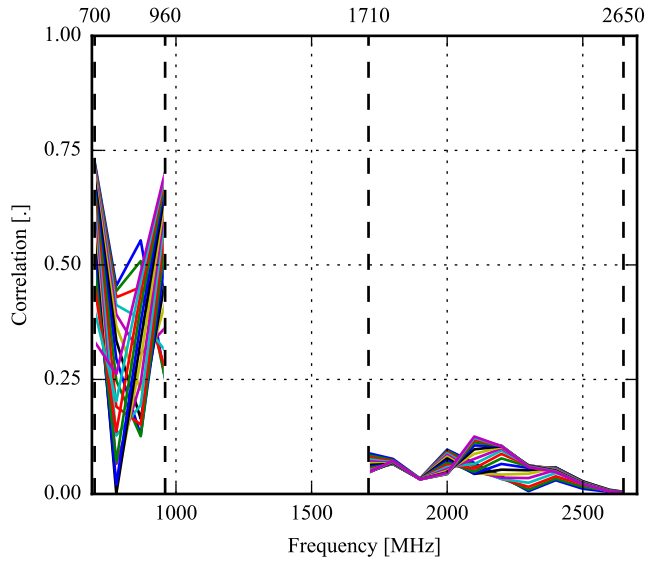
(a) Sweeping C_1 and fixing C_2 .(b) Sweeping C_2 and fixing C_1 .

Figure 8.17: Modified monopole antenna in talk mode. Correlation between antennas when sweeping tuning capacitors. Here, C_1 and C_2 are the tuning capacitor for the top and side antenna, respectively.

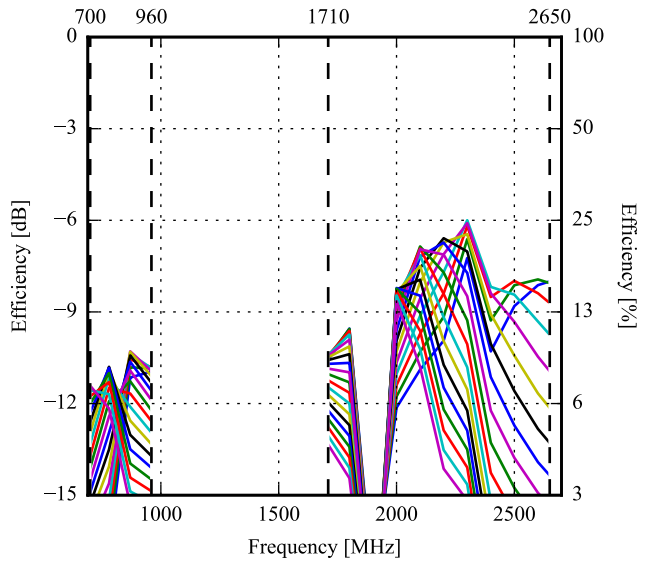
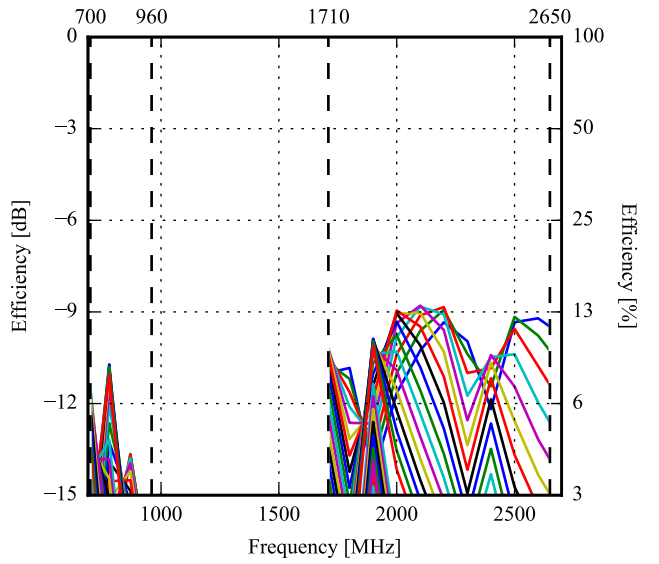
(a) Sweeping C_1 and fixing C_2 .(b) Sweeping C_2 and fixing C_1 .

Figure 8.18: Modified monopole antenna in talk mode. Efficiency for each antenna when sweeping the tunable capacitors. Here, C_1 and C_2 are the tuning capacitor for the top and side antenna, respectively.

SAR

The SAR simulation results can be seen in Figure 8.19. As seen from the figure, the SAR values for both the top and the side antenna fulfills the requirement. The top antenna has the highest SAR value of 1.5 W/kg in the high band and the side antenna has a maximum SAR value of 0.6 W/kg in the high band.

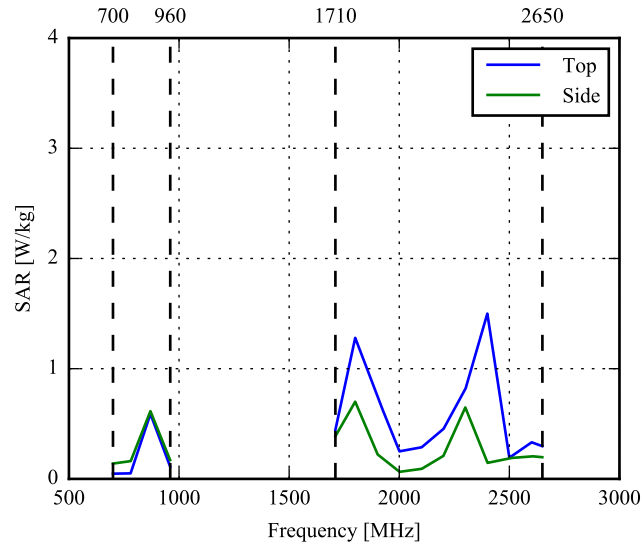


Figure 8.19: SAR simulation of the modified monopole antenna.

Preliminary Conclusion

The free-space and the user effect simulations for the modified monopole antenna have been carried out. The free-space simulation shows some promising results in the bandwidth and with an efficiency above -3 dB in most of the required bandwidth. As expected, the user effect simulations resulted in lower bandwidth and detuning of the frequency. The talk mode simulation shows the worst detuning and bandwidth coverage compared to the data and play mode simulations. However, in the worst case scenario, talk mode, the antennas are still able to cover the desired bandwidth when tuned. The data and play mode experiences some problems with the isolation loss and some improvements might be necessary to increase the isolation.

Generally, the correlation is quite high in the low band for all the simulations. The talk mode has the highest correlation value at 0.8 in the low band compared with the other user effects. This should be taken into consideration, as it could cause some MIMO capacity problems in the low band.

8.2.3 Measurements

The above simulated antennas have been built and soldered onto the PCB described in the introduction. The component values for the matching network are shown in Figure 8.20. The measured S-parameters are shown in Figure 8.21. When compared to the simulations in Section 8.2.1, it is seen that the antenna indeed detunes as expected. However, the bandwidth is severely reduced and, even with different values for the matching network, the desired bandwidth at 6 dB return loss could not be obtained.

In order to obtain better results, the transmission lines on the board have been modified for the final design and measurement. This will be described in the next section.

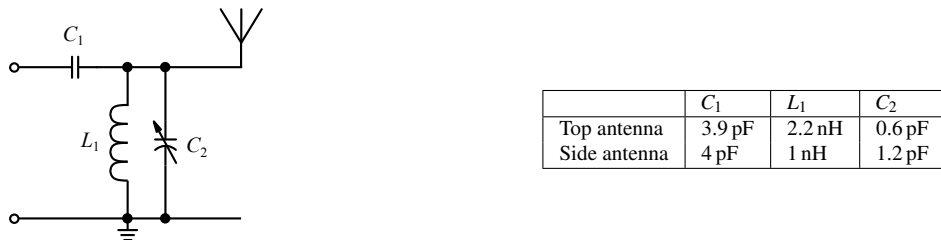


Figure 8.20: Matching circuit for the modified monopole prototype. These are the component values where the bandwidth is found to be the largest.

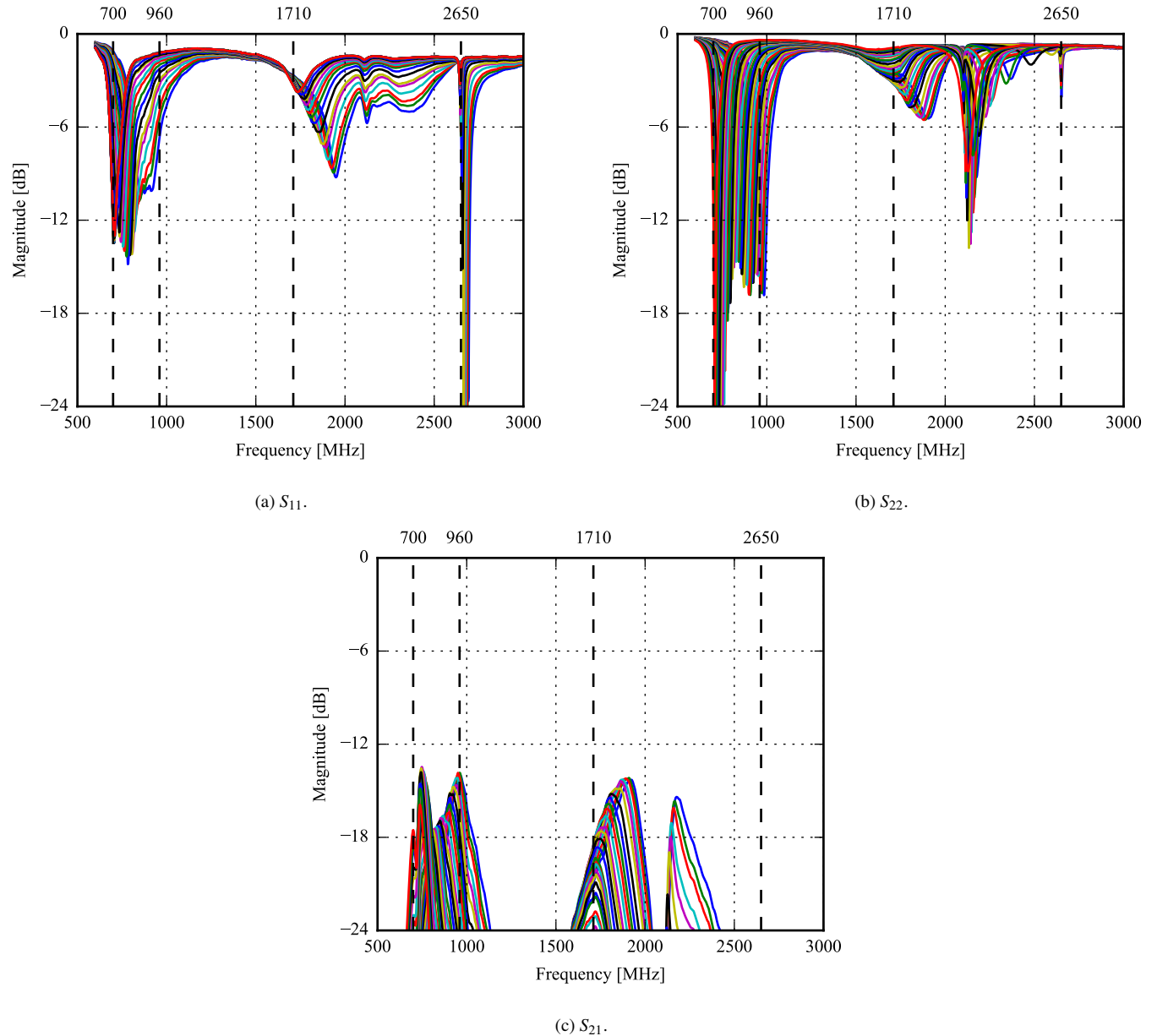


Figure 8.21: S -parameters for the modified minimized monopole prototype. The top tuner is swept from approximately 0.6 pF to 6 pF and the side-tuner is swept from approximately 1.2 pF to 12 pF. The two tuners are tracking the first half of the sweep.

8.2.4 Final Design and Measurements

In this section, the final design with all above mentioned improvements will be presented. The design is shown in Figure 8.22 and dimensions of the antenna elements are the same as shown in Figure 8.5. As shown in Figure 8.22, a capacitor has been added on each transmission line, from SMA to matching network, improving the return loss significantly. The matching network is nearly the same as in Figure 8.20. The exact component values are printed on Figure 8.22.

The measured S -parameters are shown in Figure 8.23. For the top antenna, the tunable bandwidth in the low band (by 960 MHz) is 130 MHz and can be swept all the way down to 700 MHz. The high band can be covered from 1710 MHz to around 2450 MHz. There is still a problem covering the band from 2550 MHz to 2650 MHz but all bands from 700 MHz to 2400 MHz can be covered. For the side antenna, the tunable bandwidth by 960 MHz is 75 MHz and can be swept all the way down to 700 MHz. The high band covers from 1710 MHz to 1975 MHz and from 2095 MHz to 2275 MHz. The impedance bandwidths are summarized in Table 8.5.

The measured efficiency is shown in Figure 8.24. The top antenna is able to cover the low band at -4 dB efficiency and the high band at -3 dB from 1710 MHz to 2430 MHz. The side antenna is not as good and is only able to cover the low band at -10 dB efficiency between -10 dB to -4 dB. The high band has two resonances and is covered at -3 dB from 1710 MHz to 1960 MHz and

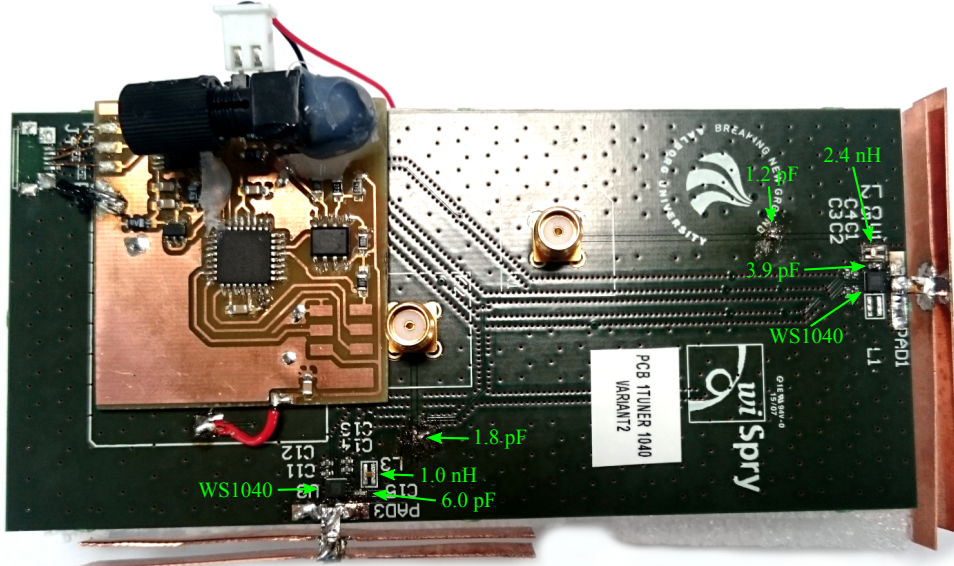


Figure 8.22: Final antenna design with capacitors added to the transmission line to improve high band performance.

Antenna	Band	Start [MHz]	Stop [MHz]	Bandwidth [MHz]
Top	Low	828	958	130
Side	Low	935	1010	75
Top	High	1773	2414	641
Side	High 1	1815	1980	165
Side	High 2	2166	2262	96

Table 8.5: Maximum measured -6 dB impedance bandwidth of the final antenna design.

from 2130 MHz to 2260 MHz. Both antennas shows a problem covering the highest bands above 2550 MHz.

From the measurements it is seen that the top antenna is performing well in all bands except the bands from 2550 MHz to 2650 MHz. The side antenna does not perform quite as good but is piecewise acceptable – especially in the high bands.

Conclusion

Both the simulations and the measurements on the modified monopole antenna are now done. Comparing the free-space simulation and measurement S-parameters, it is clear that the prototype antennas are experiencing some detuning in the high band. Both antennas are especially having trouble from 2450 MHz to 2650 MHz. The modified monopole antenna, with the extra arms, was designed to create a resonance at a higher frequency. Unfortunately, it was not possible to sweep the extra resonance, which resulted in a frequency gap that both antennas are unable to cover with more than 2 dB return loss. The low band simulation and measurement looks similar with a slightly lower bandwidth coverage for the measurements and a lower return loss for the top antenna measurement.

The measured isolation is generally higher than the simulated. The measured low band isolation is 6 dB higher than the simulated for both antennas. In the high band, it is the opposite case, where the simulation is higher than the measured, especially for the top antennas. However, this should not be a problem as the measured isolation is above 12 dB in the required bandwidth.

The measured efficiency is, as expected, generally lower than the simulated efficiency. As predicted, the most significant efficiency drop is in the high band, which is caused by the detuning. The measured low band also experiences a drop of 2 dB and 3 dB for the top and side antenna, respectively, when compared with the simulation.

The final design shows promising results for both antennas, but could also use some improvement in the high band. Both antennas fulfill the bandwidth requirements in the low band and are able to sweep the entire low band. The high band performance could use some improvement – especially for the side antenna bandwidth coverage. Overall there has been problems with the bandwidth coverage of the side antenna in all the prototypes, when used with the tuner PCB. This is also the case for the triangle-feed antenna on the tuner PCB, Section 8.1, which is also experiencing the same detuning problems as the modified monopole antenna.

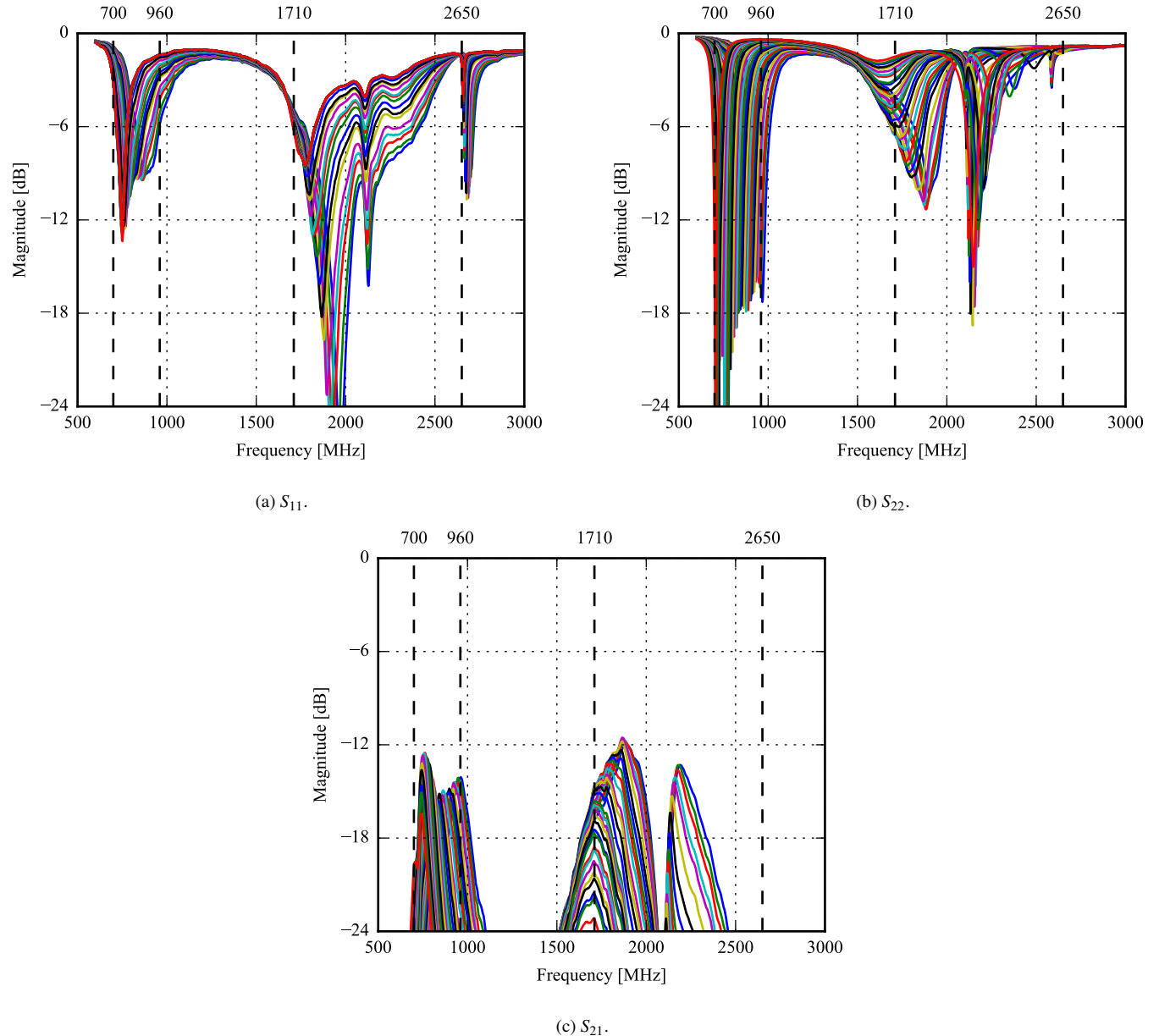


Figure 8.23: S-parameters of the final antenna design. The top antenna is swept from approximately 0.6 pF to 6 pF and the side antenna from approximately 1.2 pF to 12 pF. The tuners are tracking the first half of the sweep.

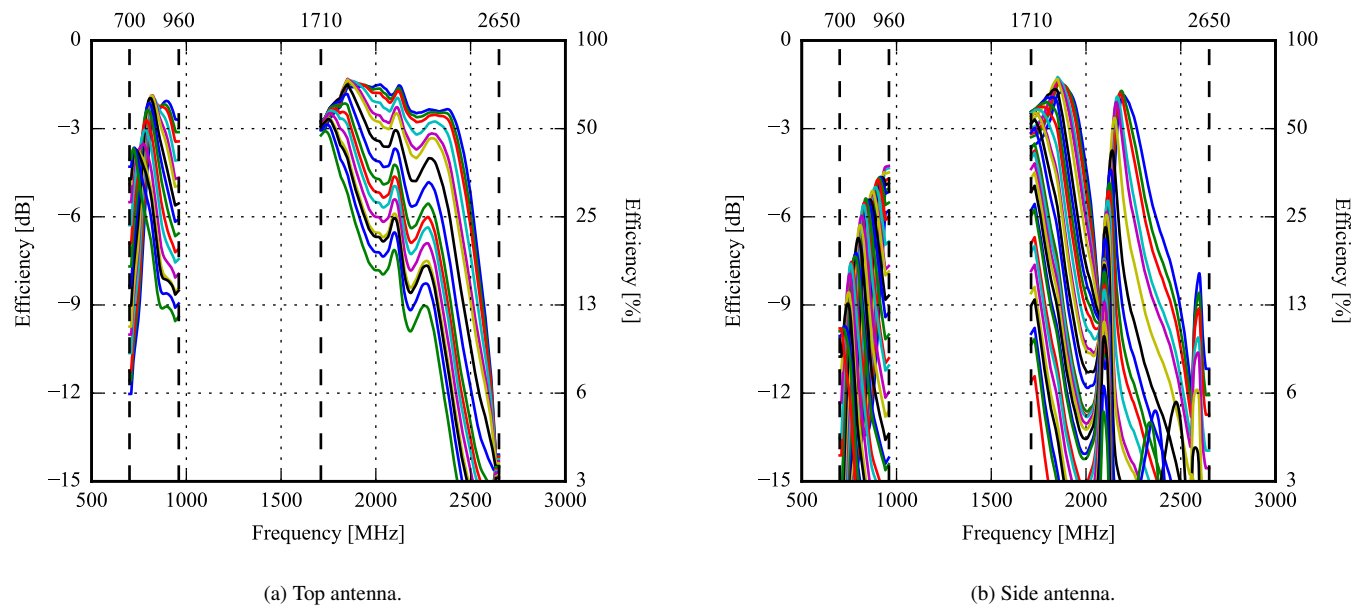


Figure 8.24: Total efficiency of the final antenna design. The top antenna is swept from approximately 0.6 pF to 6 pF and the side antenna from approximately 1.2 pF to 12 pF. The tuners are tracking the first half of the sweep.

Chapter 9

Conclusion

This report has documented the development of digitally tunable LTE antennas supporting MIMO.

Three preliminary designs, which all cover the required bands in free-space, have been designed. Each design has its strengths and weaknesses and they all use a ground clearance of 9.5 mm to 10 mm for the top antenna and 7 mm to 9.5 mm for the side antenna.

The three preliminary designs were also simulated, in the proximity of a user, in data mode, play mode, and talk mode. Here, the triangle-feed designs as well as the dual-feed design generally held up the best although severe detuning was apparent in every design. The Specific Absorption Rate (SAR) was also simulated and every design met the requirements of a maximum SAR of 2 W/kg.

The simulations were simplified, not taking into account non-ideal components, component placement, and transmission lines. To get a more accurate picture of the performance, prototypes were built of the three preliminary designs. The S-parameters and the total efficiency were measured for a variety of discrete tuning capacitor values. The folded monopole design did not cover the low band very well and the dual-feed design was not tunable in the side antenna. For this reason, the triangle-feed design was chosen as the first design to be realized on a PCB with a MEMS tuner.

As the space for antennas in today's mobile phones is limited by the large screen size, a smaller design was developed to also be implemented with the tuner PCB. An investigation of the effect of lowering the ground clearance was made, and showed that a very reasonable tunable design could be realized with only 5 mm of ground clearance – on a par with the preliminary designs over the tunable range. The minimized design was measured with the tuner PCB but showed problems covering the high band. The design was therefore modified with an extra pair of arms before the final implementation with the tuner PCB.

The triangle-feed design, like the minimized design, showed problems covering the high end of the high band when moved to the tuner PCB. The low band, for both the top and the side antenna, as well as most of the high band for the top antenna was covered acceptably, while the side antenna was not resonating as required in the high band.

The modified minimized design, while being slightly better in the high band, still had trouble in the very high end of the spectrum. For the final design, it was observed that adding a small amount of shunt capacitance near the middle of the transmission lines, going from the SMA connectors to the antennas, improved the high band performance vastly. The resulting design showed that the top antenna was able to cover the whole low band at above -4 dB total efficiency and the high band above -3 dB from 1710 MHz to around 2500 MHz. From 2500 MHz and up, the efficiency decreased. The side antenna generally showed a lower bandwidth and efficiency with a total efficiency from -10 dB to -4.5 dB in the low band and an efficiency above -3 dB from around 1710 MHz to around 2300 MHz except for a notch around 2000 MHz. These results show that a low-ground clearance design is possible while still covering most of the LTE bands at an acceptable total efficiency.

The envelope correlation has been simulated for all designs. In order to have good MIMO performance, a low correlation – below 0.5 – is desired. The modified minimized design showed a correlation above 0.5 from 700 MHz to around 900 MHz in free-space which makes it unsuited for MIMO applications in the low band. The correlation is much lower in the high band, so MIMO could still be used at these frequencies. In the user effect simulations, the correlation in the low band generally dropped, making the MIMO useful in part of the low band as well. The high correlation at low frequencies is to be expected as a large part of the ground plane is used as a radiating element for both top and side antenna, making the radiation patterns more similar. MIMO and diversity schemes would therefore be better implemented at higher frequencies.

Antenna	Note	Tuner type	Antenna volume (mm ³)	Antenna area (mm ²)	Total dimensions (mm ³)	η_{tot} of main antenna	
						Low band (%)	High band (%)
Monopole top	Monopole	Discrete	3885	555	130 × 62 × 7	38–60	43–98
Monopole side	Monopole	Discrete	2646	378	130 × 62 × 7	28–64	31–84
Triangle-feed top	Non-resonant and microstrip	Discrete	4340	620	140 × 69 × 7	47–70	59–92
Triangle-feed top	Non-resonant and microstrip	MEMS	4340	620	140 × 69 × 7	46–71	13–67
Triangle-feed side	Non-resonant and microstrip	Discrete	4550	650	140 × 69 × 7	48–72	59–91
Triangle-feed side	Non-resonant and microstrip	MEMS	4550	650	140 × 69 × 7	29–51	< 3–49 [†]
Dual-feed top	Non-resonant	Discrete	2850	570	129.5 × 67 × 6.6	61–94	23–86
Dual-feed side	Non-resonant	Discrete	3087.5	617.5	129.5 × 67 × 6.6	5–43	62–88
Mod. minimized top	Double-monopole	MEMS	2117.5	302.5	130 × 62 × 7	43–65	4–72 [†]
Mod. minimized side	Double-monopole	MEMS	2065	295	130 × 62 × 7	10–37	7–73 [†]
[8] main	Planar ProtoM	MEMS	1170	900	120 × 60 × 1.5	30–57	44–78
[8] aux	Planar ProtoM	MEMS	1170	900	120 × 60 × 1.5	29–57	43–78
[8] main	ProtoM	MEMS	3900	900	120 × 60 × 5	49–72	56–88
[8] aux	ProtoM	MEMS	3900	900	120 × 60 × 5	48–72	55–88
[9]	Monopole	MEMS	1500	?	?	28–60	45–97
[10]	IFA	CMOS	1620	270	110 × 45 × 6	54–65	70–?
[11] RX	Monopoles, not tuned	MEMS	300	300	120 × 55 × 1	50–?	–
[11] TX	Folded IFA, tuned	MEMS	640	160	120 × 55 × ?	32–59	–
[12]	Monopole	CMOS	2400	400	130 × 70 × 6.8	40–63	20–85

Table 9.1: Comparison of reconfigurable LTE antenna designs (measured free-space parameters). The total efficiencies the maximum obtainable bandwidth in-band for all measured capacitor values. [†]Not all of the bands are covered – this is the very-worst case measured in the specified band although most of the band may be covered.

All the measured designs from from the report are summarized in Table 9.1 together with the designs discussed in the introduction, Chapter . Here, the range of total efficiency for each design is shown, for both the low and the high band, as well as the dimensions of the designs.

In the low band, most of the measurements show comparable efficiencies to the state-of-the-art designs. In the high band, the prototypes a PCB with discrete components also show very comparable results. It is clear that the efficiency in the high band is severely lower on the tuner PCB. The small minimum value is due to some part of the high band not being covered while most of the band is covered at above –3 dB.

The top antenna of the modified minimized design, with only 5 mm ground clearance, is very much on a par with designs with much more ground clearance (up to 2500 MHz) while the side antenna suffers from a few in-band notches.

Compared to [8], the area is smaller due to the low ground clearance, while the volume of the antenna is larger as the height is 7 mm. A natural next step would be to try to lower the height to make the design even more compact, as done in [8]. Another next step would be to re-design the PCB to see if the high band performance can be improved. In this case, the RFFE optical interface could be incorporated into the board as well.

A 5 mm version of the triangle-feed design may be successful if capacitance is added to the transmission line as with the modified minimized design. The 10 mm version appeared to be well-behaved so this design might also be good for LTE if it could be minimized.

The results show that it is possible to design LTE antennas with only 5 mm ground clearance while still having an acceptable total efficiency over the range of the tuner.

Part III

Appendix

Appendix A

Automatic Testing

A.1 Optical RFFE Communication

The WiSpry WS1040 digital capacitor is adjusted using the MIPI RFFE (RF Front End) protocol. In order to simplify sweep-measurements, which are a large part of this project, it is advantageous to be able to adjust the capacitance from outside the anechoic chamber. As having a long copper cable running from the antenna to outside the chamber may disturb the measurement significantly, a fiber optic cable will be used for communication between computer and antenna. As the fiber optic cable contains no metal, it should be less disturbing to the measurements.

The RFFE protocol requires three signals:

SDATA Bi-directional serial data signal carrying ones and zeros from the master (PC) to the slave (WS1040) and back. Both the master and the slave can drive this line.

SCLK Serial clock. The master both clocks data to and from the slave.

VIO Reference voltage of 1.8 V. The SDATA and SCLK signals swing from 0 V to VIO so VIO is the common reference – not ground!

The WS1040 chip is rated for a supply voltage between 2.7 V and 5.0 V, so the VIO voltage is generated separately for communication.

The purpose of this communication link is solely to write to registers in the WS1040 so only one-way communication is necessary. To minimize the number of fibers, it is chosen to communicate via UART (Universal Asynchronous Receiver/Transmitter) over the fiber and generate the RFFE signals locally by a microcontroller at the antenna side. This requires only one fiber to be connected. In case a response were required, two fibers could be connected.

The schematics are shown in Figure A.1 and Figure A.2. The design files for the board can be downloaded at <http://github.com/16gr1051>. Both the transmitter and receiver is included on the PC-side board. On the PC side, the RX and TX lines are connected to a PC using an USB to UART adapter (PC2102) with external connections for an FTDI breakout board. On the antenna side, the RFFE_SCLK, RFFE_SDAT, and Vrffe lines are connected to the WS1040 chip.

In the following, each part of the design is described.

A.1.1 USB to Serial Adapter

In order to communicate from the PC using UART, a USB-to-serial adapter (PC2102) is used. The input is simply a USB connection to the PC and the output is a RX and a TX line for the optical circuit. For redundancy, the circuit is laid out with connections for an external FTDI breakout board.

A.1.2 Transmitter

The transmitter is made up from an open-collector comparator. The UART TX signal is connected to the inverting input of the comparator and a voltage divider, dividing the supply range in half, is connected to the non-inverting input. This means that when the input-signal is high (above $V_{cc}/2$), the comparator will pull down the cathode of the LED down to ground, lighting up the LED. When the input-signal is low (below $V_{cc}/2$), the output of the comparator will be floating, and no current will run through the LED – no light.

A.1.3 Receiver

The light detector (IF-D91) functions as a light-dependent current source. When lit, around $3\ \mu\text{A}$ is supplied and when dark, around $10\ \text{nA}$ is supplied. When this current is supplied to a $100\ \text{k}\Omega$ resistor, the voltage will alter between $300\ \text{mV}$ (light) and $1\ \text{mV}$ (dark).

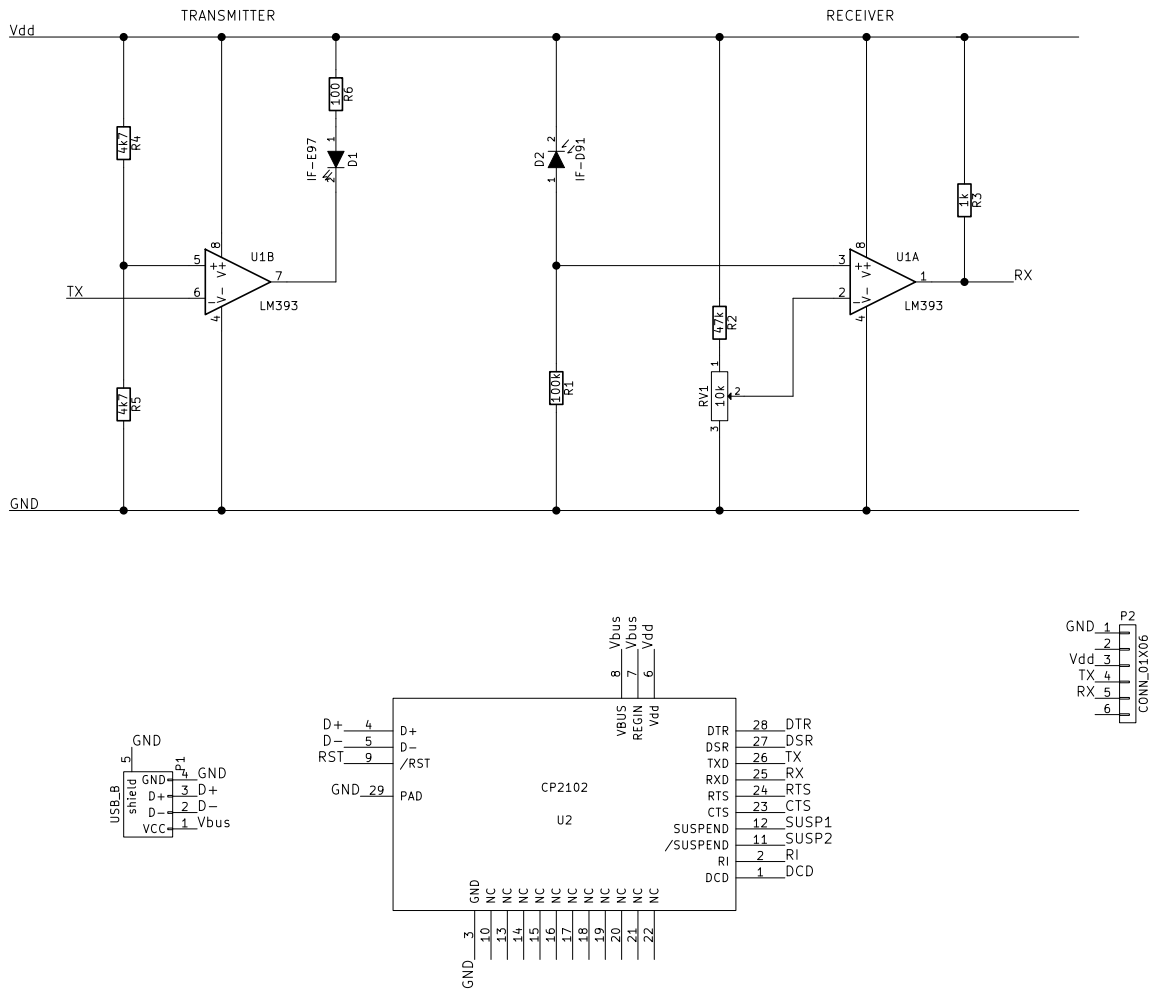


Figure A.1: Schematic for optical RFFE communication – PC-side.

The voltage divider on the inverting input is dimensioned to set a threshold in between of these two values. By the pull-up resistor on the output, this means that the output will be high when light is supplied to the light detector and the output will be low when no light is supplied.

A.1.4 Microcontroller and Protocol

The microcontroller is an Atmel ATmega168. It receives one-byte commands from the PC through UART at 9600 baud, 8 bit, no parity, one stop bit (9600 8N1). The commands are ASCII characters as described in Table A.1. The source code for the microcontroller can be downloaded at <http://github.com/16gr1051>.

Two possible addresses are valid for the WS1040, making it possible to communicate with two separate chips on the same bus. The address depends on the high/low state of the USID pin on the WS1040. The WS1040 contains four capacitors which can be set individually. The capacitance range can be increased by connecting capacitors in parallel.

The RFFE command used for writing to a register is shown in Figure A.3. The sequence is clocked out serially. A one bit is observed when the SCLK line goes high while the SDATA line is high and a zero bit is observed when the SCLK line goes high while the SDATA line is low. The start, parity, and bus park condition are described as follows:

Start SDATA pulses high while the SCLK line is kept low.

Parity The parity is low if the number of ones in the preceding byte is odd. The parity is high if the number of ones in the preceding byte is even.

Bus park SCLK is pulsed while SDATA is kept low (i.e. a zero is clocked out).

An example of an RFFE Write Register command is shown in Figure A.4, where 0x00 is written to register 1 of the slave with address 0b0111. This is the RFFE output when sending the string "Ax0" to the microcontroller, according to Table A.1.

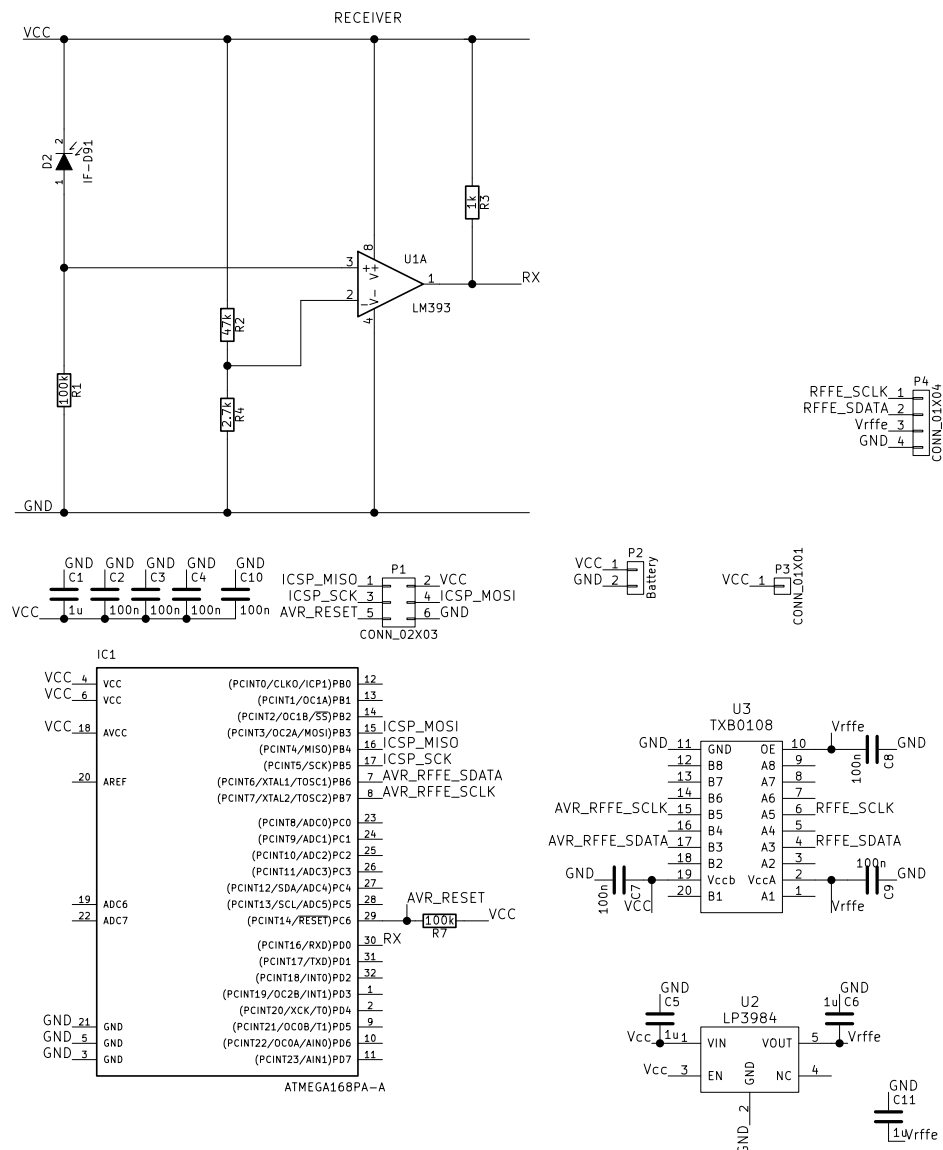


Figure A.2: Schematic for optical RFFE communication – antenna-side.

S	A3	A2	A1	A0	0	1	0	R4	R3	R2	R1	R0	P	D7	D6	D5	D4	D3	D2	D1	D0	P	BP
---	----	----	----	----	---	---	---	----	----	----	----	----	---	----	----	----	----	----	----	----	----	---	----

S	Start condition
A	Slave address
010	Write register command
R	Register to write to
P	Parity bits
D	Value to set the register to
BP	Bus park

Figure A.3: RFFE command for writing to a register.

UART command	Action	Value	Note
A	Set active slave address	0b0111	
B	Set active slave address	0b0110	
x	Set active register	1	Capacitor 1
y	Set active register	2	Capacitor 2
z	Set active register	3	Capacitor 3
t	Set active register	4	Capacitor 4
0	Set register value	0x00	0.30 pF
1	Set register value	0x01	0.39 pF to 0.48 pF
2	Set register value	0x02	0.66 pF
3	Set register value	0x03	0.75 pF to 0.83 pF
4	Set register value	0x04	1.01 pF
5	Set register value	0x05	1.10 pF to 1.19 pF
6	Set register value	0x06	1.37 pF
7	Set register value	0x07	1.46 pF to 1.55 pF
8	Set register value	0x08	1.73 pF
9	Set register value	0x09	1.81 pF to 1.90 pF
a	Set register value	0x0a	2.08 pF
b	Set register value	0x0b	2.17 pF to 2.26 pF
c	Set register value	0x0c	2.44 pF
d	Set register value	0x0d	2.53 pF to 2.62 pF
e	Set register value	0x0e	2.79 pF
f	Set register value	0x0f	2.88 pF to 2.97 pF

Table A.1: UART commands and the resulting action on the microcontroller.

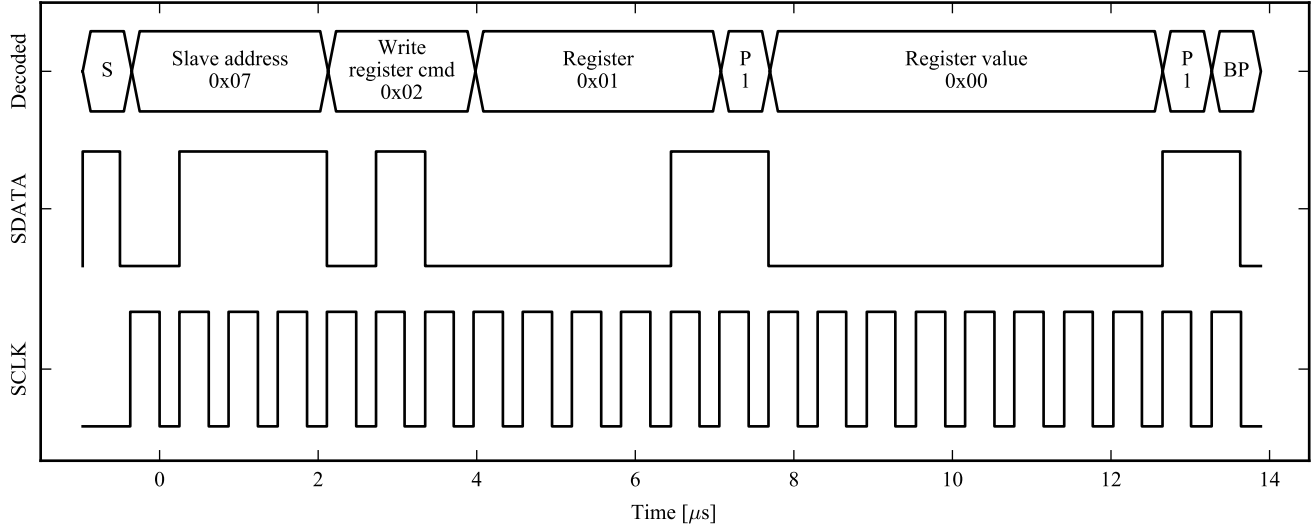


Figure A.4: Example of an RFFE command from the microcontroller.

A.1.5 Level Shifting and WS1040 Interface

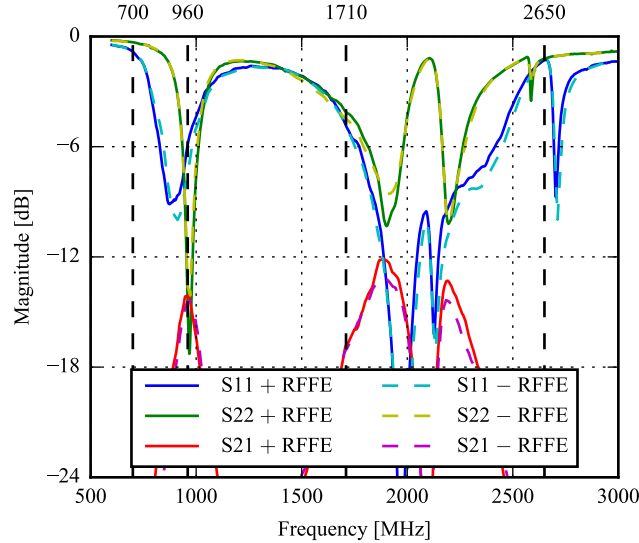
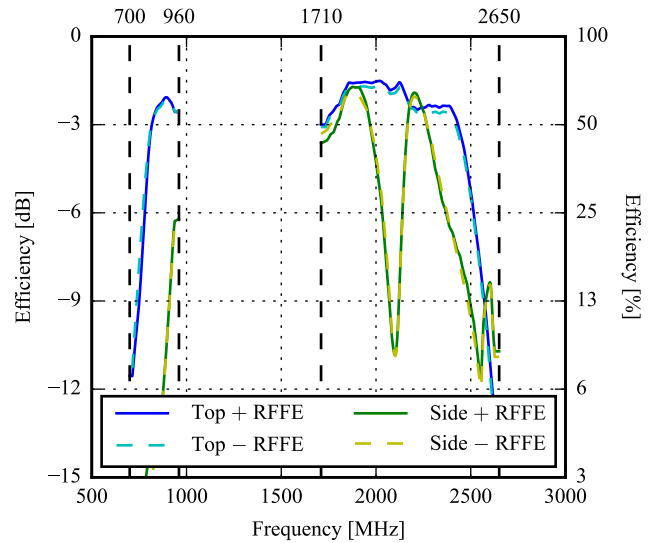
The final part of the circuit is the interface towards the tuner. The microcontroller outputs signals between 0 V and 3.3 V which is not compatible with the tuner. Therefore, a level shifter is inserted, translating the 3.3 V to 1.8 V. The 1.8 V is generated by a low-dropout voltage regulator.

A.1.6 Testing

An antenna board with tuner has been measured on a VNA and in the Satimo chamber, with and without the RFFE adaptor board to check if the S-parameters or total efficiency changes with the adaptor board present. The S-parameters and total efficiency, shown in

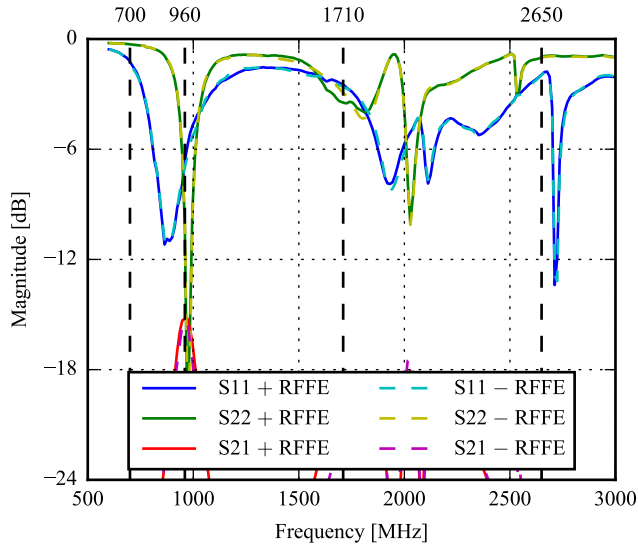
Figure A.5, shows no significant change when adding the RFFE adaptor board. The difference in the S -parameters may be because of slight bending due to handling of the antennas as the measurements were not done on the same day. The efficiency measurements were done the same day and shows no significant change. Another S -parameter measurement is shown in Figure A.6 of another antenna. Here, the measurements are done in direct succession of each other and the S -parameters shows only very little difference.

From the measurements just described, it has been verified that using the RFFE board with a fiber optic cable attached causes no significant change in S -parameters or total efficiency. Therefore, the board can be used for automating tests on a VNA and in the Satimo chamber.

(a) S -parameters.

(b) Total efficiency.

Figure A.5: Comparison of the tuner PCB with and without the RFFE adaptor PCB.

Figure A.6: Comparison of S -parameters of the tuner PCB with and without RFFE adaptor PCB.

A.2 VNA Automatic Test

In order to faster do sweep-measurements on the built prototypes, the VNA measurements have been automated and combined with the optical RFFE adapter. It is possible to control the VNA using GPIB (General Purpose Interface Bus), VISA protocol (Virtual

Instrument Software Architecture), and SCPI (Standard Commands for Programmable Instruments). This has been implemented in Python and is specifically for a Rohde & Schwarz ZVB 8 VNA, which is documented in this appendix. The library can be downloaded at <http://github.com/16gr1051>.

A.2.1 National Instruments GPIB-USB-B Adapter

A NI GPIB USB adapter is used for the communication between the PC and the VNA. For this to work in Linux, a few modifications are needed. First, the ni-gpib kernel module has to be loaded using `modprobe ni_usb_gpib`. Next, a firmware update is needed, which has to be loaded every time. To ease pain, a small script has been made that does this step:

```

1 #!/bin/bash
2 #Firmware files: http://linux-gpib.sourceforge.net/firmware/
3 usbDev=$(lsusb | grep "3923:702b National" | sed 's/:/\ /' | awk '{print $2 "/" $4}'")
4
5 if [ -z "$usbDev" ]; then
6   echo "NIgpib device not found"
7 else
8   modprobe ni_usb_gpib
9   fxload -D /dev/bus/usb/$usbDev -I %/lib/firmware/ni_usb_gpib/niusb_bb_firmware.hex -s %/lib/firmware/
10    ni_usb_gpib/niusb_bb_loader.hex
11 fi

```

A.2.2 Python Library

The procedure for installing this library is shown in Section B.1.

The Python library is based around Pyvisa, which handles the VISA and SCPI protocol part and the communication with the USB GPIB adapter. The Rohde & Schwarz ZVB 8 operating manual [57] contains a chapter with all SCPI commands used. The library handles the setup of the VNA, which includes the correct frequency range, labels, and number of samples. Besides the setup function, it also contains a save function which changes the number of samples and exports the data formatted as a s2p file. Below is an example of initializing the VNA and saving a sweep.

```

1 from vnalib import VNA
2 # Connect to VNA and initialize
3 myVNA = VNA("GPIB0::20::INSTR", "D:\\vna_measurement\\")
4 myVNA.initSettings()
5 # Save s2p file
6 myVNA.save("myfile")

```

Combining with the Optical RFFE Adapter

To fully automate the sweeping process, the code has been combined with the optical RFFE adapter board. The adapter board requires a serial command, which is sent using the pyserial library. The combined program is then able to sweep through every capacitor value and save a file for every measurement. This program is listed below.

```

1 from vnalib import VNA
2 import time
3 import serial
4 serial_port = "/dev/ttyUSB0"
5 basename = "triag"
6
7 # Connect to VNA
8 myVNA = VNA("GPIB0::20::INSTR", "D:\\vna_measurements\\")
9 myVNA.initSettings()
10 input("Perform manual calibration and press Enter...")
11
12 # Start serial port
13 ser = serial.Serial(serial_port)
14 ser.flushInput()
15 ser.flushOutput()
16
17 # Only slave address A = 0x7 is used
18 ser.write(b"Ax0Ay0Az0At0")
19
20 # Start sweep
21 for x in [
22     ["0_0_0_0", b"Ax0Ay0Az0At0"],
23     ["2_0_0_0", b"Ax2Ay0Az0At0"],
24     ["4_0_0_0", b"Ax4Ay0Az0At0"],

```

```

25     ...
26     ["f_f_f", b"AxfAyfAzfAtf"],
27   ]:
28     fname,cmd = x
29     fname = basename + "_" + fname
30     ser.write(cmd)
31     input("")
32     myVNA.save(fname)
33     print("Saved file")

```

A.3 Satimo Automatic Test

The efficiency measurements are, in general, the most time consuming, and automating this process saves a lot of time. Unfortunately, there is no public API or common interface to control the Satimo chamber. Therefore, the only way to control the chamber is to automate the GUI (Graphical User Interface), which is done in Python. The library can be downloaded at <http://github.com/16gr1051>.

A.3.1 Python Library

The procedure for installing this library is shown in Section B.1.

The Python library is based around another library called pywinauto, which is for Windows GUI Automation. Basically it sends “click” and “keystroke” events to specific buttons and input fields programmatically. Another tool called SWAPY was used to find button and input field IDs.

Currently, the created library only supports Satimo Passive measurements, and it is able to initiate a frequency sweep in a given frequency range and number of samples. The library detects when a sweep is done and automatically exports the data in a `trx` file. The library also makes it easier to calibrate Satimo, such that the user only has to change the antenna and press `Enter`, for each reference antenna. Below is an example of calibrating, starting a sweep, and exporting the data.

```

1 import satimopm
2 satimopm.calib()
3 satimopm.satimoSPM(startFreq, endFreq, samples, filename)
4 print("Sweep done")

```

Combining with the Optical RFFE adapter

As with the VNA library, the Satimo automation code can be combined with the optical RFFE adapter board. The adapter board, requires a serial command, which is sent using the pyserial library. The combined program is then able to sweep through every capacitor value and save a file for every measurement. This program is listed below.

```

1 import satimopm
2 import serial
3
4 basename = "triax_top_vert"
5 serial_port = "/dev/ttyUSB0"
6
7 # Start serial port
8 ser = serial.Serial(serial_port)
9 ser.flushInput()
10 ser.flushOutput()
11
12 # Only slave address A = 0x7 is used
13 ser.write(b"Ax0Ay0Az0At0")
14
15 # Start sweep
16 for x in [
17     ["0_0_0_0", b"Ax0Ay0Az0At0"],
18     ["2_0_0_0", b"Ax2Ay0Az0At0"],
19     ["4_0_0_0", b"Ax4Ay0Az0At0"],
20     ...
21     ["f_f_f", b"AxfAyfAzfAtf"],
22   ]:
23     fname,cmd = x
24     fname = basename + "_" + fname
25     ser.write(cmd)
26     satimopm.measure(fname)
27
28 ser.close()

```

Here, `measure()` is a function, which contains a collection of calls to the more basic `satimopm.satimoSPM()` function.

Appendix B

Post Processing

In this chapter, the libraries for post processing data from CST and Satimo will be described. The libraries are written in Python. By the end of the chapter, usage examples will be given. The libraries can be downloaded at <http://github.com/16gr1051>.

B.1 Installation

The libraries can be used on both Windows, Linux, and OSX. In order to use the libraries, they must be added to Python's PATH variable so Python can find them. The following steps show the procedure:

1. Make sure to install Python 3, numpy, scipy, and matplotlib.
2. Put the library files in a central directory (e.g. C:/PathTo/Something).
3. Add this path to the environment variable PYTHONPATH (*Environment Variables* in Windows and .bashrc or .profile in Linux/OSX). An example is shown in Listing B.1

```
1 | # ~/.profile
2 | export PYTHONPATH=$PYTHONPATH:/home/soren/pythonlibs
```

Listing B.1: Example of a .profile file for Linux, adding a library directory to the Python path.

B.2 Data Format

The .trx files, from Satimo Passive Measurement, contain data formatted in four columns:

1. Horizontal polarization, real part.
2. Horizontal polarization, imaginary part.
3. Vertical polarization, real part.
4. Vertical polarization, imaginary part.

Each column contains

$$n_r = n_f \times n_a \times n_e \quad (\text{B.1})$$

where

n_r = Total number of rows per column.

n_f = Number of different frequencies in the measurement.

n_a = Number of azimuth coordinates (usually 8).

n_e = Number of elevation coordinates (usually 15).

The first $n_a \times n_e$ rows are for the first frequency and the next $n_a \times n_e$ rows are for the second frequency. Within this, the first n_e rows are for the first azimuth angle and so on.

To get a better overview, the basic format for the following libraries is a $\theta \times \phi$ -matrix like the following:

$$M = \begin{bmatrix} m_{1,1} & m_{1,2} & \dots & m_{1,n} \\ m_{2,1} & m_{2,2} & \dots & m_{2,n} \\ \vdots & \vdots & & \vdots \\ m_{m,1} & m_{m,2} & \dots & m_{m,n} \end{bmatrix} \quad (\text{B.2})$$

The data is rearranged to have ϕ go from 0° to 360° and θ from 0° to 180° as shown in Table B.1.

Elements	θ	ϕ
$m_{1,1}$	0°	0°
$m_{1,n}$	0°	360°
$m_{m,1}$	180° [†]	0°

Table B.1: Format of $\theta \times \phi$ -matrix. [†]For Satimo measurements, this is $180 - 22.5 = 157.5^\circ$ because of the blind spot in the bottom.

B.3 Satimo Library

This library makes it possible to post-process data files extracted directly from Satimo Passive Measurement, i.e. trx files.

B.3.1 Function Documentation

col2mat(column, ntheta=SATIMO_NUM_ELEVATION, nphi=SATIMO_NUM_AZIMUTH)

Convert a Satimo PM-exported column to a matrix with ϕ on the x-axis and θ on the y-axis.

- column: Column from a Satimo PM export.
- ntheta: Number of rows in the output (theta in the input).
- nphi: Number of columns in the output (phi in the input).

Return:

Matrix with phi on the x-axis and theta on the y-axis.

ecc(Eth1, Eth2, Eph1, Eph2)

Compute the envelope correlation coefficient between two Satimo farfields. The farfields are split into theta and phi part. Each part is a matrix with theta on one axis and phi on the other. This function uses the satimo.intsphere() and not l3d.intsphere() and is therefore more accurate for Satimo measurements. *Note that no gain calibration is performed!*

- Eth1: List of E-fields, theta part, antenna 1
- Eth2: List of E-fields, theta part, antenna 2
- Eph1: List of E-fields, phi part, antenna 1
- Eph1: List of E-fields, phi part, antenna 2

Return:

Envelope Correlation Coefficients (array, one for each element in the input lists.)

Note:

https://mns.ifn.et.tu-dresden.de/Lists/nPublications/Attachments/612/Wang_Q_WSA_10.pdf

efficiency(trxfile, calfiles=[], reffiles=[], f_tot=[], P_tot=[])

Get the total efficiency of a trx file, exported from Satimo.

- trxfile: File, exported from Satimo PM, to compute the efficiency of.
- calfiles: List of calibration measurement files (trx files).
- reffiles: List of reference files relating to the calibration measurements.
- f_tot: Frequency axis of an existing total-power table.
- P_tot: Power axis of an existing total-power table. If an existing total-power table is supplied, the efficiency computation is much faster.

Return:

[f, eff] -- the total efficiency, eff, for each frequency, f.

intsphere(E)

Compute a spherical integral over the sphere recorded in Satimo. This is used for efficiency and correlation computation. The integration is not over a whole sphere, as a probe is missing at $\theta = 180^\circ$. Due to the low number of samples recorded in Satimo, the integration must be done carefully, only considering each sample one time. This is why l3d.intsphere() is not used.

- E: Field matrix to integrate (theta x phi).

Return:

Spherical integral of E.

intsphere_alt(Etot)

Alternative way of computing the radiated power/surface integral. For a small sample size, this method is not as accurate as `intsphere()`.

- `Etot`: Matrix (theta x phi) from Satimo PM to compute the radiate power of (surface integration).

Return:

Surface integral of `Etot` ~ radiated power.

loadref(f)

Load a reference file containing S_{11} , Gain, and Efficiency of a reference/calibration antenna. The reference files are cut to the following ranges, depending on file name:

- HomeRef600: No crop.
- SD740-70: 700–800 MHz.
- SD850-02: 800–900 MHz.
- SD900-52: 900–1000 MHz.
- SD1900-49: No crop.
- SD2050-36: No crop.
- SD2450-43: No crop.

Note that the 740 MHz reference file has the efficiency and gain columns swapped!

- `f`: File name.

Return:

`M[0]=frequency(Hz), M[1]=S11(..), M[2]=Gain(..), M[3]=Eff(..)`

loadtrx(f)

Load a trx measurement file from Satimo PM into memory.

- `f`: TRX file to load.

Return:

`[f, list_horiz, list_vert]` where

```
f = [f1, f2, f3, ...]
list_horiz = [E_horiz_f1, E_horiz_f2, E_horiz_f3, ...]
list_vert = [E_vert_f1, E_vert_f2, E_vert_f3, ...]
```

and each "E" is a complex matrix, (theta x phi), containing the received fields.

ma(values, window)

Moving average filter.

- `values`: Values/array to filter.
- `windows`: Size of the moving average filter.

Return:

Moving average filtered values.

mat2col(mat, ntheta=SATIMO_NUM_ELEVATION, nphi=SATIMO_NUM_AZIMUTH)

Convert a $(\theta \times \phi)$ matrix into the original column-format from the trx file.

- `mat`: Matrix with phi on the x-axis and theta on the y-axis.
- `ntheta`: Number of rows in the output (theta in the input).
- `nphi`: Number of columns in the output (phi in the input).

Return:

Column like a Satimo PM export, like the trx format.

radiatedpower(h,v)

Compute the radiated power for each frequency in the h and v list, using `satimo.intsphere()`.

- h: List of complex (theta x phi) matrices -- one for each frequency.
Horizontal polarization.
- v: List of complex (theta x phi) matrices -- one for each frequency.
Vertical polarization.

Return:

A vector with the radiated power for each frequency/element of h and v.

totalpower_table(calfiles, reffiles)

Make a table of calibrated “total power” for each frequency. Having (1) the total power and (2) the radiated power for a given antenna, makes it possible to compute the total efficiency of the antenna.

- calfiles: List of calibration measurement files (trx files) (order: lowest to highest frequency).
- reffiles: List of reference files relating to the calibration measurements (order: lowest to highest frequency).

Return:

[f,Ptot] -- the total power for each frequency.

B.4 CST Library

In order to compare measurements and simulations, a library for processing CST simulations has been created. This makes it possible to import farfields, etc, from CST and convert them to the common data format described above. Once the data is in this format, the same functions can be used on measurements and simulations (e.g. computing envelope correlation coefficient).

B.4.1 Function Documentation

col2mat(column, nx=360, ny=181)

Convert a CST-exported column to a matrix with ϕ on the x-axis and θ on the y-axis.

- column: Column from a Satimo export.
- nx: Number of columns in the output (phi in the input).
- ny: Number of rows in the output (theta in the input).

Return:

Matrix with phi on the x-axis and theta on the y-axis.

loadff(f)

Load a CST exported file to two ($\theta \times \phi$) matrices – one for θ and one for ϕ polarization.

- f: File to load.

Return:

[T,P] where T and P are each a (theta x phi) matrix.

B.5 3D Library

The 3D library is created for plotting $\theta \times \phi$ -matrices as well as computing the farfield envelope correlation coefficient between two farfields.

B.5.1 Function Documentation

ecc(Eth1, Eth2, Eph1, Eph2)

Compute the envelope correlation coefficient between two farfields. The farfields are split into θ and ϕ part. Each part is a matrix with θ on one axis and ϕ on the other.

- Eth1: E-field, theta part, antenna 1
- Eth2: E-field, theta part, antenna 2
- Eph1: E-field, phi part, antenna 1
- Eph2: E-field, phi part, antenna 2

```

Return:
Envelope Correlation Coefficient (scalar)

Note:
https://mns.ifn.et.tu-dresden.de/Lists/nPublications/Attachments/612/Wang_Q_WSA_10.pdf

```

intsphere(r, theta, phi)

Do a spherical integral of a $(\theta \times \phi)$ matrix.

- r: Matrix to integrate (x-axis=phi, y-axis=theta).
- phi: Phi axis values.
- theta: Theta axis values.

```

Return:
Scalar result of the integration.

```

plot3d(r, stride=1, th_lim=(0, 180), ph_lim=(0, 360))

Plot a matrix, $(\theta \times \phi)$, in 3D space.

- r: Matrix to plot.
- stride: Resolution of the output. 1=detailed+slow, 10=rough+fast.
- th_lim: Upper and lower theta limits (degrees).
- ph_lim: Upper and lower phi limits (degrees).

plotflat(r, th_lim=(0,180), ph_lim=(0,360), cmap="jet")

Plot a farfield-matrix as a color-map. Remember that 0° is the bottom of the plot in spherical coordinates.

- r: Matrix to plot (theta x phi).
- th_lim: Minimum and maximum theta/y-axis value (degrees).
- ph_lim: Minimum and maximum phi/x-axis value (degrees).
- cmap: Color map to use.

B.6 Plotting Library: aauplot

This library contains plotting functions to make plots consistent throughout the report. The plots contain markers for the LTE frequency bands to clearly signify what is in-band and out-of-band.

B.6.1 Function Documentation

correlation(f, ecc, c="-", label="")

Plot correlation

- f: Frequency axis.
- ecc: Envelope correlation coefficient.
- c: Color/linetype string (e.g. '--b' for dashed blue).
- label: Label for the graph's legend.

efficiency(f, e, c="-", label="")

Plot an efficiency graph.

- f: Frequency axis.
- e: Efficiency (. or dB).
- c: Color/linetype string (e.g. '--b' for dashed blue).
- label: Label for the graph's legend.

end_correlation(loc=1, fontsize=8)

Finish the correlation plot with legend, etc.

- loc: Location of the legend (like matplotlib.pyplot.legend())
- fontsize: Font size for the legend.

end_efficiency(kwargs)**

Finish the efficiency plot with legend, etc.

- kwargs: Arguments passed on to matplotlib.pyplot.legend()

end_sar(kwargs)**

Finish the SAR plot with legend, etc.

- kwargs: Arguments passed on to `matplotlib.pyplot.legend()`

end_sparam(kwargs)**

Finish the S-parameter plot with legend, etc.

- kwargs: Parameters passed onto `matplotlib.pyplot.legend()`.

figure(*args, **kwargs)

Set up a figure of the correct dimensions and the correct font for the report.

- args: Positional arguments for `matplotlib.pyplot.figure()`
- kwargs: All arguments are passed onto the `matplotlib.pyplot.figure()` function.

freqscale(f)

Scale to get frequency axis to MHz

- f: Frequency axis.

sar(f, sar, c="-", label="")

Plot a SAR graph.

- f: Frequency axis.
- e: Efficiency (. or dB).
- c: Color/linetype string (e.g. '--b' for dashed blue).
- label: Label for the graph's legend.

sparam(f, s, c="-", label="")

Plot an S-parameter.

- f: Frequency axis for the plot.
- s: S-parameter (abs-value in dB) to plot.
- c: Color/linetype string (e.g. '--b' for dashed blue).
- label: Label for the legend

to_db(x)

Convert/preserve data in dB

- x: Data to convert (e.g. efficiency).

Return:

Data in dB.

B.7 Examples

In this section, examples will be given of the libraries described above. The several libraries may be used in each example.

B.7.1 Extract Efficiency from Satimo

In the following example, the efficiency of an antenna is extracted. In order to do this, calibration measurements must be added to the `calfilenames` list. The `reffilenames` list contains reference data of the antennas used for calibration. *Note, that the files from these two lists must be written in ascending order, i.e. lowest frequency first.* In this example, the file `antenna_meas.trx` is the antenna from which the efficiency is extracted. The output is saved to the file shown in Figure B.1.

```

1 | import satimo
2 | from matplotlib.pyplot import *
3 |
4 | # Calibration measurements
5 | calfilenames = [
6 |     "calib/calib2450.trx",
7 | ]

```

```

8
9 # Reference files
10 reffiles = [
11     "calib/SD740-70.ref",
12     "calib/SD850-02.ref",
13     "calib/SD900-51.ref",
14     "calib/SD1800-45.ref",
15     "calib/SD1900-49.ref",
16     "calib/SD2050-36.ref",
17     "calib/SD2450-43.ref",
18     "calib/SD2600-28.ref",
19 ]
20
21 f,eff = satimo.efficiency("antenna_meas.trx", calfiles, reffiles)
22
23 plot(f/1e9, eff)
24 grid()
25 xlabel("Frequency [GHz]")
26 ylabel("Efficiency [.]")
27 savefig("ex1_efficiency.pdf")
28
29 show()

```

Listing B.2: Extracting efficiency from Satimo.

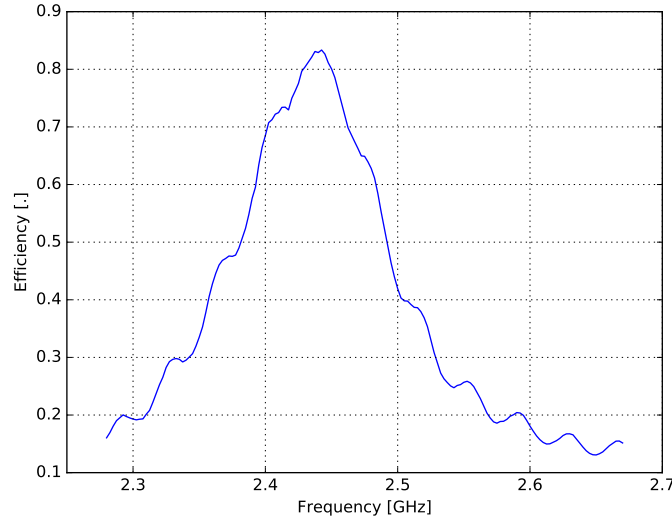


Figure B.1: Output from Listing B.2.

B.7.2 Plot 3D Farfield

The (rough) farfield directly exported from Satimo's 15 probes can be plotted in 3D as shown below. The result is shown in Figure B.2. A similar plot – a 2D color plot – is also plotted.

```

1 from numpy import *
2 from matplotlib.pyplot import *
3 import satimo
4 import l3d
5
6 f,h,v = satimo.loadtrx("antenna_meas.trx")
7
8 # Choosing one specific frequency
9 print("Farfield frequency: %.2f GHz" % (f[0]/1e9))
10 h = h[0]
11 v = v[0]
12
13 E = sqrt(abs(h)**2 + abs(v)**2)

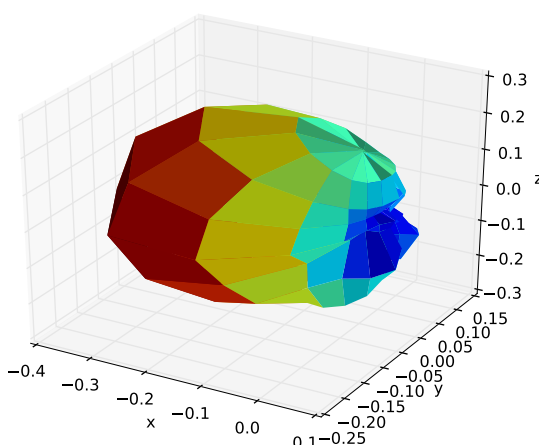
```

```

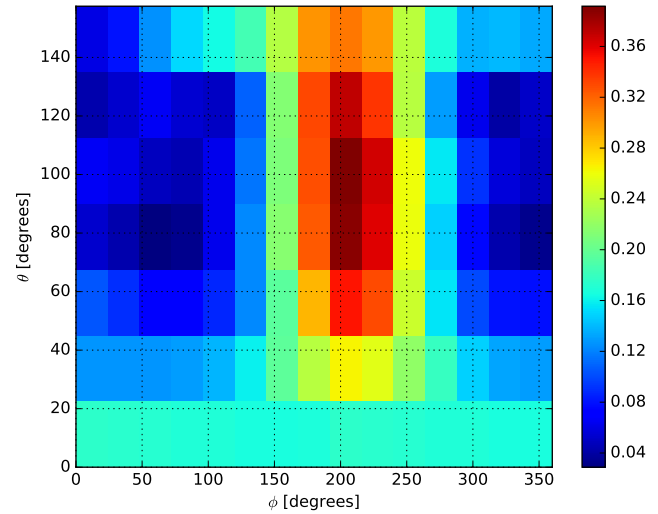
14
15 figure()
16 l3d.plot3d(E, th_lim=(0, 180-22.5)) # No probe at theta = 180
17 savefig("ex2_3dfarfield.pdf")
18
19 figure()
20 l3d.plotflat(E, th_lim=(0, 180-22.5))
21 savefig("ex2_2dfarfield.pdf")
22
23 show()

```

Listing B.3: Plot 3D Farfield.



(a) 3D.



(b) 2D.

Figure B.2: Output from Listing B.3.

B.7.3 Import a Farfield from CST

The following example will import and plot a farfield from CST. The farfield should be exported under the Post Processing tab. The output is shown in Figure B.3.

```

1 from numpy import *
2 from matplotlib.pyplot import *
3 import cst
4 import l3d
5
6 T,P = cst.loadff("cst_farfield.txt")
7
8 E = sqrt(abs(T)**2 + abs(P)**2)
9
10 figure()
11 l3d.plot3d(E, stride=10)
12 savefig("ex3_3dfarfield.pdf")
13
14 figure()
15 l3d.plotflat(E)
16 savefig("ex3_2dfarfield.pdf")
17 show()

```

Listing B.4: Import a Farfield from CST.

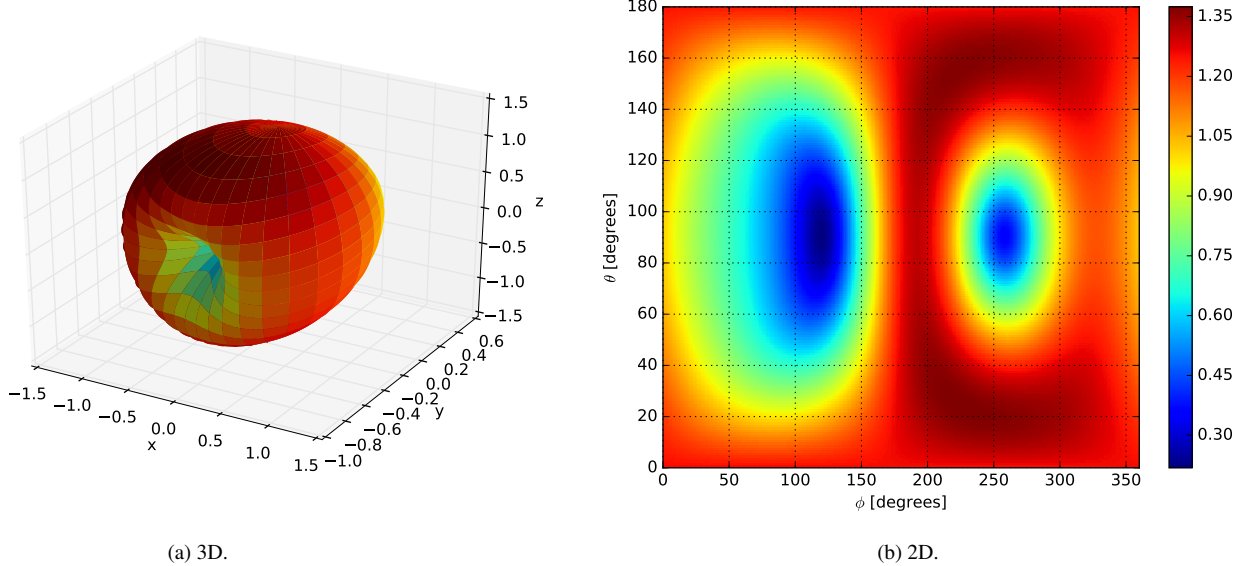


Figure B.3: Output from Listing B.4.

B.7.4 Export Efficiency for Further Analysis

Using Python and numpy, analysis and comparison can be done just as easily as in MATLAB. However, if one is more familiar with MATLAB or need the data for other software, it is advantageous to export the data. Here is a simple example of exporting the efficiency as a data file.

```

1 import satimo
2 from numpy import *
3
4 calfiles = ["calib/calib2450.trx"]
5 reffiles = [
6     "calib/SD740-70.ref",
7     "calib/SD850-02.ref",
8     "calib/SD900-51.ref",
9     "calib/SD1800-45.ref",
10    "calib/SD1900-49.ref",
11    "calib/SD2050-36.ref",
12    "calib/SD2450-43.ref",
13    "calib/SD2600-28.ref",
14 ]
15
16 f,eff = satimo.efficiency("antenna_meas.trx", calfiles, reffiles)
17 savetxt("ex4_efficiency.txt", transpose([f, eff]))

```

Listing B.5: Export efficiency for further analysis.

The output is a tab-separated file (`ex4_efficiency.txt`) which can easily be imported into MATLAB or similar software.

B.7.5 Plots for IEEEtran Articles

It is often desirable to export graphs in a format that is compliant with the text used articles. In the standard IEEEtran format, a *Times* font is used. For figures, the default font size is 8 pt. The column width is 3.5 inches. In the example, the figure size is set to 3.5inches \times 3inches.

Note that math symbols can easily be used in figure text (e.g. labels) in the same way as symbols are written in L^AT_EX, e.g. “\$\\theta\$ in degrees” becomes “ θ in degrees”.

The result is shown in Figure B.4.

```

1 import satimo
2 from matplotlib.pyplot import *
3 rcParams['font.family'] = "Times New Roman"
4 rcParams['font.size'] = "8"
5

```

```

6 # Calibration measurements
7 calfiles = [
8     "calib/calib2450.trx",
9 ]
10
11 # Reference files
12 reffiles = [
13     "calib/SD740-70.ref",
14     "calib/SD850-02.ref",
15     "calib/SD900-51.ref",
16     "calib/SD1800-45.ref",
17     "calib/SD1900-49.ref",
18     "calib/SD2050-36.ref",
19     "calib/SD2450-43.ref",
20     "calib/SD2600-28.ref",
21 ]
22
23 f,eff = satimo.efficiency("antenna_meas.trx", calfiles, reffiles)
24
25 figure(figsize=(3.5, 3)) # Figure size.
26 plot(f/1e9, eff)
27 grid()
28 xlabel("Frequency [GHz]")
29 ylabel("Efficiency [.]")
30 tight_layout() # Clean up figure.
31 savefig("ex5_efficiency.pdf")
32 show()

```

Listing B.6: Plots for IEEEtran articles.

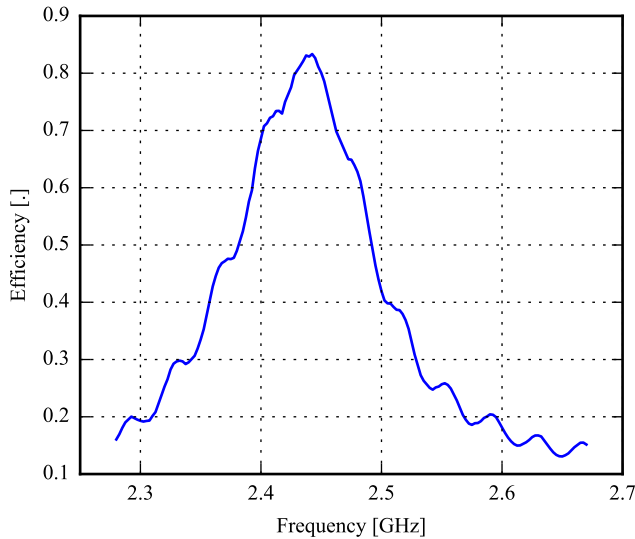


Figure B.4: Output from Listing B.6.

B.7.6 aauplot: Plot S-Parameters

In the following script, a CSV file from a VNA is plotted using the aauplot library. The output is shown in Figure B.5

```

1
2
3
4
5
6
7
8

```

```

1 | from numpy import *
2 | from matplotlib.pyplot import *
3 | import aauplot
4 |
5 | aauplot.figure()
6 | m = loadtxt("ex1_sparams.csv", skiprows=3).T
7 |
8 | aauplot.sparam(m[0], m[1], label="S11")

```

```

9 | aauplot.sparam(m[0], m[3], label="S21")
10| aauplot.sparam(m[0], m[5], label="S22")
11| aauplot.end_sparam(loc=1)
12|
13| savefig("ex1_sparams.pdf")
14| show()

```

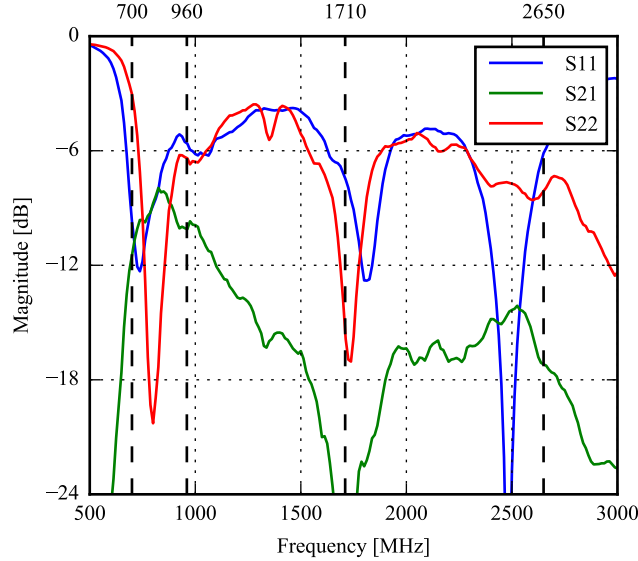


Figure B.5: Output from Listing B.7.6.

B.7.7 aauplot: Plot Efficiency

The Satimo library is here used to extract the efficiency of an antenna measured in the Satimo chamber. The aauplot library is used to plot the result. Note that, as opposed to the efficiency example shown above, a calibration table is computed prior to analysis. This means that the calibration is only loaded once, making the processing faster. This can be done when several measurements from the same calibration are analyzed. The result is shown in Figure B.6.

```

1 | from numpy import *
2 | from matplotlib.pyplot import *
3 | import aauplot
4 | import satimo
5 |
6 | reffiles = [
7 |     "satimo/ref/HomeRef600.ref",
8 |     "satimo/ref/SD740-70.ref",
9 |     "satimo/ref/SD850-02.ref",
10|    "satimo/ref/SD900-51.ref",
11|    "satimo/ref/SD1800-45.ref",
12|    "satimo/ref/SD2050-36.ref",
13|    "satimo/ref/SD2450-43.ref",
14| ]
15|
16| calfiles = [
17 |     "satimo/cal/665RefDipole.trx",
18 |     "satimo/cal/740RefDipole.trx",
19 |     "satimo/cal/850RefDipole.trx",
20 |     "satimo/cal/900RefDipole.trx",
21 |     "satimo/cal/1800RefDipole.trx",
22 |     "satimo/cal/2050RefDipole.trx",
23 |     "satimo/cal/2450RefDipole.trx",
24 | ]
25|
26| # Compute calibration table for measurement
27| f_tot,P_tot = satimo.totalpower_table(calfiles, reffiles)
28|

```

```

29 # Load low and high band measurement
30 f_L,eff_L = satimo.efficiency("satimo/antenna/ant_lb.trx", f_tot=f_tot, P_tot=P_tot)
31 f_H,eff_H = satimo.efficiency("satimo/antenna/ant_hb.trx", f_tot=f_tot, P_tot=P_tot)
32
33 # Combine the low and high band
34 f = hstack((f_L,f_H))
35 eff = hstack((eff_L,eff_H))
36
37 # Plot the results
38 aauplot.figure()
39 aauplot.efficiency(f,eff)
40 aauplot.end_efficiency(loc=4);
41
42 savefig("ex2_efficiency.pdf")
43 show()

```

Listing B.7: aauplot: Plot Efficiency

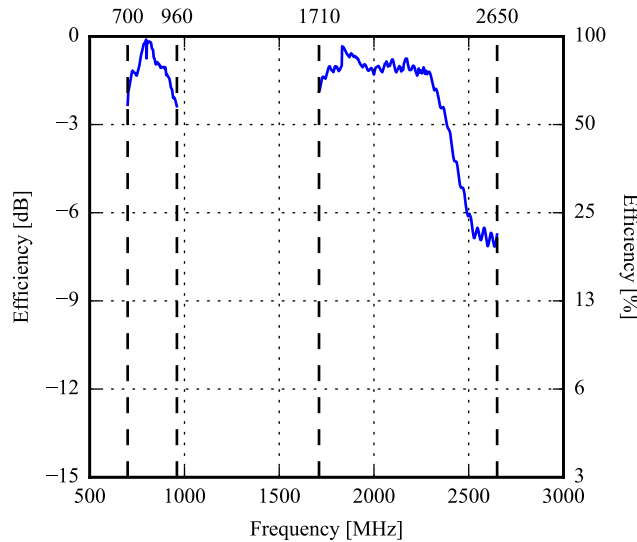


Figure B.6: Output from Listing B.7.

B.7.8 aauplot: Plot Correlation from a Satimo Measurement

In this example, the farfield of two antennas measured in Satimo. The Satimo Library and the aauplot library is used to plot the envelope correlation coefficient. The result is shown in Figure B.7. Note that the two measured antennas must be positioned in *exactly* the same position.

```

1 from numpy import *
2 from matplotlib.pyplot import *
3 import aauplot
4 import satimo
5
6 f_L1,h_L1,v_L1 = satimo.loadtrx("ex3/antenna/top_lb.trx")
7 f_H1,h_H1,v_H1 = satimo.loadtrx("ex3/antenna/top_hb.trx")
8 f_L2,h_L2,v_L2 = satimo.loadtrx("ex3/antenna/side_lb.trx")
9 f_H2,h_H2,v_H2 = satimo.loadtrx("ex3/antenna/side_hb.trx")
10
11 ecc_L = satimo.ecc(h_L1,h_L2, v_L1,v_L2)
12 ecc_H = satimo.ecc(h_H1,h_H2, v_H1,v_H2)
13
14 f = hstack((f_L1, f_H1))
15 ecc = hstack((ecc_L, ecc_H))
16
17 aauplot.figure()
18 aauplot.correlation(f,ecc)

```

```
19 | aauplot.end_correlation(loc=4);
20 |
21 | savefig("ex3_correlation.pdf")
22 | show()
```

Listing B.8: aauplot: Plot correlation from a Satimo measurement.

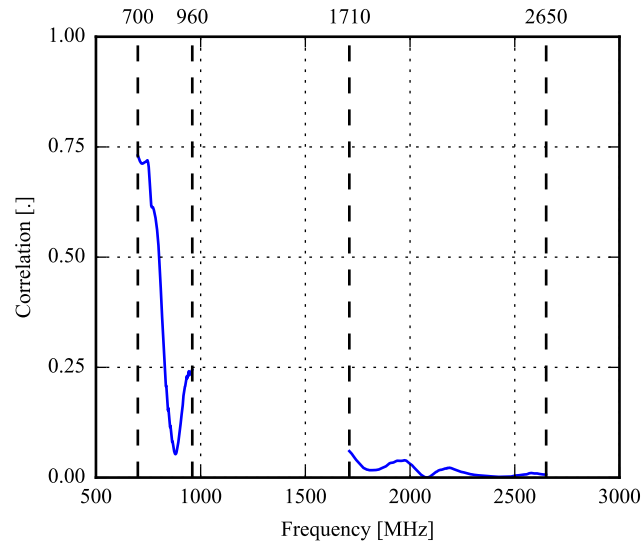


Figure B.7: Output from Listing B.8.

Appendix C

CST Macros

This chapter contains macros for automating CST Microwave Studio. In order to use a macro, go to Macros → Make VBA Macro → “MacroName” → Paste the macro code.

C.1 Sweep Total Efficiency

The following macro makes it possible to sweep a parameter (used in Schematic View) and save the System Total Efficiency to a file for each value. In order to use the script, the following must first be done:

- Create a farfield monitor in 3D View for each frequency of interest.
- In Schematic View, create an AC, Combine results-task. Use this to obtain farfields which are updated when the schematic is updated. This creates “AC”-versions of the farfields and efficiencies in 3D View.

The macro creates a graphical user interface where the user must input

Parameter The parameter to be swept.

From The initial parameter value.

To The final parameter value.

Step The step-size.

Output dir The directory where the output files will be stored (should *not* end on /).

AC The AC parameter to be stored (e.g. AC1).

The macro is shown in Listing C.1. The output is one text file for each parameter, located in the given output directory.

```
1 ' ExportEfficiency
2
3 Sub Main ()
4     Dim Studio As Object
5
6     Begin Dialog UserDialog 360,161,"Export Efficiency Sweep" ' %GRID:10,7,1,1
7         Text 0,0,180,14,"Parameter",.LParameter
8         Text 0,21,180,14,"From",.LFrom
9         Text 0,42,180,14,"To",.LTo
10        Text 0,63,180,14,"Step",.LStep
11        Text 0,84,180,14,"Output dir",.LOutputdir
12        Text 0,105,180,14,"AC (e.g. AC1, AC2, ...)",.LAc
13        TextBox 180,0,180,21,.EParameter
14        TextBox 180,21,180,21,.EFrom
15        TextBox 180,42,180,21,.ETO
16        TextBox 180,63,180,21,.EStep
17        TextBox 180,84,180,21,.EOOutputDir
18        TextBox 180,105,180,21,.EAc
19        OKButton 180,140,90,21
20        CancelButton 270,140,90,21
21    End Dialog
22    Dim dlg As UserDialog
23    Dialog dlg
24
25    ' Do parameter sweep. Save txt file for each iteration
```

```
26 | Dim ThisVal As Double
27 | For ThisVal = CDbL(dlg.EFrom) To CDbL(dlg.ETO)+0.01 STEP CDbL(dlg.EStep)
28 |     StoreParameter(dlg.EParameter, ThisVal)
29 |     DS.UpdateResults
30 |     SelectTreeItem "1D Results\Efficiencies\System Tot. Efficiency [" + dlg.EAc + "]"
31 |     ExportPlotData dlg.EOutputDir + "\\" + CStr(ThisVal) + ".txt"
32 | Next
33 | End Sub
```

Listing C.1: Sweep Total Efficiency macro for CST.

Bibliography

- [1] K. Hilbert, Jeffrey L.; Iniewski, *Tunable RF components and circuits: Applications in mobile handsets*. Devices circuits and systems, CRC Press, 2015.
- [2] A. Tanenbaum and D. Wetherall, *Computer Networks*. Pearson Education, 2012.
- [3] H. Holma and A. Toskala, *LTE for UMTS: Evolution to LTE-Advanced*. Wiley, 2011.
- [4] T. Brown, P. Kyritsi, and E. De Carvalho, *Practical Guide to MIMO Radio Channel: with MATLAB Examples*. Wiley, 2012.
- [5] S. C. D. Barrio, A. Morris, and G. F. Pedersen, “Mems tunable antennas to address lte 600 mhz-bands,” in *2015 9th European Conference on Antennas and Propagation (EuCAP)*, pp. 1–4, May 2015.
- [6] M. Pelosi, O. Franek, M. B. Knudsen, M. Christensen, and G. F. Pedersen, “A grip study for talk and data modes in mobile phones,” *IEEE Transactions on Antennas and Propagation*, vol. 57, pp. 856–865, April 2009.
- [7] Q. Gu, *RF Tunable Devices and Subsystems: Methods of Modeling, Analysis, and Applications*. EBL-Schweitzer, Springer International Publishing, 2014.
- [8] J. Ilvonen, R. Valkonen, J. Holopainen, and V. Viikari, “Multiband frequency reconfigurable 4g handset antenna with mimo capability,” vol. 148, pp. 233–243, 2014.
- [9] A. Morris, S. C. D. Barrio, J. Shin, V. Steel, and G. F. Pedersen, “Tunable antennas for mobile devices: Achieving high performance in compelling form factors,” in *2014 IEEE MTT-S International Microwave Symposium (IMS2014)*, pp. 1–4, June 2014.
- [10] H. Xia, H. Wang, L. Meng, and G. Yang, “A compact multi-band tunable lte antenna for mobile applications,” in *2015 IEEE International Symposium on Antennas and Propagation USNC/URSI National Radio Science Meeting*, pp. 1152–1153, July 2015.
- [11] A. Tatomirescu and G. F. Pedersen, “Alternative duplexing for lte fdd using the theory of characteristic modes,” in *2015 9th European Conference on Antennas and Propagation (EuCAP)*, pp. 1–4, May 2015.
- [12] L. H. Trinh, F. Ferrero, L. Lizzi, R. Staraj, and J. M. Ribero, “Reconfigurable antenna for future spectrum reallocations in 5g communications,” *IEEE Antennas and Wireless Propagation Letters*, vol. 15, pp. 1297–1300, 2016.
- [13] R. Prasad, *Universal Wireless Personal Communications*. Artech House Mobile Communications Library, Artech House, 1998.
- [14] Radio-Electronics, “Resources and analysis for electronics engineers – cellular/telecommunications.” <http://www.radio-electronics.com/info/cellulartelecomms/lte-long-term-evolution/lte-frequency-spectrum.php>, 2015.
- [15] FCC, “Auction of 700 mhz band licenses scheduled for january 16, 2008.” https://apps.fcc.gov/edocs_public/attachmatch/DA-07-3415A1.pdf, 2007.
- [16] J. Rogerson, “4g and lte: everything you need to know.” <http://www.techradar.com/news/phone-and-communications/mobile-phones/4g-and-lte-everything-you-need-to-know-926835>, 2014.
- [17] D. Pozar, *Microwave Engineering, 4th Edition*. Wiley, 2011.
- [18] C. Balanis, *Antenna Theory: Analysis and Design*. Wiley, 2012.

- [19] A. D. Yaghjian, A. D. Yaghjian, and S. R. Best, "Impedance, bandwidth, and q of antennas," vol. 53, pp. 1298,1299,1300,1301,1302,1303,1304,1305,1306,1307,1308,1309,1310,1311,1312,1313,1314,1315,1316,1317,1318,1319,1320,1321,2005.
- [20] K. Fujimoto, *Mobile Antenna Systems Handbook*. Artech House antennas and propagation library, Artech House, 2008.
- [21] D. Sánchez-Hernández, *Multiband Integrated Antennas for 4G Terminals*. Artech House antennas and propagation library, Artech House, 2008.
- [22] H. A. Wheeler, "Fundamental limitations of small antennas," *Proceedings of the IRE*, vol. 35, pp. 1479–1484, Dec 1947.
- [23] L. Chu, "Physical limitations of omni-directional antennas," *J. Appl. Phys.*, vol. 19, no. 12, p. 1163, 1948.
- [24] J. McLean, "A re-examination of the fundamental limits on the radiation q of electrically small antennas," *IEEE Trans. Antennas Propag.*, vol. 44, p. 672, May 1996.
- [25] H. Ebert and P. Raskmark, *Grundlæggende Transmissionsledningsteori*. Aalborg Universitet, 1998.
- [26] C. Bowick, *RF Circuit Design*. RF Bundle, RF Circuit Design Series, Elsevier Science, 2011.
- [27] J. D. Irwin and R. M. Nelms, *Engineering Circuit Analysis*. Wiley, 2011.
- [28] R. Sarapeshkar, *Ultra Low Power Bioelectronics: Fundamentals*. Cambridge University Press, 2010.
- [29] R. L.-R. J. T. Aberle, *Active Antennas with Non-Foster Matching Networks*. Morgan and Claypool Publishers, 2009.
- [30] A. Goldsmith, *Wireless Communications*. Cambridge University Press, 2005.
- [31] J. Parsons, *The Mobile Radio Propagation Channel*. Wiley, 2000.
- [32] J. Seybold, *Introduction to RF Propagation*. Wiley, 2005.
- [33] "REPORT ITU-R SM.2028-1 Monte Carlo simulation methodology for the use in sharing and compatibility studies between different radio services or systems." White Paper, 2002.
- [34] C. Balanis, *Modern Antenna Handbook*. Wiley, 2008.
- [35] Z. Zhang, *Antenna Design for Mobile Devices*. John Wiley & Sons, John Wiley & Sons (Asia), 2011.
- [36] E. Buskgaard, A. Tatomirescu, S. Del Barrio, O. Franek, and G. Pedersen, "User effect on the mimo performance of a dual antenna lte handset," in *Antennas and Propagation (EuCAP), 2014 8th European Conference on*, pp. 2006–2009, April 2014.
- [37] FCC, "Specific absorption rate (sar) for cell phones." <https://www.fcc.gov/consumers/guides/specific-absorption-rate-sar-cell-phones-what-it-means-you>, 2015.
- [38] E. Biglieri, *MIMO Wireless Communications*. Cambridge University Press, 2007-01-08.
- [39] P. V. David Tse, *Fundamentals of Wireless Communication*. Cambridge University Press, 2005-07-11.
- [40] A. Tatomirescu, M. Pelosi, M. Knudsen, O. Franek, and G. Pedersen, "Port isolation method for mimo antenna in small terminals for next generation mobile networks," in *Vehicular Technology Conference (VTC Fall), 2011 IEEE*, pp. 1–5, Sept 2011.
- [41] *Design and performance evaluation of handset MIMO antenna prototypes*, 2010.
- [42] A. Z. Alain Sibille, Claude Oestges, *MIMO: From Theory to Implementation*. Academic Press, 2010-11-15.
- [43] R. Tian, B. K. Lau, and Z. Ying, "Multiplexing efficiency of mimo antennas," *Antennas and Wireless Propagation Letters, IEEE*, vol. 10, pp. 183–186, 2011.
- [44] A. Taflove and S. C. Hagness, *Computational Electrodynamics: The Finite-Difference Time-Domain Method*. Artech House, 2000.
- [45] F. Hirtenfelder, "Effective antenna simulations using cst microwave studio®," in *Antennas, 2007. INICA '07. 2nd International ITG Conference on*, pp. 239–239, March 2007.

- [46] K. S. Kunz and R. J. Luebbers, *Finite Difference Time Domain Method for Electromagnetics*. CRC Press LLC, 1993.
- [47] "Introduction to network analyzer measurements – fundamentals and background." White Paper.
- [48] "Understanding the fundamental principles of vector network analysis." Application Note, Dec. 2012.
- [49] "Electronic vs. mechanical calibration kits: Calibration methods and accuracy." White Paper, June 2003.
- [50] Satimo, "Starlab 18 ghz in paris." <http://satimo.com/content/starlab-18-ghz-paris>.
- [51] R. Valkonen, J. Ilvonen, C. Icheln, and P. Vainikainen, "Inherently non-resonant multi-band mobile terminal antenna," *Electronics Letters*, vol. 49, pp. 11–13, January 2013.
- [52] J. Ilvonen, R. Valkonen, J. Holopainen, and V. Viikari, "Design strategy for 4g handset antennas and a multiband hybrid antenna," *Antennas and Propagation, IEEE Transactions on*, vol. 62, pp. 1918–1927, April 2014.
- [53] A. Tatomirescu, E. Buskgård, and G. F. Pedersen, "Correlation coefficient control for a frequency reconfigurable dual-band compact mimo antenna destined for lte," in *Antenna Technology: "Small Antennas, Novel EM Structures and Materials, and Applications" (iWAT), 2014 International Workshop on*, pp. 80–83, March 2014.
- [54] S. S. Zhekov, A. Tatomirescu, and G. F. Pedersen, "Compact multiband sensing mimo antenna array for cognitive radio system," in *Antennas Propagation Conference (LAPC), 2015 Loughborough*, pp. 1–5, Nov 2015.
- [55] S. Zhang, K. Zhao, Z. Ying, and S. He, "Diagonal antenna-chassis mode for wideband lte mimo antenna arrays in mobile handsets," in *Antenna Technology (iWAT), 2013 International Workshop on*, pp. 407–410, March 2013.
- [56] CITA Certification, 1400 16th Street N.W., Suite 600 Washington, DC 20036, *CITA Certification – Test Plan for Wireless Device Over- the-Air Performance*, 3.5.2 ed., September 2015.
- [57] Rohde and Schwarz, *R&S ZVA/ZVB/ZVT Vector Network Analyzers Operating Manual*. Rohde and Schwarz.